Hydroxyapatite Nanoparticles and Nanobiocomposite Scaffold for Protein Adsorption and Release

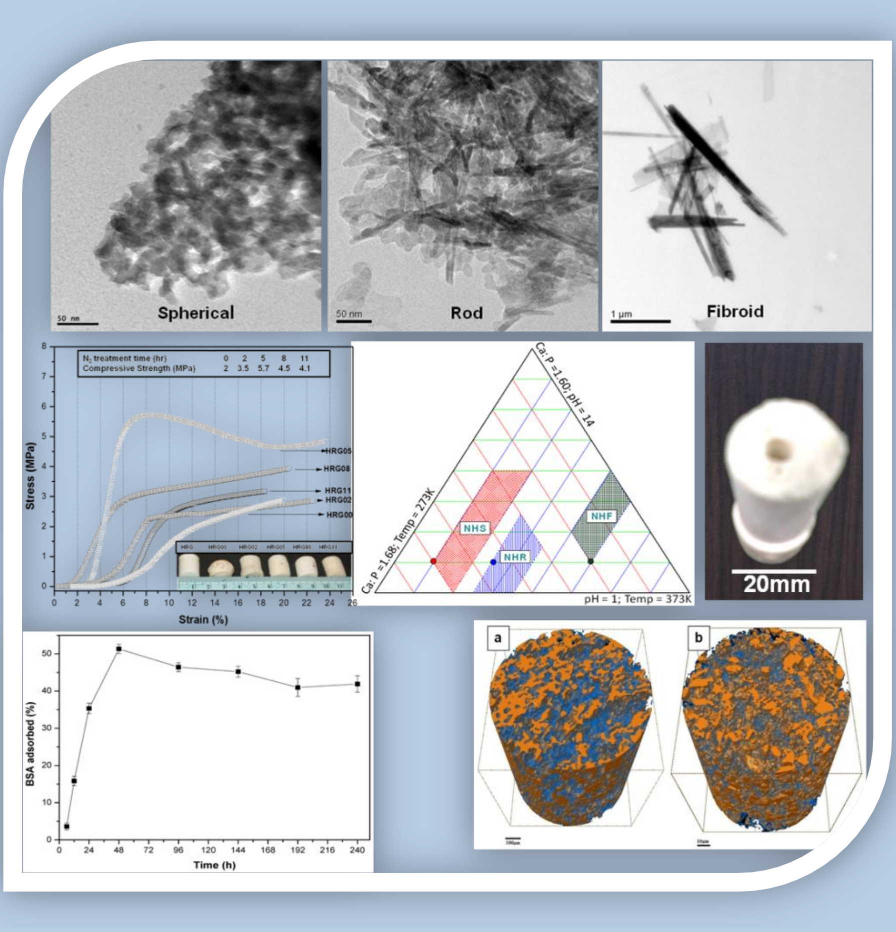

Sanjaya Kumar Swain

Hydroxyapatite Nanoparticles and Nanobiocomposite Scaffold for Protein Adsorption and Release

A THESIS SUBMITTED IN PARTIAL FULFILMENT
OF THE REQUIREMENT FOR THE DEGREE OF

Doctor of Philosophy
in
Ceramic Engineering

By
Sanjaya Kumar Swain
(509CR102)

Supervisor:
Dr. Debasish Sarkar

Department of Ceramic Engineering
National Institute of Technology
Rourkela

January 2014

CERTIFICATE

This is to certify that the thesis entitled, "Hydroxyapatite Nanoparticles and Nanobiocomposite Scaffold for Protein Adsorption and Release" submitted by Mr. Sanjaya Kumar Swain in partial fulfilment of the requirement for the award of Doctor of Philosophy Degree in Ceramic Engineering at the National Institute of Technology, Rourkela is an authentic work carried out by him under my supervision and guidance.

To the best of my knowledge, the matter embodied in the thesis has not been submitted in any other University/Institute for the award of any Degree or Diploma.

Date: 14/01/2014

Prof. Debasish Sarkar
Department of Ceramic Engineering
National Institute of Technology
Rourkela-769008

Declaration

I declare that this thesis is my own work and has not been submitted in any form for another degree or diploma at any university or other institution of tertiary education. Information derived from the published or unpublished work of others has been acknowledged in the text and a list of references given.

14/01/2014

Date

Sanjaya Kumar Swain

SKSwain

Signature

Abstract

Spherical, rod and fibrous hydroxyapatite (HA) nanoparticles synthesize through a common co-precipitation technique and fabricate macroporous HA-gelatin nanobiocomposite scaffolds for protein adsorption/release study. Three fundamental processing parameters such as solution pH, temperature and Ca/P ratio synchronize the morphology and crystallinity of nano HA from identical precursors $Ca(CH_3COO)_2$ and KH_2PO_4. Dispersion study illustrates the HA nanoparticle suspension stability phenomenon in aqueous media. Rod shaped HA exhibits relatively better bovine serum albumin (BSA) protein adsorption efficacy with compare to other two morphologies. In aqueous media, one gram nanorod HA particle adsorb 28 mg BSA within a time frame of 48 h and subsequently 75 wt.% release after 96 h in phosphate buffer solution. Low temperature freeze casting of homogenous aqueous slurry of HA nanoparticles, gelatin and biocompatible polyvinyl alcohol binder develops nano HA – gelatin nanobiocomposite macroporous scaffolds. Freeze casted nanorod HA-gelatin macroporous (70 vol.%) scaffold demonstrate highest yield compressive strength of ~2 MPa compare to other scaffolds prepared from spherical and fibrous HA because of high surface area and the effective anchoring. An optimum cryogenic treatment time at 77K promotes the mechanical response of this low strength scaffold and designates as cryo-treated hydroxyapatite–gelatin macroporous scaffold (CHAMPS). CHAMPS has a high degree of interconnected pores of 50-200 μm in size, compressive strength up to 5.6 MPa and larger strain failure up to 25%. L929 mouse fibroblast cell interaction supports the cytotoxicity and cell adherence behaviour with CHAMPS. Porous scaffold exhibits bioactivity in simulated body fluid (SBF) solution through preferable deposition of carbonated apatite layer around the pores. Biodegradation of scaffold in tris-HCl solution reveals a slow but systematic decrease in weight over incubation up to 7 days. Importantly, the excellent adsorption (upto 50 wt.%) and release (upto 60 wt.% of adsorbed protein) of BSA within 48 h has been uniquely attributed to the inherent porous microstructure of the CHAMPS. Protein adsorption behaviour for both of the particles and scaffolds follow the classical Langmuir isotherm. The extensive micro-computed tomography (micro-CT) analysis establishes cancellous bone-like highly interconnected and complex porous architecture of the protein loaded and original CHAMPS. Overall, the present study provides an assessment of the interaction of protein with HA nanoparticles and their cryotreated HA-gelatin scaffold *in vitro* to support as drug delivery media and tissue engineering, respectively.

Keywords: Hydroxyapatite, Nanoparticle, Nanobiocomposite, Protein, Scaffold, Adsorption, Release.

Acknowledgements

I wish to express my deep sense of gratitude and indebtedness to Prof. Debasish Sarkar, Department of Ceramic Engineering, N.I.T Rourkela for assigning me the project "Hydroxyapatite Nanoparticles and Nanobiocomposite Scaffold for Protein Adsorption and Release" and for his inspiring guidance, constructive criticism and valuable suggestion throughout this research work.

I express my sincere thanks to Prof. Swadesh Pratihar, Head, Department of Ceramic Engineering for providing me all the departmental facilities required for the completion of the thesis. I am thankful to INAE Distinguished Professor H.S. Maiti, Department of Ceramic Engineering, for valuable suggestions and encouragement. I am also thankful to all other faculty members of Ceramic Engineering Department, NIT Rourkela for their constructive suggestions and encouragement at various stages of the work.

I am thankful to Director, SCTIMST, Thiruvananthapuram for permitting me to carry out cytotoxicity and cell viability tests in his institute. I am also thankful to Director, PSG College of Technology, Coimbatore for permitting to carry out TEM analysis. The authors also thank Dr. Phil Salmon of the Skyscan, Belgium for assistance in micro-CT evaluation.

I am also thankful to Mr. Ganesh Kumar Sahoo, Mr. Balaji Kumar Choudhury, Mr. Satya Narayan Tripathy and all the research scholars in the Department of Ceramic Engineering for their kind help and providing all joyful environments throughout this work. Last but not least, my sincere thanks to all my friends who have patiently extended all sorts of help for accomplishing this undertaking.

Sanjaya Kumar Swain
Ph.D
Ceramic Engineering

Table of Contents

List of Figures

List of Tables

Chapter-1

Introduction

Chapter 1 Introduction

1.1 General introduction

Now-a-days the artificial biomaterial use increases due to limited accessibility of autograft and significant disadvantage of allograft include the risk of induction of transmissible diseases in the recipient [1,2]. As a consequence, the interest shifts toward the use of synthetic implantable biomaterial for repair of bone defect, bone fracture repair, alveolar ridge augmentation, dental implant, ear implants, spine fusion that simulating the bone bonding properties and morphology of natural bone.

Bone is a structure composed of hydroxyapatite ($Ca_{10}(PO_4)_6(OH)_2$) crystals deposited within an organic matrix collagen [3,4]. Commercial and clinical viable synthetic hydroxyapatite (HA) demonstrate as calcium phosphate based most potential biomaterial to be used as an efficient carrier for bone growth factors or drug delivery media [5]. The nano-biomaterial with an advantage of nanosized HA particles and compatibility with the inorganic bone crystal of the human body is extensively considering for tissue engineering. Nano size HA is an excellent bioactive site because of high surface to volume ratio, and reactivity than the same micron size material [6]. Thus, nano sized HA particles have arouse intensive interest and the same time high effort concentrate since the last decade to synthesis and understand their structure and properties. However, it is always difficult to synthesise HA nanoparticles with well defined size, morphology and crystallinity with respect to desire biological applications [7]. Moreover, nano HA has extensive market for the biocoating on the implants because of bioactive and biocompatible similarity with human hard tissue and biodegradable properties, which finally reduce the failure of the implants [8,9]. Hence, HA nanoscale particle and their biocomposite have direct or indirect influence as drug delivery media or scaffold. Nano HA ceramics has attractive ability to create direct bonding with host bone and their strong interface. The formation of the active interface is the result of sequence events involving interaction between biological fluid and cells as well as the formation of carbonated HA, which is similar to bone mineral [10]. Slow, localized and continuous release drug efficacy has also been recognized as a better choice for the treatment of many ailments. One of the potential candidate for such controlled drug delivery system is porous ceramic, and, therefore, much attention paid to fabricate biocompatible porous HA or their biocomposites [11]. For example, chronic disease or localized surgical intervention is relying on a continuous local drug delivery through ceramic capsule suitable to release drug at a controlled rate [12]. Bone drug delivery systems develop using porous HA ceramic bonded with antibiotics through a biodegradable polymeric matrices. Hence, porous HA has extensive demand and applied for artificial bone substitutes [10,13].

Porous HA implants have been served as bone substitute in the clinics since long [14]. However, lower mechanical strength of pure HA deteriorate adequate use as a bone implant material because of conflicting requirements of porosity and strength [4,15]. The primary purpose of tissue engineering need to repair, regeneration and reconstruction of lost, damaged or degenerative tissues by the combinations of cells, biomaterials and biologically active molecules by applying the principles of engineering and life science [16,17]. Most of the existing tissue engineering techniques based on the use of macro structured porous scaffolds, which act as supporting material for the initial cell attachment and subsequent tissue formation, both *in vitro* and *in vivo* [18,19]. Scaffolds for bone regeneration should meet certain criteria to serve this function, including mechanical properties similar to those of the bone repair site, biocompatibility and biodegradability at a rate commensurate with remodelling.

HA and collagen are the main constituents of bone [20,21]. Collagen has a high cost and easily denatured during processing. However, gelatin is an irreversible hydrolysed form of collagen and has similar chemical composition, easy availability and low cost [22,23]. Thus, gelatin has a similar composition as natural collagen and consider mimicking the scaffolds [24,25]. In addition, gelatin has several clinical utility as temporary defect filler and wound dressing [26,27]. So, HA-gelatin biocomposite scaffolds has significant attention for tissue engineering [28]. Moreover, as the cryogenic engineering attracts more attention owing to its extensive applications in superconducting fields, nuclear fusion and so on. There is an urgent need of researchers to study and enhance the mechanical properties of nanobiocomposites at cryogenic temperature due to their favourable plasticity, gelation properties of gelatin which could meet the demand of cryogenic engineering [29,30].

Protein is the first living entity to interact with the surface of the biomaterial during contact in the host environment [31,32]. Thus, the surface of the material gets covered by a layer of proteins momentarily, after implantation in a competitive process. Protein layer adsorb first onto the foreign material surface to interact with the cell receptors towards cell membrane surface, since cells do not have any interaction capacity with bare biomaterial surface [33]. Hence, the presence of protein molecules is mandatory for a suitable attachment and proliferation of cells onto the surface of a given substrate [34,35]. Proteins are the key elements creating a bridge between the implant materials surface and cells. Furthermore, the adsorption behaviour of proteins is highly dependent on surface area, crystallinity, size and morphology of nanoscale biomaterials [36,37]. These parameters of the implant's surface will determine not only the amount of proteins adsorb but also their type and confirmation [38,39]. Osteobleast cell and mesenchymal cell attachment and proliferation solely depend upon the concentration of the serum protein in culture media [40]. Serum albumin is important constituents for cell culture, and it supports the cell growth factor, attachment factor and provide nutrients to cell [41]. The adsorbed serum proteins consider promoting better adhesion of cells than other peptides. Therefore, the rate of adsorption and release of serum albumin affect the *in vitro* study of the composite biomaterials.

In this backdrop, HA nanoparticle synthesis and fabrication of their nanobiocomposite porous scaffold with sufficient mechanical properties will encounter to develop a reliable and tailor made protein bearing media for biological application.

1.2 Hydroxyapatite ceramics

Hydroxyapatite is calcium phosphate based ceramics and known to be one of the most important implantable biomaterials due to its biocompatibility and osteoconductive properties [42,43]. Natural bone made of hydroxyapatite (~70 wt%), organic substances such as collagen, proteins and water. Bone skeleton has HA nanocrystals with an average size less than 50 nm and collagen through the formation of an interconnected net like open porous structure. Hydroxyapatite is one of the most biocompatible ceramic because of its significant chemical and physical resemblance to the mineral constituents of human bones and teeth [10]. It is a bioactive ceramic and widely use as powder or in particulate forms in various bone repairs, and as coatings for metallic prostheses to improve their biological properties [44]. HA is a thermodynamically stable calcium phosphate ceramic compound nearest to the pH, temperature and composition of the physiological fluid. Recently, HA has been used for a variety of biomedical applications, including matrices for drug release control [45]. Synthetic HA exhibits strong affinity to host hard tissues because of the chemical similarity between HA and mineralized bone of human tissue. Formation of the chemical bond with the host tissue offers a greater advantage in clinical applications over most other bone substitutes, such as allograft or metallic implants [46]. However, despite chemical similarities, mechanical performance of synthetic HA is very poor compared to bone. In addition, the bone mineral present a higher bioactivity compared to synthetic HA [47].

Many researchers have observed that the mechanical strength and fracture toughness of HA ceramic can be improved by the use of different sintering techniques or incorporation of the second phase which include, incorporation of sintering additives and use of nanoscale ceramic powders influenced by large surface area to volume ratio [48]. The preparation of HA bioceramic materials have been carried out using different approaches like sol–gel, hydrothermal processing, microwave route, wet chemical route, emulsion system and sonochemical synthesis. Most of the researcher follows the wet chemical route due to the ease of handling, environment friendly and simple to optimise the process parameters.

1.3 Porous hydroxyapatite scaffold

Bone is a complex structure with micro, macro and the interconnected pores useful to allow body fluid to carry nutrients and provide a medium where interfacial reactions between hard tissue and soft tissue can occur. Two types of bone structures have been described: cancellous and cortical structures. Cancellous bone differs from cortical bone consist of sponge-like highly open macroporous structure and high surface area. Currently, natural materials have been selected as bone substitute for bone grafting surgery. These include auto- or allograft, bovine and coral blocks but their source is limited. Therefore, the fabrication of the grafting material for bone tissue application takes more attraction. Porous HA has been applied for cell loading, drug releasing media, chromatography analysis and most extensively for hard tissue scaffolds [49]. Various cell products have therapeutically significance including hormones, enzymes, vaccines and nucleic acids which improves the diagnosis and treatment of human diseases. Mammalian cells can be grown and maintained *in vitro*, but anchorage-dependent which means, it needs solid substrate for growth [50,51]. Since, porous HA is more resorbable and osteoconductive than dense HA, there is an increasing interest in the development of synthetic porous HA bone replacement materials for the filling of both load-bearing and non-load-bearing osseous defects [52].

Scaffolds are the three dimensional templates that serve as supporting material for repair, reconstruct of a musculoskeletal system. It guides the cell to grow and facilitate grow of new bones. Ideal scaffold has several criteria for bone regeneration, which include bioactivity (ability to bond to bone), osteogenic (stimulation of bone growth), biocompatible (induce minimal toxic or immune response), resorb safely and effectively in the body, similar mechanical properties to bone (such as load absorption), ability to shape to a wide range of defect geometries and meet all regulatory requirements for clinical application [53,54]. In terms of the osteogenic material, the material should be osteoinductive (capable of promoting the differentiation of cells), osteoconductive (support bone growth and encourage the ingrowth of surrounding bone) and osteointegrate (integrative to the surrounding bone) [55]. Furthermore, mechanical conditioning often has a direct effect on cellular behaviour such as differentiation, extracellular matrix production, migration and proliferation. Recently, the regeneration of tissues in biomedical application is taking place using synthetic implants and tissue grafts applying tissue engineering approach, where degradable porous material scaffolds integrated with protein molecules or living biological cells. Mass transports balance the tissue regeneration and their temporary mechanical response. Since, bone tissue is the most commonly replaced organ of the body, the necessity to engineer the proper scaffold material is of a growing need. Synthetic bone graft substitute require to repair large bone defects associated with trauma, malignancy and congenital diseases [56]. In particular, the replacement of structural bone loss remains a challenging clinical problem. Millions of patients in the worldwide suffer each year from considerable bone loss resulting from trauma, osteoporosis, osteomyelitis, malignancy and congenital diseases and this number is expected to increase substantially with the doubling of the population over the age of 65 years [57].

1.4 Bovine serum albumin

Albumin is a soluble monomeric protein, which comprises about half of serum proteins. It is a carrier material for steroids, fatty acids and thyroid hormones and stabilizes extracellular fluid volume. Bovine serum albumin (BSA) is a serum albumin protein produced from cows. It is used as a protein concentration standard. The full-length BSA precursor protein consists of 607 amino acids in length with a molecular weight of 66.5 kDa. BSA is the most abundant plasma protein accounting of 55-60% of the measured serum protein. The chain is characterized by having no carbohydrate moiety, scarcity of tryptophane and methionine residue such as lysine, arginine, glutamic acid and aspartic acid. The mature circulating molecule is arranged in a series of α-helices folded and held by 17 disulphide bridges. The folding creates sub-domains of three continuous α-helices in parallel. It can be seen as cylindrical structures with polar outer walls and a hydrophobic central core. The tertiary structure of human albumin crystal has been isolated by X-ray crystallography. The molecule is very flexible and changes shape rapidly with variation in environmental conditions and binding of ligands. Denaturation occurs only with dramatic and non-physiological changes in temperature, pH and the ionic or chemical environment. BSA has numerous biochemical applications including ELISAs (Enzyme-Linked Immuno sorbent Assay), immune blots and immune histochemistry [58]. It is also used as a nutrient in cell and microbial culture. BSA is used to stabilize some enzymes during digestion of DNA and need further stabilization [59]. BSA has a common use to quantify other proteins, by comparing an unknown quantity of protein to known amounts of BSA. BSA is considered as standard protein because of its stability, lack of effect in many biochemical reactions and low cost. Large quantities of BSA can be readily purified from bovine blood, a by-product of the cattle industry.

BSA is usually used as a supplement to cell culture media [60]. It supports cell growth and product formation by providing a broad spectrum of macromolecules [61], attachment factors, nutrients, hormones and growth factors [62,63]. The most commonly used animal serum supplement is fetal bovine serum, FBS (or alternatively called FCS, fetal calf serum). However, a well defined structure of serum such as BSA over FBS is used prior to cell culture. Bovine Serum Albumin (BSA) is cheaper than human serum albumin (HSA) and has potential use in clinical research.

High soluble albumin protein is present in human plasma at normal concentration between 35 and 50 g/l [64]. Albumin has several important physiological and pharmacological functions, which transport metals, fatty acids, cholesterol, bile pigments and drugs. It is a key element in the regulation of osmotic pressure and distribution of fluid between different compartments [65]. In general, albumin represents the significant and predominant antioxidant in plasma, a body compartment is known to be exposed in constant oxidative stress. A large proportion of total serum antioxidant properties can be attributed to albumin. Research report has been revealed that more than 70% of the free radical-trapping activity of serum is due to HSA [66]. Usually, albumin concentrations remain very low in cerebrospinal, aqueous humor, synovial and lung bronchoalveolar lining fluids in comparison with plasma [67]. A beneficial effect albumin concentrations could be found in sites of inflammation, for the protein to exert its multiple antioxidant properties [68]. Physiological or pathological functions modifying the antioxidant properties of albumin are also reported.

1.5 Biomaterials protein interaction

Protein–biomaterials surface interaction has significance importance to develop a new class of biomaterials, specifically in the field of pharmaceuticals and tissue engineering. When a solid material (e.g., a catheter, stent, hip joint replacement or tissue engineering substrate) comes in contact with a fluid that contains soluble proteins (e.g., blood, interstitial fluid, cell culture media), which rapidly adsorb onto the surface of the material [6,69]. Similarly, living cells does not fascinate direct interaction with molecular structure of the material itself, but prefers to adsorb protein molecular layer as discussed earlier [32,70]. The type and amount of adsorb proteins refer the type and surface density of bioactive sites that may be available for cell interactions and orientation, confirmation and packing density of the adsorbed proteins. Accordingly, it is important to know that how surface chemistry and topology affect the formation of the adsorbed protein layer and the available bioactive sites by this layer to control the cellular response [71]. Recent advances in biotechnology demonstrate that peptides and proteins are the basis of a new generation of drugs [72]. A deficiency of protein in the body causes the diseases like thrombosis, colon cancer, breast cancer, diabetes and osteoporosis. Proteins are transported orally or through injection. High molecular weight, structural fragility and their hydrophilicity does not support to transport of proteins towards the targeted site [9]. Hence, the proper sustained and targeted delivery of pharmaceutical offers several advantages in compare with classic administration through increment of drug amount towards the targeted area, improve the transportation mechanism, and protect the drug against inactivation, degradation and metabolization phenomena. In recent, HA nanoparticles has been elucidated to be an efficient carrier for bone growth factors or drug deliver [73]. High molecular weight proteins will tend to be more tightly adsorb on HA, but protein charge also plays a critical role [74]. Instead, the goal here is to provide an overview of the basic understanding of protein interaction with biomaterials, surface properties, adsorption kinetics and driving force for interactions.

Cells are not adhering without the presence of intermediate protein layer within foreign host biomaterial, and cell molecules [75]. The protein properties like hydrophobicity and surface charge attribute the most effective contribution towards the adsorption of protein on biomaterials [76]. The described features are needed to encounter to understand the protein adsorption phenomena (Table 1.1).

Table 1.1 Effect of protein properties on the adsorption phenomenon [76].

Properties	**Effect**
Size	Large molecules have more sites for surface contact
Charge	Molecules near their isoelectric point adsorb more readily
Hydrophobicity	More hydrophobic molecules adsorb more readily on hydrophobic surface
Stability	Less stable proteins form more surface contact points
Unfolding rate	Molecules that rapidly unfold can form surface contacts more quickly

Mutual protein interaction depends on both protein and biomaterial surface properties. The most effective surface properties of the biomaterial on the protein adsorption are represented in Table 1.2. Relative bulk concentration of each protein and intrinsic surface activity has two driving forces of protein adsorption. Along with two major contribution, van der Waals force of interaction and electrostatic force of attraction plays an important role in protein interaction [77]. Surface behaviour has a significant impact on protein adsorption phenomenon. It has been seen that neutral, hydrophilic material surface shows little adsorption, whereas hydrophobic surface has strong adsorption in an aqueous environment. A charged surface has variable adsorption depending on the electrostatic interaction of protein and surface [78]. The adsorption of biomaterials on different surface is represented in Figure1.1.

Table 1.2 Biomaterial surface that affect protein adsorption [76].

Feature	Effect
Topography	Greater texture exposes more surface area for interaction with protein
Composition	Chemical makeup of a surface will determine the type of intermolecular forces governing interaction with proteins
Hydrophobicity	Hydrophobic surfaces tend to bind more proteins
Heterogeneity	Non-uniformity of surface characteristic results in domains that can interact differently with proteins
Potential	Surface potential will influence the distribution of ions in solution and interaction with proteins

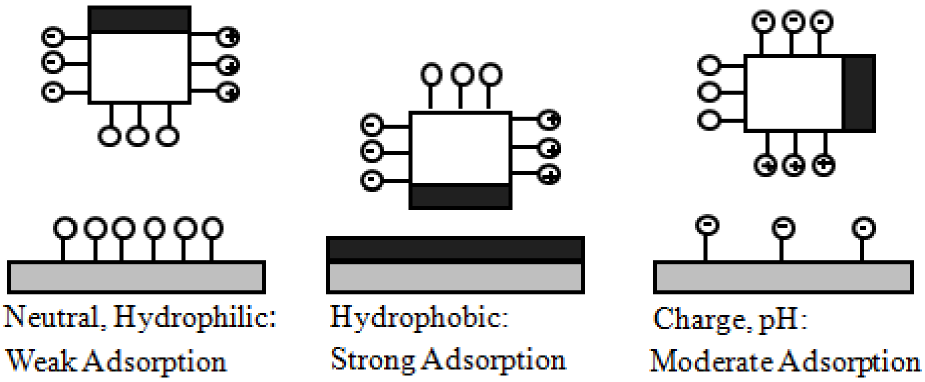

Figure1.1 Schematic for the adsorption of biomaterials on different biomaterial surfaces [79].

In addition, the protein adsorption kinetics on the biomaterial surface study is also essential to develop new class of materials. Let us consider a reaction between protein (P) in solution and the biomaterial unoccupied surface site (A). Hence, the existing equilibrium between the protein occupied surface site (PA) and unoccupied surface site can be represented as:

$$P + A \leftrightarrow PA$$

According to Langmuir,

$$[PA] = \frac{K[P][A_T]}{1 + K[P]}$$

Where, A_T = Maximum amount of protein adsorbed (mg/g)

K = Affinity constant (ml/g)

The adsorption isotherm of protein on the surface of biomaterial is represented in Figure 1.2. Figure 1.2 (A) reveals that very rapid initial phase of adsorption proteins has been arrived quickly to an empty surface [80]. Slower phase is approaching towards a steady-state value. Protein molecule covers the entire surface and difficult to identify of any empty spots (Figure 1.2 (B)).

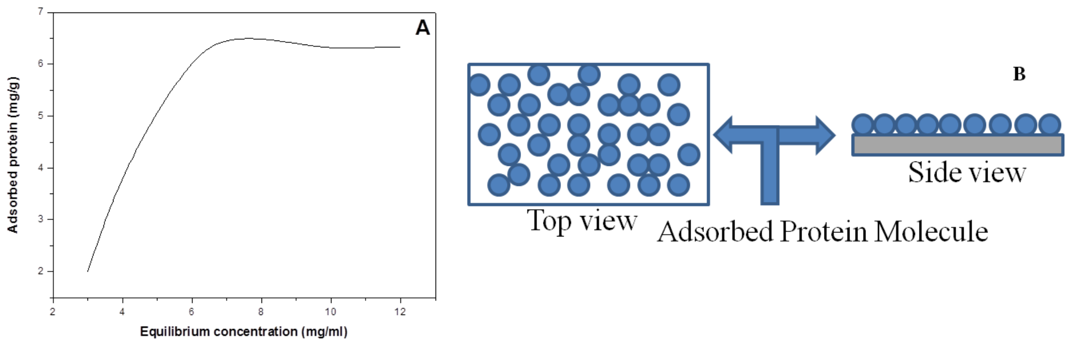

Figure 1.2 Adsorption isotherm (A) and monolayer of protein adsorption (B).

1.6 Protein delivery

Protein delivery is the method or process of administering a protein compound to achieve a therapeutic effect in humans or animals [81]. This acute process is effective to modify drug release profile, absorption, distribution and elimination for the benefit to improve drug efficacy and safety, as well as patient convenience and compliance [82]. Most common routes of administration includes the preferred non-invasive peroral (through the mouth), topical (skin), transmucosal (nasal, buccal/sublingual, vaginal, ocular and rectal) and inhalation routes [83]. Many medications such as peptide and protein, antibody, vaccine and gene based drugs, in general may not be delivered using these routes because they might be susceptible to enzymatic degradation or cannot be absorbed into the systemic circulation efficiently due to molecular size. Thus, much protein and peptide drugs have to be delivered by injection or a nanoneedle array. For example, many immunizations are based on the delivery of protein drugs and are often done by injection. However, the current efforts concentrate on the development of targeted delivery media which can release the drug overtime in a controlled manner. In order to achieve efficient targeted delivery, the designed system must avoid the host's defence mechanism and circulate to its intended site of action [84]. Different drug release media formulation are available include liposomes, drug loaded biodegradable microspheres and drug polymer conjugates.

1.7 Thesis structure

On the basis of the above findings, the entire structure of the dissertation elaborates in different chapters. Introduction on the essential background about the existing field is discussed in Chapter 1. The literature reviews related to the HA nanoparticle synthesis, BSA adsorption and release on HA nanoparticle, fabrication of HA scaffold, cryogenic treatment of the scaffold, biocompatibility, cytotoxicity and protein adsorption/release phenomena on scaffold describes in Chapter 2. This chapter includes the aim and objectives of this investigation and also reviews recent reports by other investigators in different aspects. Preparation of different morphologies of HA scaffolds (spherical, rod and fiber), low temperature treatment of scaffold (77K), protein adsorption/release, *in vitro* cytotoxicity and their relevant characterizations illustrates in Chapter 3. Results and discussion part of the dissertation is represented in Chapter 4. This section has seven subsections, which illustrate as follows. Preparation of different morphologies of HA nanoparticles with respect to three important parameters such as temperature, pH and Ca:P ratio has been discussed and optimized their preparation conditions. The process of homogeneous and stable dispersion of the HA nanoparticles in aqueous media has illustrated through complexomatric reaction. BSA protein interaction phenomenon, and their adsorption and release kinetics on the synthesized nanoparticles are also discussed. Porous HA-gelatin scaffold has fabricated through freeze casting technique and attempted to enhance mechanical properties of optimized scaffold at liquid nitrogen temperature. Bioactivity and biodegradation of cryotreated HA-gelatin macroporous scaffold (CHAMPS) has investigated *in vitro*. The cytotoxicity and L929 mouse fibroblast cell adherence of CHAMPS demonstrates in chronologic sense. BSA protein adsorption and release is also studied on CHAMPS. Protein concentration determination and characteristic bonding behaviour of amides of scaffolds are also reported systematically. Micro-CT analysis illustrates the fractal dimension, degree of anisotropy and pore interconnectivity before and after protein adsorbed CHAMPS. In the beginning of Chapter 5, all the results are summarized of the present research finding along with the possible direction for future works. A complete list of references has provided at the end of the dissertation.

Chapter-2

Literature Review

Chapter 2 Literature Review

2.1 Hydroxyapatite

Synthetic hydroxyapatite (HA) is one of the most foreign implantable materials among other calcium phosphate based ceramics because of similar biocompatibility and bioactivity properties with bone. HA has a high degree of *in vivo* stability in compare with other calcium phosphates. Elliott et al. [85] reported that bone and teeth mineral are an inorganic composite of HA in which Ca/P molar ratio varies from 1.6 to 1.7 along with a few percent of carbonate and water. The mineral is preferable crystalline with hexagonal crystal structure for adult bone and semicrystalline for fetus [86]. Typically, the crystals appear as 400 Å long and 150 Å wide in bone, whereas 400 Å wide and 1000 Å long in dental enamel [87]. The basic crystal structure of apatite is reported by Naray-Szabo [88] and Mehmel [89] in 1930 and represented in Figure 2.1. HA possesses a hexagonal structure with a $P6_3/m$ space group and cell dimensions a = b = 9.42 Å, and c=6.88 Å, where $P6_3$/m as space group has six-fold symmetry axis and three-fold helix structure [90]. It has an exact stoichiometric Ca/P ratio of 1.67 and chemically very similar to the mineralized human bone [91].

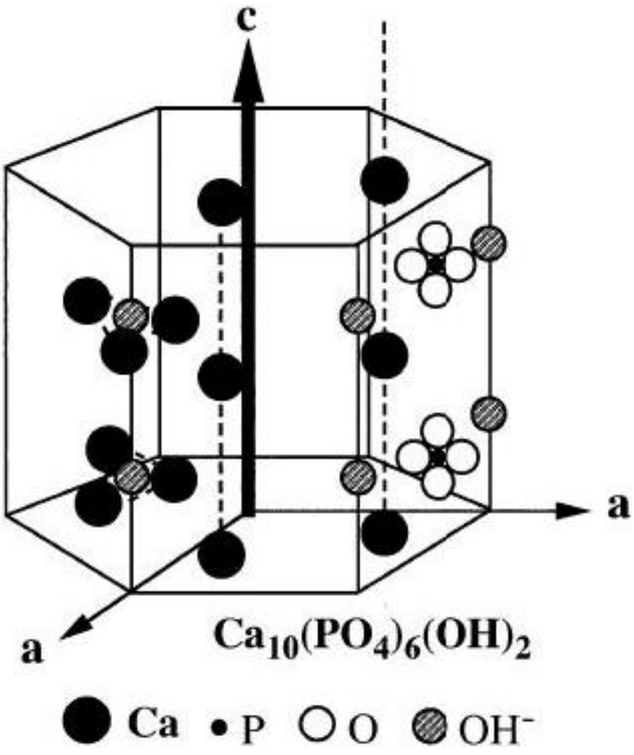

Figure 2.1 Crystal structure of hydroxyapatite [92].

Day –to –day clinical demand insists on preparing synthetic HA by a number of methods in preference solid state, sol-gel, microwave irradiation, wet-chemical precipitation, hydrothermal technique etc [93,94]. Researchers, academician, clinician and manufacturer are trying to find out the best choice of HA material with respect to purity, morphology, size, crystallinity and Ca/P ratio. Generally, solid state technique is relatively needed less effort, but difficult to control the pure HA phase and particle size similar to original HA crystal for bone and dental applications. On the other hand, low temperature chemical techniques are preferably suitable to produce different morphology of HA through control over the processing parameters such as precursor concentration, temperature, pH, structure directing agent and Ca:P ratio. Therefore, it is important to understand and need elaborate discussion on the different processing methods and parameters to achieve desire morphology with purity and crystallinity of HA phase.

2.2 Preparation techniques of HA nanoparticles

Extensive literature data suggests the availability of versatile HA particle processing techniques to achieve different morphologies followed by either low or high temperature process. Most relevant synthesis process and their details analysis related with the project objective are discussed as follows.

Feng et al. [95] synthesized spherical HA nanoparticles through sol-gel method with starting of P_2O_5 and $Ca(NO_3)_2.4H_2O$ as precursor material. It has been seen that the degree of crystallinity and morphology of synthesized HA nanoparticles are depended on the calcination temperature and aging time. The obtained HA particles exhibit low temperature stability and gradually destabilized beyond 800 ^oC through decomposition of β-tricalcium phosphate (β-TCP). The crystal size of the HA nanoparticle increases along with aging time. Near spherical morphology 10-15 nm dimension is found after calcination at 700 ^oC for 4 h.

Qui et al. [96] prepared spherical nano-HA by biomimetic method using $Ca(NO_3)_2.4H_2O$, $(NH_4)_3PO_4.3H_2O$ precursors and 2-6 wt.% polyethylene glycol (PEG) as morphology and crystallinity manipulator, respectively. Effect of PEG concentration on the HA morphologies is also reported in this research work. Synthesized HA powder is more crystalline in presence of PEG higher than without content of any PEG. High concentration PEG favours formation of spherical and isotropic growth of crystalline HA. The prepared HA nanoparticle persists spherical morphology in the size range of 30–50 nm.

Zhang et al. [97] prepared spherical and crystalline nano HA through wet chemical precipitation at low temperature from inorganic precursors $Ca(NO_3)_2$ $4H_2O$ and $(NH_4)_2HPO_4$. It has been observed that the reaction temperature influences the phase formation, crystallinity, grain size and morphologies of HA. Rapid mixing mode develops spherical HA nanoparticle at 40 ^oC with an average diameter of 20–50 nm.

Mejoo et al. [98] employed microwave heating module to achieve pure and thermally stable nanocrystalline HA phase. The received ceramic powder possesses needle-shaped nanocrystals with dimension about 50 nm diameter and 200 nm in length. Phase stability and microstructure evolution are discussed in terms of the formation of secondary phase at 700 ^oC.

Wang et al. [99] synthesized and controlled the HA nanorod size through chemical precipitation of $Ca(NO_3)_2$ $4H_2O$ and H_3PO_4 precursors in the presence of organic modifier dodecyl sulphate and sodium dodecylbenzene sulphonate at low synthetic temperature range from 100 to 200 ^oC. The crystallinity of the prepared HA increases with increasing autoclave temperature, whereas HA nanorod size influences by different structure organic modifiers and synthesis temperature. Interaction between anions of the modifiers and HA nuclei controls the ultimate growth pattern. Strong adhesion prefers to form small-sized HA nanorods. HA nanorod size 12 nm diameter and aspect ratio ~2 results at lower autoclave temperature (100 ^oC), but HA nanorod 18 nm diameter and aspect ratio ~ 2.73 forms at relatively higher temperature (200 ^oC) in the presence of sodium dodecyl sulphate and sodium dodecylbenzene sulphonate.

Liu et al. [100] synthesized HA nanorods through wet chemical method at low temperature and suitable surfactant. Common precursors $CaCl_2$, NH_4NO_3 and Na_3PO_4 with addition to PEG-400 and cetyl trimethyl ammonium bromide (CTAB) as surfactant are used for this study. Synthesized nanorods have a diameter of 50–80 nm and length of 0.5-1.2 µm under condition of solution pH-4.5 and temperature 85 ^oC. PEG-400 and CTAB surfactant directs the formation of classic needle like structure of HA.

Suzuki et al. [101] prepared needle like HA through wet chemical method using $(CH_3COO)_2Ca$ and K_2HPO_4 with adjustment of stoichiometric ratio of Ca:P ~ 1.67 at 100 ^oC. The study investigates that HA is grown to long needle-like shape with Ca-deficient HA in the weak acidic regions. The developed needle-like HA has near to ~18.6 (mean length: 5.8 µm) aspect ratio, Ca:P ~ 1.59 and 92 wt.% yield. This needle-like HA particle has Ca:P ratio of 1.59, which is less than the stoichiometric ratio of 1.67. Aspect ratio below 3.6 or less does not favour formation of stoichiometric HA.

Feruichi et al. [102] prepared fibrous morphologies of nano HA through wet chemical process using the starting materials $Ca(NO_3)_24H_2O$, $NH_4H_2PO_4$ and organic additive gelatin at a temperature of 95°C and solution pH ~ 10. Nanotextured and nanofibrous HA are produced through topotactic transition of dicalcium phosphate dihydrate (DCPD) containing gelatin molecules. Resultant nanoscale effects due to the formation of dicalcium phosphate (DCP) through dehydration of DCPD. High hydrolysis rate of DCP favours formation of 20 nm spherical nanoparticles whereas moderate hydrolysis by ammonia produces elongated nanorods with diameter of 50 nm. Hierarchical nanostructured HA results of organic molecule assisted phase transformation with the existence of high surface area (100 m^2/g).

Zhang et al. [103] prepared HA multiform morphologies like nanowire, nanorods, microspheres, microflowers and microsheets through hydrothermal process using water as reaction medium. $Ca(NO_3)_24H_2O$ and $(NH_4)_2HPO_4$ are considered as common precursor in addition of structure directing agent hexadecyl trimethyl ammonium bromide and organic additive trisodium citrate. Hydrothermal process at the temperature of 180 °C has been studied to understand the effect of solution pH in the range of 4–9 and organic additive (trisodium citrate) on different morphologies of HA. Different hydrothermal treatments in absence of trisodium citrate at 180 °C (pH–7.0) influence the formation of one dimensional nanostructure HA. However, average diameter 25 nm and 50–70 nm in length nanoparticle obtain at solution pH–9, whereas low solution pH~ 7 forms longer with average length~120 nm and diameter of about 25 nm. Bur-like 7–9 µm HA microsphere develops in the range of solution pH–5 and 10 micron flower-like architecture in pH–4.

Li et al. [104] demonstrated the effect of surfactant citric acid on resultant size of the HA nanoparticles when coprecipitated $CaCl_2$ and Na_3PO_4 precursors in the solution pH range of 9 – 11 and aging 24h. Rod like morphology 10-20 nm width and 50–70 nm length HA develops in the presence of surfactant citric acid, but it become 1µm diameter and 100 µm length HA nanoparticles in absence of citric acid. However, in the oil-in-water emulsion method favours HA ellipse-like nano-HA particles of 20–40 nm width and 50–60 nm in length.

Zhang et al. [105] reported the formation mechanism of nano and micro scale fluorinated HA (FHA) prickly spheres, whisk brooms, flowers, dandelions, nanofibers and nanoribbons through adjusting reaction conditions and content of glutamic acid. The precursors $Ca(NO_3)_2$ $4H_2O$, K_2HPO_4, NaF and glutamic acid are used for the preparation of different morphologies of FHA at 60 ^{o}C. FHA crystals are found in a non-equilibrium growth process. The processes are influenced by the interaction with glutamate ions and precipitates surfaces related to the formation of FHA. Processing parameter and glutamic acid concentration have a significant contribution to develop spheroidal nanoparticles to anisotropic growth of fibers and flower like aggregates. Low concentration glutamic acid favours 80 nm spheroidal, whereas intermediate and large quantity transforms to 80 nm fibers and 2 µm flower like morphology, respectively.

Neira et al. [106] prepared different morphology of HA through urea-assisted hydrothermal reaction between $Ca(NO_3)_2$ $4H_2O$ and $(NH_4)_2HPO_4$ at low temperature of 90 °C. Particle morphology of the prepared HA crystals has been controlled by varying the decomposition kinetics of urea and concentration of the precursor components in the course of hydrothermal process. Hexagonal prism and needle like morphologies of HA particles preferentially grows along the c-axis of HA crystal. The hydrothermally prepared HA powder contains CO_3^{2-} ions in the crystal lattice and exhibits AB-type carbonated HA. AB-type carbonated HA is formed through partial substitution of CO_3^{2-} on OH^{-} and PO_4^{3-} of apatite crystals.

Brown et al. [107] illustrated on the effect of synthesis temperature on morphology of HA. The study investigates the impact of temperature on the kinetics of calcium-deficient HA (CDHA) by an acid-base reaction. The kinetics of HA formation are initially controlled by surface area of reactant, and their rate of reaction is found as diffusion controlled. Diffusion control mechanism experiences the epitaxial formation of HA on the surface of dicalcium phosphate reactant. The study reveals that seeding with HA initiate and accelerates the response, but it has not long-term effect on the fractional degree of reaction or microstructural development.

Thorough literature survey depicts; no trial has been conducted to prepare different aspect ratio of spherical, rod and fibrous morphology through co-precipitation route from identical precursors control over their concentration, solution pH and temperature. This selective nano HA morphologies will be utilized for fabrication of nanobiocomposite scaffold and protein adsorption – release study. Hence, this challenging task has been considered as one of the objectives in this research work.

2.3 Dispersion of hydroxyapatite

Nano scale HA is a classic bioactive and biocompatible material, which on rationale simulate both of the bone and dental mineral compartments. Nanoparticles are needed to disperse to investigate *in vitro* cell interaction and *in vivo* circulation/ reciprocation phenomena. Preparation of well-dispersed HA nanoparticles are required not only for protein delivery but also facilitating as the drug carrier. Therefore, brief literature reports are discussed as future work reference.

Tan et al. [108] prepared nano HA rods using $Ca(NO_3)_2$ $4H_2O$ and $(NH_4)_3PO_4$ as precursor material and followed by aqueous dispersion through sodium citrate and sodium hexametaphosphate. Primarily, the dispersion of HA nanoparticles is an attribute to the ion exchange reaction between sodium citrate and sodium hexametaphosphate which improves the colloid stability of HA and their complexometric reaction with citrate ions. Sodium hexametaphosphate addition to the dispersed HA increases the stability of a dispersion as well as increases the zeta potential value from –30 mV to – 44 mV.

Han et al. [109] prepared stable nano HA suspension through ultrasound assisted precipitation technique in presence of glycosaminoglycans (GAGs). HA nanoparticles suspension has been prepared by using the precursor materials $Ca(H_2PO_4)_2$ and $Ca(OH)_2$ in a solution state. Suspension is primly composed of both 20–50 nm short rod-like and 10–30 nm spherical HA nanoparticles. The average particle size of a stable suspension predicts as 30 nm at the zeta potential (ζ) of –60.9 mV. Stability of HA nanoparticles suspension mainly depends on the electrostatic and steric effect of GAGs. It is also discussed that prepared HA nanoparticles suspension has easy mode of transport into the cancer cells and exhibit good potential as gene or drug carrier system.

Borum-Nicholas et al. [110] studied the colloidal stability of nanophase hydroxyapatite both in water as well as ethyl alcohol at 115 ^{o}C. An increase in colloid stability has been observed for HA just by altering the solvent from water to ethyl alcohol. The study demonstrate that the sedimentation time for HA is 3 h in water and 7 days in ethyl alcohol. The origin of the enhanced stability of HA in ethyl alcohol is because of electrostatic effect that is influenced by Lewis acid–base interaction. Ethyl alcohol readily accepts more electrons from the HA surface than water resulting in enhanced colloid stability. The colloidal stability of HA in water is dictated by Lewis acid–base interactions (electron donor–electron acceptor interactions), in addition to the traditional electric, double layer repulsion and van der Waals interactions.

Li et al. [111] prepared hydrocolloids of HA using aqueous ammonium phosphate and calcium nitrate in the presence of citrate ions. A hydrocolloid of HA formation mechanism is proposed based on the interaction of citrate ions with the calcium ions on HA surface. During the low-temperature (30 ^{o}C) reaction stage, the HA primary particles are like to link together by carboxylate–calcium bridges, which results relatively large aggregates. These aggregates have broken into small colloidal particles at the higher temperatures (90 ^{o}C) of aging stage due to the disassociation of the carboxylate–calcium links imparting negative charges to the HA, forming stabilized colloidal particles by surface charge. Citrate ions and temperature are the two key factors for stability of the HA colloids.

Sadat-shojai et al. [112] studied the colloidal stability of synthesized hydroxyapatite nanorods in the dental adhesive solution. Homogenous dispersion is obtained through preparation of 0.2 wt.% HA nanorods incorporated into the adhesive solution and homogenized by ultra-sonication using a probe sonicator apparatus. The prepared HA nanorod colloid exhibits a low tendency to agglomerate and stabilized for 60h, which might be result for the surface charge of the nanorods.

In this context, the dispersion study of proposed particles will be carried out to fulfil our objective.

2.4 BSA adsorption and release on HA nanoparticles

This study is essential to understand the importance of such study and future development as delivery media of HA nanoparticles. Brief classic examples with relevant data are described as reported by a different group of researchers.

Kandori et al.[78] studied the adsorption of BSA on HA particle of 50 nm size with respect to Ca/P molar ratio variation from 1.55 to 1.70. Prior to such study, the HA surface has been modified by silicate and fluoride ions at pH ~6.0 and 288 K. Adsorption isotherm of BSA on HA particle follows Langmuir type and adsorption of BSA develops a negative charge on HA. However, unmodified HA particles exhibit high Ca/P molar ratio, which results larger electrically positive zeta potential because of their electrostatic attractive force and turns to high saturation BSA adsorption. Surface modification by silicate ion increase surface acidity and made surface more electrically negative to yield lesser amount of adsorbed BSA. Fluoride ions assisted surface modification and increases two-fold adsorption of BSA over that on the unmodified surface.

Calcium fluoride facilitates to adsorb high amount of BSA on the HA surface. Hydrophobic silica surface adsorbs higher amount of BSA than a hydrophilic surface.

Macritochie et al. [113] studied adsorption isotherm of BSA on the solid-water interface. Hydrophilic surface has weak adsorption efficiency and high electrical factors sensitivity. Large adsorption energy is required for the adsorption at hydrophobic surface end as compared to hydrophilic silica surface. However, air-water interface adsorption isotherm for both of the two surfaces is similar in nature. The role of interfacial coagulation and slow desorption has been discussed in relation to the reversibility of adsorption. Colloidal silica both in its natural state and with methylated surface groups is used in order to compare the effects of hydrophilic and hydrophobic surfaces. The protein adsorption at solid-liquid interface follows monomolecular behaviour.

Boonsongrit et al. [114] studied the desorption behaviour of protein BSA on commercial HA microspheres and their control delivery phenomenon. Desorption behaviour is carried out in phosphate buffer solution (PBS). The result shows that desorbed BSA concentration increases with an increase in the amount of phosphate. BSA protein desorption phenomenon is related to PBS concentration and time, for e.g. a rapid and larger amount (70%) BSA protein desorption is obtained after 30 min in 10 mM phosphate buffer solution, whereas a low release profile is recorded in deionized water (DI) only. The release rate of BSA-loaded HA microspheres is controlled in physiological condition, through encapsulate with a biodegradable polymer, poly (lactic acid-co-glycolic acid) (PLGA).

Shirkhanzadeh et al. [115] studied on the adsorption and release of L-lysine on HA. Controlled release of osteoinductive proteins from HA has been discussed in this work. An investigation on the nature of interfacial interaction between L-lysine and HA is reported in point of the formation of hydrogen bonding between C=O groups of L-lysine and polar –OH groups of HA. This incident phenomenon has significance influence on the chemical intermolecular attractions. The rate of release of biomolecules from HA in simulated physiological solution depends on the number of polar groups and molecular weight of these compounds. Proteins of high molecular weight particularly, phosphoproteins are strongly adhered by HA coatings, which is because of multi attachment of their polar groups to HA crystals.

Wu et al. [116] studied the BSA protein adsorption and release on semi-crystalline mesoporous nano-hydroxyapatite. The BSA loading increases with the specific surface area and the pore volume of nano HA. The release rates of BSA are different due to their different pore sizes and pore structures. The synthesized nano HA demonstrates the capacity of 20 mg of BSA adsorption and 75% release in 24h. Nano HA sample reveals an initial burst release of about 40% BSA within 2h and following 75% in 24h. The adsorbed amount of BSA protein on nano HA has a high correlation with the specific surface area and pore volume of nano HA.

Iafisco et al. [117] studied on the interaction mechanism of BSA with biomimetic carbonated HA nanocrystals. Smaller size (20 nm) and the lower crystallinity degree with the high surface area (120 m^2/g) of carbonated nanocrystals facilitate to adsorb 25 mg of BSA in 12h. Protein adsorption follows the Langmuir adsorption isotherm pattern. The reaction mechanism between protein BSA and carbonated HA crystals surface is due to hydrophobic and electrostatic interactions.

Literature data suggests the HA-BSA adsorption and release study have significance importance in view of the development of a delivery media, which will be considered another important aspect for current research topic. This study will also assist to identify a particular HA nanoparticle morphology with respect to BSA protein adsorption/release efficiency.

2.5 Fabrication of porous HA scaffolds

Since the last decade, different group of researchers are concentrated to fabricate different class of HA porous bioceramics by adopting different processes and their utility for tissue engineering. Herein, several pioneer works are discussed to understand the basic physical properties of pure HA porous scaffold characteristics prior to fabricate nanoHA-biocomposite scaffold.

Hou et al. [118] fabricated porous scaffold for tissue engineering application through coagulation, compression moulding and particulate leaching technique. High molecular weight polymer–salt composite is processed at 115 ^{o}C. Porosities of scaffolds are varied between 70 % and 95 vol.% by adjusting the polymer to salt ratio, whereas the size of leachable particles control the pore size of scaffold. The resulted scaffold exhibit homogeneous pore morphology with pore diameter ~ 300 µm along with compressive modulus ~ 1.5 MPa.

Li et al. [119] prepared porous HA scaffold by approaching a dual phase mixing technique. Combination of HA and polymehtylmethacrylate (PMMA) slurry technique has been adapted to fabricate the scaffold. Naphthalene particles are used to enhance the porosity (> 50%) of such scaffold. Majority of pores are located within the range of 200–300 μm with 50% porosity, and average compressive strength ~ 8.9 MPa. Ultimate pore volume, porosity, pore size and interconnectivity of the scaffold are adjusted through controlling over the process parameters such as viscosity of HA slurry and HA/PMMA mixing time.

Potoczek et al. [120] prepared HA foams through gel casting via agarose as gelling agent and control over rheological behaviour of suspensions. The viscosity of slurries has been adjusted by agarose concentration and HA solid loading. The study demonstrate that a pore size of HA foams depend on the slurry concentration. HA solid loading (24–29 vol.%) and agarose concentration (1.1–1.5 wt.% with regard to water) in the starting slurry controls the mean pore size in the range of 130 to 380 μm. Porosity of HA foam has found to be in the range 73–92 % and the compressive strength ~ 0.8–5.9 MPa.

Tadic et al. [121] prepared carbonated porous HA by mixing polyvinyl alcohol fibres (PVA) and sodium chloride as porogens. The mixture is compacted by cold isostatic pressing (CIP) followed by dissolution of porogens and develop interconnecting porosity with pore diameter in the range of 250–400 μm. The invented method is applicable to prepare macroscopic porous scaffold through any kind of water-insoluble ceramic materials compacted without sintering.

Ramay et al. [122] prepared calcium phosphate biphasic porous scaffold for tissue engineering application. Biodegradable nanocomposite porous scaffold comprises of β-tricalcium phosphate (β-TCP) matrix and HA nanofibers. Composite scaffolds are fabricated by combined gel casting and polymer sponge techniques, where nanofiber has a dramatic effect to improve the mechanical properties. Porous scaffold exhibits a compressive strength of 9 MPa with porosity 73 %. Toughness of the scaffold increases from 1.0×10^{-3} to 1.7×10^{-3} $\mathrm{MPa.m}^{1/2}$ when concentration of HA nanofiber increases from 0 to 5 wt. %.

Kwon et al. [123] developed a large range of porous bioceramics using polyurethane sponge replica technique. The volume porosity has controlled by the number of coating on the sponge struts. Complete interconnected pores are observed after single coating of HA with porosity content of ~ 90%. However, the porosity of a sintered specimen is drastically reduced to 65 vol.% after 5 times coating of the scaffold and subsequent sintering at 1250 °C. Compressive strength primly depends on the porosity volume. Maximum strength ~3 MPa could be achieved for 65 vol.% porous scaffold.

In a recent article preparation of macroporous scaffold using polymeric sponge technique has been discussed [124]. Interconnected macroporous microstructure is obtained starting with near spherical HA powder and PVA used as binder and subsequent sintering at 1250 °C. The prepared scaffold appears a significant fraction of pore diameter in the range ~50–125 µm and 60 vol.% porosity. The pore content, pore morphology, pore interconnectivity of scaffold and their compressive strength depend on the solid loading and binder content. Low compressive strength ~1.8 MPa is observed after sintering at 1250 °C. Scaffold pore morphology, pore distribution, pore interconnectivity and compressive strength consider the prime factors to optimum the solid loading in around 40 wt.%.

Koc et al. [125] studied the fabrication and characterization of porous tricalcium phosphate (TCP) scaffold using a modified slip casting technique. The prepared slip exhibit stability when TCP powder and PMMA beads are suspended in an aqueous medium and stabilized with an acrylic deflocculant. Porous TCP ceramics is produced by sintering the polymer-free preform for 2 h at 1000 °C. It is observed that prepared slurry has 70 wt.% polymer beads in the size range 210–250 µm with porosity of 65 vol.%. The average pore size in the sintered ceramic is around 190 µm. Pore size in the slip casted porous TCP scaffold has a restriction because of polymeric bead size. Porous scaffold wall thickness and degree of porosity depends on the content of polymer beads. As the amount of polymer beads increased, the dimension of interconnect passage increases proportionately.

Lin et al. [126] prepared macroporous calcium silicate ceramics by using PEG as pore former. Sintered porosity varies in the range of 40-75 vol.% influenced by ceramic solid loading, volume of PEG particles and sintering temperature 900 to 1200 °C. The work is preciously focused on the effect of molecular weight of PEG, which assists to achieve desire morphology, pore structure and pore size of the macroporous calcium silicate. The PEG particle size directs the macropore formation mechanism.

Ebaretonbofa et al. [127] prepared high porous HA scaffold through low silica polyurethane as the organic vehicle and coarsening agent n-heptane. High temperature 1225 °C fabrication process develops 90 vol.% porosity and ~100 µm pore diameter. However, the sintered scaffold retain the HA phase but compressive strength exhibits a dramatic lower value ~ 0.2 MPa.

Huang et al. [128] prepared porous HA scaffold by a combination of H_2O_2 foam with polyurethane sponge and modified with PLGA for achieving high mechanical properties to mimic bone tissue engineering scaffold. Micropores are seen in the HA scaffold due to infiltration of PLGA. HA scaffold exhibits the porosity in the range of around 61-65% and micro pore size of 200–600 µm. It has been seen that use of PLGA infiltration improves compressive strength of the scaffold from 1.5-1.8 MPa to 4.0-5.8 MPa. PLGA has vital role for the development of micropores and obvious their compressive strength.

Deville et al. [129] developed porous HA scaffold through another different freeze casting method for bone tissue engineering. Both porosity and pore size are manipulated by altering the freezing rate of slurries and slurry concentration. Freeze casted porous scaffold exhibits 56 vol.% porosity and gradation of pore in the range ~50–500 µm. The developed open pore has unidirectional lamellar morphology. Pore formation mechanism in the freeze casted body follows by the basic principle of physics of ice formation. Lamellar pore architecture and pore shape anisotropy are associated for the enhancement of compressive strength of scaffolds. The phase change of liquid vehicle during freeze drying is shown in Figure 2.2 (A). Details freeze casting principle has been described in next section 2.6. Different zone of porosities that developed in the direction of ice crystal formed is represented in Figure 2.2 (B).

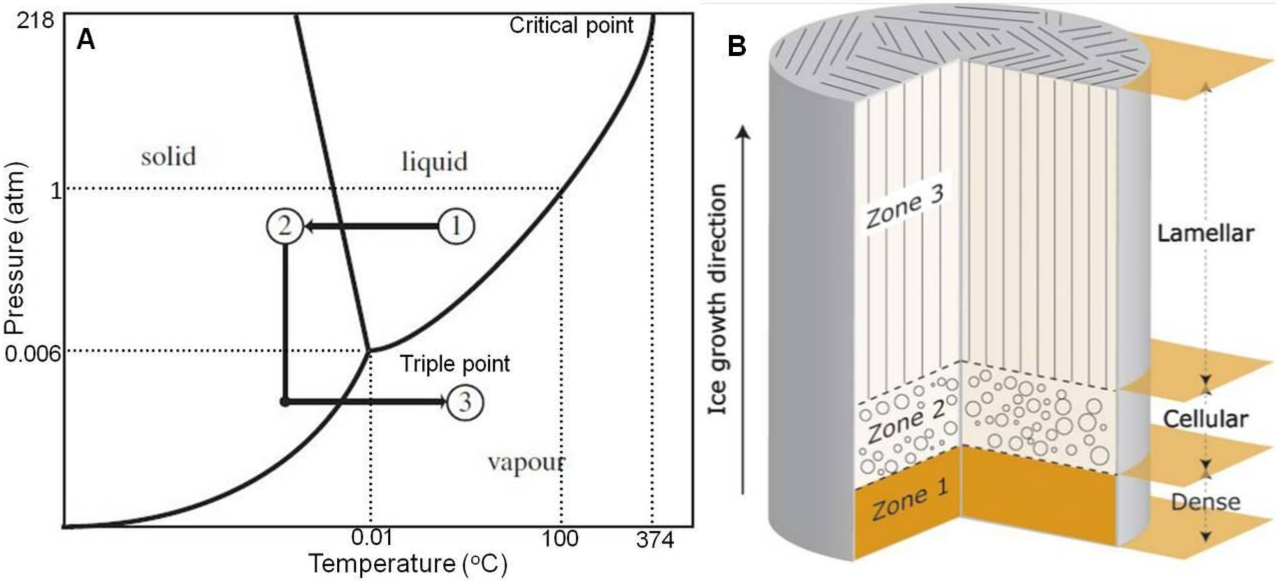

Figure 2.2 Phase change of the liquid vehicle (A) and ice growth direction during freeze casting (B)[129].

Fu et al. [130] prepared porous HA scaffold through freeze casting technique followed by sintering process. The study demonstrates the effect of sintering conditions on the microstructure and the mechanical behaviour of freeze-cast HA. The freeze casted scaffold dramatically enhances 50% compressive strength when porosity reduced to < 5% at prerequisite temperature. The scaffold with a porosity of 52 vol.% has compressive strengths of 12 MPa and 5 MPa in the directions parallel and perpendicular to the freezing direction, respectively. Compressive strength of freeze-casted HA scaffold strictly depends on the sintering temperature. Mechanical response reveals high strain tolerance at the yield stress (5–10 %) and the strain at the failure high (> 20 %) as represented in Figure 2.3. Microstructure and mechanical properties of the fabricated scaffold alters by adding glycerol and 1,4- dioxane to an aqueous suspension. Optimum strength could be observed after sintering for 3h at 1350 °C. The fabricated scaffold exhibits porosity of around 52% and pore size 5–30 µm. The scaffold prepared from aqueous suspensions with 20 wt.% glycerol has higher strength, but lower porosity with finer pores. Whereas, HA scaffold prepared from aqueous suspensions (10 wt.% particles) with 60 wt.% dioxane has compressive strength of 7.5 MPa, strain to failure of 60 % and favourable microstructure with porosity ~ 65 % and pore size~ 100 µm.

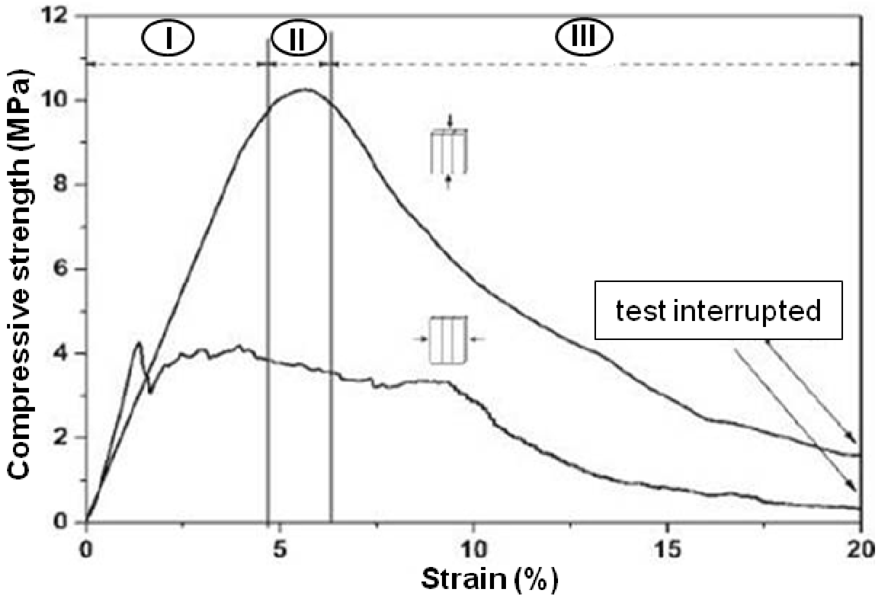

Figure 2.3 Stress-strain behaviour in compression testing parallel and perpendicular to the freezing direction of freeze casted scaffold [130].

Several porous scaffold fabrication techniques such as immediate combination of HA and organics, dissolving porogens, gel casting, salt leaching, high temperature replica method, freeze casting, combine freeze casting/sintering has been adopted to improve and achieve different pore structure and compressive strength. However, direct macroporous hydroxyapatite-gelatin nanobiocomposite scaffold fabrication from suggested HA nanoparticles is limited.

2.6 Freeze casted porous nanobiocomposite scaffolds

The freeze-casting of porous materials in particular has received a great attention during the past few years, because of simplicity; fabrication of tailor made shapes and desirable properties. In freeze casting, a material suspension is simply frozen at solvent triple point, and their sublimation provides a unique porous architecture. The triple point of a substance is the temperature and pressure at which the three phases (gas, liquid, and solid) of that substance coexist in equilibrium. The porosity produced is almost a direct replica of the frozen solvent crystals. Proper control of the freezing condition yields elongated and continuous porosity along the solidification management, which form indigenous morphology from other methods.

Importance of freeze drying

Freeze casting method has excellent and attractive features to make different class of implantable materials for biomedical applications because of:

a) All class of materials, such as polymers, ceramics, metals and their composites can be shaped without alteration of morphology, chemical composition and in-situ reaction within organic matrix.
b) Freeze casting permits to manufacture tailor made complex, hybrid materials through excellent control of structural and mechanical properties.
c) The processing can be carried out with biocompatible liquid carriers such as water; the hierarchical microstructure can be carefully controlled by the physical and chemical properties of the components used and processing parameters such as freezing temperature, rate of freezing etc.
d) Porosity gradient obtained at different zone.

This characteristic attracts more towards the fabrication of ceramic – polymer scaffold through freeze casting process although it is limited to laboratory only. Few interesting literature results are incorporated as references.

Kang et al. [24] fabricated porous HA-gelatin scaffold through freeze drying method to understand the effect of freezing temperature on scaffold microstructure. Hydrogels are prepared in aqueous solution through glutaraldehyde crosslinker of gelatin. Water and their ice crystal acts as a porogen to develop porous structure. Freeze-drying favours to form ice within a hydrogel and develop porous network structure through sublimation. Different porous microstructure is achieved by varying the freezing temperature from –20 °C to –80 °C. Porous scaffold prepared at –20 °C results an interconnected porous structure. Porosity and pore size of dried hydrogels are controlled by the size of ice crystals formed during freezing. Different microstructures of the gelatin scaffold are obtained by changing freezing rate. The scaffold has average pore diameter ~250 µm with very weak mechanical properties.

Landi et al. [131] fabricated HA/gelatin composite porous scaffold with ice-designed channel-like porosity through freeze casting method. The fabricated scaffold exhibits lamellar morphology with aligned channel-like pores. With changing the process parameters, lamellar ice crystals with different thickness grows throughout the sample from bottom to top of HA scaffold as represented in Figure 2.4. The scaffold results 45–55 vol.% of porosity with pore diameter in the range ~100 µm and compressive strength ~ 4 MPa. Compressive strength and elastic modulus of lamellar scaffold increase with the addition of gelatin.

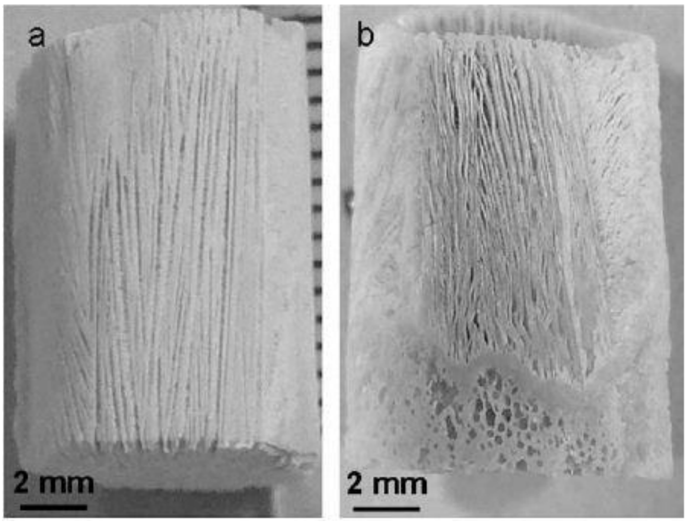

Figure 2.4 Different gradient of porosity in the direction of freezing [131].

Panzavolta et al. [132] prepared porous composite scaffolds of gelatin and tricalcium phosphate (40 wt.%) through freeze casting for 24 h at –50 °C. Mean pore dimension decreases from 350 to 170 µm with increment of inorganic phase content, which finally enhances the compressive strength and Young’s modulus. A wide range of pore dimensions can be obtained by varying the relative amount of gelatin and inorganic components. However, the pore wall seams as microporous with mean dimension micropores of 2–4 µm. The scaffold represents a porous interconnected microstructure with 85 vol.% porosity, ~ 200–400 µm pore diameter and compressive strength 0.3 MPa.

Zhang et al. [133] fabricated HA-gelatin porous biocomposite scaffold by freeze casting technique to evaluate the effect of gelatin addition on the microstructure of scaffold. Pore morphology and microstructure of the porous composite has been synchronized by gelatin content. Gelatin addition changes the viscosity of slurry and pore morphologies of composite scaffold from the large and non interconnected lamellar pores into small and interconnected cellular pores.

Zuo et al. [134] prepared HA-poly vinyl alcohol (PVA) porous composite scaffold by freeze casting process to explore the effect of PVA on microstructure of scaffold. The composite morphologies are modified by adjusting the concentration of PVA additive in the HA slurries. The resulting composite without PVA additive has non interconnected macroscopic lamellar pores and porous ceramic walls, whereas with PVA (10%) additive made up of small lamellar pores or three-dimensional reticulate pores and porous ceramic walls. PVA additive has no effect on the phase composition of HA. The HA solid loading of slurry and the concentration of PVA additive have great effects on the process of PVA gelation and manners of ice crystals growth, resulting in different morphologies.

Azami et al. [135] prepared HA-gelatin nanocomposite scaffold to mimic the mineral and an organic component of natural bone using glutaraldehyde as crosslinking through freeze casting method. Composite scaffolds are prepared with 10 wt.% gelatin and 30 wt.% HA. The compressive strength of composite has improved up to 2.5 MPa with increase in the gelatin concentration. HA-gelatin nanocomposite exhibits macroporous connected structure with pore size in the range of 200–400 µm and the thickness of pore inter wall is about 6–20 µm.

Kim et al. [136] fabricated HA-gelatin composite scaffold through freeze drying technique for tissue engineering. HA powder up to 30 wt.% is found as effective solid content during freeze casting of HA-gelatin slurry. The pure gelatin foam has a well-developed pore configuration with porosity and pore size of ~90 vol.% and 400–500 µm, respectively. Pore volume 85 vol.% and pore size (200–400 µm) decreases with an increment of HA powder content but pore shape irregularity increases for the same. The HA foams experience as high as compressive stress ~0.6 MPa with HA content and exhibits elastic modulus of ~ 4 MPa.

Yook et al. [137] studied on the improvement of compressive strength of porous HA scaffolds by adding polystyrene polymer as a binder to HA/camphene slurries. The compressive strength is significantly increased from 1.1 to 2.3 MPa, with increase in polystyrene content (0 to 20 vol.%), which is an attribute to minimization of pore size from 277 to 170 μm. The study investigates the improvement of compressive strength because of the prevention of microcrack on the green body by addition of polystyrene during freeze drying.

Heinemann et al. [138] prepared hydroxyapatite-collagen nanobiocomposite scaffold followed by freeze drying method. Freeze dried (–20 ^{o}C) nanobiocomposite macroporous scaffold has open and interconnected porosity with pore size varying in the range of 100–200 μm. Compressive strength of the biocomposite scaffold increases with addition of the mineral HA volume content. The Young's modulus of the nanocomposite scaffold exhibits about 0.4 MPa, whereas compressive strength is found as 0.085 MPa, only.

Asefnejad et al. [139] prepared nano-fluoro-hydroxyapatite (nFHA)/polyurethane composite scaffolds through freeze drying technique. The study demonstrates that composite scaffold has interconnected and homogeneously distributed pores along with 80 vol.% porosity. The scaffold has a pore size in the range of 50–250 μm. Compressive strength and modulus increases with increase content of nFHA. Highest compressive strength 0.6 MPa and their modulus 0.8 MPa are reported for 20 wt.% nFHA.

Kane et al. [140] studied the effect of hydroxyapatite reinforcement on the architecture and mechanical properties of freeze dried collagen scaffold. The scaffold exhibits elongated linear pore structure with 90 vol.% of porosity and pore width of 50 μm. The compressive modulus of composite scaffold at 60 vol.% HA content is 0.2 MPa, whereas 30 vol.% HA exhibits 0.02 MPa. High aspect ratio elongated morphology (length-18 and aspect ratio-8) of HA whiskers has a low level of reinforcing effect compare to conventional equiaxed 1.3 μm HA powder.

Several study demonstrate the fabrication of nanobiocomposite scaffold has significant influence on HA solid content, HA morphology and freeze casting conditions. In this backdrop, suggested different morphologies of nano HA will be considered to achieve high level of compressive strength for porous nanobiocomposite scaffold with variation of HA solid content.

2.7 Materials at cryogenic temperature

Coefficient of thermal expansion is generally reduced bellow 273K and enhanced above it. This basic philosophy would be encountered to enhance the mechanical response of freeze casted nanobiocomposite. Brief literatures as relevance with proposed work are discussed as follows.

Yang et al. [141] studied on the improvement of mechanical properties of polymer in cryogenic temperature. Mechanical properties improvement after low temperature treatment is seen for epoxy resins such as di-glycidyl ether of bis-phenol A (DGEBA). The study demonstrate that hydroxyl functionalized hyperbranched polymer (H30) is introduced to improve the mechanical properties of DGEBA epoxy resin at liquid nitrogen temperature (77 K). Tensile strength, failure strain (ductility) and impact strength at 77 K are also simultaneously improved by the addition of H30. The maximum tensile strength at 77 K has increased by 17.7% from 98.2 MPa of pure epoxy resin to 115.6 MPa at 10 wt.% H30 content. Failure strain at 77 K increases consistently with the increase of H30 content. The maximum impact strength at 77 K is observed by incorporation of 10 wt.% H30 with an improvement of 26.3% over that of pure epoxy resin. The achieved maximum tensile strength at 77 K is attribute to optimum content of 10 wt.% H30.

Chen et al. [142] studied on the reinforcement of multi-walled carbon nanotubes (CNT) in epoxy resin matrix to enhance the cryogenic mechanical properties. The study represents that when the temperature decreases from room temperature to liquid nitrogen temperature (77 K). A strong CNT–epoxy interfacial bonding exhibits stronger interaction at 77 K compared to room temperature due to coefficient of thermal expansion minimization from 5.1×10^{-5} K^{-1} to $0.73–1.49\times10^{-5}$ K^{-1}. Cryogenic tensile strength, Young’s modulus and failure strain and impact strength at 77 K all are enhanced by the appropriate concentration of CNT.

Yang et al. [29] studied on enhancement of mechanical properties of montmorillonite/epoxy (MMT/epoxy) nanocomposites at cryogenic conditions. The comparative study reveals the mechanical behaviour of MMT/epoxy nanocomposites both at room temperature (RT) as well as liquid nitrogen temperature (77 K). The strength and modulus of nanocomposites are significantly higher at 77 K than at RT, and these observations are explained in terms of interfacial adhesion and constituent properties at 77 K and RT. Cryogenic treatment enhances the room temperature tensile strength of MMT/epoxy nanocomposites from 3.1% and 13.2%. Tensile modulus of nanocomposites at 77 K almost linearly increases with increase of organo-MMT content. The notched impact strength at RT increases from 4.0 kJ/m^2 for the epoxy matrix to 5.0 kJ/m^2 for nanocomposite with 1 wt.% organo-MMT content.

Yamaoka et al. [143] studied on the mechanical and chemical properties of plastic film at cryogenic temperature, where tensile strength and elongation of plastic film at 77 K are found to decrease with an increase in the degree of crystallinity. Since, the polymers include those whose main chains are composed of oxygen, sulphur or various heterocyclic linkages only. The study focuses on chemical behaviour of polymers which able to change bond angles of the main chain seem to excel in the cryogenic environment. This is due to their segmental motion frozen out at cryogenic temperature and subsequent polymer deformation.

Polymer based HA composite exhibits better mechanical properties in the cryogenic conditions and, hence the cryogenic process optimization for enhancement of mechanical properties of the proposed freeze casted HA-gelatin scaffold are needed to explore.

2.8 *In vitro bioactivity and biodegradation*

Utilization of HA based biomaterial preferably depends on its bioactivity and biodegradation during *in vivo* application. In this aspect, *in vitro* assessment is mandatory prior to clinical use and therefore, different classical research is pointed out to understand these phenomena.

Kim et al. [144] studied the bioactivity of HA scaffold as a function of soaking time in simulated body fluid (SBF). The mechanism of bone like apatite formation has been examined and described on the surface of HA. After soaking in SBF, HA form a Ca-rich amorphous calcium phosphate (ACP) and Ca-deficit ACP and finally crystallizes to bonelike apatite. HA surface reveals negative surface charge during exposure to SBF, thereby interacting with the positive calcium ions in the fluid to form Ca-rich ACP, which ultimately gains positive surface charge and described in Figure 2.5. The Ca-rich ACP on HA then interacts with negative phosphate ions in the fluid to form Ca-deficient ACP, which finally stabilize and crystallized into bonelike apatite with a low solubility in the SBF. However, this exposure time retards the bone like apatite formation on high crystalline HA compared with less crystalline HA. This phenomenon is attributing to initial lower negative surface charge of the higher crystalline HA to scarcity in surface hydroxyl and phosphate ions.

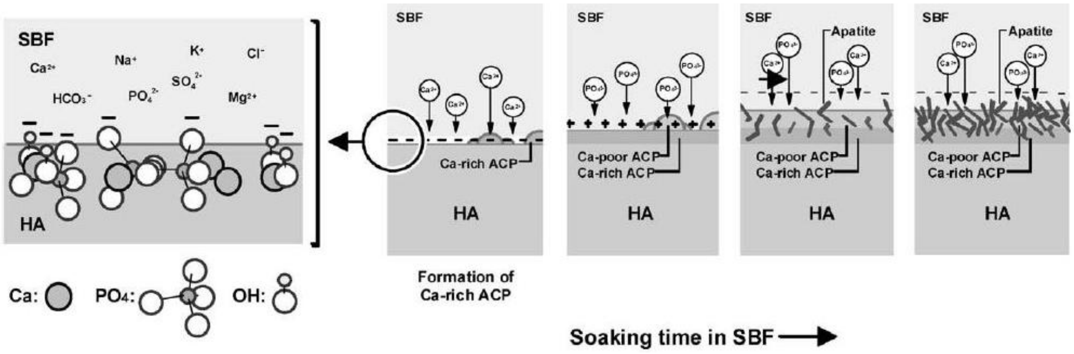

Figure 2.5 Schematic presentations of the origin of negative charge on the HA surface and the process of bone like apatite formation [144].

Takadama et al. [145] demonstrated *in vitro* mechanism of biomineralization of apatite on Na_2O-SiO_2 glass as a function of soaking time in SBF. First stage of soaking, favours the Na^+ ions exchange with H_3O^+ ions in SBF to form silanol (Si-OH) groups on its surface. Calcium ions prefer to incorporate within Si-OH group during immersion condition and forms amorphous calcium silicate. Following that, phosphorous ion insertion is observed within calcium silicate to form amorphous calcium phosphate with a low Ca:P atomic ratio of 1.43. The amorphous calcium phosphate is gradually transformed into crystalline apatite, which contains small amounts of Na, Mg, and Cl with Ca/P ratio of 1.65, similar to bone mineral. This work also illustrates the spontaneous bone like apatite growth phenomenon by consuming the remaining calcium and phosphate ions in the fluid. In brief, the original formation of calcium silicate is a consequence of an electrostatic interaction of negatively charged -Si-O- units which formed by dissociation of Si-OH groups and positive charged calcium ions in the fluid. Calcium silicate is postulated to gain a positive charge and interact with negatively charged phosphate ions in the fluid to form an amorphous calcium phosphate.

Kokubo et al. [146] studied the apatite formation on the surface of ceramic, polymer and metal. Bioactive ceramics bond to the living bone through a bonelike apatite layer formed at an optimum condition. The apatite is nucleated by -Si-OH groups on their surfaces and grows by consuming the calcium and phosphate ions from the body fluid. Bonelike apatite layer formed even on metal surfaces such as silicon, titanium and its alloys, tantalum as well as organic polymers such as poly(ethylene terephthalate), polyether sulfone and polyethylene in a simulated body fluid with ion concentration nearly equal to those of human blood plasma. Ti-OH and Ta-OH groups can also induce an apatite nucleation in SBF. The study demonstrates the mechanism of formation of bonelike apatite layer on the surfaces of bioactive ceramics.

Tas et al. [147] prepared biomimetic HA powders at 37 °C in synthetic body fluids. Nano HA powder is prepared from $Ca(NO_3)_2$ $4H_2O$ and $(NH_4)_2HPO_4$ salts dissolved in modified synthetic SBF solutions at 37 °C and pH of 7.4 through chemical precipitation technique. The prepared HA powder is spherical in morphology with average particle size in the range of 30–50 nm and stabilized up to 1600 °C an air atmosphere. The as-synthesized biomimetic HA powder has near to 96% densification characteristic.

Okazaki et al. [148] studied on dissolution behaviour of fluoridated HA. The dissolution rate of synthetic fluoridated apatite pellets with different fluoride content is measured in acetate buffer solution at pH~ 4. The observed dissolution rate depends on degree of fluoridation, interestingly lowest at low fluoride levels. The experimental data are analysed by means of a diffusion-controlled model in which initial dissolution rate is greatly affected by both the solubility and the overall mass transfer resistance. Overall mass transfer resistance is influenced by fluoride content in HA. The study has discussed that the solubility of fluoridated apatite is more strongly affected by fluoride content than by crystallinity and morphology.

Xu et al. [149] studied the biodegradation behaviour of porous scaffolds. Composite scaffolds of poly(D,L-lactide)(PDLLA) bioactive wollastonite powders are prepared through a salt-leaching method using NH_4HCO_3 as a porogen. The *in vitro* bioactivity of composite scaffold is evaluated in SBF solution and reported the apatite layer formation mechanism on its surface. *In vitro* degradation behaviour of these scaffolds is systematically monitored at varying time schedule in the presence of tris-HCl buffer solution at 37 ^oC. Apatite formation on the surface of scaffolds is seen after 7 days of immersion in SBF. The measurement of weight loss, pH and molecular weight of the samples indicates that PDLLA/wollastonite composite scaffold degrades slower than the pure PDLLA scaffolds. The wollastonite addition enhances the mechanical properties of the composite scaffolds.

Martinez-Valencia et al. [150] studied *in vitro* bioactivity and biodegradability on polyurethane HA composite scaffold. Biodegradability and bioactivity studies are carried out by immersion into phosphate buffer saline (PBS) and SBF solutions, respectively. Biodegradation rate increases with the content of nano HA content. The study reveals 3 wt.% loss in the composite contains 10 wt.% nano HA, where as 4 wt.% loss is seen for 40 wt.% nano HA content composite during 56 days of study. *In vitro* bioactivity shows that the composite exhibit advantages over polyurethane, although the bone-like apatite formation is regulated both in composite as well as in polyurethane.

Similarly, bioactivity and biodegradation assessment of HA-gelatin biocomposite porous scaffold will be carried out after optimization of pore morphology and mechanical strength.

2.9 In vitro cytotoxicity and cell viability

Cell viability and cytotoxicity assessment will support to understand the *in vivo* cell compatibility and level of toxicity of the synthetic biocomposite scaffold for clinical application. Therefore, different schools are continuously evaluated and reported this phenomenon for the future development of a new class of biomaterials.

Filho et al. [151] studied on the cell attachment, cellular interactions and modulation of osteoblast cells on biocompatible materials such as porous HA scaffold. Biocompatibility of material has been studied through consideration of human osteoblast (HOB) cells on the fibronectin coated glass surface and mono layers formation of HOB observed. The cellular adhesion to material interaction includes two phenomena: (a) physico-chemical properties of the interacting surface and (b) molecular properties of both surfaces and also the interaction medium. The study pointed out that cell attachment is a property which depends on physical and topological features of both biomaterial and cell surfaces.

Oliveira et al. [152] studied the cytocompatibility and cell viability on porous HA scaffold using mouse fibroblast cells (L929 cells). Fibroblast cells partially proliferated and covered scaffold surface, after prolong 72h seeding. The scaffold extract fluid is investigated by carrying out a cellular viability assay (MTT {3-(4,5-diamethyl thiazol-2-yl)-2,5- diphenyltetrazolium bromide} test) using mouse fibroblastic-like cells. L929 cells percentage relative viability determine for each extract concentration and compare to tissue culture polystyrene. Cells morphology, proliferation and monolayer formation are observed through inverted microscope. The study reveals that materials do not have any cytotoxic effect.

Kim et al. [153] studied *in vitro* cellular response and attachment on freeze dried HA–gelatin composites. Osteoblast-like human osteosarcoma cells are spreading and actively proliferate on composite scaffold. The cell proliferation rate is calculated indirectly on the cells cultured on Ti discs coated with gelatin and HA–gelatin composites using MTT assay. The alkaline phosphate activities express by the cell culture on composites and HA coatings on Ti discs enhances significantly compared with those on pure gelatin. This finding suggests that HA–gelatin composite has great potential for use as hard tissue regeneration scaffolds.

Silvio et al [154] studied *in vitro* effect of surface composition of human osteoblast (HOB) cell behaviour on different content of HA reinforced polyethylene (PE) composite. HOBs are cultured in direct contact with test materials containing 20% and 40 vol.% HA. The study reveals that 40% HA/PE enhanced cellular activity by increasing proliferation rate and differentiation compared to 20 vol.% HA composite. HOBs cultured on 40% HA/PE is flatter, enhanced rate of cytoskeletal organisation and an increase in focal contact points compared to 20% HA/PE. Here, the surface topography has importance for cell attachment, where cellular response enhances with increasing

HA volume. Cytoskeletal studies have suggested that HA particle provides anchorage for osteoblastic cells and reveals a favourable surface for cell attachment.

Dalby et al. [155] studied the original attachment of osteoblast like cells on HA reinforced polyethylene composite (HAPE), which is designated as a second-generation orthopaedic biomaterial with suitable mechanical and biological characteristics for bone augmentation. Optimisation of the material features like mechanical properties enhancement has important role for effective attachment of osteoblasts cells. Polishing followed by roughening the surface of HAPE enhances osteoblast proliferation.

Gou et al. [156] studied cytotoxicity and ostioconductive properties of Ca-deficient HA (CDHA) scaffold using MSCs (Mesenchymal stem cell). MSCs are cultured, expanded and seeded on the scaffold surface. Proliferation and differentiation of MSCs on scaffold is evaluated through MTT assay. CDHA scaffolds are biocompatible and have no negative effect on the MSCs *in vitro*. The *in vivo* biocompatibility and osteogenicity of the scaffolds are also investigated and is implanted in rabbit mandibles. It exhibits good biocompatibility and osteoconductivity. Biodegradation up to 36% of CDHA scaffolds are degraded after 12 weeks in Tris–HCl solution. Effective new bone formation could be seen after implantation of MSCs into the scaffold within 2–4 weeks.

In this perspective, it is important to assess the cytotoxicity and cell viability of developed scaffold.

2.10 Protein loaded porous scaffold

Cell attachment on the biomaterial interface and their proliferation is only possible when protein molecule make bridge within these two moieties. Several pioneer works has been carried out to understand the cell viability and attachment with synthetic biocomposite scaffolds through the protein adsorption and release.

Jaklenec et al. [157] discussed a novel method for incorporating proteins in 3D biodegradable scaffolds by utilizing protein-loaded microspheres as the building blocks for scaffold formation. Poly(L,D-lactic-co-glycolic acid) (PLGA) microspheres containing BSA are combined with scaffolds using a dichloromethane vapor for different time intervals. The microspheres are loaded with 0.4, 1.5 and 4.3 wt.% BSA protein. The protein release study has been quantified *in vitro* and demonstrate a slight lower (up to 20%) release over 10 days. Well spread and attachment of fibroblast cells observed on the protein loaded scaffold after 4 h of incubation.

Mohan et al. [158] fabricated biodegradable egg albumin based gelatin porous scaffold. Gelatin is functioning as promoter for good cell adhesion due to its hydrophilic nature. Hydrophobic–hydrophilic balance has been controlled by egg albumin. Monolayer fibroblast and chondrocyte calls are cultured in the fabricated scaffold and also examined on the stem cell differentiation to chondrocytes. Proliferation and differentiation of mesenchymal stem cells to chondrocytes is studied in presence of growth factors. Chondrocyte culture on the porous scaffold shows the deposition of cartilage specific matrix molecules.

Lyu et al. [159] developed polyethylene oxide/chitin/chitosan porous scaffolds grafted with albumin and applied for the neocartilage formation. The albumin grafted porous scaffold is cultured with porcine knee chondrocytes cells to understand the regeneration of articular cartilage. Albumin coating on the pore surface of a scaffold accelerates the proliferation of porcine knee chondrocytes, secretion of glycosaminoglycans, which favours generation of collagen and formation of cartilaginous components.

Sawyer et al. [160] studied the effect of adsorbed serum protein on adhesion of mesenchymal stem cells (MSC). RGD (Arg-Gly-Asp) and proteoglycan-binding peptide combination do not have remarkable enhancement of MSC attachment spreading on HA surface. The study reveals that peptide-modified surfaces are not able to stimulate the same degree of cell attachment and to spread as that seen on serum-coated HA. The results suggest that the possibility of optimal cell-material interaction insist by native HA exposed to blood *in vivo*, instead of surface functionalization with RGD/proteoglycan-binding peptides.

Kou et al. [161] studied the formation of neocartilage by cultivating chondrocytes in elastin and poly-l-lysine modified scaffolds. Bovine knee chondrocytes are seeded on the scaffolds and cultured in a spinner-flask bioreactor over 4 weeks. Surface elastin reveals a better efficiency in the adhesion and proliferation of bovine knee chondrocytes in the scaffolds than surface poly-l-lysine. Elastin and poly-l-lysine grafted scaffolds are found to be effective in producing cartilaginous components to generate neocartilage by cultivating chondrocytes in elastin and poly-l-lysine modified scaffolds. The study illustrates that elastin and poly-l-lysine graft enhance the peptide rich surroundings for chondrocyte growth. The effect of surface elastin and poly-l-lysine improves cell adhesion, viability and chondrogenesis in the scaffolds.

Kilpadi et al. [162] investigated that HA binds more serum proteins, purified integrins and osteoblast precursor cells than pure titanium or 316L stainless steel. The implant material HA exposed to the patient's blood during surgery adsorbs known cell adhesive proteins such as fibronectin and vitronectin from the serum. The study shows that an osteoblast precursor prefers to adhere of these proteins through integrin-mediated mechanisms. The enzyme-linked immunosorbent assay (ELISA) and cell adhesion assay test suggests that the increased protein adsorption would lead to better binding of fibronectin, vitronectin and osteoblast precursor cells to HA than to the metals. It has been suggested that osteoblast attachment is one of the potential targets for clinical improvement of bone formation at implant surfaces.

Literature suggests a protein interaction behaviour is an important issue and need to explore when development of a new scaffold is concern. Hence, optimized scaffold will be considered to understand the common and easy available BSA protein adsorption-release phenomena.

2.11 Micro-CT analysis of scaffold

The quantitative analysis of pore interconnectivity, pore volume content and pore wall thickness of the adsorbed protein layer are effective information for *in vivo* assessment of biomaterial composite scaffold. Till to date, selective work has only been carried out to accumulate this information which are summarized for future reference.

Segvich et al. [163] studied the deposition of protein incorporated calcium phosphate mineral layer on three dimensional porous polymer scaffold through micro-CT analysis. Micro-CT analysis illustrate the mineral volume percent (MV%) (7.86 ± 3.25 MV) increment and the uniform distribution of BSA protein on polymer scaffold. Near to 10-fold increase of BSA incorporation is observed in polymer scaffold. The 3D mineralization is observed through the thickness of porous material and provides the option of inclusion of co-precipitated biomolecules within the mineral layers.

Simon et al. [164] studied the micro-CT analysis of HA bone repair scaffold to evaluate the scaffold architecture on bone ingrowth. Bone volume ingrowth with respect to the total region of interest, bone volume ingrowth with respect to available ingrowth volume and soft tissue volume are analysed. The study illustrates that factorial analysis is the greatest determinant factor for soft tissue ingrowth, whereas pore volume is the greatest determinant of bone volume ingrowth. Pore interconnectivity, thickness of pore wall and pore size distribution also analysed.

Henslee at al. [165] studied the micro-CT analysis of biodegradable composite scaffold for bone morphogenic protein deliver and bone regeneration in segmental long bone defects. The work describe a 3D micro-CT and pore partitioning study to derive pore scale parameters including pore radius distribution, accessible radius, throat radius and connectivity over the pore space of a tissue engineered constructs. The amount of bone formed within the defect is evaluated both qualitatively and quantitatively only after at 12 weeks with micro-CT. Tissue response is evaluated for the bone-rod interface, bone sleeve interface and within the pores of the sleeve for 12 weeks.

However, no trial has been conducted to get detail quantification data for the internal architecture, pore interconnectivity and pore wall thickness of scaffold and their protein loaded scaffold.

2.12 Summary of contribution

The extensive literature survey shows that no trial has been conducted to make different aspect ratio particles such as spherical, rod and fibrous morphology co-precipitation route and control over identical precursor concentration, solution pH and temperature. Stable aqueous homogeneous dispersion of such developed three different morphologies of HA nanoparticles in physiological temperature and solution pH is obvious not reported. Moreover, no trial has been conducted to study the effect of HA nanoparticle morphologies and their aspect ratio on the adsorption and release of protein. The assessment of macroporous hydroxyapatite-gelatin scaffold with connected pore architecture, optimized compressive strength, and effect of HA solid content on porosity and strength at low temperature are also needed to explore. Consideration of cryogenic temperature (77K) and effect of curing time for the enhancement of compressive strength and bonding behaviour on HA-gelatin macroporous scaffold is limited. Understanding on the apatite nucleation in simulated body fluid, cytotoxicity, cell viability and rate of biodegradation on the cryotreated nanocomposite scaffold is essential for the development of such scaffold. Protein adsorption capacity and efficient release kinetic for both particles and cryotreated HA-gelatin macroporous scaffold have not been found, which may assist to understand the efficiency of protein interaction activity. The study of scaffold internal architecture, pore interconnectivity and pore wall thickness in cryotreated macroporous HA-gelatin scaffold and their protein loaded scaffold is also not documented. Based upon the above findings the objective of the present investigation has been summarized.

2.13 Thesis objective

a) To pursue low temperature synthesis of different spherical, rod shaped and fibroid morphologies of hydroxyapatite nanoparticles and study of their dispersion phenomenon.

b) To prepare HA nanoparticle – protein (bovine serum albumin) conjugate and study of their adsorption and release.

c) To fabricate freeze casted nanobiocomposite (HA-gelatin) scaffolds and evaluation of their compressive strength.

d) To improve and optimization of compressive strength through cryogenic treatment of scaffold.

e) To study bioactivity and biodegradability of developed and optimized porous scaffolds.

f) To evaluate cytotoxicity and cytocompatibility of nanobiocomposite scaffolds.

g) To prepare nanobiocomposite scaffold – protein conjugate and evaluation of their adsorption and release.

Chapter-3

Methods

Chapter 3 Methods

3.1 Preparation of HA nanoparticles

A simple wet chemical process and systematic design of experiment were conducted to synthesis and achieved specific properties of HA spherical nanoparticles, nanorods and nanofibers. Three different morphologies of HA nanoparticles were prepared from two common precursors; $(CH_3COO)_2Ca$ and KH_2PO_4. A representative microsturcture of calcium acetate was taken and discussed later. In aqueous media, two inorganic salt solutions were separately prepared and slowly mixed to maintain the Ca:P molar ratio of 1.67 in HA. Both of the solutions ($(CH_3COO)_2$ Ca = 0.1M and KH_2PO_4 = 0.06M) were separately added at a constant rate of 0.5 lh^{-1} and stirred within one litre of water. Solution pH were controlled through NH_4OH and tris-buffer (Tri-methylhydroxy aminomethane) solution for spherical and rod morphology, respectively. A specific tailor-made temperature sensor attached glass vessel was used to measure accurate reaction vessel temperature during synthesis of these nanoparticles. Different 35 sets of experiment were conducted in account of Ca/P ratio, solution pH and temperature, wherein 22 numbers of data found as HA phase with desired morphology; i.e. spherical, rod and fibroid shape. However, five numbers of experiment supported the formation of Ca:P near to 1.67. Calcium (Ca) and phosphorus (P) was determined by complexometric titration with EDTA and gravimetric method through ammonium molybdate, respectively [166]. The entire experimental setup for the preparation of nano HA powder represented in Figure 3.1. However, three optimized conditions were chosen to achieve the desired morphology and Ca:P ratio of pure HA nanoparticles. A typical flow diagram for the preparation of HA nanofibers described in Figure 3.2. Spherical HA nanoparticles (NHS), rod HA nanoparticles (NHR) and fibroid HA nanoparticles (NHF) were developed at pH = 12.25, temperature = 298K; pH = 9.5, temperature = 303K and pH = 5.25, temperature = 353K, respectively. The individual precipitates were washed with de-ionised water followed by isopropyl alcohol and separated through centrifuge at 14,000 rpm. Semi dried particles were freeze dried at 220 K and 77 torr pressure and finally obtained 12 gram of nanoparticles. Similarly, bulk quantity (60 gms) nanoparticles were prepared to carry forward their characterizations, preparation of nanocolloids and making scaffolds from all morphologies.

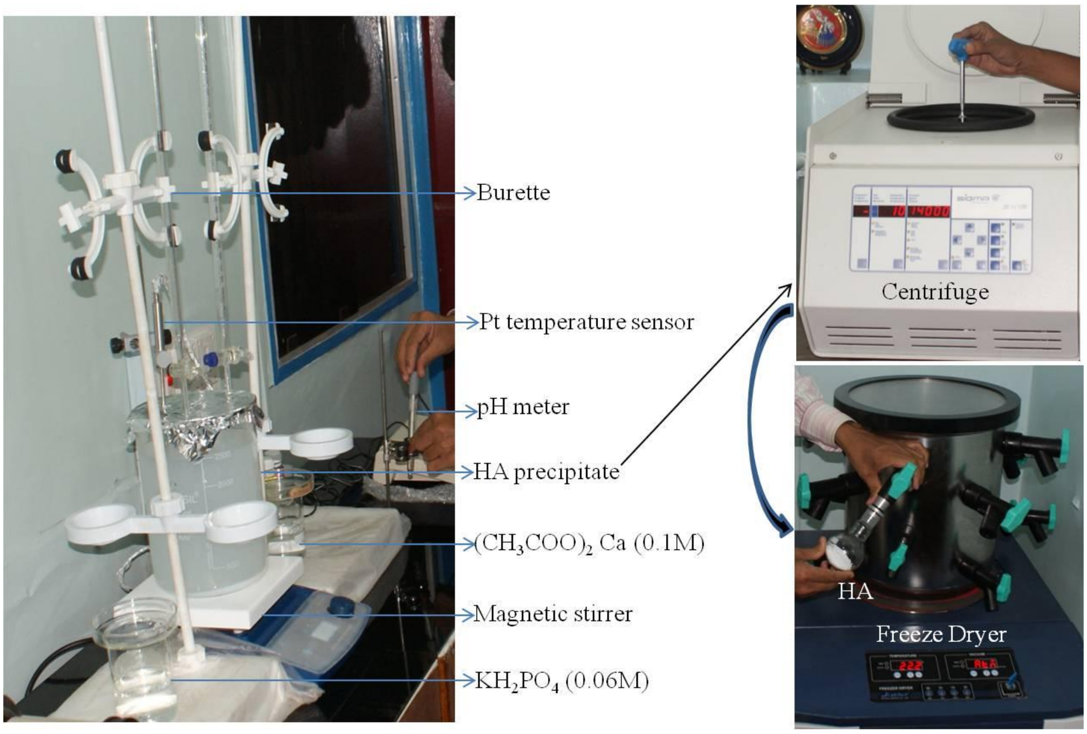

Figure 3.1 Experimental setup for the preparation of HA nanoparticles through precipitation method.

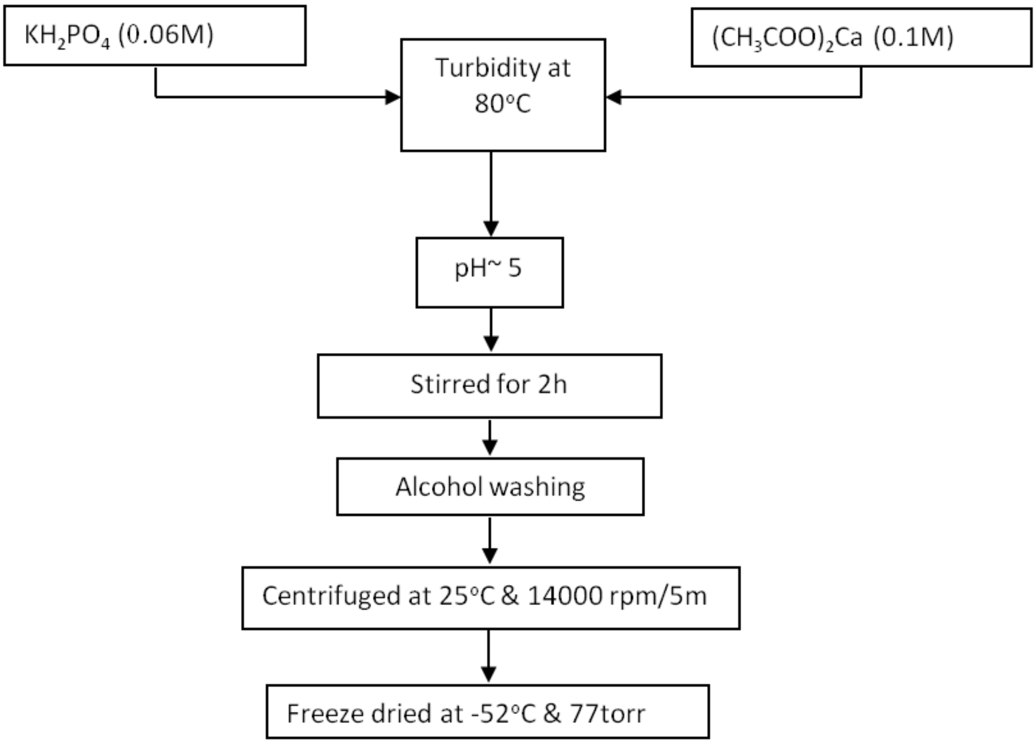

Figure 3.2 A typical flow diagram for the preparation of HA nanofibers.

3.2 Characterizations of HA nanoparticles

3.2.1 Phase analysis of HA nanoparticles

Phase and crystallinity of HA powders were analysed using room temperature powder X-ray diffraction (Philips PAN analytical, Netherland) with an attachment of Ni-filter 0.154 nm and Cu K-α radiation as source. The diffractometer was operated at 35 kV and 30A. All powder samples were scanned in a continuous mode over a 2θ range from 20 to 80 with a scanning rate of 0.02 degree/sec. The peak position, phase purity, peaks of different atomic planes and the relative intensities of the powder pattern were identified in comparison with the reference powder diffraction data (JCPDS). The average crystallite size of all nano HA samples were calculated using Scherrer's formula [167,168].

$$D = \frac{0.9\lambda}{\beta\cos\theta} \text{ .... (i)}$$

Where, D = Average crystallite size

λ = Wavelength of X-ray

β = Wavelength of the full-width at half-maximum

θ = Diffraction angle

3.2.2 Rietveld refinement of calcined HA nanoparticles

All three different powders were calcined to evaluate their probable crystal pattern, crystal structure, lattice parameter, cell volume as for reference. FullProf.2k program was used for Rietveld refinement of X-ray diffraction powder patterns. As synthesized three different grade of HA nanopartiles were calcined at predetermined temperature 700 ^{o}C with isothermal soaking of 2h. HA nanoparticles were analysed using room temperature X-ray diffraction with Ni-filtered using Cu K-α radiation source, and data were collected in continuous mode from 20 to 80^{o} 2θ with a scanning rate of 0.02^{o}/sec [169]. Apatite starting atomic parameters from the refinement based on X-ray diffraction data in $P6_3/m$ space group. Rietveld structure refinement method was corresponded to the general guideline as adopted by the International Union of Crystallography Commission on Powder Diffraction. Scale factors, zero shift, line profile parameters, lattice parameters, preferential orientations and asymmetry parameters were refined at first step. Atomic displacement factors, as well as atomic coordinates from the HA structure, were refined in a second step. Site occupancies of cations, phosphate and hydroxyl anions were also systematically checked in the last run.

3.2.3 FT- IR study of HA nanoparticles

The phase purity and presence of major functional groups were analysed through Fourier Transmission Infrared (FT-IR) spectra method (Perkin Elmer RXI, Spectrum, USA) in the wave number 4000 – 400 cm^{-1} and KBr as reference. The discs were prepared by pressing the mixture of 5 mg of HA nanoparticles with 100 mg of KBr at pressure of 3 ton.

3.2.4 Determination of Ca:P ratio of HA

Calcium to phosphate ratio for as-synthesized HA nanoparticles were estimated through chemical analysis. Calcium was estimated by complexometric titration technique with EDTA (Ethylenediaminetetraacetic acid), whereas phosphorus was estimated by gravimetric method through ammonium molybdate precipitation method.

Preparation of stock solutions:

(a) Preparation of HA solution: Spherical (NHS), rod (NHR) and fibroid (NHF) HA stock solutions were prepared by taking 0.1g of each sample in 250 ml volumetric flask and made complete solution by the addition of few drops of nitric acid. Volume of each flask was adjusted up to the mark by distilled water.

(b) Preparation of 0.01M EDTA solution: EDTA (0.9306 gm) was taken in 500 ml volumetric flask and prepared homogeneous solution by distilled water and considered as primary solution.

(c) Preparation of 0.01M $CaCO_3$ solution: $CaCO_3$ (0.1gm) was taken in 100 ml volumetric flask, added HCl to dissolve and volume marked up through distilled water.

(d) Preparation of ammonium molybdate reagent: Initially, solid 125 gm ammonium nitrate was dissolved in 125 ml water and added 175 ml nitric acid (sp.gr. 1.42) to prepare their nitrate solution. Solid ammonium molybdate (12.5 gm) was dissolved in 75 ml water and subsequent slowly added into ammonium nitrate solution through constant stirring. Mixture solution further diluted to 500 ml, heated the flask in a water bath at 60 ^{o}C for 30 minute and finally filtered the precipitate. The resultant filtrate (heptamolybdate) was further used for the estimation of phosphorus atom concentration of hydroxyapatite nanoparticles.

Standardization of EDTA:

10 ml of 0.01M $CaCO_3$ solution was taken in 250 ml conical flask, added 10 ml of ACC (ammonium acetate) buffer (pH~10) and 2-3 drops of Eriochrome Black-T indicator followed by titration with 0.01M EDTA solution. The end point detected when solution was changed from wine red to blue in colour. The experiment was repeated 2-3 times to get concordant value.

Estimation of Ca^{2+} in HA:

As similar with EDTA standardization, 10 ml of HA $[Ca_{10}(PO_4)_6(OH)_2]$ solution was taken in 250 ml conical flask, followed by added 10 ml ACC buffer solution to maintain pH~12 and 2-3 drops of Eriochrome Black-T indicator and subsequently titrated with standard EDTA solution. The end point was reached when colour of the solution changed wine red to blue. Similar experiment was carried out for all HA solutions as obtained from three different grade nanoparticles. The experiment was also repeated 2-3 times as earlier.

Determination of phosphate in HA:

The as prepared 15 ml ammonium molybdate reagent (heptamolybdate) was added to 10 ml of HA solution into a conical flask and heated at 60 °C for an hour through constant stirring. The resultant yellow precipitate was separated by filtration and washed with 2 wt.% ammonium nitrate solution. The precipitate was calcined at 825 °C and develop $P_2O_5 24MoO_3$, which was gravimetrically estimated the content of phosphate ions and thereof concentration of phosphorous atom [166]. The equation is leading to phosphate determination through the molybdate reagent as:

$$24H^+ + 12MoO_4^{2-} + PO_4^{3-} \xrightarrow{60^o C} [PMo_{12}O_{40}]^{3-} + 12H_2O \qquad ....(ii)$$

$$2[PMo_{12}O_{40}]^{3-} \xrightarrow{825^o C} P_2O_5\,24MoO_3 \qquad ....(iii)$$

3.2.5 Transmission electron microscopy of HA nanoparticles

Transmission electron microscopy (TEM) is a technique to study the high resolution morphology, lattice fringe and crystallinity of materials, in which a beam of electrons is needed to transmit through the specimen. An image is developed from interaction of electrons transmitted through the specimen. The particle size and morphology of as synthesized HA powder were studied by TEM, whereas lattice parameters and crystallinity was estimated by TEM and SAED (Selected Area Electron Diffraction) pattern, respectively. The TEM samples were prepared by dispersing a small amount of powder in acetone using 20 kHz and 500W ultrasonic energy for 30 minute. A well-dispersed suspension was dropped on a carbon coated copper grid and dried to evaporate the solvent. The powder morphology was observed under bright field mode transmission electron microscope (JEOL JEM-2100, TEM).

3.2.6 BET surface area study of HA nanoparticles

BET technique was coined according to inventor Stephen ***B***runauer, Paul ***E***mmett and Edward ***T***eller, who scrutinized the surface phenomena of a powder or porous body by help of gas adsorption method. The approach assumes each gas molecule occupy a specific surface area. Low pressure adsorption isotherm provides a mean to take the mass of adsorption corresponding to a single gas molecule layer and calculated the surface area from it. BET surface area is then calculated from adsorption behaviour under a range of partial pressures. The BET equation [170] is represented as:

$$\frac{P}{X(P_o - P)} = \frac{1}{X_m C}\left[1 + \frac{P}{P_o}(C-1)\right] \text{.............................(iv)}$$

Where,

P = Measured partial pressure of adsorbate.

P_o = Saturation or equilibrium pressure of adsorbate, which depends on the gas and temperature.

X = Mass of the gas adsorbed at pressure P.

X_m = Adsorption capacity of the powder (the mass of gas necessary to form a saturated surface coating one atomic layer thick).

C = Constant relating to the adsorption enthalpy. ‘C’ is calculated from the exponential of the difference in adsorption enthalpy for the outer surface layer versus an inner layer.

BET equation is a linear equation and valid for measuring the surface area of a powder when the pressure range P/P_o varies from 0.05 to about 0.35. The S_{BET} equation can be represented in a general form as:

$$S_{BET} = \frac{X_m N_o A_o}{WM} \text{.......................(v)}$$

Where,

M = Molecular weight of the adsorbate,

A_o = Average occupational area of an adsorbate molecule (nitrogen is the most popular adsorbate gas and it has an average occupational area of 16×10^{-20} m^2)

N_o = Avogadro’s number

W = Mass of the sample

BET specific surface area could be demonstrated with consideration of equivalent spherical diameter of monosized spheres. The BET equivalent spherical particle diameter is generally, calculated from surface area as follows [171].

$$D_{BET} = \frac{6}{\rho_t \times s_{BET}} \text{...(vi)}$$

Where,

S_{BET} = Specific surface area of the powder measured in m^2/g

ρ_t = Theoretical density of the powder

D_{BET} = Particle size measured in micrometer.
In this form the proportionality factor of 6 reflects an assumed spherical shape.

The BET specific surface area and BET isotherms of synthesized powders were taken at nitrogen adsorbate, using BET (Quantachrome Autosorb, USA). The HA powder was degassed at 200 °C and measurement was performed at five different points for specific surface area. The N_2 gas adsorption-desorption isotherms of the samples were conducted at liquid nitrogen temperature (77K). Approximately 40 mgs of powder was taken to remove contaminant water vapour and adsorbed gases from the samples at 200 °C in nitrogen atmosphere. BET isotherms (40 points) measurement were done in liquid nitrogen environment and represented as the amount of nitrogen adsorption or desorption on the material as a function of pressure (P/P_o = 0.025 – 0.999). The sample cell pressure altered until equilibrium established during adsorption or desorption. Average pore diameter and Barrett, Joyner & Halenda (BJH) adsorption pore distribution curves of the samples were estimated according to BJH model.

3.2.7 Scanning electron microscopy of HA precursor

Scanning electron microscope (SEM) is a typical electron microscope that images formed by simply scanning it with a beam of electrons. The electrons (secondary electrons, back-scattered electrons (BSE), characteristic X-rays) interact with the surface atoms which initiate to develop relevant information about the sample's microstructure, morphology and elemental composition. The microstructure of calcium acetate precursor was elucidated using scanning electron microscope (JEOL JSM 6480LV) after platinum coating in secondary electron mode at 15KV source. Several SEM images were taken similarly in later stage of the experiment.

3.3 Dispersion of HA nanoparticles in aqueous media

Different three grade HA nanoparticles were dispersed in aqueous media at optimum solution pH separately. The dispersion of 50 mg HA nanoparticle was executed in 400 ml double distilled water by the addition of (2 ml) 0.1M citric acid and (2.5 ml) 0.1M NaOH solutions. The solid – liquid mixture solution was treated at 348 K and 350 rpm for 30 minute. The synthesized HA nanoparticles and colloidal HA-citrate complex was analysed through FT-IR technique to understand the moiety adhesion phenomenon. Zeta potential at different step was measured during preparation of these homogenous suspensions.

3.4 Characterizations of dispersed HA

3.4.1 Zeta potential measurement of dispersed HA

Zeta potential provides the information about the magnitude of the electrical charge at the double layer in a colloidal system. Usually, it describes the potential difference between the dispersed medium and the stationary layer of fluid attached with the dispersed particles. The zeta potential value has significance to achieve and maintain the stability of colloidal dispersions. It indicates the degree of repulsion between adjacent, similarly charged particles in dispersion phase. Zeta potential (ζ) was measured through the zetasizer nano analyser (Zetasizer nano ZS, Malvern) by Smoluchowski's theory at room temperature and calculated by following equation-vii.

$$\zeta = \frac{4\pi\eta\upsilon}{\xi} \text{.........................(vii)}$$

Where,

ξ = Dielectric constant

η = Viscosity of the solution

υ = Electrophoretic mobility of ions

3.4.2 Particle size analysis of dispersed HA

The particle size and its distribution were estimated through zetasizer nano analyser (Zetasizer nano ZS, Malvern). The most important parameter for the dynamic light scattering is refractive index, and absorption of the particles and medium. Refractive index for both of the HA and water was considered as 1.5 and 1.33, respectively and absorption of HA powder was 0.01 [172]. The dispersed HA nanoparticles were used for the particle size analysis.

3.4.3 FT- IR study of dispersed HA

The dispersed HA nanoparticles were centrifuged at 800 rpm and freeze dried at 220 K and 120 torr pressure. The dried HA-citrate complex was analysed through FT-IR technique as discussed in section 3.2.3.

3.5 HA nanoparticle protein conjugates

3.5.1 SEM of BSA Protein

The morphology of BSA protein was studied through SEM analysis. Pt coated samples were analysed at 15KV through secondary electron mode. The detailed procedure was represented in section 3.2.7.

3.5.2 Measurement of BSA concentration through UV-visible

UV-vis spectroscopy technique was used to determine the absorbance of samples at visible region (400-800 nm). The concentration of an absorbing species in solution was quantitatively calculated by applying Beer-Lambert law. The Beer-Lambert law states that absorbance of a solution is directly proportional to the concentration of the absorbing species in the solution and their path length [173]. The mathematical relation is represented in equation (viii). Thus, for a fixed path length and wavelength, UV-vis spectroscopy was used to determine the concentration of the absorber in a solution. The schematic for the beer-Lambert's law is shown in Figure 3.3.

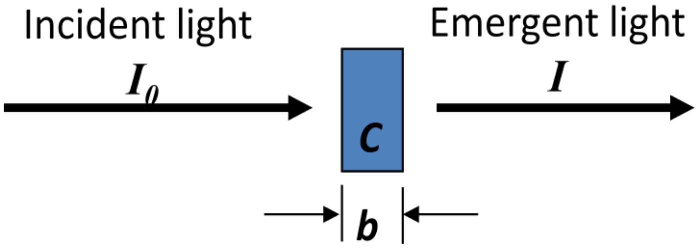

Figure 3.3 Schematic for the Beer-Lambert's law

$$\Rightarrow \log \frac{I_0}{I} = abc \equiv A \qquad \text{........(viii)}$$

Where,

I_o = Intensity of the incident light

I = Intensity of the transmitted light

A = Absorbance

b = Path length in cm (the distance that light pass through the material)

c = Concentration of the solution

a = Absorption coefficient (Lmol^{-1}cm^{-1})

UV-vis spectroscopy (Perkin Elmer, Lambada 35) at 562 nm was used to characterize the absorbance peaks and estimation of BSA concentration through the use of a predetermined standard concentration – intensity calibration curve.

3.5.3 Dilution of standard BSA

One ample of standard BSA contains 1 ml of concentration 2.0 mg/ml. A set of diluted standards with different ion concentration was prepared with the help of digital micropipette by taking one ample of standard BSA. BSA standard samples were prepared according to the following Table 3.1.

Table 3.1 BSA standard ion concentration for test tube protocol working range (20-2000 µg/ml).

No. Vial	Volume of diluents (µl)	Volume of BSA(µl)	Final BSA Concentration (µg/ml)
A	0	300 of stock	2000
B	125	375 of stock	1500
C	325	325 of stock	1000
D	175	175 of vial B	750
E	325	325 of vial C	500
F	325	325 of vial E	250
G	325	325 of vial F	125
H	400	100 of vial G	25
I	400	0	0

3.5.4 Preparation of BCA working reagent

BCA (bicinchoninic acid) working reagent was prepared by adding 50 parts of BCA reagent A with 1 part of BCA reagent B (50 : 1, reagent A : B). Reagent A composed of Sodium carbonate (0.1M), Sodium bicarbonate (0.1M), Bicinchoninic acid (0.02M) and Sodium tartrate (0.1M) in 0.1M Sodium hydroxide in solution pH – 11.25, whereas reagent B contains 4% $CuSO_4.5H_2O$ (0.25M) only. A clear green working reagent prepared with addition of reagent B. The prepared working reagent was stored in a closed container at room temperature of 25 ^oC.

3.5.5 Test tube procedure for protein concentration determination

Test tube procedure was adapted for the protein concentration determination through UV-vis spectroscopy. In the beginning, BCA working reagent (2 ml) was added within 0.1 ml of each diluted standard BSA protein and mixed thoroughly. The small liquid volume estimation was maintained by micropipette. Each tube was fitted tightly with a cover and then incubated at 37 ^oC for 30 minutes. Incubated tube was cooled down to room temperature say 25 ^oC. Intensity of the developed colour was measured through UV-vis spectrometer. The spectrometer was fixed at 562 nm and base line correction was done through de-ionized water. All the measurements were completed within 10 minute. The detailed test tube procedure for the estimation of protein concentration through UV-vis spectroscopy is shown in Figure 3.4.

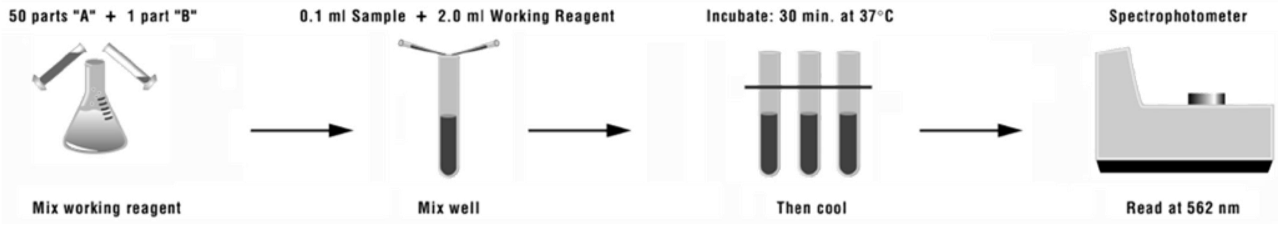

Figure 3.4 Schematic for the protein concentration determination through UV-spectrometers.

3.5.6 BSA adsorption/release on HA nanoparticles

Commercial grade crystallized and lyophilized BSA (Grade A9418, Sigma Chemical Co.) protein with molecular weight of 69 KDa and isoelectric point ~ 4.74 was used for the protein adsorption/release study. BSA protein was dissolved in deionized water. Nano HA particles (0.1gms) was separately added in 10 ml BSA solution of 5 mg/ml concentration and kept in an incubator at 37 ^{o}C for different time schedule from 6 h to 240 h. The supernatant solutions were collected after formation of each BSA–HA conjugate specimens through a centrifuge at 800 rpm and temperature 4 ^{o}C. BSA-HA conjugated residue product was freeze dried and further used for the release study. Identical procedure was followed for all three spherical, rod and fibroid HA nanoparticles. The amount of BSA protein uptake was quantified by taking 0.1 ml of supernatant from each specimens and mixing 2 ml of bicinchoninic acid solution (Thermo Pierce, Bicinchoninic acid protein assay kit, BCA-1 and 10N8010904) as discussed in the previous section. Similarly, BSA release study was also conducted in contact of HA-BSA conjugate and 20 ml of phosphate buffer solution (PBS) at pH 7.4 and temperature 37 ^{o}C. Detail schematic for release study has been represented in section 3.13.3.

3.5.7 Determination of peptide bond through FT- IR

FT-IR technique was employed for the determination of protein purity and the attachment feasibility of protein conjugate with HA nanoparticles. The protein samples were scanned in the wavenumber range 400-4000 cm^{-1} by following the KBr pellet technique. The detailed procedure was represented in section 3.2.3. The secondary structure and denaturation of protein was characterized through FT-IR analysis. However, circular dichroism (CD) spectroscopy is more apposite technique to determine the secondary structure and denaturation of protein [174].

3.5.8 Thermal analysis of HA-BSA conjugate

Thermal analysis technique is an excellent approach to determine decomposition behaviour, crystallization temperature, glass transition temperature, phase transition and reaction kinetic of materials which depends on the resultant heat content of sample with respect to temperature.

Thermo Gravimetric (TG) and Differential Scanning Calorimetry (DSC) (Netzsch STA/409 C) analysis of BSA and BSA adsorbed HA nanoparticles were carried out in an ambient atmosphere with the heating rate of 10 °C per minute, using α-Al_2O_3 as reference material. This experiment will predict the indirect organic protein molecule attachment efficacy with ceramic HA nanoparticles.

3.6 Fabrication of porous HA scaffold

HA-gelatin scaffolds were prepared from all three morphologies (NHS, NHR and NHF) of freeze dried HA nanopowders with adjustment of different solid loading 30, 40 and 50 wt. %. A slurry was prepared by addition of HA nanopowders, biocompatible 10 wt.% polyvinyl alcohol (PVA), 15 wt. % gelatin and rest amount of water. An optimum amount of gelatin was calculated on the basis of organic matrix content in bone [136]. Gelatin (Gelatin granules, Fisher Scientific Qualigens) was added in transparent PVA solution and mixed till homogenization. Highly dispersed HA nanoparticles were slowly added within the mixed solution of gelatin and PVA through continuous magnetic stirring. The solid–liquid mixture was gradually turned into high viscous slurry at 60 °C. The slurry was poured in a cylindrical glass mold and refrigerated at 268 K for 12 h to avoid sudden liquid solidification and evaporation. Semi–dried mass was then freeze dried at 221 K and 77 torr pressure. The detail process flow diagram is represented in Figure 3.5.

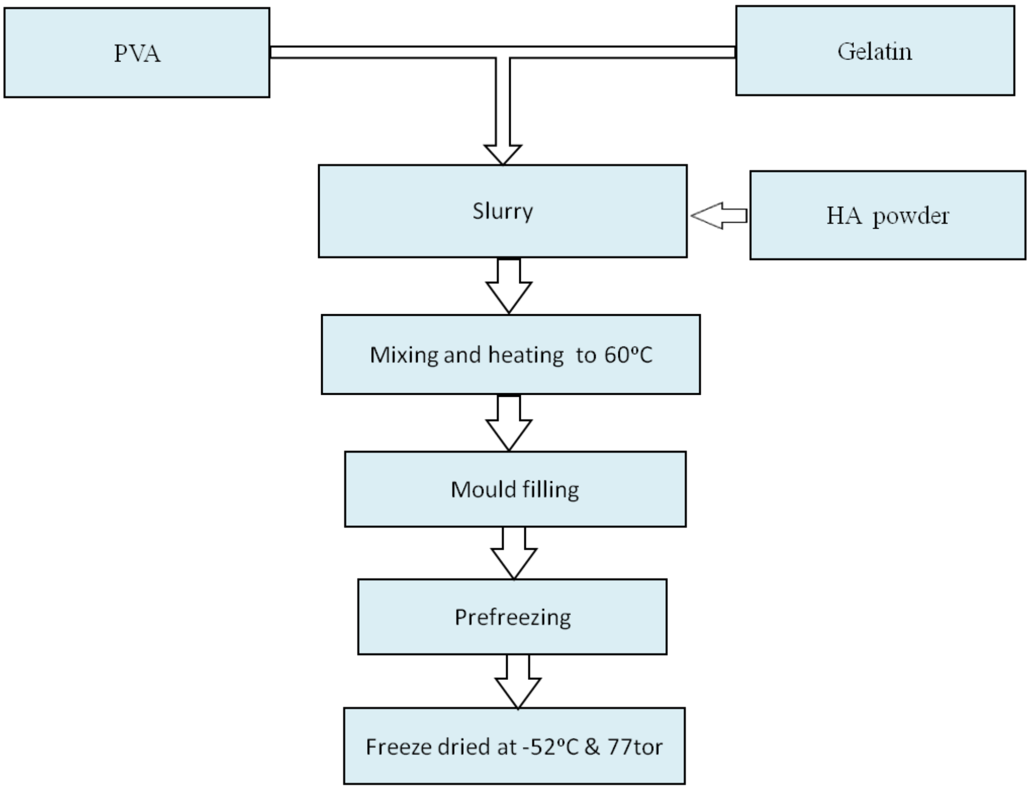

Figure 3.5 Flow diagram for the preparation of freeze dried HA scaffold.

Here it is necessary to mention that only gelatin-PVA composite without HA nanopowder was prepared to differentiate the effect of HA nanoparticles, but unfortunately high porous scaffold did not sustain any particular shape and easily scrambled at very low load. Because of this reason no further study was conducted for gelatin-PVA composite only.

3.7 Characterization of fabricated scaffold

3.7.1 Scanning electron microscopy of the scaffold

Surface morphology, microstructure, pore shape and pore size distribution of HA scaffolds were studied by SEM (JEOL JSM 6480LV). The SEM images of platinum coated scaffolds were seen in secondary electron mode at 15KV. Average pore diameter was estimated considering five different micrographs of identical scaffold. High resolution FESEM (NOVA NANO SEM-450) image was taken to illustrate the particle dispersion in the scaffold matrix.

3.7.2 Apparent porosity measurement

Porosity of HA-gelatin scaffold was measured by applying Archimedes' principle using ethanol as solvent [175]. Dry weights of all the freeze dried HA samples were taken accurately using a digital balance. HA samples were kept inside a beaker filled with ethanol and kept inside a vacuum desiccator for half an hour to remove entrapped air present inside the scaffold. Suspended as well as soaked weights of the samples were taken using four digit accuracy electronic balance. Apparent porosity and density of sample was estimated as:

$$\text{Apparent porosity} = \frac{S - D}{S - H} \times 100 \ldots\ldots\ldots\ldots\ldots\ldots\ldots\ldots\text{(ix)}$$

$$\text{Bulk density} = \frac{D \times \rho}{S - H} \ldots\ldots\ldots\ldots\ldots\ldots\ldots\ldots\ldots\text{(x)}$$

$$\text{Relative density} = \frac{\text{Bulk density}}{\text{Theoretical density}} \times 100 \ldots\ldots\ldots\ldots\ldots\ldots\text{(xi)}$$

$$\text{Porosity} = 1 - \text{Relative density} \ldots\ldots\ldots\ldots\ldots\ldots\ldots\ldots\text{(xii)}$$

Where,
D = Dry weight of HA scaffold
H = Suspended weight of HA scaffold
S = Soaked weight of HA scaffold
ρ = Density of ethanol (0.789 cc/g)

3.7.3 Mercury intrusion porosimetry

Mercury intrusion porosimetry is generally used for the quantification of volume porosity, nature of pores, pore volume and pore size distribution for specifically porous materials. Bulk density and sample weight are important parameters for this measurement because mercury intruded volume depends upon sample volume. Nature of pores and pore size distribution was evaluated through porosimetry (Poremaster-33, Quantachrome, USA). The freeze dried HA scaffold samples were placed in a penetrometer and infused with mercury under increasing pressure. The pore morphology behaviour was measured on the approached theory by Washburn, which defined as "pressure required to force a non-wetting liquid to enter a capillary of circular cross section is inversely proportional to the diameter of the capillary and directly proportional to the surface tension of the liquid and the angle of contact with the solid surface" [176]. Mathematically Washburn equation is given as:

$$\mathrm{P} = \frac{2\sigma \cos\theta}{\mathrm{r}} \text{ ....(xiii)}$$

Where,

P = Pressure of Hg

r = Radius of the pore

б = Surface tension of mercury

θ = Contact angle.

As the pressure (P) increase, the radius of pores (r) that can be filled decrease according to the Washburn equation. The open porosity л (porosity accessible to mercury intrusion) is given as

$$\pi = \mathrm{V}_{\mathrm{Intrusion}} - \mathrm{V}_{\mathrm{Scaffold}} \text{ .... (xiv)}$$

Where, $V_{Intrusion}$ was the total intrusion volume of mercury and $V_{Scaffold}$ is the volume of the scaffold. The closed porosity ω is not accessible to mercury and can be determined as:

$$\omega = \Pi - \pi \text{ .... (xv)}$$

Where, Π = Total porosity of scaffold. The applied pressure during mercury intrusion porosimeter measurement was varied slightly higher than 0.5 to 60,000 psi.

3.7.4 Compressive strength measurement

Compressive strength of the material is that value of uniaxial compressive stress reached when the material tend to reduce size or fails completely. It is usually obtained experimentally by means of a specimen under compression at constant load. Compressive strength of the cylindrical (14 mm diameter and 15 mm thickness) porous scaffolds was measured by universal testing machine (H10 KS, Tinius Olsen) using the load cell of 10 KN with a cross head speed of 2 mm/minute and determined by the following formula:

$$\text{Compressive Strength} = \frac{\mathrm{P}}{\mathrm{A}} \text{....................(xvi)}$$

Where,

P = Load in KN

A = Cross sectional area of the cylindrical sample

3.7.5 Elastic modulus of scaffold

Modulus of elasticity is the mathematical representation of a substance that tends to deform elastically when a force applied and is defined as the slope of its stress–strain curve in the elastic deformation region [177]. Elastic modulus of the HA scaffolds was determined through the stress-strain curve that obtained during compression measurement. The elastic modulus of an object is represented as:

$$E = \frac{Stress}{Strain} \quad \text{..(xvii)}$$

Where, E is the elastic modulus; stress is the restoring force caused due to the deformation divided by the area to which the force is applied and strain is the ratio of the change caused by the stress to the original state of the object.

3.8 Scaffold at cryogenic temperature

The freeze dried HA-gelatin scaffold sample was treated in liquid nitrogen at 77 K for different time schedule say 2, 5, 8 and 11 hours inside a cryochember. Original HA-gelatin scaffold as well as liquid nitrogen treated scaffolds were further characterized specifically porosity measurement, compressive strength, XRD and FT-IR analysis.

3.9 Characterization of cryo-treated scaffold

3.9.1 Morphologies of cryo-treated scaffold

Surface morphology, microstructure, pore shape and variation of pore size of liquid nitrogen treated HA-gelatin scaffolds with varying the soaking time were analysed through SEM (JEOL JSM

6480LV). The SEM images of platinum coated scaffolds were observed in secondary electron mode at 15 KV.

3.9.2 Room temperature phase analysis

Phase analysis of the liquid nitrogen treated HA scaffold was studied through XRD analysis (as represented in section 3.2.1) to understand the effect of low temperature on crystallization behaviour polymer matrix. The scaffold samples were scanned in the range of 2θ from 20-80 in a continuous mode with a rate of 0.02 degrees/sec.

3.9.3 Porosity measurement

Porosity of the N_2 treated scaffold was characterized through mercury porosimetry. Pore size and size distribution was characterized though intrusion porosimetry. The detailed procedure was represented in section 3.7.3.

3.9.4 Compressive strength measurement

The room temperature compressive strength of the liquid nitrogen treated scaffold samples were measured by universal testing machine (H10 KS, Tinius Olsen). The detailed procedure was represented in section 3.7.4. Surface morphology, microstructure, pore shape and pore size distribution of HA scaffolds were studied by SEM (JEOL JSM 6480LV). The SEM images of platinum coated scaffolds were observed in secondary electron mode at 15 KV.

Nano rod HA based scaffold exhibited highest compressive strength after optimum cryo-treatment and designated as cryo-treated HA-gelatin macroporous scaffold (CHAMPS), which was further considered for bioactivity, biodegradability, cytotoxicity, cell viability, protein adsorption/release and micro-CT scan study.

3.10 Bioactivity of the cryo-treated HA-gelatin macroporous scaffold (CHAMPS)

In vitro bioactivity test of the scaffold materials evaluate the ability of apatite formation, soaking in simulated body fluid (SBF) solution [178]. The SBF solution is known to be a metastable buffer solution and even a small, undesired variance in both of the preparation steps and the storage temperature may drastically affect the final nucleation of apatite phase. SBF solution was prepared in accordance with the chemical ion concentration nearly equal to those of the inorganic constituents of human blood plasma and were used by A. Cuneyt Tas et al. [147]. Analytical grade pure NaCl (99.5%), $NaHCO_3$ (99.5%), KCl (99.0%), Na_2HPO_4 $2H_2O$ (99.5%), $MgCl_2$ $6H_2O$

(99.0%), Na_2SO_4, $(CH_2OH)_3CNH_2$ (99.5%), $CaCl_2$ H_2O (99.0%) and HCl (37 vol.%) were used in the preparation of SBF solution for this study. Fresh 1000 ml SBF solution was prepared by dissolving the required amount chemical reagents into a 2000 ml polystyrene (Tarson) beaker as mentioned in Table 3.2. In the beginning, reagents were added to 700 ml deionised water continuously one by one in the sequence only after the previous reagent has completely dissolved. During the preparation of SBF solution, pH ~7 was maintained by addition of 1M HCl in each step and temperature 33 ^{o}C. Finally, volume of the solution was adjusted up to 1000 ml by deionised water with maintaining solution pH~7.4 and temperature 37 ^{o}C. The resulting solution was stored in air tight polystyrene (Tarson) container at 5 ^{o}C.

Table 3.2 Chemical composition of SBF [147].

Order	Reagent	Amount (gpl)
1	NaCl	6.547
2	$NaHCO_3$	2.268
3	KCl	0.373
4	$Na_2HPO_42H_2O$	0.178
5	$MgCl_2$ $6H_2O$	0.305
6	$CaCl_2$ $2H_2O$	0.368
7	Na_2SO_4	0.071
8	$(CH_2OH)_3CNH_2$	6.057

Table 3.3 Ion concentration of SBF solution and human blood plasma[146,147]

Order	Ion	Kokubo et al. (mM)	Cuneyt Tas et al. (mM)	Human plasma (mM)
1	Na^+	142.0	142	142.0
2	Cl^-	147.8	125	103.0
3	HCO_3^-	34.2	27	27.0
4	K^+	5.0	5.0	5.0
5	Mg_2^+	1.5	1.5	1.5
6	Ca_2^+	2.5	2.5	2.5
7	HPO_4^{2-}	1.0	1.0	1.0
8	SO_4^{2-}	0.5	0.5	0.5

The ion concentrations of the SBF solutions used in this study were more closely similar with those of human plasma than reported by Kokubo et al [179]. The difference between the ion concentrations of SBF solutions and those of human plasma are represented in Table 3.3. Bioactivity test was conducted by taking SBF solution at pH ~ 7.4 and temperature 37 °C. The HA porous scaffolds (0.5 gm, 3 × 6 × 10 mm^3) were soaked in 20 ml of SBF solution inside a closed polystyrene (Tarson) Petridis and kept in an incubator with adjust of solution pH ~ 7.4 and temperature 37 °C. The SBF soaked sample was repeatedly cleaned by de-ionized water and dried at 40 °C for 12 h. Feasibility of the apatite nucleation was demonstrated through SEM microstructure attached with EDX.

3.11 Biodegradation of CHAMPS

In vitro biodegradation was carried out in 0.05M Tris-HCl buffer solution at 37 °C and pH ~ 7.4. HA scaffolds were taken in a sealed polystyrene (Tarson) Petridis followed that soaked in Tris – HCl buffer solution for different time interval inside an incubator at 37 °C and pH ~ 7.4. The tris-HCl soaked samples were repeatedly washed with deionised water and dried at 100 °C. The final weight of the sample was taken through digital weighing balance. The weight loss was correlated with biodegradability of scaffold. The percentage of weight loss was estimated as:

$$\%\ \text{Weight loss} = \frac{W_t - W_0}{W_0} \quad \text{..(xviii)}$$

Where,

W_t = Weight of sample at time‘t’

W_0 = Weight of sample before Tris- HCl treatment

3.12 In vitro cytotoxicity and cell viability of CHAMPS

3.12.1 Cytotoxicity Test

An *in vitro* cytotoxicity test of steam sterilized cryo-treated HA-gelatin macroporous scaffold (CHAMPS) was performed using mammalian mouse fibroblast cell line L929 by direct contact method as per ISO-10993-5 guideline [180]. L929 cells were used in the present study because it can be easily cultured in a reproducible manner and also this cell line is widely used for basic biocompatibility. It has ease rate of proliferation and adheration with most of the biomaterial surface. In the beginning, guide line L929 cells were subcultured, trypsinized and seeded on to multiwall tissue culture plates. The L929 fibroblast cells were cultured with DMEM (Dulbecco's Modified Eagle Medium), 10% FBS (Fetal Bovine Serum) and incubated at 37 °C in 5% CO_2 atmosphere till formation of a cell monolayer. The test specimen (CHAMPS) was incubated with monolayer cells at 37 °C for 24 h to 26 h. The CHAMPS was examined using a fluorescence microscope for cellular response after the requisite incubation. *In vitro* cytotoxicity of the test specimen was also compared with the negative control (high density polyethylene) nontoxic material and positive control (stabilized poly vinyl chloride disc) toxic material. Cell monolayer was examined microscopically for the response around the test specimens.

3.12.2 Cell viability study with scaffold

The MTT assay was performed to measure the metabolic activity of cells and assessed through ‘color-change’ phenomenon from yellow colored tetrazolium salt, MTT {3-(4,5-diamethyl thiazol-2-yl)-2,5- diphenyltetrazolium bromide} to purple colored formazan. Fresh test specimens (CHAMPS) were sterilized by steam sterilization at 121 °C for 20 minute and extract was prepared after 24–26 h incubation at 37 ± 1 °C in 1 ml culture medium with containing of serum protein. The extract solution was further diluted to 50, 25 and 12.5% in same culture medium. Equal volume (100 µl) of extract as obtained from CHAMPS, negative control (high density polyethylene), positive control (dilute phenol) and cells were placed on a subconfluent monolayer of L929 cells and incubated for 24 ± 2 h at 37 ± 1 °C. The cultured cells were treated with 50 µl of MTT and further incubated at 37 ± 1 °C for 4 h in humidified and 5% CO_2 atmosphere. The excess amount of MTT was removed by aspiration, and subsequently 100 µl of isopropanol was added in order to dissolve the formazan crystals. Cytotoxicity tests were performed in triplicate. The colour exchange was quantified by measuring absorbance at 570 nm using a spectrophotometer.

3.13 BSA protein CHAMPS conjugate

3.13.1 BSA protein adsorption on CHAMPS

BSA protein solution was prepared as described in section 3.5.6. In the beginning, the identical shaped eight different small pieces of CHAMPS (0.5 gm, Ø–14 mm and thickness–2.5 mm, volume – 0.38 cm^3) was sliced down by steel blade and immersed in 10 ml BSA solution of 5 mg/ml initial concentration and kept in an incubator at 37 °C for different time scale from 6 h to 240 h. The supernatant solutions were collected from individual BSA – CHAMPS conjugate specimens through centrifuge at 100 rpm for 4 °C. The adsorbed BSA protein amount was quantified by taking 0.1 ml of supernatant from each specimen and mixed 2 ml of bicinchoninic acid solution (Thermo Pierce, Bicinchoninic acid protein assay kit, BCA-1 and 10N8010904). The detailed flow diagram for protein adsorption was represented in Figure 3.6. UV-vis spectroscopy (Perkin Elmer, Lambada 35) at 562 nm was used to characterize the absorbance peaks and to estimate of BSA concentration through the use of a predetermined standard concentration – intensity calibration curve. SEM

(JEOL JSM 6480LV) and FT-IR (Perkin Elmer RXI, Spectrum, USA) analysis were carried out to understand the protein adsorption and surface bonding of CHAMPS, respectively.

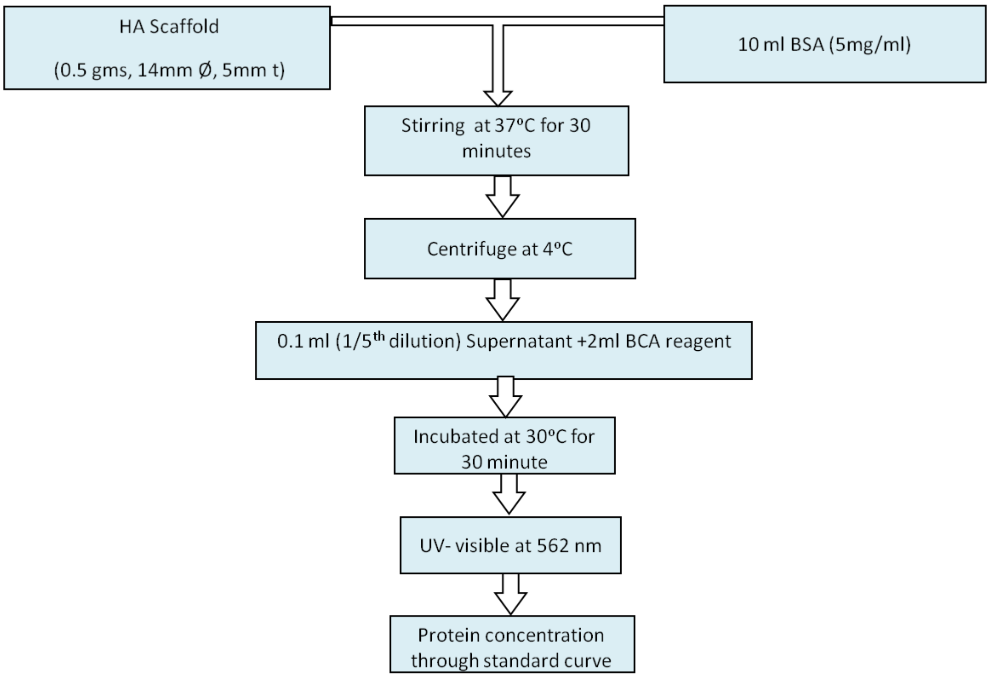

Figure 3.6 Flow diagram for the preparation HA-BSA conjugates.

3.13.2 Micro-CT analysis of protein adsorbed CHAMPS

Micro-CT system is an effective tool, where micro-focal X-ray projections rotated through multiple viewing directions in order to obtain 3D reconstructed images, spatial distribution maps of linear attenuation coefficients and scaffold composition [165]. The as-fabricated nanorod HA/gelatin scaffold as well as their protein loaded scaffold were first fixed in 10% neutral buffered formalin and thoroughly washed with PBS (phosphate buffer saline). Subsequently, the test samples (as-synthesized scaffold and protein loaded scaffold) were analyzed using high resolution X-ray micro-computed tomography (Skyscan 1172, Bruker micro CT, Kontich, Belgium). The scanning parameters include, X-ray beam energy = 40 kV and current = 250 μA. Under the operating conditions, the pixel size was around 4 μm and typically the scaffold length of 5-6 mm is sectioned into 600-700 parallel slices of equal height during the micro-CT analysis. While analyzing the test scaffolds, the rotation step was 0.25 degrees and 30 degree rotation was completed. Typical timescale for scanning a test sample was around 4.5 hours. The reconstruction of the selected region was made using the commercial NRecon reconstruction program (cone beam convergence/back projection algorithm-based software). Based on the density variation of various regions of the test scaffold, the 3D image of the scaffold was extracted on the basis of the distinction between ROI (region of interest) and VOI (volume of interest). Also, various views (side view, top view, front view) of the 3D images are studied in order to realize the pore interconnectivity or pore distribution along the entire volume of the scaffold and this aspect can only be studied using micro CT technique. From the experimentally measured CT database, multiple 2D slices were analysed to quantify the distribution of the pore size, pore volume as well as strut thickness for the entire scaffold volume.

3.13.3 BSA release study on CHAMPS

BSA release study was also carried out for the same BSA protein loaded CHAMPS after immersion in 20 ml of phosphate buffer solution at pH 7.4 and temperature 37 °C. UV-vis spectroscopy (Perkin Elmer, Lambada 35) at 562 nm was used to characterize the absorbance peaks and to estimate BSA concentration through the use of a predetermined standard concentration–intensity calibration curve. Flow diagram for the release of loaded BSA from HA scaffold is represented in Figure 3.7.

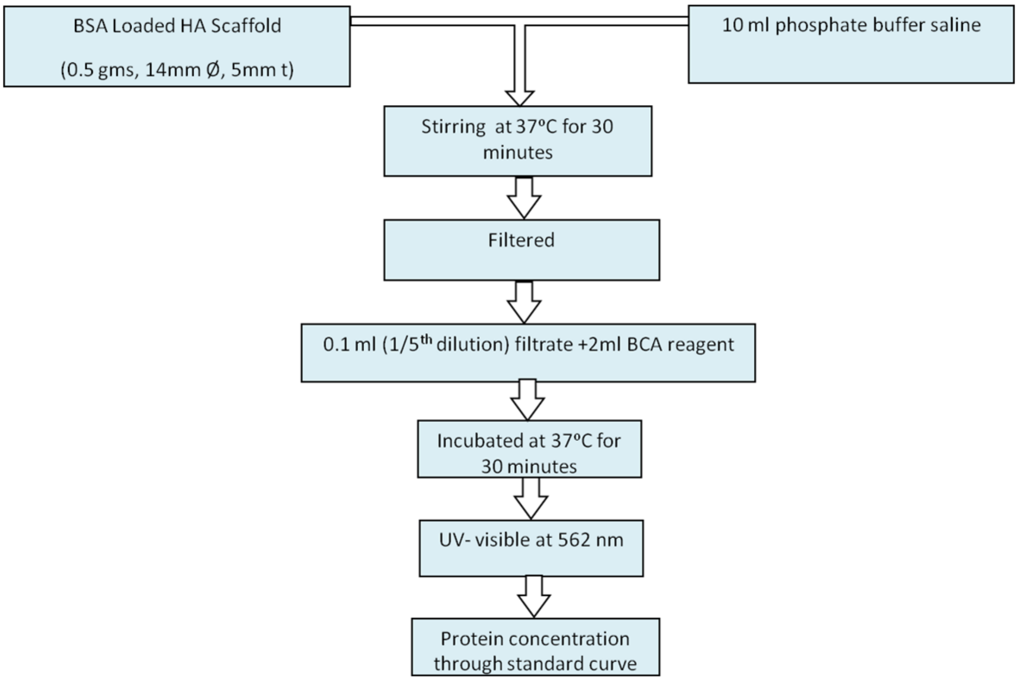

Figure 3.7 Flow diagram for release of BSA from loaded scaffold.

3.14 Statistical analysis of experimental data

Statistical analysis was conducted to understand the variation of experimental data for mechanical properties, protein adsorption and release on both nanoparticles and scaffolds. Each data point was taken from the mean of three repeated experiments. Data were represented as the mean ± standard deviation (SD) (n=3) through Origin Pro8. Numerical data were analysed statistically using standard analysis of variance (*ANOVA*) considering statistical significance at $p < 0.05$ [181,182].

Chapter-4

Results and Discussion

Chapter 4 Results and Discussion

Morphology, crystallinity and Ca/P ratio are prime factors to simulate the surface characteristic and bioresorption of hydroxyapatite nanoparticles. Moreover, the pore interconnectivity of hydroxyapatite-gelatin nanobiocomposite porous scaffold has a significant effect on mechanical properties and binding affinity of foreign molecules like BSA protein. In this context, necessary explanation for the above findings has been discussed in a different section as follows. Section 4.1 illustrates a systematic synthesis technique of different morphologies such as spherical, rod and fibroid HA nanoparticles and their relevant characterizations. The dispersion of HA nanoparticles needs to consider for the delivery media and hence discussed in section 4.2. Section 4.3 describes on the detailed analysis of protein adsorption and release behaviour on all three different grades HA nanoparticles. Fabrication of freeze casted micro/macro porous nanobiocomposite scaffolds and their different characterizations has been discussed in section 4.4. Low grade mechanical properties of freeze casted scaffolds are further enhanced through optimum cryogenic treatment and discussed their mechanical properties with respect to microstructure in adjacent section 4.5. A particular scaffold has been optimized with respect to adsorption-release phenomena of HA particle/protein conjugate and mechanical strength of nanobiocomposites for relevant *in vitro* characterization. Bioactivity, biodegradability and cytotoxicity of developed cryotreated hydroxyapatite macroporous scaffold (CHAMPS) have discussed in next section 4.6. Finally, section 4.7 illustrates the improved protein adsorption and release efficacy of developed scaffold through FT-IR, UV-spectroscopy and micro computed tomography.

4.1 Synthesis and characterization of hydroxyapatite nanoparticles

Synthetic nano scale hydroxyapatite has classic bioactive and biocompatible properties to simulate bone minerals and binding affinity with foreign molecules, which specifically depends on Ca:P ratio, crystallinity and their morphology [103,183]. For example, semi-crystalline hydroxyapatite has a high level of bioresorption capability compared to high crystalline HA; moreover, high aspect ratio nanoparticle exhibit low binding affinity with protein molecules compare to the low aspect ratio nanoparticles [184,185,186]. Therefore, control over the size, morphology, degree of crystallization and composition of HA phase has significant importance for bio-applications, which could be synchronized through temperature gradient, structure directing reagent, solution pH and an atomic ratio of Ca/P [187,188]. Thus, a common strategy has been adapted to the synthesis three different morphologies such as; spherical, rod and fibroid with control over the size and crystallinity, from common precursors for the fabrication of nanobiocomposite scaffold and their protein adsorption-release study.

4.1.1 Process optimization and formation mechanism of HA nanoparticles

The entire set of experimental conditions and their outcome has been represented in Figure 4.1. However, three optimized conditions are chosen to achieve the desired morphology, crystallinity and Ca/P ratio of pure HA nanoparticles. Spherical HA nanoparticles (NHS), rod HA nanoparticles (NHR) and fibroid HA nanoparticles (NHF) develops at pH = 12.25, temperature = 298K; pH = 9.5, temperature = 303K and pH = 5.25, temperature = 353K, respectively. A ternary diagram is sketched out on the support of the process conditions temperature, pH and Ca:P ratio in Figure 4.1. Crystalline and desired morphologies are achieved only for 22 sets of data, which is projected as hatched region. Beyond these hatched regions most of the particles appear to be calcium phosphate which deviates from an elemental composition of HA.

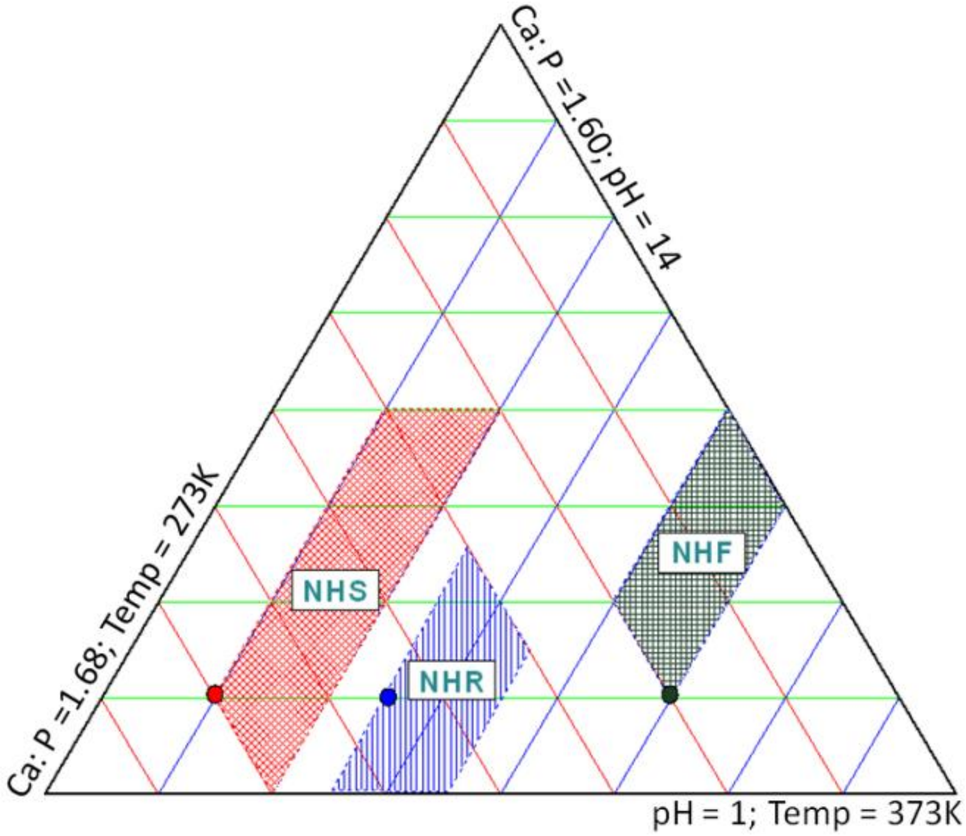

Figure 4.1 Hatched area of ternary diagram indicates the projected region for the formation of spherical (NHS), rod (NHR) and fibroid (NHF) morphology. Coloured circular point represents the optimum conditions to achieve Ca:P ~ 1.67 for diversified morphologies.

Ca-acetate SEM image provides the precursor morphology, which exhibits flower like structure influenced by individual fibrous Ca-acetate crystals as shown in Figure 4.2. However, such morphology develops different spherical, rod and fibrous hydroxyapatite nanoparticles in particular reaction condition. This observation indicates that starting precursor morphology has no significant effect when it completely dissolves in aqueous media; whereas HA morphology is predominately governed by the solution pH and temperature.

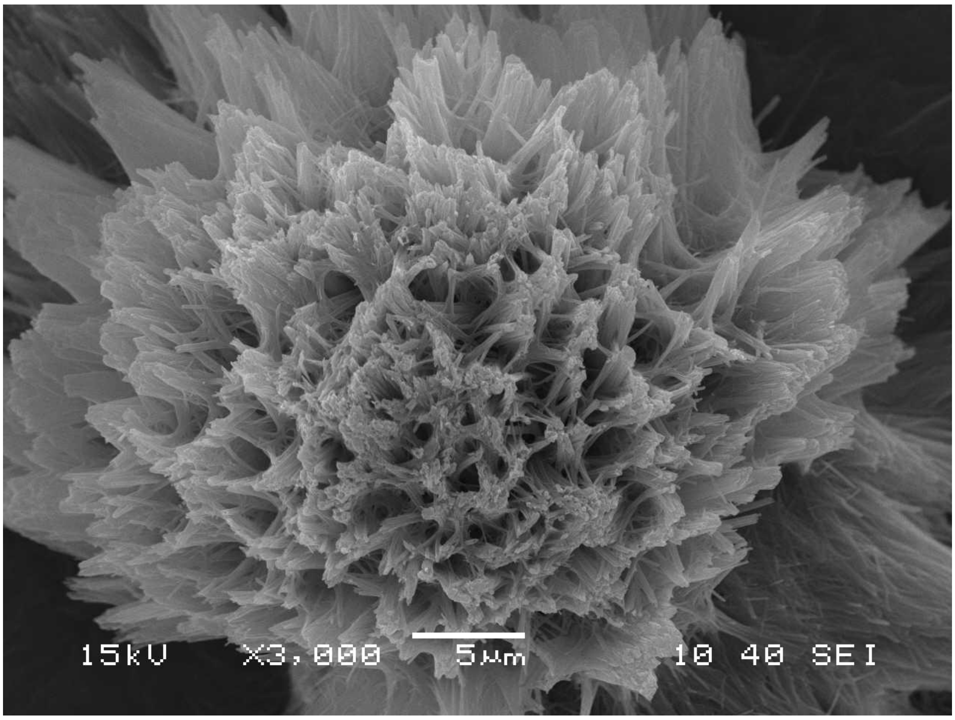

Figure 4.2 SEM microstructure of calcium acetate that used as precursor material for the preparation of HA nanoparticles.

A probable HA morphology formation mechanism are represented in Figure 4.3. High concentration of hydroxide ($12.25 \geq pH \geq 10.5$) ion and low temperature (298 K) favours isotropic growth of spherical shape, medium concentration ($9.5 \geq pH \geq 7.75$) and low temperature (303K) initiates the anisotropic growth of rod and finally low concentration ($7 \geq pH \geq 5.25$) with high temperature (353 K) accelerates the confined growth to fibroid morphology as confirmed by microscopic analysis. High concentration hydroxide ions are expected to present when pH solution is 12.25, which adsorbs on HA nuclei surface and favours non-confined three-dimensional growth to spherical morphology [103]. However, at intermediate solution pH, a small amount of hydroxide ions release from tris-buffer is likely to adsorb on selective site of HA nuclei, which results in a weak isotropic growth with the formation of nano rods. Hence, minimization of OH^- concentration has benefit to restricted and directional growth of HA nanoparticles. At low solution pH and high temperature (353 K) the probability of OH^- ion adsorption from alkali on HA nuclei is decreasing and favours anisotropic growth of HA nuclei to fibroid morphology, which enhances one directional growth as a similar mechanism proposed by Bu et. al [189]. The optimized process parameters for the synthesis of HA nanoparticles are represented in Table 4.1.

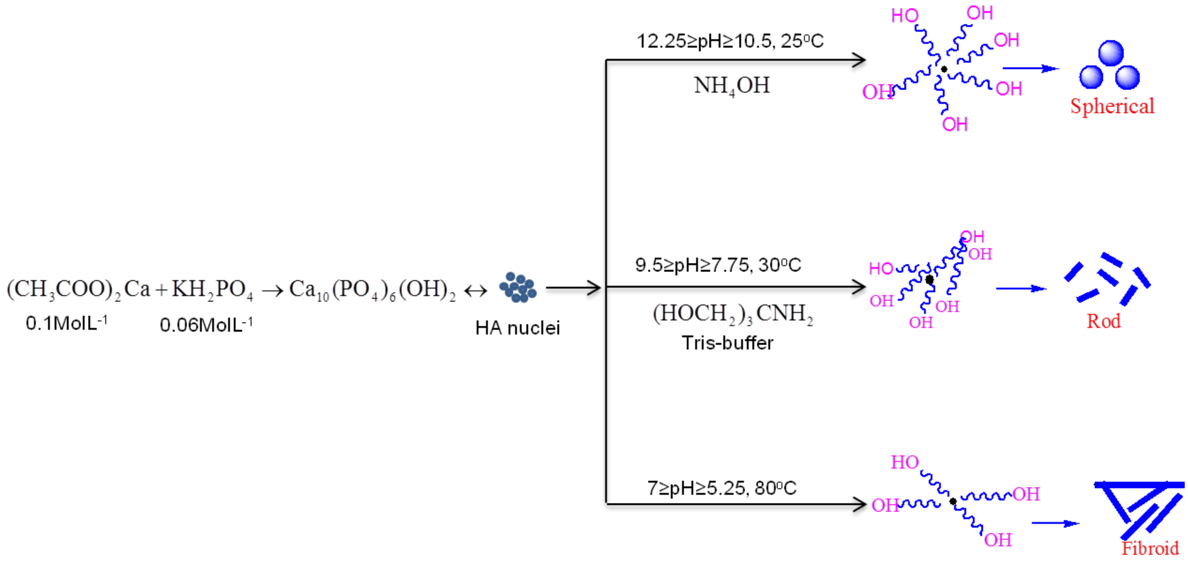

Figure 4.3 Schematic representation for the mechanism of different morphologies of HA.

Table 4.1 Optimised parameters for the synthesis of HA nanoparticles.

Sample	Temperature (^{o}C)	Ca:P	pH
NHS	25	1.655	10.5-12.25
NHR	30	1.66	7.75-9.5
NHF	80	1.64	5.25-7

4.1.2 Phase content and crystallinity of different morphologies

Phase content, purity and crystallinity of these HA nanoparticles are assessed by XRD and plotted in Figure 4.4. The diffraction peaks are indexed as HA hexagonal phase with a = b = 9.4180, c = 6.8840 and space group $P6_3/m$ (JCPDS No. 09-0432). It has been clearly seen that NHS and NHR appears to be poorly crystalline while NHF is well crystalline. The crystallinity of pure phase is increasing with aspect ratio; highest for fibroid morphology. The calculated crystallite size as preferred (211) plane for NHS, NHR and NHF samples are 7 nm, 15 nm and 50 nm, respectively. Bonding behaviour of the characteristic functional groups and Ca/P ratio has been determined through FT-IR and chemical method, respectively.

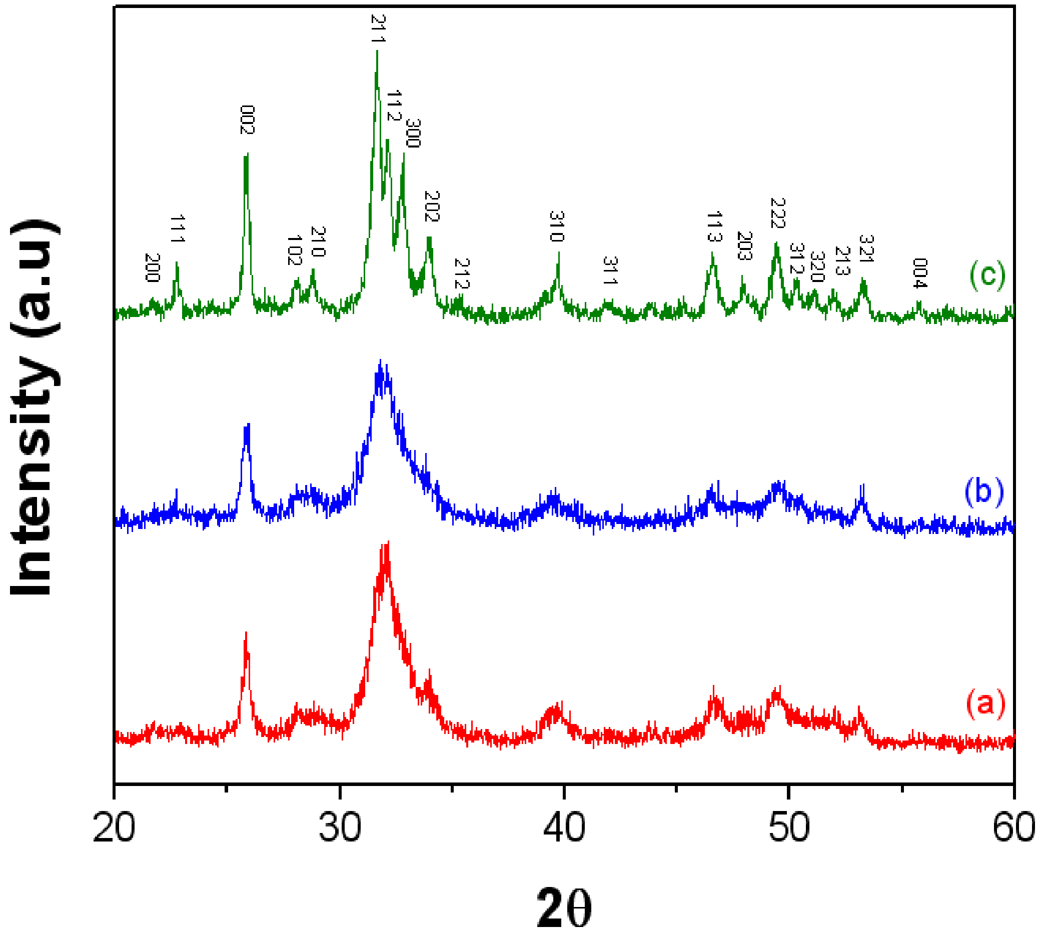

Figure 4.4 Room temperature XRD pattern of (a) NHS, (b) NHR and (c) NHF after freeze drying at 220 K and 120 tor pressure.

4.1.3 Rietveld refinement of HA

X-ray diffraction patterns of as synthesized HA nanoparticles have low crystallinity along with pure HA phase. In order to study of their crystal structure behaviour, lattice parameter, cell volume and phase purity of different morphologies of as synthesized HA nanoparticles, powders were calcined at a predetermined temperature 700 ^{o}C and studied their Rietveld refinement analysis. The background of selection temperature is attribute to the phase and morphology stability of HA nanoparticles irrespective of morphologies up to 700 ^{o}C only [190]. Figure 4.5 represents the Rietveld refinement results of three different morphologies of HA nanoparticles. It is clearly seen from the figure that all the morphologies show the pure phase of HA with no impurities on the $P6_3/m$ space group. The observed patterns of three morphologies of HA nanoparticles have good agreement with the calculated patterns with χ^2 (goodness of fit) are 1.39, 1.41 and 1.31 for NHS, NHR and NHF, respectively. The refinement is carried out taking account on the lattice parameter, scale factor while the background is modelled by six co-efficient polynomials for different morphologies. It is to be noted that there is a change in peak shape, position and broadening which is reflected in terms of lattice parameter as shown in Table 4.2. The refine parameter is found as similar in previous literature [191,192].

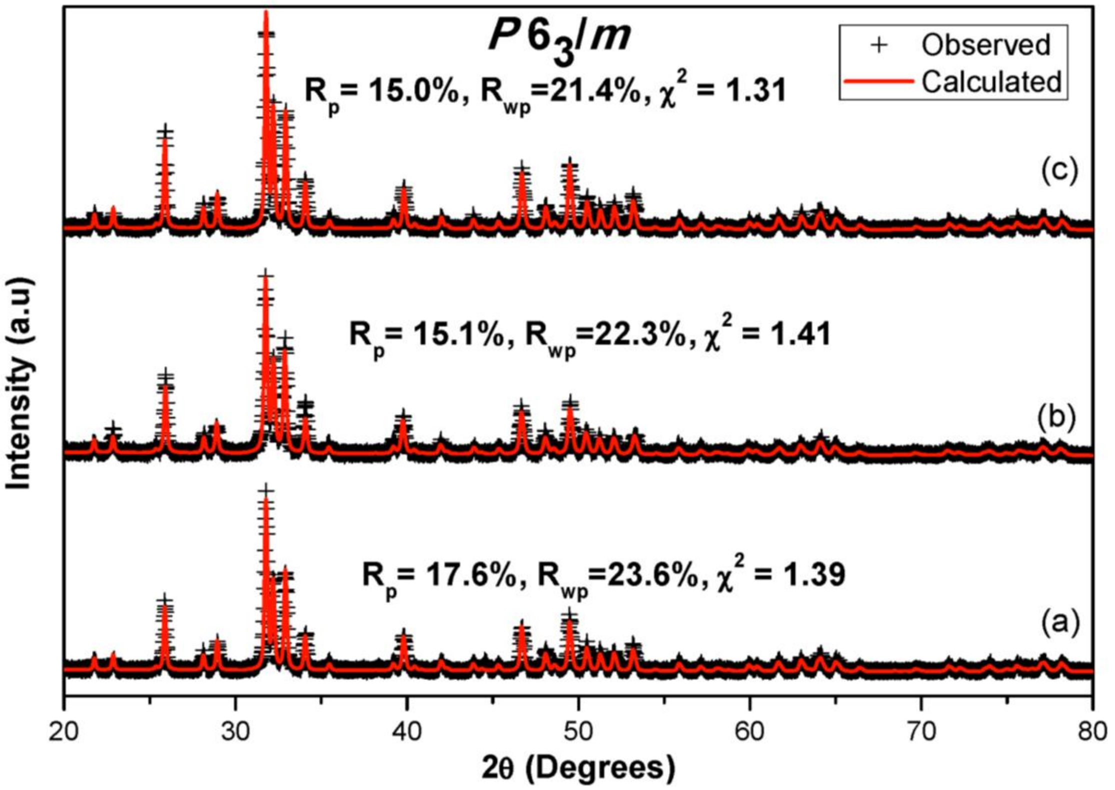

Figure 4.5 Rietveld refinement fit to powder XRD spectra of HA (a) NHS, (b) NHR and (c) NHF.

Table 4.2 Unit cell constants of HA from XRD Rietveld refinement against space group $P6_3/m$.

Parameters			**NHS**	**NHR**	**NHF**
a =b (Å)			9.4351 (05)	9.4247 (03)	9.4223 (04)
c (Å)			6.8748 (06)	6.8840 (04)	6.8833 (05)
Volume (Å)^3			530.017 (20)	529.563 (18)	529.235 (16)
			x	y	z
Atomic Positions	4f	Ca^{+2}	0.6666	0.3333	0.0007
	6h	Ca^{+2}	0.2426	0.9904	0.2500
	6h	P^{5+}	0.3948	0.3657	0.2500
	6h	O^{2-}	0.3270	0.4849	0.2500
	6h	O^{2-}	0.5791	0.4618	0.2500
	12i	O^{2-}	0.3417	0.2578	0.0711
	2a	O^{2-}	0.0000	0.0000	0.1837
	2b	H^{1+}	0.0000	0.0000	0.0608
R_p			17.6 %	15.1 %	15.0 %
R_{wp}			23.6 %	22.3 %	21.4 %
χ^2			1.39	1.41	1.31

In order to get a better fit, atomic position and site occupancy are also refined. The reliable parameters R_p (Profile residue), R_{wp} (weighted profile residue) and χ^2 are well fitted within the accepted values [193]. A small change in lattice parameter due to may be the different morphologies, which is obvious since different shapes have different strains [194]. It is also being pointed out that volume of cell decreases from spherical to fibroid.

4.1.4 Vibrational spectra of HA nanoparticles

Functional group and bond behavior of different class of HA nanoparticle confirms through FT-IR analysis. FT-IR spectrum of NHS, NHR and NHF powders are shown in Figure 4.6. The absorption bands are detected at wavenumbers 3435, 1040, 605, and 570 cm^{-1} for the synthesized HA nanoparticles. The absorption band at 1430 cm^{-1} is detected in the spectrum of NHS due to the partial absorption of atmospheric CO_2 on the surface of NHS. HA has more affinity towards the absorption of CO_2 at basic media during synthesis but that corresponding peak is absence in NHR and NHF since both are synthesized at low solution pH. The bands at wavenumber 1040 and 570 cm^{-1} are associated with the characteristics of PO_4^{3-} group but bands at 3435 and 605 cm^{-1} represents the characteristic stretching and bending modes for OH^- group, respectively [195]. Thus, the low temperature synthesized HA nanoparticles are composed of PO_4^{3-} and OH^- anions and free from other impurities.

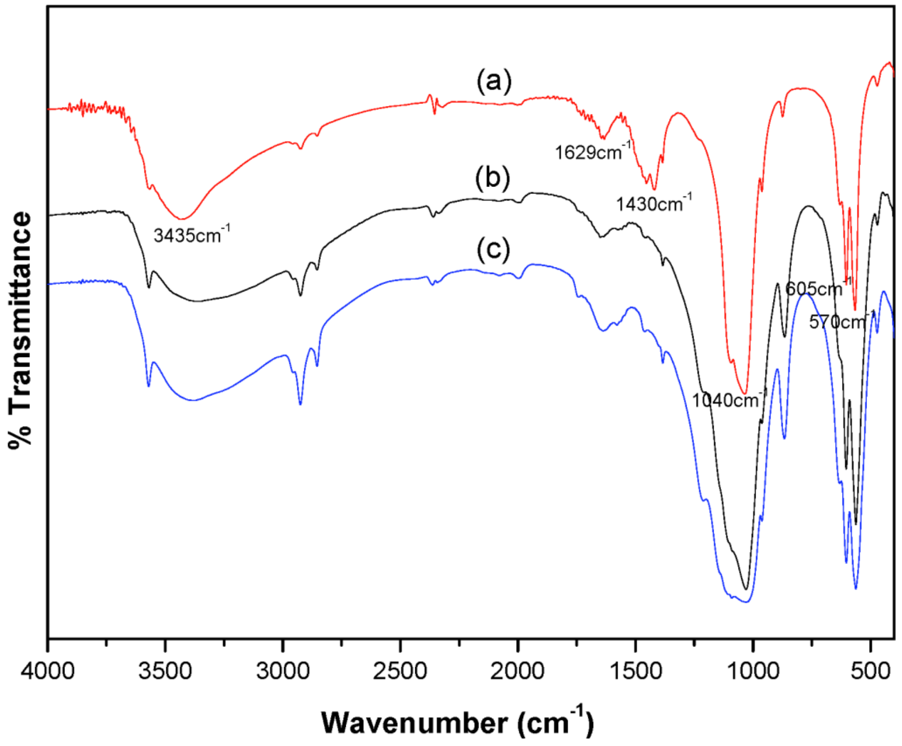

Figure 4.6 FT-IR spectrum of (a) NHS, (b) NHR and (c) NHF as synthesized nanoparticles.

4.1.5 Ca:P ratio of HA nanoparticles

The amount of calcium (Ca) and phosphorous (P) present in HA nanoparticles is estimated by complexometric titration with EDTA (Ethylenediaminetetraacetic acid) and gravimetric method with ammonium molybdite, respectively [166]. EDTA makes complex reaction with the content of Ca^{2+} in HA at 25 °C and solution pH~12. The amount of Ca^{2+} consumed by EDTA is estimated with the use of ACC (Ammonium Acetate) buffer and Eriochrome Black-T indicator. The Ca- EDTA complex is shown in Figure 4.7 as:

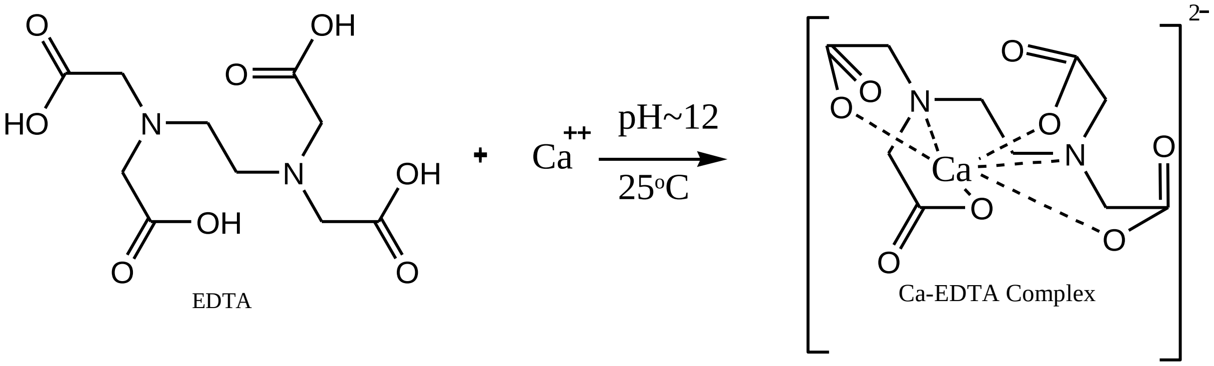

Figure 4.7 Schematic representation of the reaction between Ca^{2+} and EDTA.

Phosphate reacts with ammonium molybdate in warm nitric acid solution and precipitates yellowish ammonium 12-molybdophosphate $[(NH_4)_3(PMo_{12}O_{40})]$ after drying at 200-400 °C or molybdenum oxide phosphate ($P_2O_524MoO_3$) at 800-825 °C for 30 minute [166]. XRD pattern represents the identity of $P_2O_524MoO_3$ complex after reaction within ammonium molybdate and hydroxyapatite nanoparticles (Figure 4.8). The amount of phosphorus is estimated from the yield of the final complex. XRD represents the phase of ammonium phosphomolybdate. Ca:P ratio for spherical, rod and fibroids are found as 1.656, 1.66 and 1.64, respectively. The Ca:P ratio plays an important factor to control the surface reactivity of nano HA particles. The result shows that the calculated Ca:P ratios for the synthesized HA has a lower value as compared to the stoichiometric HA (Ca:P ratio ~ 1.67). Thus synthesized HAs could be considered as calcium deficient HA with relatively low crystallinity.

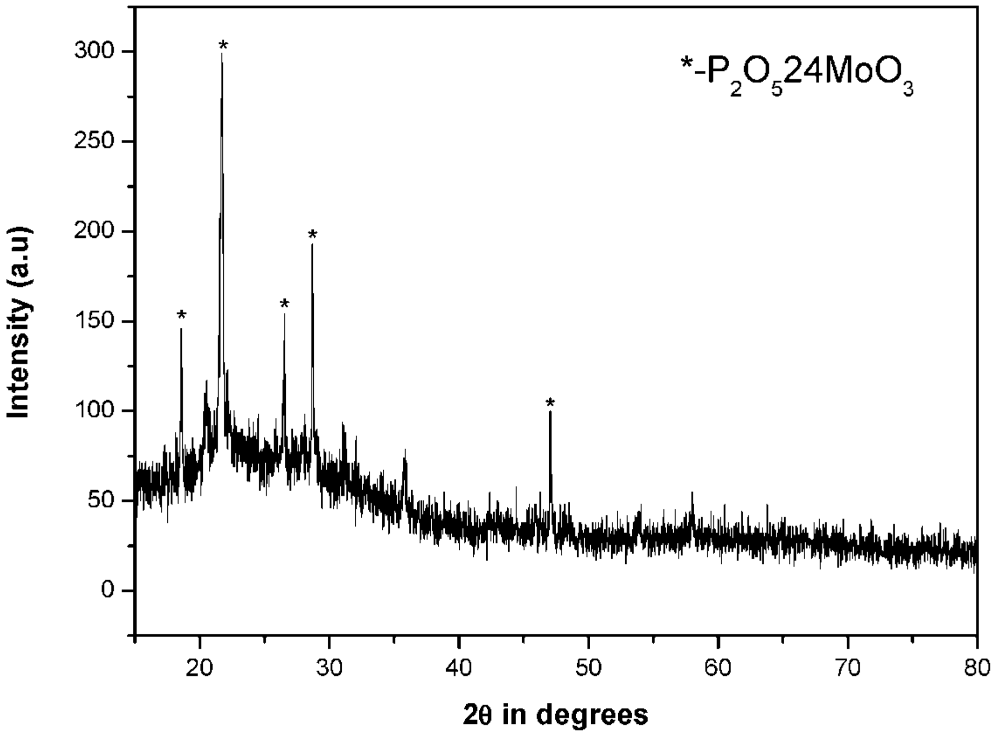

Figure 4.8 XRD pattern of ammonium phosphomolybdate at 825 ^{o}C.

4.1.6 Transmission microscopy of HA nanoparticles

Morphology, crystallinity and particle size are investigated through TEM and SAED techniques. TEM images of these HA powders and their SAED patterns are represented in Figure 4.9. A close look reveals the formation of spherical particles near to 10 nm diameter with a consist of strong concentric ring pattern for (002), (211), (112) and (300) plane of polycrystalline HA [196]. Rod shaped morphology exhibits near to 7 nm diameter with aspect ratio of ~5. The dotted SAED pattern is also well matched with ring, which confirms a better crystallinity of rod morphology compare to spherical powder. High crystallinity and purity of fibrous morphology as defined by XRD pattern are well matched with represented SAED pattern. Average diameter is gradual increament up to 30 – 40 nm with very high aspect ratio for fibroid morphology.

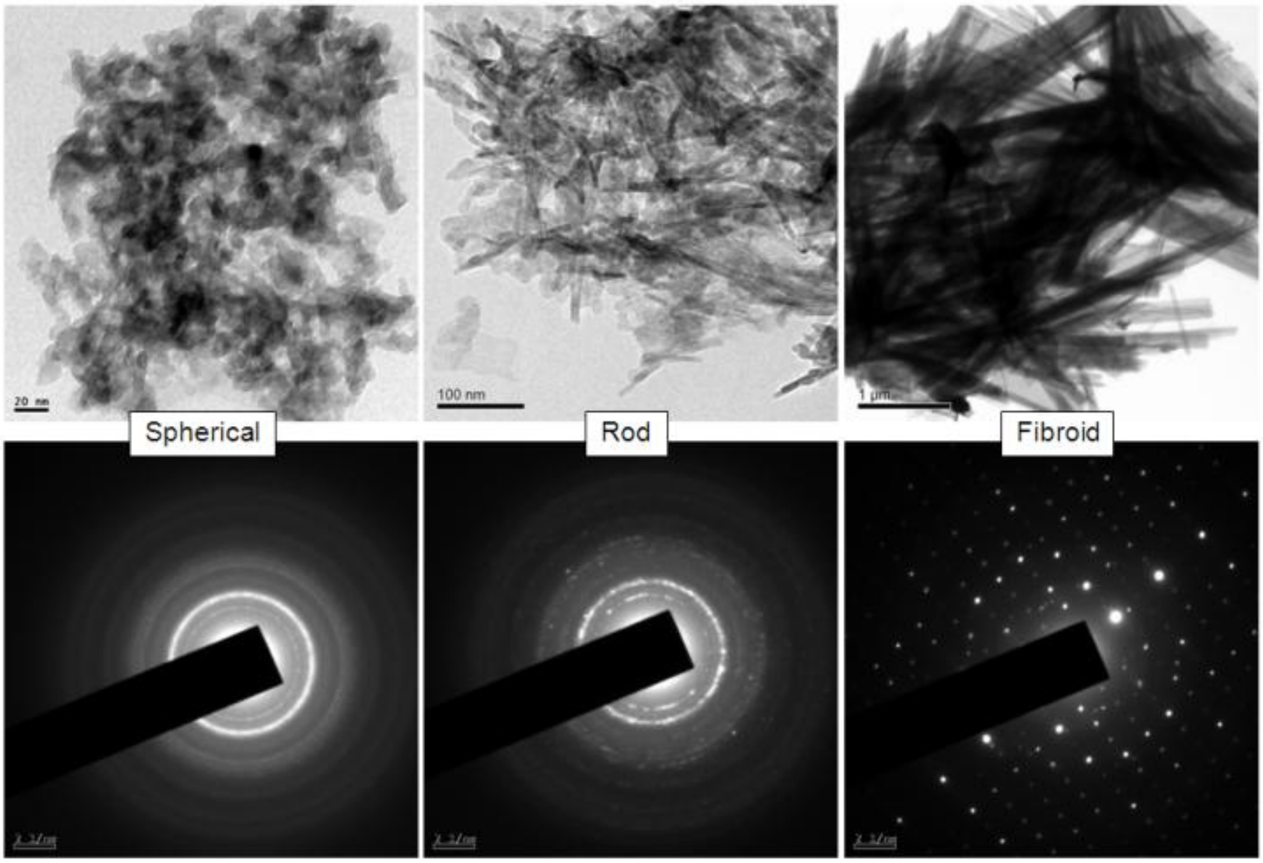

Figure 4.9 HRTEM and SAED represent the morphology and crystal pattern of NHS, NHR and NHF.

4.1.7 BET isotherm of HA nanoparticles

BET specific surface area plots for the prepared HA nanoparticles are represented in Figure 4.10. The measured specific surface area of NHS, NHR and NHF are 256 m^2/g, 217 m^2/g and 47 m^2/g and calculated crystallite sizes (D_{BET}) are found as 7, 9 and 40 nm in diameter, respectively [197]. BET isotherm with BJH (Barrett, Joyner and Halenda) pore size distribution of the synthesized HA powders are shown in Figure 4.11. All particles exhibit type – IV isotherm. A characteristic feature of the type–IV isotherm is represented by hysteresis loop and occurs due to capillary condensation taking place in micropores over a range of high p/p^o [198]. The initial part of the type–IV isotherm is an attribute to monolayer-multilayer adsorption phenomenon. Enhance pore volume and decrease relative pressure depend on low surface area as well as high aspect ratio of HA nanoparticles. Identical nature of pore diameter is observed for all three morphologies. However, difference in the adsorption hysteresis curve for the synthesized HA nanoparticles are observed with varying the saturation pressure due to the presence of different levels of nano scale pores. Detailed properties of BET isotherm and the size of the observed micro pores of the synthesized HA powders are represented in Table 4.3. The adsorption hysteresis curves for the synthesized HA nanoparticles are varying with the saturation pressure due to the presence of different levels of nano scale pore. A large extent of surface area and insignificant pore diameter variation has been found with respect to morphologies.

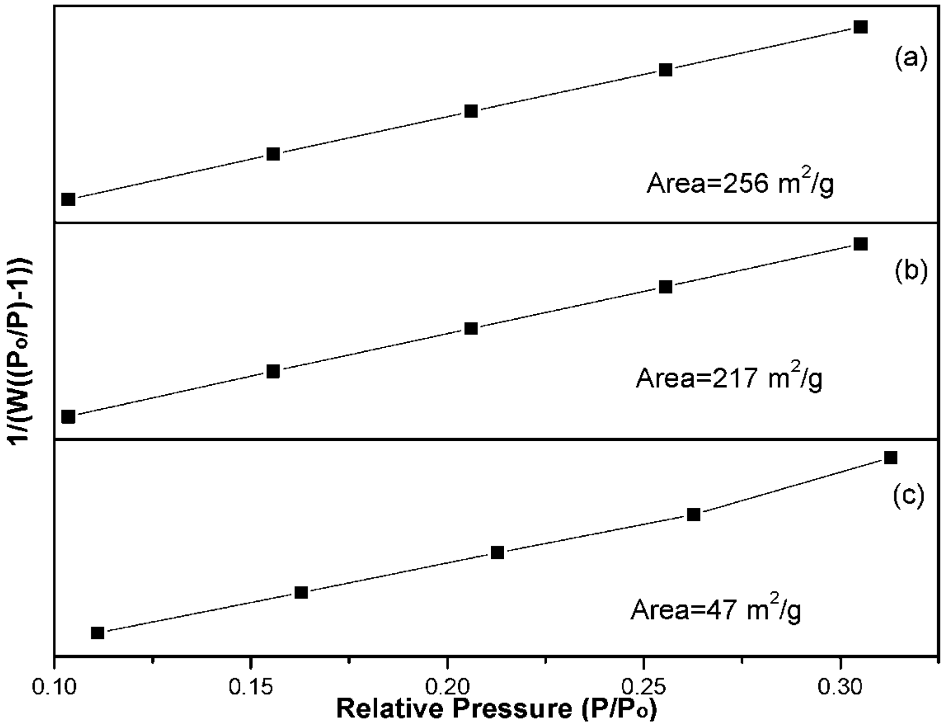

Figure 4.10 BET plots for (a) NHS, (b) NHR and (c) NHF.

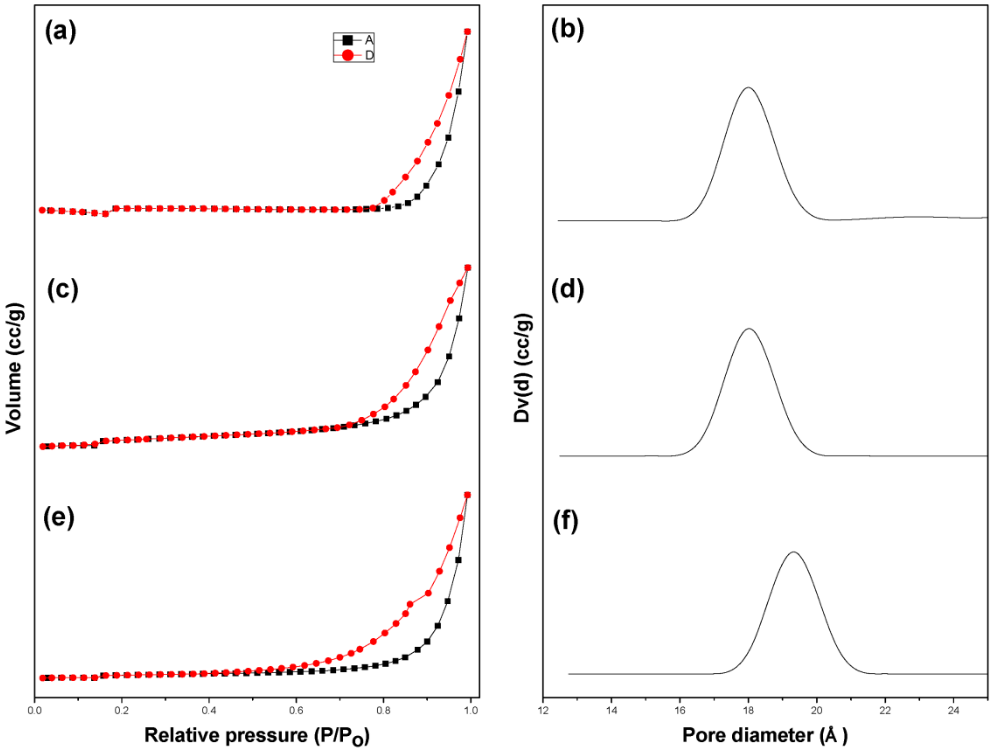

Figure 4.11 BET adsorption and desorption isotherms (a), (c) and (e) and BJH pore size distribution (b), (d) and (f) for HNS, HNR and HNF respectively.

Table 4.3 BET surface area and micro pore properties of HA.

Sample ID	BET surface area in m^2/g (S_{BET})	Average particle size in nm (D_{BET})	Pore volume in cc/g V_{BJH}	Pore diameter in Å (BJH)
NHS	256	7	0.788	17.9
NHR	217	9	0.821	18.01
NHF	47	70	0.903	19.3

4.1.8 Conclusion

HA nanoparticles are successfully prepared through chemical precipitation method using the common precursor materials as $Ca(CH_3COO)_2$ and KH_2PO_4 over the control of solution pH, temperature and Ca:P ratio. High hydroxyl ion concentration ($12.25 \geq pH \geq 10.5$) and low temperature (298 K) favours isotropic non-confined spherical shape, intermediate concentration ($9.5 \geq pH \geq 7.75$) and low temperature (303 K) initiate the anisotropic growth of rod particles and low concentration ($7 \geq pH \geq 5.25$) but high temperature (353 K) accelerates the restricted expansion to fibroid morphology of HA. NHF has high crystallinity with compare to NHS and NHR. The prepared HA nanoparticles have 8 nm, 10 nm and 40 nm size for NHS, NHR and NHF, respectively. Vibrational spectra of HA nanoparticles reflects the presence of functional groups PO_4^{3-} and OH^- of HA only. BET isotherm and specific surface area reveals the formation of high specific surface area of synthesized HA; highest for spherical and lowest for fibrous morphology. HA nanoparticles exhibits type-IV adsorption isotherm and ~2 nm nanoscale pores through BJH pore size distribution. Thus, the prepared three morphologies of HA nanoparticles have been considered for the fabrication of nanobiocomposites with gelatin and studied the BSA protein adsorption and release behaviour.

4.2 Dispersion of HA nanoparticles

Dispersed nano HA particles have importance in the sense of gene carrier, protein delivery media, slurry for the preparation of freeze casted porous scaffold and artificial bone regrowth because of high absorption efficiency and binding affinity with versatile molecules [199,200]. However, dispersion in aqueous medium and stability of such hydrophobic nanoparticles is a challenging task. Most of the techniques are used to disperse HA nanoparticles such as ultrasonication and mechanical milling with variant dispersants [201,202]. However, the above mentioned methods have no prolong stability in aqueous media. Therefore, a typical dispersion mechanism has been adopted as followed to make silica sol from silica nanoparticles [203].

In a similar fashion, three morphologies of HA nanoparticles are dispersed in aqueous media using sodium citrate as chelating agent. Na-citrate is developed from combination of citric acid and NaOH. The dispersed state of different HA nanoparticles in aqueous media are shown in Figure 4.12. In the proposed research work, HA-citrate complex is obtained at 90 ^{o}C and pH~7.4.

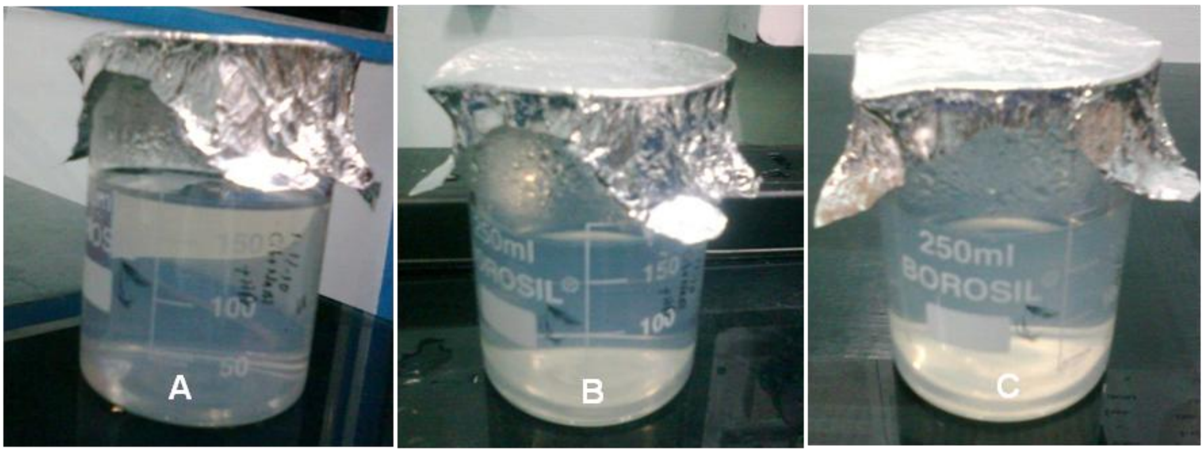

Figure 4.12 Illustration of dispersed nano HA particles (A) NHS, (B) NHR and (B) NHF.

Stability of the HA-citrate depends upon the reaction temperature and pH of the solution. Two molecules of citrate ions $C_3H_5O(COO)_3^{3-}$ are likely to interact with three molecules of Ca^{2+} of HA and form chelate complex (Figure 4.13). The formation of chemical bonding between nano HA and citrate is represented through hydrogen bonding and or carboxyl-calcium-carboxyl ((COO-)-Ca-(COO-)) complex, which allows the homogenous dispersion of nano HA [204]. Thus, the complex formation and dispersion phenomenon are influenced by the available Ca^{2+} site and surface characteristics of particles. Prepared homogenous dispersion exhibits stability up to six months without appearance of the creamy layer or sedimentation on the surface of the solution.

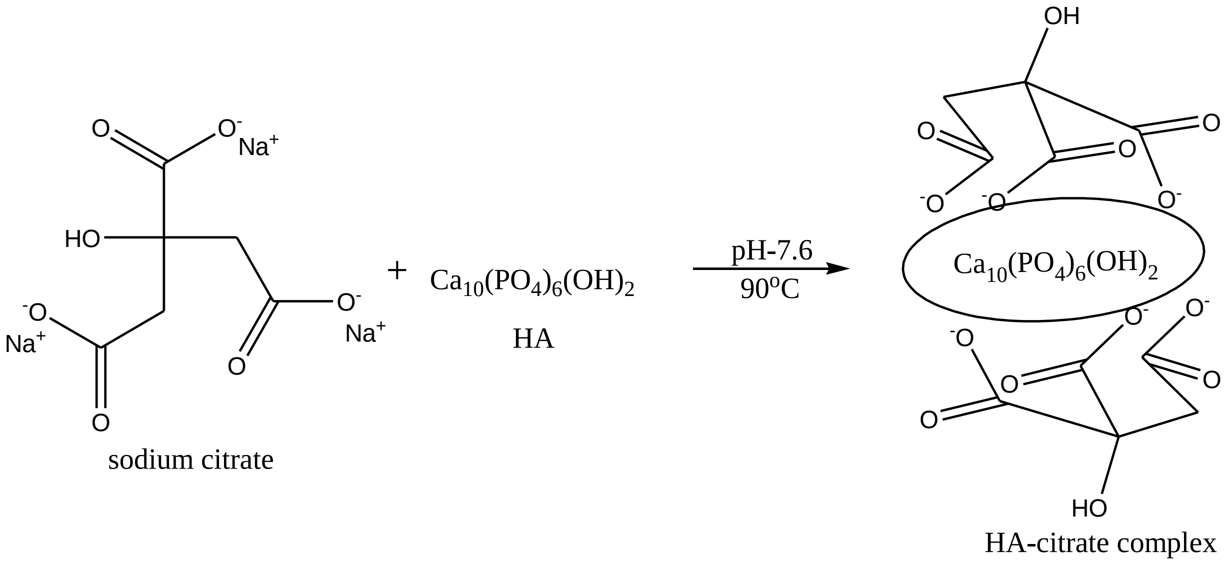

Figure 4.13 Schematic for the reaction of HA-citrate complex formed between the sodium citrate and HA.

4.2.1 Zeta potential measurement

An assessment of zeta potential (ξ; mV) is essential to achieve homogenous dispersion of different grade HA nanoparticles. Dispersed nanoparticles exhibits stability for the extent of more than six months with a constant zeta potential, -19.2 mV, -17.6 mV and -15.2 mV for NHS, NHR and NHF, respectively. The negative zeta potential favour to form homogenous dispersion because of the excellent chelating ability within citrate ions and Ca^{2+} ions, which develops negative electrophoretic mobility of HA in citrate solution [99,205]. HA-citrate complex increases the interfacial surface area due to the repulsion between particles and increases the dispersibility of nanoparticles.

4.2.2 Particle size distribution of dispersed HA nanoparticles

Particle size distribution of the dispersed HA nanoparticles is represented in Figure 4.14. Mono modal size distribution of HA nanoparticles with an average size of the dispersed HA nanoparticles are found as 148 nm, 168 nm and 220 nm for NHS, NHR and NHF respectively as indicated in Table 4.4. NHS and NHF both have wider size distribution whereas NHR represents relative narrow distribution; although all seems in higher size range with respect to original particle size. Both NHS and NHR have the tenacity to coagulate within the particles because of high surface area. However, the particle size of relatively low surface area NHF is also shifted towards the right side after dispersion because of strong particle interaction associate with irregular shape and non-uniform stress distribution around the surface edge of elongated morphology [206]. The deviations of observed particle size from TEM and BET surface area analysis attribute to the tendency to form agglomerate within the range of 150-220 nm because of van der Waals force of attraction with unsaturated citrate molecules. A representative FT-IR spectrum is further discussed the HA-citrate complex behaviour as follows.

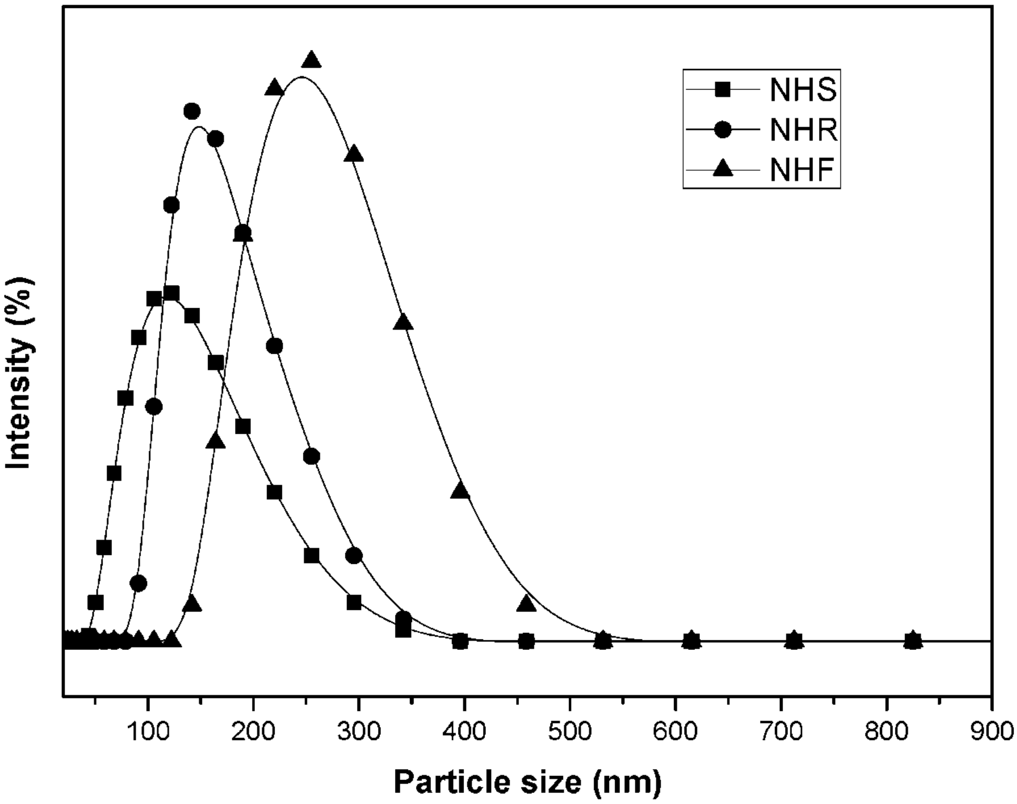

Figure 4.14 Particle size distribution of dispersed HA.

Table 4.4 Zetapotential and size of the dispersed HA nanoparticles.

Samples	Zetapotential (mV)	Size (nm)
NHS	-19.2	148
NHR	-17.6	168
NHF	-15.2	220

4.2.3 Vibrational spectra of dispersed nanoparticles

The characteristic stretching and bending vibrational spectrum of HA-citrate complex is shown in Figure 4.15. FT-IR spectrum of HA – citrate complex exhibits characteristic vibrational bands of C – O and spectral bands of υ^{as} (COO^{-}) at 1619 cm^{-1} and υ^{s} (COO^{-}) at 1416 cm^{-1}, respectively [99,205]. Most intense and broad peak at 3458 cm^{-1} describes the presence of OH^{-} ions from citrate group on the HA surface. The most prominent characteristic peaks of COO^{-} and OH^{-} reveal the feasibility of the formation of HA citrate complex. Furthermore, the vibrational band at wave number 1034 and 566 cm^{-1} show the characteristic stretching and bending modes for PO_4^{3-} group of HA nanoparticles, respectively. The spectral band difference between before and after dispersion of HA nanoparticles confirms the formation of HA-citrate complex.

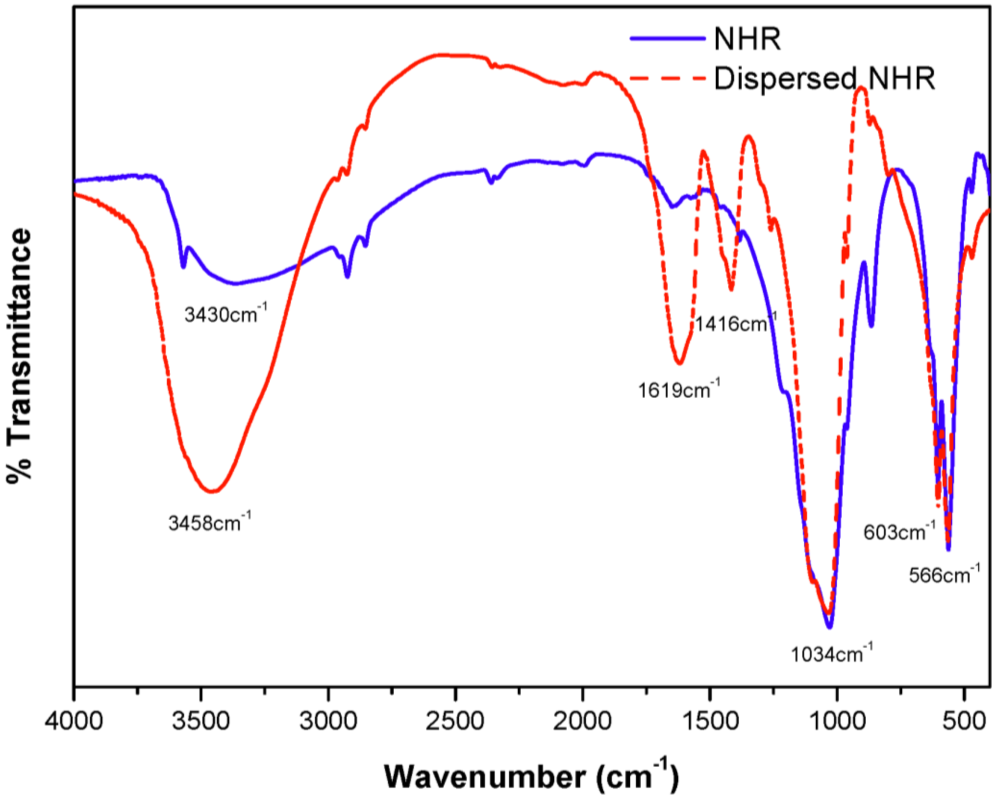

Figure 4.15 FT-IR of before and after dispersion of NHR nanoparticles.

4.2.4 Conclusion

Dispersed HA nanoparticles follow complexometric reaction with sodium citrate. The resulting HA citrate has homogeneous dispersibility and more than six months stability without the appearance of sedimentation. FT-IR analysis confirms the complexation reaction feasibility between the HA and the citrate ions. High negative zeta potential attributes the stability of the HA dispersion. Dispersed HA nanoparticles could be used for the preparation of homogenous slurry or suspension and their fabrication of porous scaffold with apposite solid loading, as well as protein delivery media.

4.3 BSA adsorption and release study on synthesized HA nanoparticles

Hydroxyapatite is a major constituent of hard tissue, bone and teeth and hence synthetic biocompatible HA has clinical use as filler and delivery media [207]. A common conjecture in biomaterials research is the cellular interaction towards bioimplant surfaces, mediated through adsorbed proteins, since protein is an essential component to support cell nutrients, cell growth and attachment. Hence, different class of protein first adsorb on foreign biomaterial surface prior to initiate *in vivo* activity [208,209]. Serum albumin is such an essential protein ingredient for *in vitro* cell culture [210,211]. In addition, the adhesion and proliferation of osteobleast cells and mesenchymal cells depend on the concentration of the serum protein in culture media [160,212]. Osteoporosis, osteomyelitis, arthritis, etc., are bone related disease and sustain drug release at the bone site is desirable [209]. The bone-implant interfaces consist of bonding zone of calcium and phosphorus-rich proteinaceous matrix [152,213]. Serum protein adsorption onto implant materials form bond through interfacial film. Development of advanced materials for bone tissue replacement, coatings on medical prosthesis or tissue engineering applications, is needed to understand the mechanisms within protein–biomineral interface. In this aspect, HA could be considered as a reliable source as protein delivery media to the requisite site. Thus, protein HA interaction and their adsorption / release are important phenomena. In this backdrop, BSA has been considered as a model protein as it is available in a highly purified form and soluble in water. It is, therefore, convenient to use this protein in a series of repeated experiments comparing the adsorption and release behaviour of HA. Here in, synthesized HA nanoparticles are used for BSA protein adsorption and release study. Protein concentration, adherence on HA nanoparticles surface and bonding behavior are studied through UV-visible, BET isotherm, FT-IR and DSC/TG analysis.

4.3.1 Microstructure of BSA protein

Microstructure of the BSA is represented in Figure 4.16. SEM microstructure of BSA shows plate like structures with channeled pores. The sizes of the channeled pores are found in the range ~10 µm whereas lengths are around 300 µm of BSA. The intercalating spaces assist to develop moderate conjugation with nano scale HA particles and its biocomposite because of the electrostatic interaction between the BSA protein and HA nanoparticles [214].

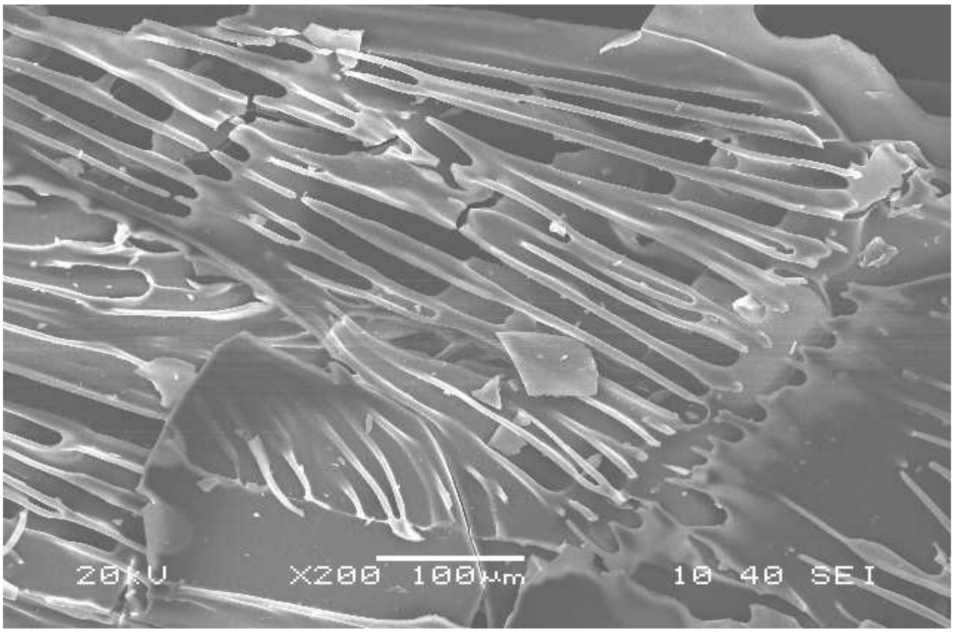

Figure 4.16 SEM microstructure of the pure BSA.

4.3.2 Mechanism of copper complex with BSA

The BCA™ Protein Assay is a bicinchoninic acid (BCA) reagent for the colorimetric quantification of protein. This method describes the well-known reduction of Cu^{+2} to Cu^{+1} process by protein in an alkaline medium and selective colorimetric detection of cuprous cation (Cu^{+1}) using a unique reagent containing bicinchoninic acid (Equation xix) [215]. The purple-colored reaction product of this assay is the result of chelation of two molecules BCA with one cuprous ion [216]. The chelation product that formed with the two molecules of the BCA and Cu^{+1} is shown in Figure 4.17. This water-soluble complex exhibits a strong absorbance at 562 nm, which follows linear relationship with increasing protein concentration over a broad working range of 20-2,000 µg/ml [217].

$$\text{Protein} + Cu^{+2} \xrightarrow{OH^-} Cu^{+} \text{ ....(xix)}$$

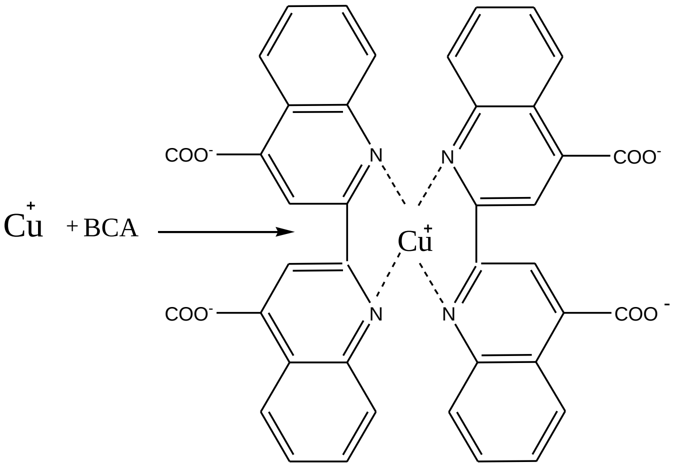

Figure 4.17 Schematic of BCA Cu ion complex.

4.3.3 Standard curve for protein BSA determination

The concentration of the standard BSA protein is calculated by measuring the absorbance. The maximum absorbance of standard BSA protein is found in the wavelength A_{max} ~562 nm. A standard plot is drawn by measuring the concentration of predetermined dilution and the maximum absorbance of diluted standard BSA. The dilutions with the corresponding absorbance are represented in Table 4.5.

Table 4.5 UV-spectroscopic measurement of the maximum absorbance at A_{562} nm.

No. of Vial	BSA (µg/ml)	Working reagent (ml)	Volume of sample (ml)	Absorbance (A_{562})
A	2000	2	0.1	2.2485
B	1500	2	0.1	1.7655
C	1000	2	0.1	1.4305
D	750	2	0.1	0.8911
E	500	2	0.1	0.5823
F	250	2	0.1	0.3329
G	125	2	0.1	0.1559
H	25	2	0.1	0.0798
I	0	2	0.1	0.0413

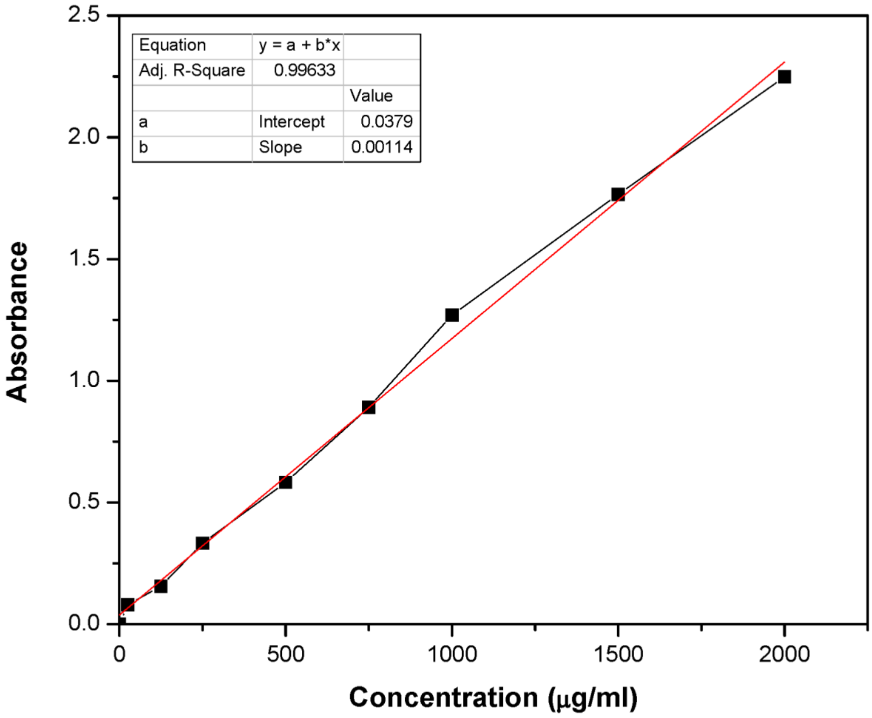

Figure 4.18 BSA protein standard curve for the protein concentration determination.

The maximum absorbance with concentration of the known BSA protein gives linear plot as shown in Figure 4.18. Linear plot with the correlation factor (R^2) 0.996 is calculated from the standard plot, which is latterly used for the determination of amount of BSA adsorbed by the HA nanoparticles and nanobiocomposite scaffold.

4.3.4 BSA adsorption on HA nanoparticles

BSA adsorption on HA nanoparticles phenomenon has evaluated for different time interval from 10 to 240h as shown in Figure 4.19. UV-visible absorbance behavior of BSA adsorbed HA nanoparticles are observed in the wavelength region of ~560-570 nm. The maximum absorbance depends upon the intensity of the color developed and also the period of incubation. A rapid rate of protein adsorption on HA nanoparticles is found after 48 h incubation and follows steady state beyond this time area. Wassell et al. [218] demonstrated that BSA adsorption on HA reaches a steady state at very shorter time scale of around 2h. The maximum absorbance of BSA protein for 48h is studied through UV-visible spectrometer as revealed in Figure 4.20. Absorption study shows that rod morphology of the HA nanoparticles adsorbes higher amount of BSA in comparison of spherical and fibroid morphology. A slight higher adsorption capacity of rod morphologies is presumed to be the reason of semicrystalline behavior, high surface area and higher Ca:P ratio compare to others. High degree of cationic charge prefers to interact with anionic part of protein molecules [219]. Adsorption isotherms of the BSA adsorbed HA nanoparticle is shown in Figure 4.21 The results of adsorption isotherm clearly indicates that BSA adsorption on HA follows the Langmuir adsorption isotherm and develops monolayer [220]. Adsorbed amount of BSA protein increases sharply at low solution concentration of BSA protein and levels off at higher protein concentration approaching a limiting adsorbed value. The amount of adsorbed protein at the plateau of the adsorption isotherm is close to the closed-packed monolayer. Amount of BSA uptake by HA nanoparticles surfaces are 26.5 mg/g, 28 mg/g and 25.7 mg/g for NHS, NHR and NHF, respectively. The result shows that rod morphology of the HA nanoparticles uptake is relatively higher amount of BSA as compared to the counterpart spherical and fibroid morphology.

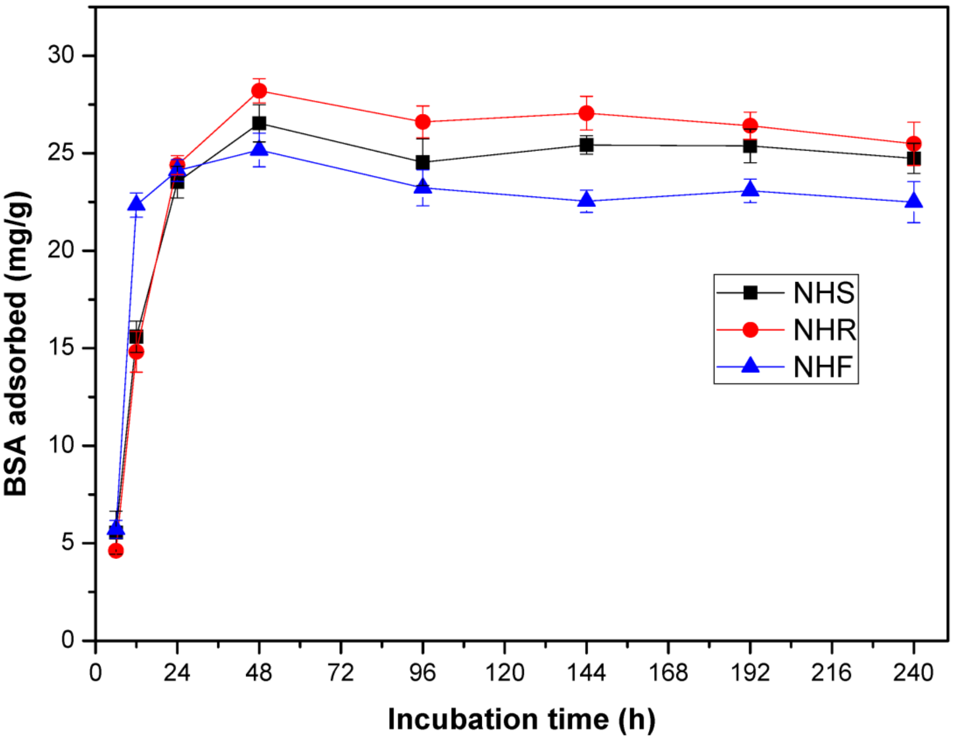

Figure 4.19 Uptake of BSA by different morphologies of HA nanoparticles with incubation time.

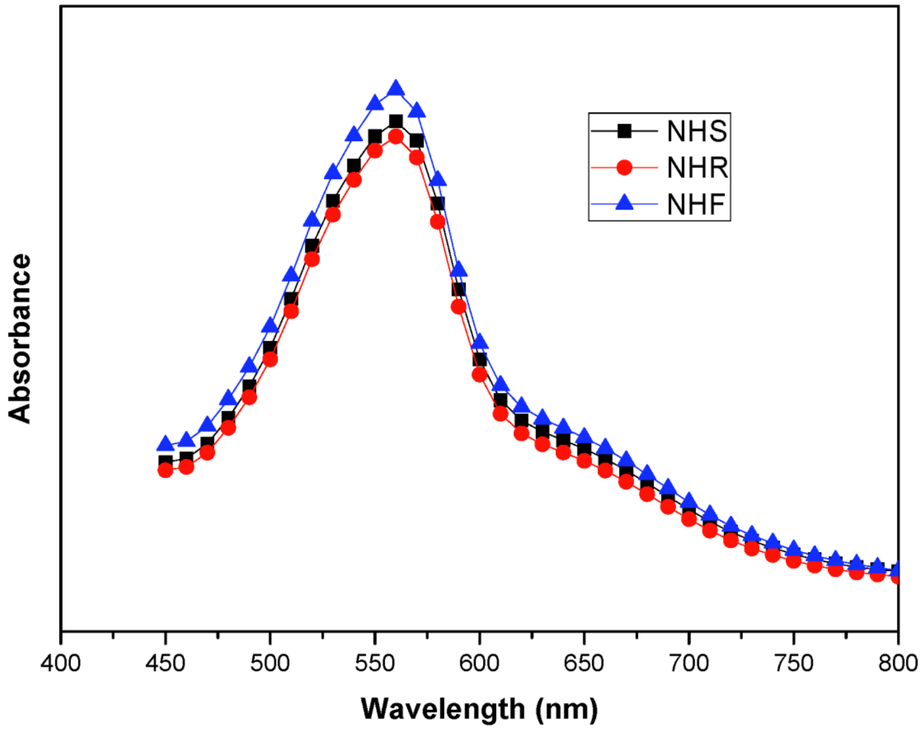

Figure 4.20 UV-visible of BSA adsorbed HA nanoparticles after 48 h studies.

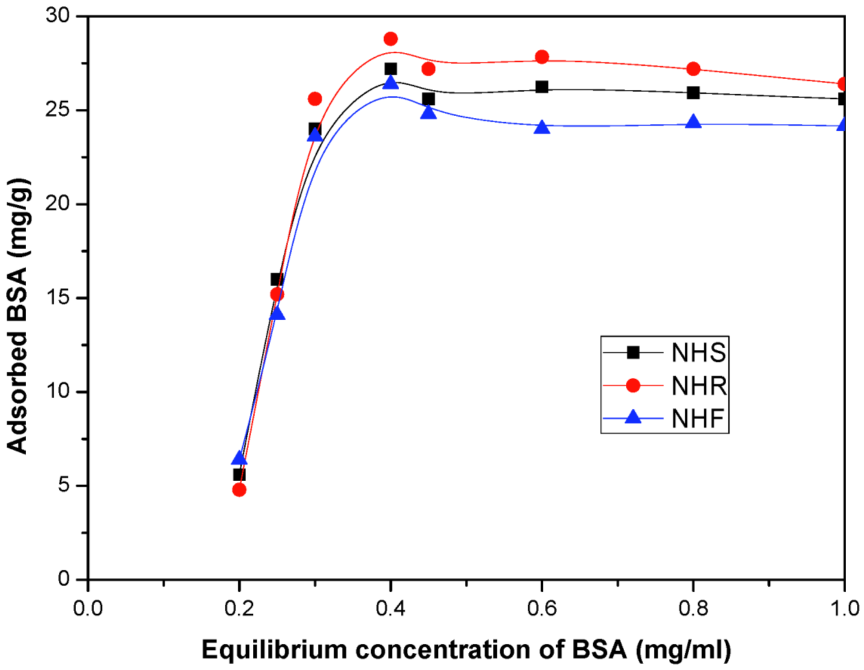

Figure 4.21 Adsorption isotherm of BSA on HA nanoparticles.

Langmuir adsorption isotherm represented as:

$$q = \frac{q_{\max} Ce}{(\frac{1}{a_L}) + Ce} \qquad \text{....................(xx)}$$

Where,

q = Amount of BSA adsorbed on HA (mg/g)

q_{max} = Maximum adsorption capacity (mg/g)

C_e = BSA concentration in solution at the equilibrium

a_L = Langmuir constant (ml/mg)

The amount of BSA adsorbed is calculated by applying the Equation xxi. The equation can be represented as:

Amount of BSA adsorbed $q = \frac{(C_0 - C_e)V}{M}$ ....(xxi)

Where,

C_o = Initial BSA concentration

V = Volume of BSA solution in ml

M = Mass of HA in grams.

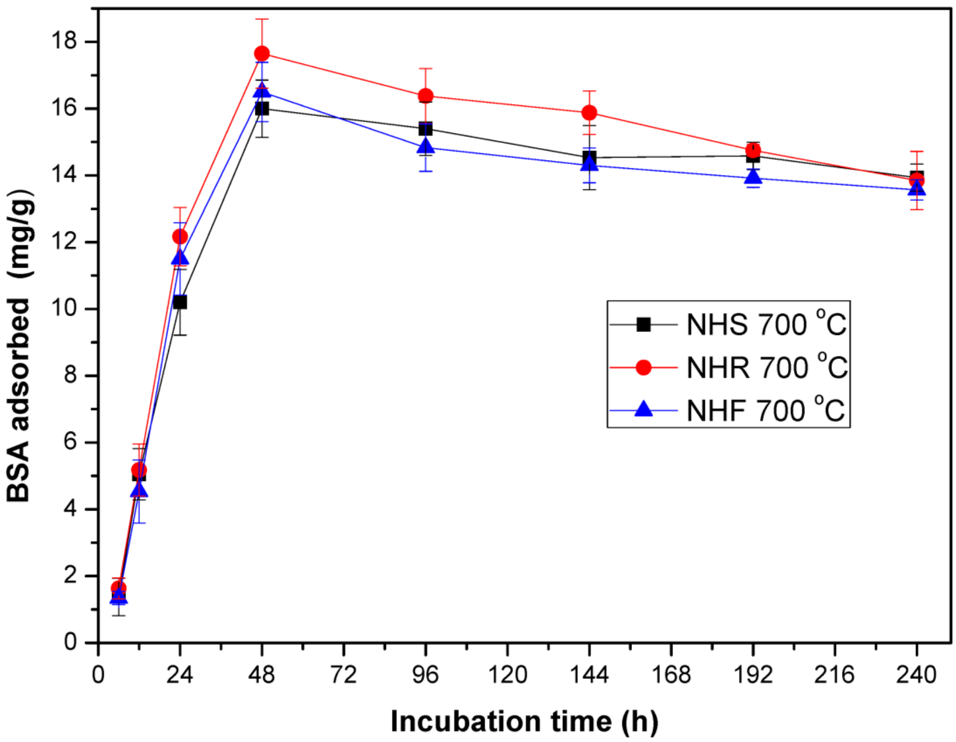

Figure 4.22 Uptake of amount of BSA by HA powders calcined at 700 °C

In a similar fashion, the protein intake is also determined for calcined HA particles to justify the effect on surface area and crystallinity. Figure 4.22 represents the BSA uptake content by 700 °C calcined HA nanoparticles. Amount of BSA uptakes by calcined HA nanoparticles are calculated as previous and found as 16 mg/g, 17 mg/g and 15 mg/g for NHS, NHR and NHF, respectively. The low adsorption capacity of calcined (700 °C) HA particles due to the low specific surface area 158 m^2/g, 115 m^2/g and 20 m^2/g against the as-synthesized HA nanoparticles for NHS, NHR and NHF, respectively. Hence, as-synthesized HA nanoparticles are considered for protein adsorption/release as well as the fabrication of scaffold. A comparison study of BSA protein adsorbed by as-synthesized and calcined HA represented in Table 4.6.

Table 4.6 Comparative study of protein adsorption by as-synthesized and calcined HA particles.

	As-Synthesized HA		**Calcined HA**	
Samples	Surface area (m^2/gm)	BSA adsorbed (mg/gm of HA)	Surface area (m^2/g)	BSA adsorbed (mg/gm of HA)
NHS	256	26.5	158	16
NHR	217	28	115	17
NHF	47	25.7	20	15

4.3.5 BET adsorption isotherm of BSA adsorbed HA nanoparticles

BET specific surface area plots of BSA adsorbed HA nanoparticles and the pure BSA are represented in Figure 4.23. The specific surface area of the HA powders is likely to be decreased from their corresponding initially data 256 m^2/g, 217 m^2/g and 47 m^2/g for NHS, NHR and NHF during BSA adsorption onto the HA nanoparticles. BET specific surface area of pure BSA (sigma Aldrich) is 25.85 m^2/g, whereas BSA adsorbed NHS, NHR and NHF powders has 59.74 m^2/g, 41.47 m^2/g and 5.01 m^2/g, surface area respectively. The BET plots are not linear because of the adsorption and existence of BSA molecules on the HA surface. Specific surface area decrement of the adsorbed HA nanoparticles supports the adherence of BSA particles on the HA surface.

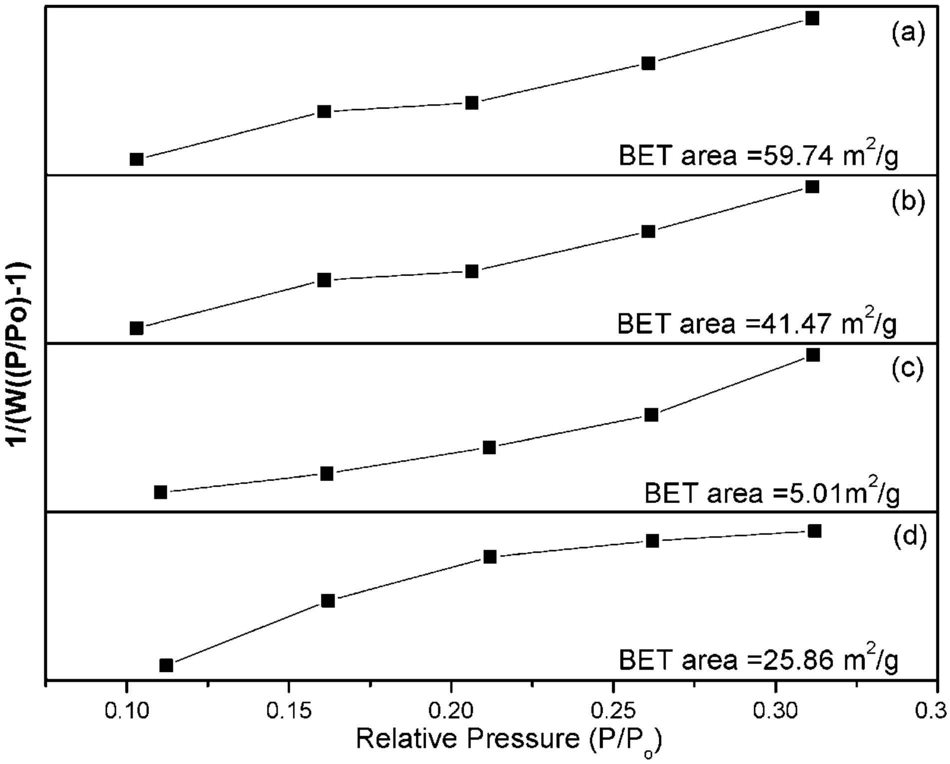

Figure 4.23 BET specific surface area plots of BSA adsorbed HA nanoparticles (a) NHS, (b) NHR, (c) NHF and (d) pure BSA.

BET adsorption isotherm plots associated with the micro pores on BSA adsorbed HA nanoparticles as shown in Figure 4.24. BSA adsorbed HA nanoparticles show isotherm-IV type and the saturation pressure starts earlier as compared to the isotherm for untreated HA. The hysteresis curve is wider due to the presence of micro pores on HA nanoparticles. Pore diameter in the range 1.65 nm, 1.419 nm and 1.241 nm for NHS, NHR and NHF, and is detected by applying BJH pore size analysis method. Reduction of micro pores and pore volume content are attributed to the adsorption of BSA on HA nanoparticles. BJH pore size distribution, surface area of pores and volume of pore are represented in Table 4.7.

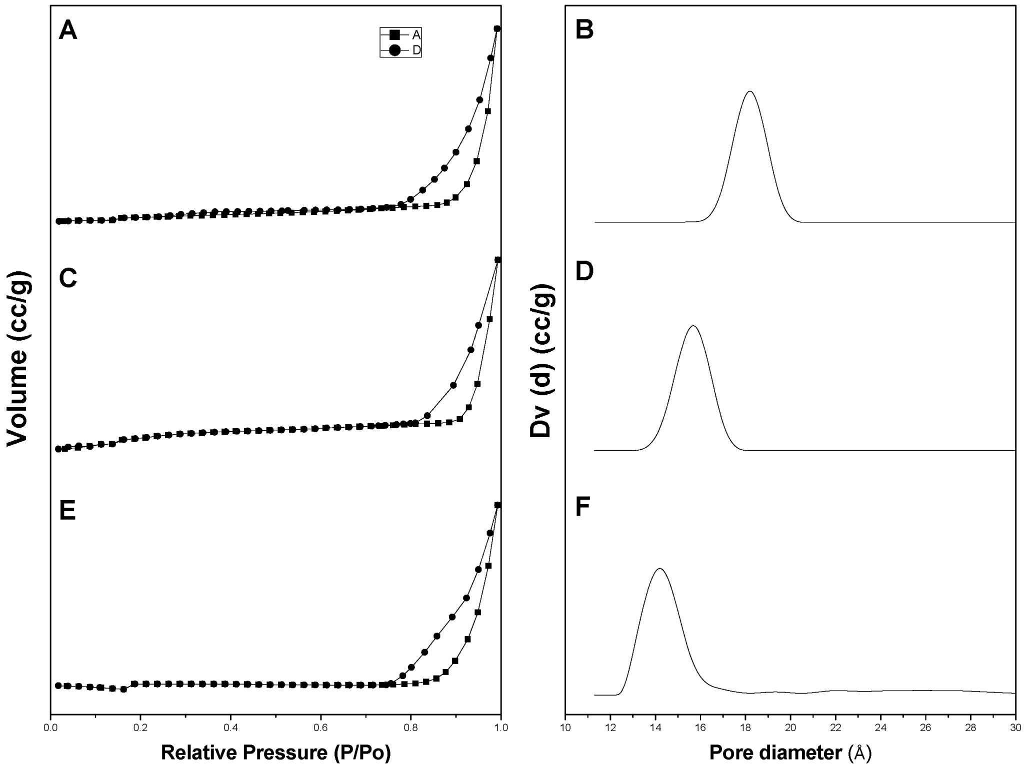

Figure 4.24 BET isotherm plot (A) NHS, (B) NHR and (C) NHF and their corresponding micropore size distribution (B), (D) and (F).

Pore volume calculated from the BJH method is decreased when protein BSA conjugates with HA nanoparticles. The reduction of surface area, micro pore diameter and pore volume clarifies the feasibility of HA-BSA conjugates formation.

Table 4.7 BET specific surface area and properties of the micro pores.

Sample ID	BET surface area of HA in m^2/g	BET surface area BSA-HA in m^2/g	Pore volume in cc/g V_{BJH}	Pore diameter in Å (BJH)
NHS	256	89.74	0.037	16.51
NHR	217	41.47	0.039	14.19
NHF	47	5.01	0.037	12.41
BSA	-	25.86	0.0047	25.12

4.3.6 Mechanism of BSA- HA adsorption

The plausible schematic representation of BSA protein adsorption mechanism on HA nanoparticles is illustrated in Figure 4.25. Nano HA binds the protein BSA with high affinity on its surface due to high surface to volume ratio. Binding is thought to depend on the interaction of calcium with anionic site (COO^-) of protein whereas, the phosphate group of same HA follows a strong interaction with a basic moiety ($–NH_3^+$) of identical protein molecules [78,221]. The Ca^{2+} site of HA also repulse with NH_3^+ group of protein, but $PO_4^{3–}$ tends to attract toward NH_3^+. Similarly, anionic $PO_4^{3–}$ of HA also repulses with $COO^–$ of a protein molecule and attracts with Ca^{2+} through electrostatic force of attraction. Thus simultaneous attraction and repulsion mechanism between HA and protein facilitate to make strong HA–protein conjugates. Higher molecular weight proteins such as fibronectin, transmembain protein, bone morphogenic protein has tendency to adsorb on HA surface more tightly as predicted by Rauschmann et al [222].

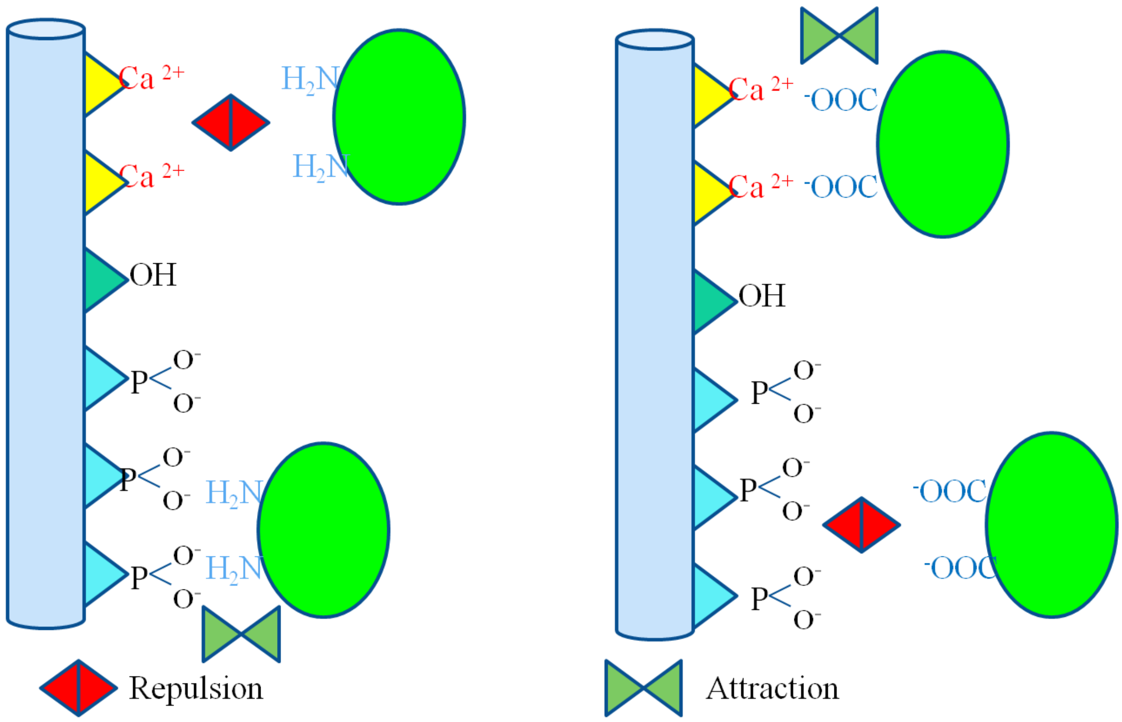

Figure 4.25 Mechanism for protein BSA and HA interaction.

4.3.7 FT- IR analysis of adsorbed BSA

FT-IR is sensitive to secondary protein structure [223]. Secondary protein structure is nothing but a specific geometric shape caused by the hydrogen bonds between backbone amide and carboxyl groups in protein [224]. Characteristic vibrational functional groups for the BSA and BSA adsorbed HA nanoparticles are represented in Figure 4.26. Different wavenumber 1654 cm$^{–1}$, 1536 cm$^{–1}$ and 1441 cm$^{–1}$ represents the vibratioanal bands for amides of the adsorbed BSA [225]. The terminal alkyl –CH stretching for the adsorbed BSA is observed at wavenumber 2963 cm^{-1}. Broad adsorption peaks for OH^{-} stretching vibration are resulted due to the presence of OH^{-} of HA as well as the adsorbed BSA. Wavenumber 1059 $cm^{-1}$and 559 cm^{-1} represents for the characteristic stretching vibration for PO_4^{3-} group. FT-IR result reveals that BSA protein adsorbs on the HA nanoparticles without any denaturation. Furthermore, the characteristic vibrational band of amide shows the secondary structure of BSA, as well as the BSA adsorbed on HA surface [226]. The nature of bonding behavior and position of vibrational wavenumbers are summarized in Table 4.8.

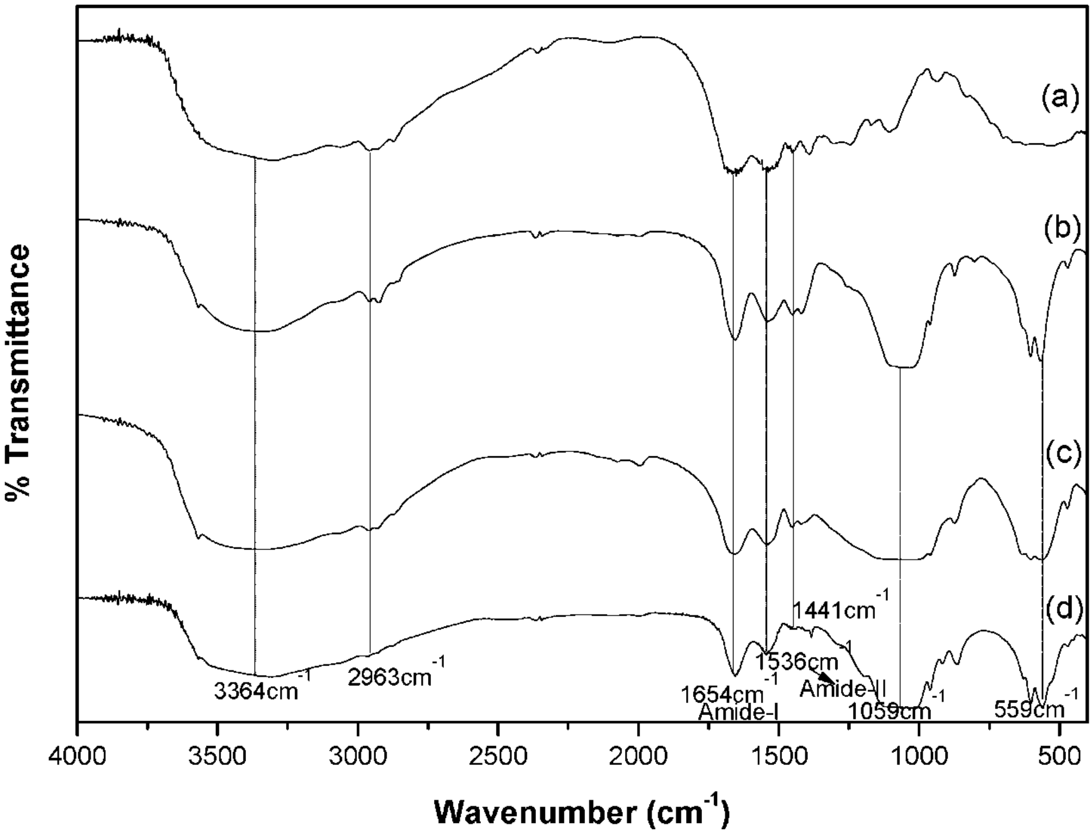

Figure 4.26 FT-IR study of the BSA adsorbed HA nanoparticles (a) Pure BSA, (b) NHS-BSA, (c) NHR-BSA and (d) NHF-BSA.

Table 4.8 Characteristic vibrational bands of BSA adsorbed HA nanoparticles.

Functional Groups		**BSA**	**HSB**	**HRB**	**HFB**
Groups	Mode of vibration	ν_o(cm^{-1})	ν_o(cm^{-1})	ν_o(cm^{-1})	ν_o(cm^{-1})
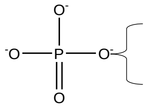	P–O stretching	–	1038 Strong	1041 strong, broad	1035 strong, broad
	P–O bending	–	553 Weak	545 weak	559 weak
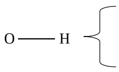	O–H stretching	3314 strong	3350 Strong	3320 strong, broad	3327 strong, broad
	O–H bending	610 weak	605 Weak	603 broad, strong	608 weak
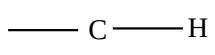	C–H stretching	2953 weak	2933 Weak	2960 weak	2951 very weak
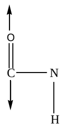	Amide-I stretching	1662 strong	1650 Weak	1658 strong	1654 strong, intense
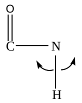	Amide-II bending	1544 strong	1532 Weak	1546 strong	1536 strong, intense

4.3.8 Thermal analysis of BSA adsorbed HA nanoparticles

The relevance of this study is allied with the indirect assessment about the adherence of BSA protein with HA nanoparticles; since high temperature will allow to remove the adsorbed organic molecules at elevated temperature. In this study, rod shaped HA morphology is encountered because it has maximum BSA protein adsorption behavior. Thermal analyses of BSA and BSA adsorbed nano rod HA particles are represented in Figure 4.27. Thermal analysis of BSA shows an endothermic peak at 90 ^{o}C for the presence of physical adsorbed moisture and broad exothermic peaks observed at 450 ^{o}C associate with the decomposition of amides bonds in BSA [227]. Thermo gravimetric analysis of the pure BSA shows mass loss of around 70% at temperature 420 ^{o}C and the remaining mass is due to the formation of some carbonaceous products [228]. Broad exothermic peak in the temperature range 350 to 550 ^{o}C is because of decomposition of pure BSA as shown in Figure 4.27(A). In the same time, BSA adsorbed NHR shows 22% mass loss at 450 ^{o}C which is associated with the decomposition of BSA. Differential scanning calorimetry data for the NHR-BSA powder shows an exothermic peak at 340 ^{o}C associate with decomposition of amide bonds of BSA as represented in Figure 4.27(B). The exothermic peak attribute to the thermal decomposition of BSA molecules that tightly bound with HA crystals through electrostatic force [229]. Thus, the thermal analysis of BSA adsorbed HA nanoparticles clarifies the adherence of BSA particles on the surface of the HA through electrostatic force of attraction.

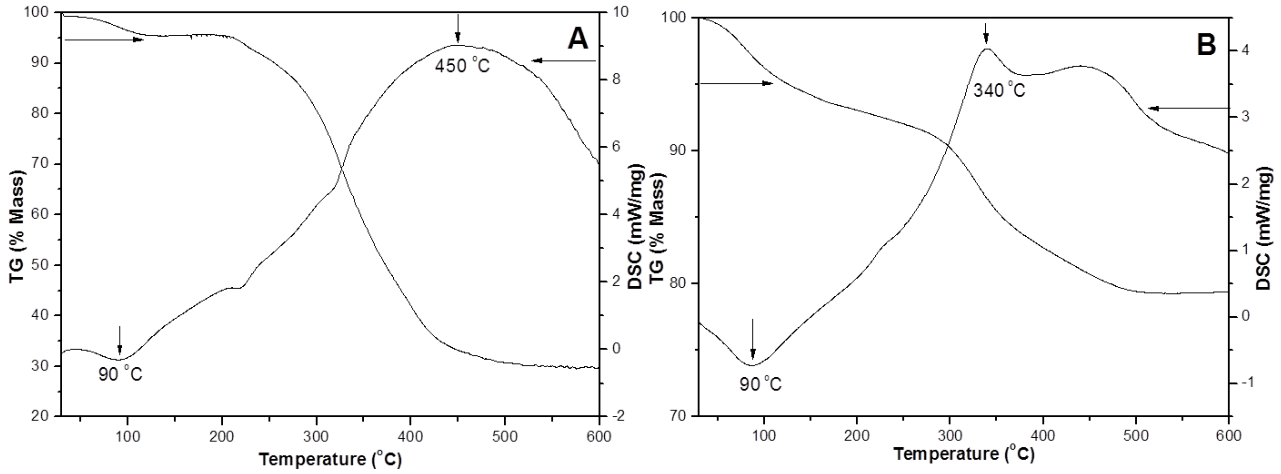

Figure 4.27 Thermal analysis of BSA adsorbed HA powders (A) pure BSA and (B) NHR-BSA.

4.3.9 BSA release study on HA nanoparticles

Release study of the BSA loaded HA nanoparticles are also studied through UV spectrometer. The amount of BSA release amount percentage is plotted against the release time represented in Figure 4.28. The high rate of release is observed ~75% in 96h and then follows slow release rate.The absorbance performance of the released BSA from HA nanoparticles after 96h is shown in Figure 4.29. Rod morphology shows the highest absorbance followed by spherical and fibroid.

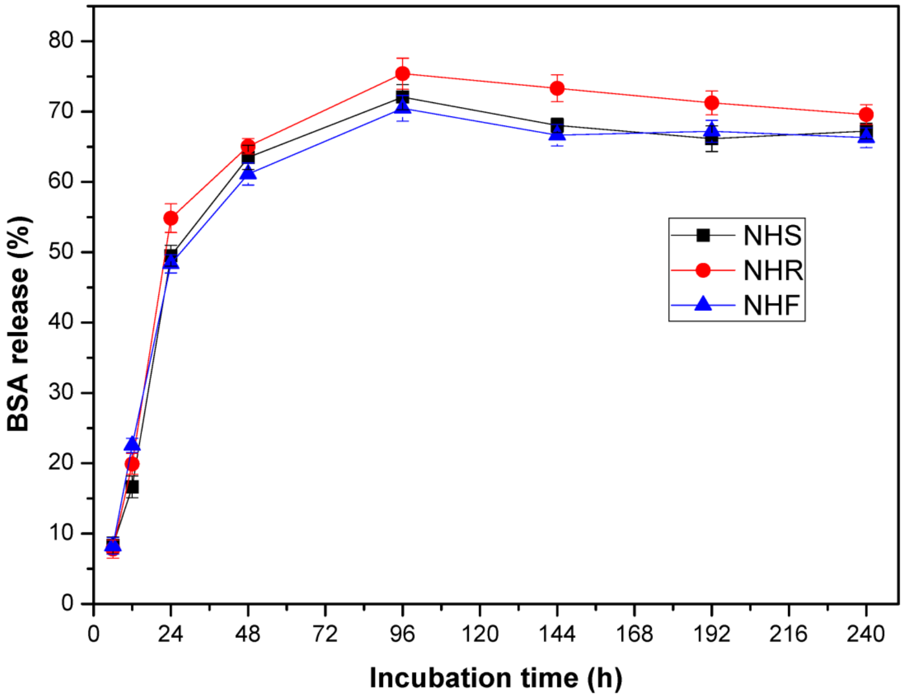

Figure 4.28 Amount of BSA released from the loaded HA nanoparticles.

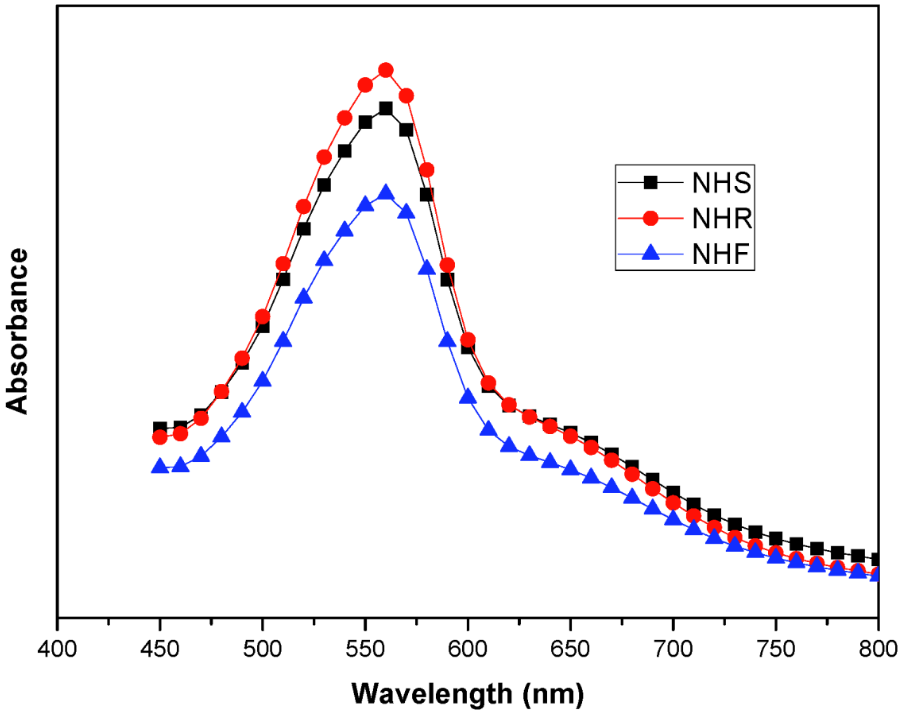

Figure 4.29 UV-visible release of BSA from HA nanoparticles.

Mechanism of BSA release from the BSA loaded HA nanoparticle is illustrated in Figure 4.30. Both of BSA and phosphate ions in PBS are efficient to adsorb onto Ca-sites on HA [230]. However, a competition occurs between BSA and phosphate ions in PBS. Phosphate ions have high affinity to HA compared to BSA [114]. So, most of adsorption sites on HA are occupied by phosphate ions, leading to desorption of adsorbed BSA. As a result, adsorbed BSA protein molecules are easily released from nano HA and displaced by phosphate ions.

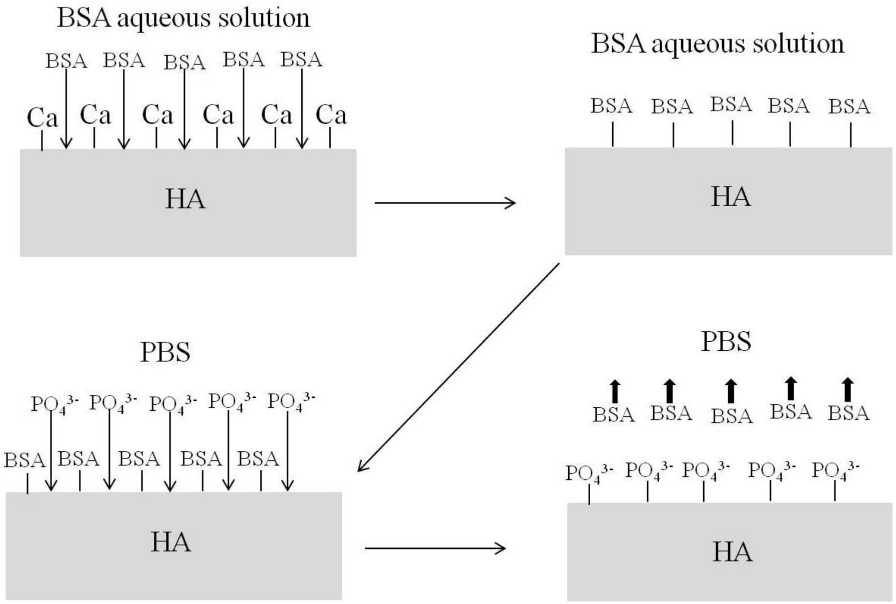

Figure 4.30 Release mechanism of BSA from the HA-BSA in PBS solution

4.3.10 Conclusion

Rod morphology HA nanoparticle adsorb higher amount of BSA as compare to the counterpart spherical and fibroid morphologies. One gram of nanorod HA particles adsorb 28 mgs of BSA. Higher protein adsorption capacity of nano HA has also high release rate. Slow and steady release of loaded BSA from HA nanoparticles is observed up to 75% within 96 h. FT-IR analysis of BSA–HA shows the secondary structure of protein. BSA adsorbed HA nanoparticles may be used as bone filling material and tissue engineering. In addition, high adsorption and steady release of BSA protein from synthesized nano-rod are supposed to be beneficial for the delivery of protein drugs, treatment of cancer cells and bone related diseases.

4.4 Fabrication of freeze casted HA-gelatin scaffold

Porous scaffold allow cell growth and their proliferation when pore diameter exist near to 100 μm as resemble with bone morphology [231]. Scaffolds provide adequate space and effective surface for cell seeding into the temporary scaffold before implantation and support cells for better attachment and proliferation. Hence, bioactive porous HA scaffolds are considered as a large extent for repairing and tissue engineering because of effective nutrients transport, tissue growth and formation of bone – extracellular matrix to support the adequate structure [232]. Different results are reported for the fabrication of porous scaffolds in several ways particularly using pore formers [137], polymeric template [233], dual phase mixing [234], salt leaching and foaming [118,235]. In another end, nanoparticle has high temperature phase and morphology instability when prepared from $Ca(CH_3COO)_2$ and KH_2PO_4 [190]. Moreover, high crystallinity and less reactivity towards protein molecule have been observed after 700 ^{o}C calcination of HA nanoparticles. In another end, gelatin is generally coined as the hydrolysed form of collagen and has clinical use as a drug delivery carrier because of its sufficient plasticity, hydrogel properties and resemble with bone matrix [236,237]. Hence, low temperature freeze casting technique has been adopted for the fabrication of macroporous nanobiocomposite scaffolds from as-synthesized HA nanoparticles and gelatin and studied their details porous architecture, pore size distribution and mechanical response of freeze casted HA-gelatin nanobiocomposite scaffold systematically.

4.4.1 Interaction between polyvinyl alcohol and gelatin

Polymeric binder polyvinyl alcohol (PVA) has terminal hydroxyl groups, and gelatin contains amino acid residue with terminal acidic and amino groups. Esterification process within hydroxyl groups of PVA and the terminal acidic groups of the amino acid residue of the gelatin favors formation of whitish high viscous slurry at temperature 60 ^{o}C [238]. The schematic for the probable chemical reaction likely to occur between PVA and gelatin is shown in Figure 4.31. A detail nanobiocomposites of HA – gelatin preparation technique has already been illustrated in the experimental section. The gelling properties of gelatin interact and bind with HA powder through covalent network to form porous scaffold.

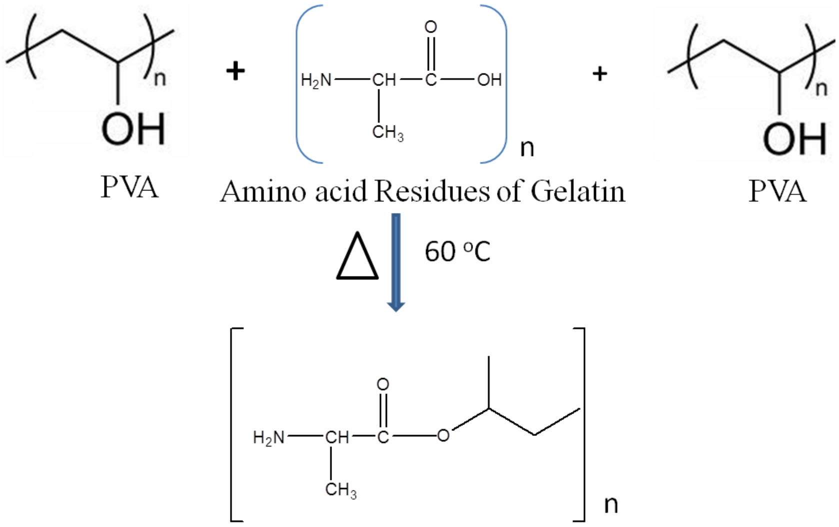

Figure 4.31 Schematic for the chemical reaction between PVA and gelatin.

4.4.2 Vibrational spectra of freeze dried HA-gelatin scaffold

Figure 4.32 shows the FT-IR spectrum of the freeze dried HA-gelatin scaffold. The characteristic stretching and bending vibration bands of HA are found at the wavenumber of 1035 cm^{-1} and 603 cm^{-1} for PO_4^{3-} and 3433 cm^{-1} and 559 cm^{-1} for the OH^{-} group, respectively [239]. Wavenumber 2919 cm^{-1} occurs due to the stretching vibration of –CH of alkyl residue present in both of the PVA and gelatin [240]. The characteristic wavenumber at 1661 cm^{-1} is due to the $–COO^{-}$ group of the ester formed by the mixing of PVA and gelatin. Broad and prominent peak for OH^{-} are the result of an interaction between gelatin and PVA. The FT-IR spectrum analysis confirms the presence of pure HA as well as the gelatin.

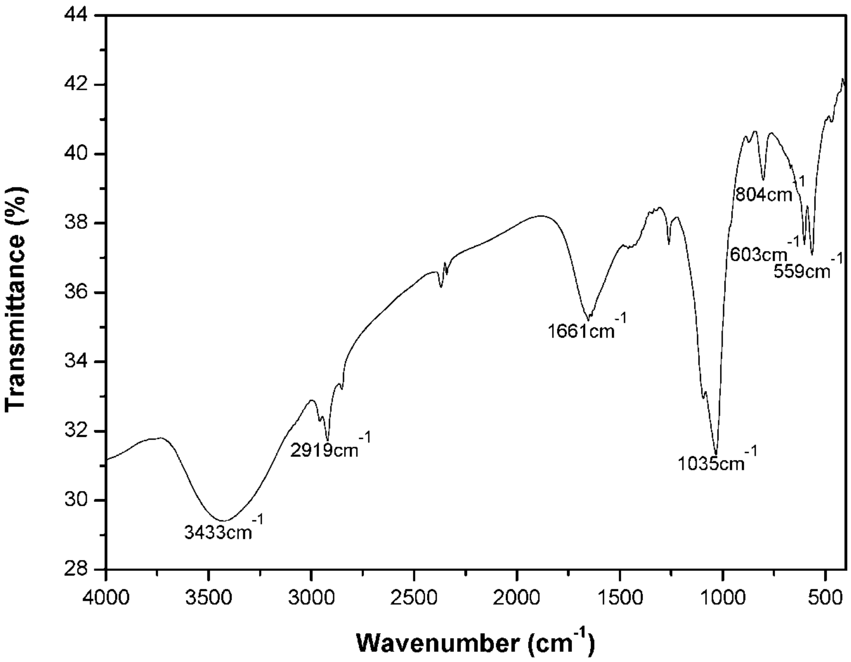

Figure 4.32 FT-IR study of the freeze dried HA-gelatin scaffold.

4.4.3 SEM microstructure of fabricated scaffold

As-synthesized three different spherical, rod and fibroid hydroxyapatite nanoparticles are considered to fabricate HA-gelatin porous scaffolds. SEM microstructure of freeze dried HA scaffolds is represented in Figure 4.33. The reason of optimum (40 wt.%) solid content with consideration of pore dimension, pore size distribution and their mechanical properties is discussed in next Section 4.4.5. Interconnected near circular pore morphology macro porous structure has seen with a pore diameter ~ 50-180 µm for NHS-gelatin (HSG) scaffold (Figure 4.33(A)) and HA particle dispersion is shown in Figure 4.33 (B). Similarly, the SEM result shows open macropores morphologies with average pore diameter in the range ~ 40-150 µm for NHR-gelatin (HRG) scaffold in Figure 4.33(C) and distribution of NHR particles shown in Figure 4.33 (D). Pores are found as circular in shape with partly interconnected structure through polymeric matrix. The SEM microstructure of NHF-gelatin (HFG) scaffold as represented in Figure 4.33(E) and NHF particle distribution is shown in Figure 4.33(F). Circular open macro pores with an average pore diameter varies in the range ~ 50-200 µm. HFG scaffolds has relatively larger pore diameter than the counterpart HRG and HSG scaffold. Different pore morphologies resulted is the replica of the developed ice crystal during freeze drying. Heinemann et al [138] demonstrated HA-collagen scaffold through freeze casting exhibits 100-200 µm pore size, 80 vol.% porosity and 0.085 MPa compressive strength. HRG scaffolds shows well pore size distribution with reticulated open porous structure as compared to HSG and HFG and hence considered for micro-CT analysis in later. Most of the pores are open macroporous along with elliptical shape. NHR particles are well dispersed and arranged within the polymer matrix as compared to the counterpart spherical and fibroid particles. Thus, the mechanical properties of rod morphology scaffold exhibits improved mechanical response relative to others.The morphologies of different pores are resulted due to the anchoring effect of the different morphologies of HA nanoparticles. However, freeze drying process parameter assist pore morphology synchronization could be considered as another futuristic challenging task to manipulate the mechanical properties and *in vitro* bioactivity.

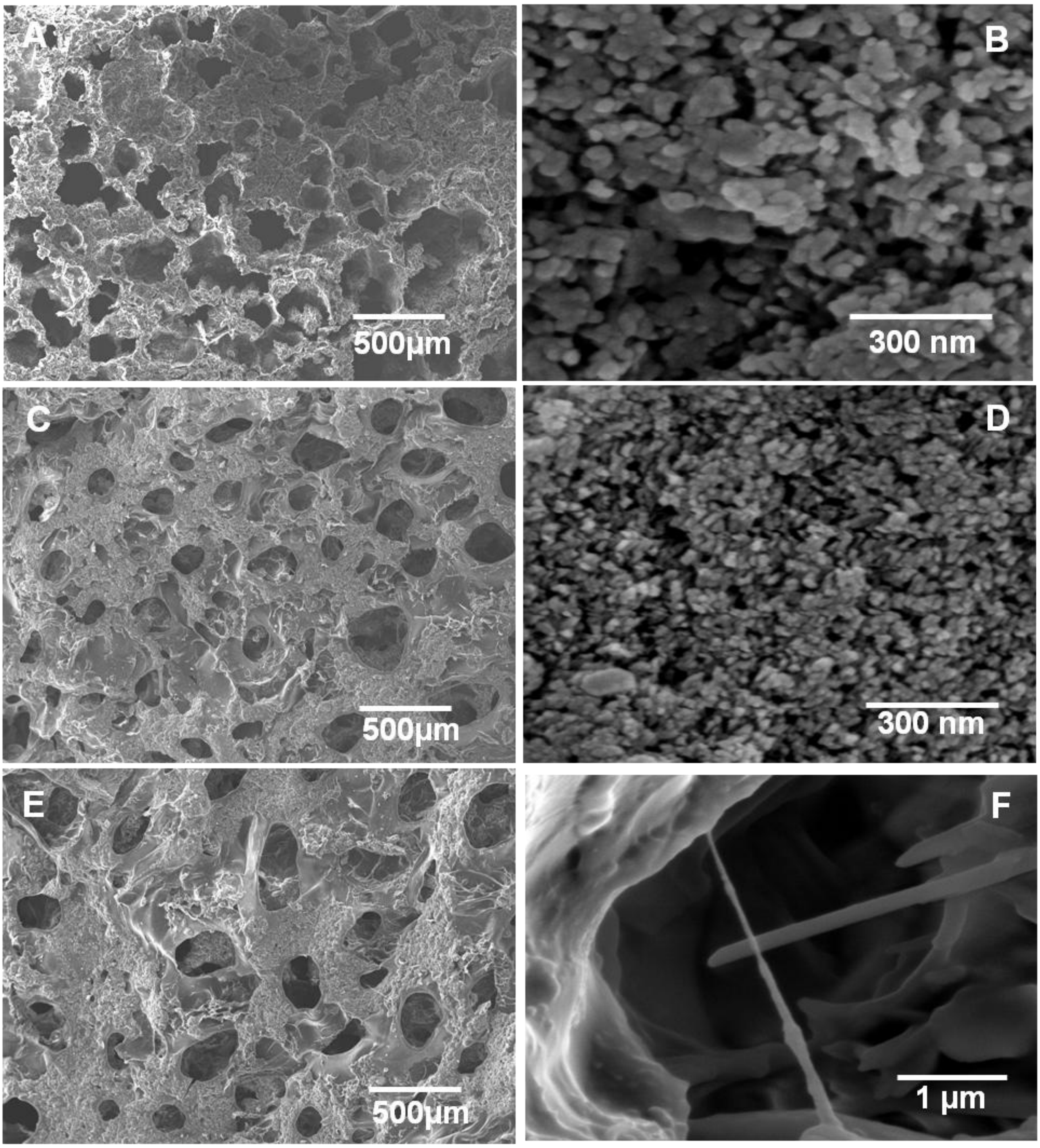

Figure 4.33 Scanning electron micrographic image of the freeze dried HA-gelatin scaffold (A) HSG, (C) HRG and (E) HFG and their particle distribution is (B), (D) and (F) respectively.

4.4.4 Mercury poresize distribution of HA scaffold

Pore size distributions of all three different freeze dried scaffolds are studied through mercury intrusion porosimetry, as represented in Figure 4.34. Multimodal pore size distribution is seen for the HSG with average pore diameter in the range ~80 µm and consist micro pores in the range ~1-10 µm (Figure 4.34(a)). Mercury porosimetric includes both open and close pore in the range of pore size from 0.1 – 200 µm and, hence exhibits lower range of pore size compared to pore size from SEM microstructure (Table 4.9). Apparent porosity of scaffolds is also cross checked through Archimedes method and total porosity by mercury porosimeter. Total volume porosity measured in the mercury intrusion is 74%. Figure 4.34(b) shows multimodal pore size distribution for HRG scaffold with the average pore diameter in the range ~ 70 µm. Some micron pores are also observed in the range ~0.1-1 µm with a resultant porosity of 72 vol.%. Development of micro pores due to the ice crystal that are grown in the walls of the pores [241]. Figure 4.34(c) shows multimodal pore size distribution of HFG scaffold. The average pore diameter is observed in the pore diameter ~100 µm along with porosity of around 76%. Different gradations of micro pores are observed in the range of ~0.1-10 µm. Diverse pore size distribution as revealed by porosimetry from SEM microstructure results due to the anchoring of the HA nanoparticles with the PVA-gelatin slurry and the development of ice crystals during freezing at 221 K. This pore size distribution analysis confirms the presence of micro/macro pores in fabricated scaffolds, which is presumed to be excellent media for adhesion of foreign organic molecules and scaffold.

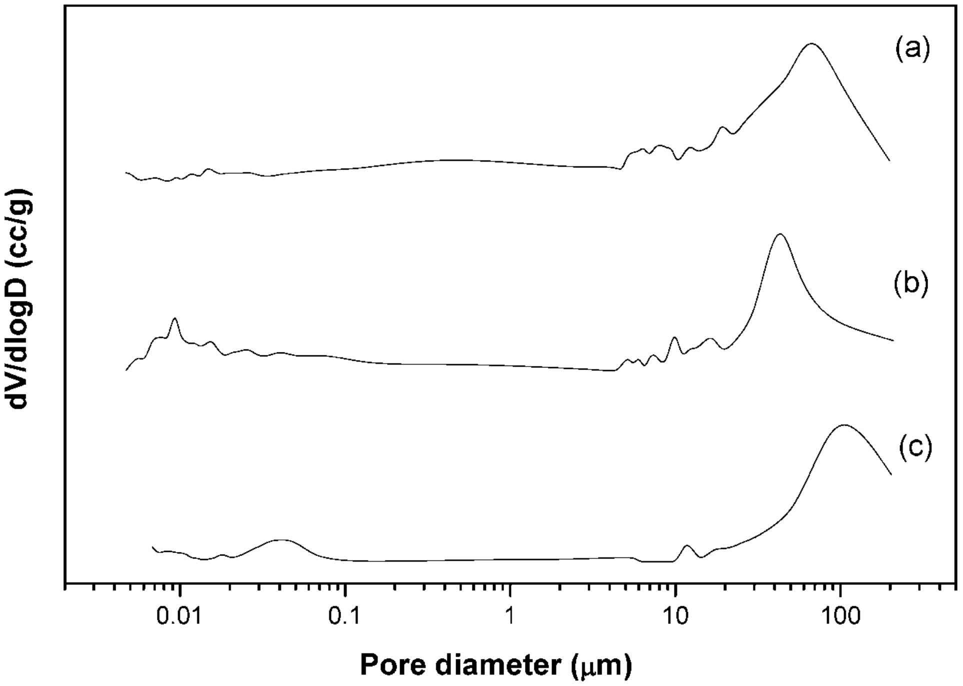

Figure 4.34 Pore size distribution of the freeze dried scaffold (a) HSG, (b) HRG and (c) HFG.

4.4.5 Effect of HA loading on compressive strength and porosity of scaffold

Solid loading has been optimized on the support of two prime properties such as apparent porosity and compressive strength, which are systematically described in Figure 4.35. All scaffolds HSG, HRG and HFG exhibits decrement of apparent porosity and their compressive strength increment with increasing solid loading from 30 to 50 wt.%, although these two fundamental properties are non-linearly related [242]. Reasonable compressive strength with adequate porosity of the scaffold is seen in 40 wt.% HA solid content. Due to the above cause, the scaffolds are fabricated by selective 40 wt.% HA solid content and considered for next step compressive strength enhancement.

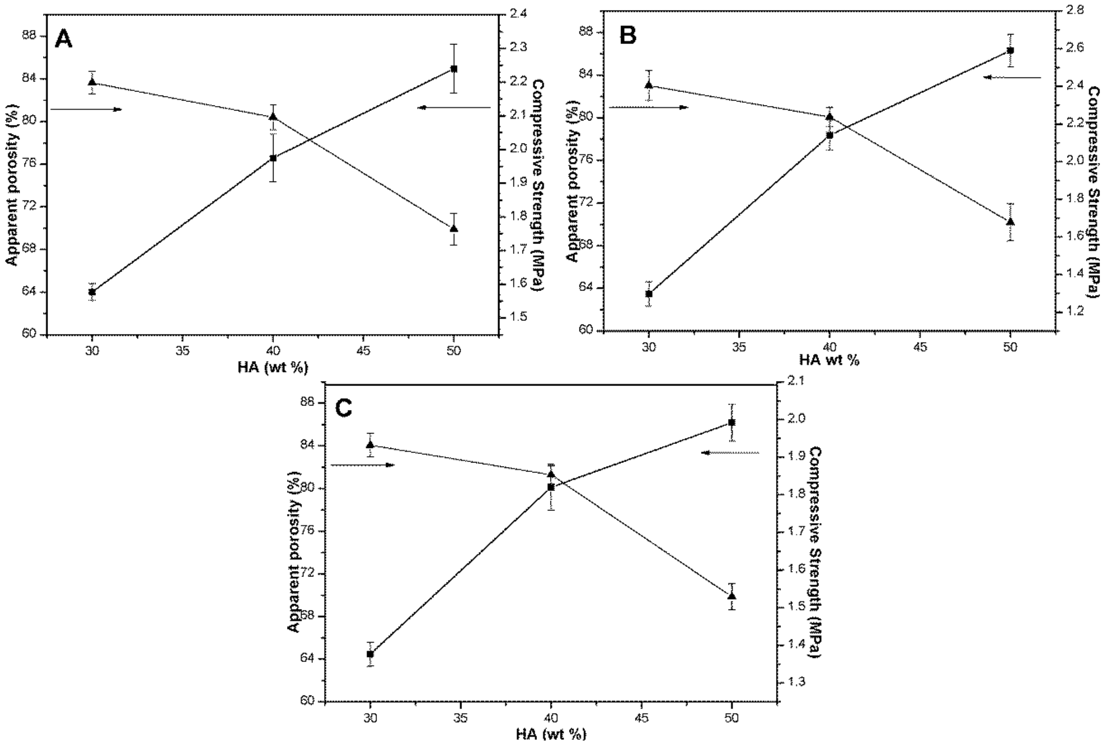

Figure 4.35 Plots of apparent porosity and compressive strength (A) HSG, (B) HRG and (C) HFG.

Stress-strain behavior of HA-gelatin scaffolds is represented in Figure 4.36. The compressive test of the HA-gelatin scaffold samples are studied under uniaxial compression for specifically 40 wt.% HA solid bearing scaffold. The scaffold shows the stress of 2.2 MPa for HRG, 2.05 MPa for HSG and 1.87 MPa for HFG scaffold, respectively. The result shows strain of the scaffolds at the yield stress ~12%. This slow strain rate confirms the ductility nature of freeze dried scaffold. Due to the low compressive stress with ductility, it is essential further development of stress of scaffolds by means of surface modification. The overall properties such as porosity, strength, elastic modulus and average pore diameter of the as freeze dried HA-gelatin porous scaffold is shown in Table 4.9. A close look on Table 4.9, reveals that HRG scaffold has comparative high compressive strength, elastic modulus with low porosity and average pore diameter 120 µm. Asefnejad et al. [139] demonstrated freeze casted nanoHA-polyurethan composite has 50-200 µm pore size, 80 vol.% porosity and 0.6 MPa compressive strength.

Table 4.9 Properties of freeze dried HA-gelatin porous scaffold.

Sample ID	Porosity (%)	Compressive Strength (MPa)	Elastic modulus (MPa)	Pore size (μm) (SEM)	Pore size (μm) Hg-porosimeter
HSG	74 ± 2	2.0 ± 0.03	64 ± 3	152 ± 4	80
HRG	72 ± 3	2.1 ± 0.05	70 ± 2	140 ± 5	70
HFG	78 ± 2	1.8 ± 0.02	62 ± 3	155 ± 3	100

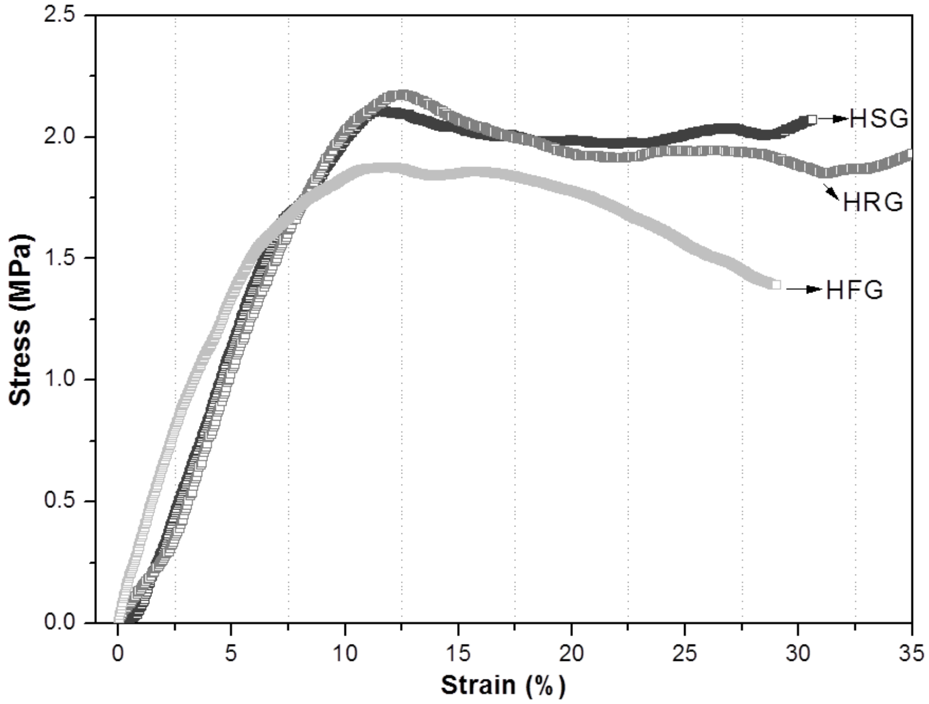

Figure 4.36 Stress-strain behaviour of the prepared HA scaffolds at HA loading 40 wt. %.

4.4.6 Conclusion

Low temperature freeze casting favors the formation of HA-gelatin micro/macroporous scaffold from high viscous slurry of rod shaped HA nanoparticles and gelatin. Circular open macropores of scaffold has average pore diameter ~150 μm and compressive strength in the range ~2 MPa. Optimum strength and average pore microstructure obtains in presence of 40 wt.% HA solid content. Stress-strain behaviour reveals the ductile to quasiplastic nature at strain of 12%. However, improvement of mechanical response of high porous scaffold is always a challenging task and hence, it will be encountered as a next challenging tax in our research work.

4.5 Properties of freeze casted scaffold after cryo-treatment

High porous trabecular bone has ease stress dissipation characteristic through articular contact loads and more compliance than cortical bone [243,244]. Porous trabecular bone resides at the ends of bone with 50 – 90 percentage pore volume, 100 – 400 µm pore diameter and ~2 – 10 MPa compressive strength [245]. Mechanical competence such as compressive strength and elastic modulus of this class of bone is influenced by age and initiate to fracture under stress [246,247]. In accordance with the previous compressive strength observation, further cryogenic treatment has been carried out to enhance the mechanical response of developed scaffold. Herein, freeze casted porous scaffolds are attempted to improve the mechanical properties under cryogenic temperature and discussed their phase and interfacial bonding behavior, compressive strength, pore structure, fracture behavior and machining capability.

4.5.1 Chemical behaviour of polymeric matrix at cryogenic temperature

FT-IR spectrum of freeze casted scaffold and the liquid nitrogen treated scaffold is shown in Figure 4.37. The absorption bands at wavenumbers 3421 and 602 cm^{-1} are associated with the characteristic stretching and bending vibrational modes of OH^{-}, respectively. However, 1032 and 562 cm^{-1} for the characteristic of PO_4^{3-} groups of HA in HRG00 scaffold. The absorption band at 2926 and 1558 cm^{-1} describes the C – H stretching vibration of vinyl group and N – H stretching vibrations of amide groups in HRG00 scaffold [248]. The bands at 1649 and 1458 cm^{-1} shows the stretching of carbonyl in ester groups, which confirms the esterificaiton during processing of scaffold. Absorption band for the same carbonyl group at 77 K is found at 1670 cm^{-1}, which indicates the absorption at higher wavenumber with high intensity due to shorter and stronger bond length between the consecutive atoms. Thus, cryogenic environment weakens the thermal oscillation of atoms, which is leading to strengthen of hydrocarbon matrix, anchoring the HA nanoparticles and alteration the mechanical properties.

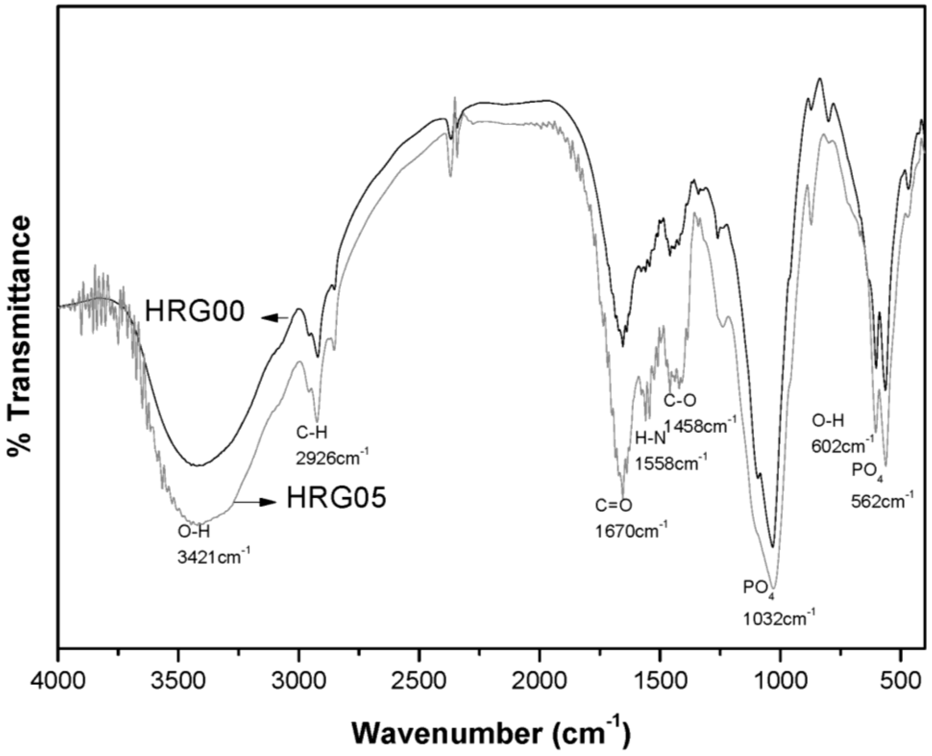

Figure 4.37 FT-IR pattern of freeze casted and liquid nitrogen treated scaffolds for 5h.

4.5.2 Optimization mechanical properties of cryo-treated scaffolds

In the beginning, nanorod based scaffold has been considered to optimize the cryogenic treatment time since nanorod HA has maximum BSA protein adsorption efficiency and their HA-gelain scaffold has highest compressive strength. The other relevant characterization for all other scaffolds is estimated only after cryotreatment process optimization. Figure 4.38 shows the representative compressive stress – strain curves for original and modified HRG00 porous scaffolds compliance within 5 – 10 % strain. The original HRG00 exhibits plastic yielding and thereby a plateau without linear elastic region. HRG00 are micro – buckled beyond peak stress 2 MPa; causing plastic collapse of the hydrocarbon matrix and hence, cell wall touched each other. The stress behavior is slightly improved under short time 2h liquid nitrogen treatment, but reasonably improved the compressive strength (~6 MPa) for 5h treatment at 77 K. The mechanical performance of this class of material depends on the bonding and strengthens hydrocarbon matrix behavior. A close look on compressive strength data indicates that HRG05 has maximum strength among others. Two different regions can be observed for HRG05; an initial linear – elastic region that reaches a peak stress, followed by a significant stress drop after the linear – elastic region, which corresponds to fracture of HRG05. The initial linear elastic region corresponds to the cell walls bending related to reversible deformation. The plateau regimes in HRG05 are distinct due to different deformation mechanisms. Figure shows that HRG00 scaffold has high strain tolerance behavior compare to

HRG05. The strain tolerance is less consistent beyond 5h and observes gradual reduction of compressive strength of scaffolds [249]. The continuous increment and then decrement after optimum liquid nitrogen treatment is due to the change in bond behavior and internal stress associated with thermal conductivity mismatch at such low temperature. Thus, micro cracking is caused due to the generation of internal stress and mismatching of the thermal coefficient of HA and gelatin at 77 K. The coefficient of thermal expansion (CTE) for hydrocarbon matrix at cryogenic temperature should be somewhat lower than this value because thermal expansion coefficient is closely related to the oscillation of phonon, while the intensity of thermal oscillation becomes weaker as temperature decreases, leading to a lower CTE [250]. As a consequence, the HA nanorod shaped particles are clamped more tightly within hydrocarbon matrix at 77 K than HRG00, resulting in higher compressive strength at 77 K than that as such freeze casted scaffold. The hydrogen bond in HRG scaffold becomes stronger at 77 K due to the shorter bond length caused by thermal shrinkage. The free spaces and free volumes in the cured scaffold smaller at 77 K due to thermal shrinkage, which contributes to increase intermolecular force and higher strength at 77 K compared to the as – fabricated scaffold.

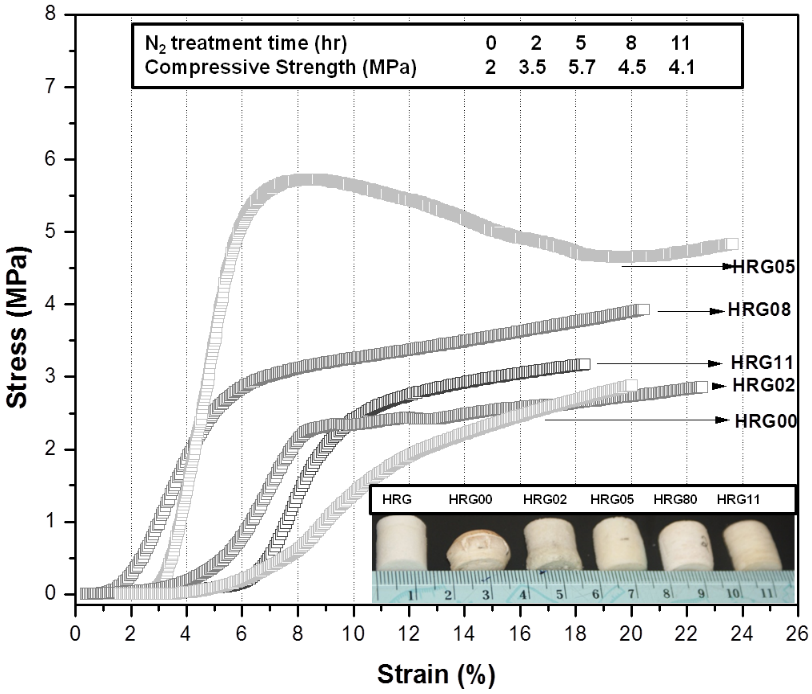

Figure 4.38 Stress – strain behavior of freeze casted and liquid nitrogen treated scaffolds.

4.5.3 Phase study of cryo-treated scaffold

X-ray analysis of the HRG00 scaffold and HRG05 are shown in Figure 4.39. HA peaks are identified by referring the JCPDS file (74-0565). Cryogenic treatment alters the peak intensity of hexagonal hydroxyapatite gelatin composite. The polymeric matrix of HA scaffold undergoes crystallized during cryogenic curing of HA-gelatin scaffold. Decrease in the crystallinity of the HA peaks after treatment with 5h in liquid nitrogen resulted is associate with the increase in the crystallinity of the polymeric matrix [251]. XRD analysis confirms that polymers present in the HA scaffold under a goes transformation of ductile behavior to brittle nature by inducing internal stress [252].

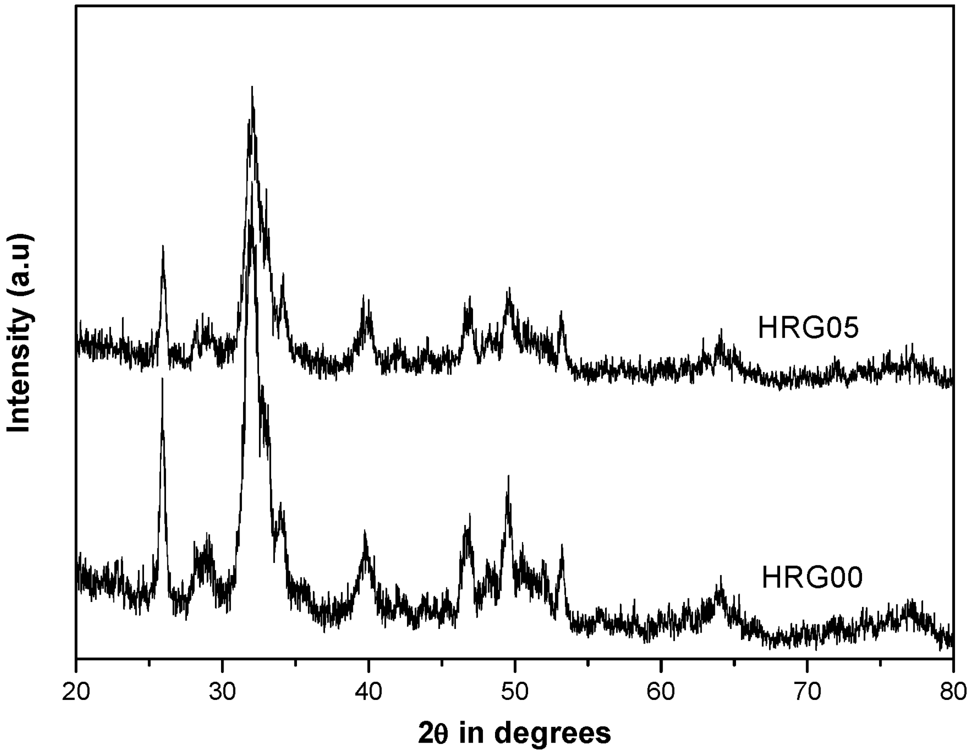

Figure 4.39 XRD analysis of HA scaffold and N_2 treated scaffold.

4.5.4 SEM microstructure of cryo-treated scaffolds

Hydroxyapatite nanorod ~8 nm diameter and 20 – 50 nm length powder (see Figure 4.9) has been used for the fabrication of HA-gelatin scaffold. Original (HRG00) and liquid nitrogen treated specifically 5h treated porous scaffolds are critically characterized to understand the pore morphology and their size distribution. Figure 4.40(A) illustrates the morphology of original scaffold with existence of average pore size 140 µm and transverse interconnected tiny pores. The pore shape, morphology and interconnectivity nature of the scaffold depends on the freezing point of solvent, reactivity within organic molecules, growth direction of ice crystals and temperature gradient during freeze drying [253]. Inset represents the development of ~2 µm interconnected pores along the hydrocarbon pore wall. The generations of such tiny micro pores are due to the gelation of gelatin [254]. The temperature gradient at the interface between solid HA and liquid phase is caused the formation of many small ice crystals, which is expected to increase much internal stress and porosity in the cryogenic environment. Figure 4.40(B) represents the SEM image for HRG05 scaffold, where inset indicates the initiation of web of microcracks within hydrocarbon matrix due to adaptation of bonding characteristics, shrinkage and internal stress in scaffold. The diameter and pore struts have also been changed and expected to have an effect on the size distribution. The cumulative porosity increases from 75 vol.% to 80 vol.% when scaffold treated for 5h, however, beyond this critical aging, the porosity and their distribution behavior changes abruptly due to the propagation of fine microcracks along the hydrocarbon matrix. The intensity of HA phase crystallinity in HRG00 suppresses with compare to HRG05 scaffold, which is because of the rapid esterification and intermolecular hydrogen bonding within – COOH of gelatin and – OH of PVA and their cross linking in hydrocarbon matrix. The C – H, C – O and O – H bond length becomes stronger at 77 K due to the shorter bond length caused by low temperature thermal shrinkage [255]. This phenomenon is also further confirmed by FT-IR analysis of HRG00 and HRG05 scaffolds.

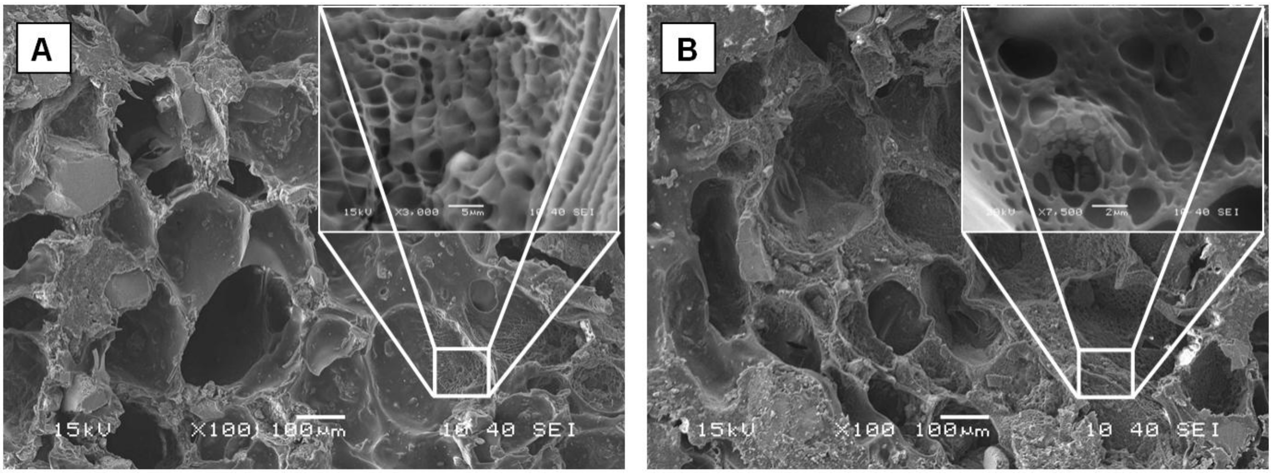

Figure 4.40 Scanning microscopic image of (A) freeze casted HA nanorods – gelatin scaffold and (B) liquid nitrogen treated scaffolds for 5h. Inset represents the behavior of micro pores in the pore wall, before and after liquid nitrogen treated scaffolds.

Morphologies of the other two HGS and HGF scaffolds after 5h cryo-treatment are represented in Figure 4.41. The open pore structure of the HGS scaffold along with circular in shape and the average pore diameter are found ~ 170 µm (Figure 4.41 (A)) whereas 5h cryo-treated scaffold (Figure 4.41(B)) shows higher average pore diameter that resulted due to the shrinkage and the polymeric conversion of ductile to brittle. In-addition the HGF scaffold shows open circular pores with the average pore diameter ~180 µm (Figure 4.41(C)) whereas its liquid nitrogen treated sample shows higher pore diameter with connected pores (Figure 4.41(D)). Thus, liquid nitrogen treated scaffold shows higher pore diameter with the interconnected pore morphologies. Polymer matrix more crystallizes and brittle after cryogenic treatment as revealed by XRD analysis. In cryogenic environment, the polymer matrix present in the strut of the pore is more crystallized and brittle [143].

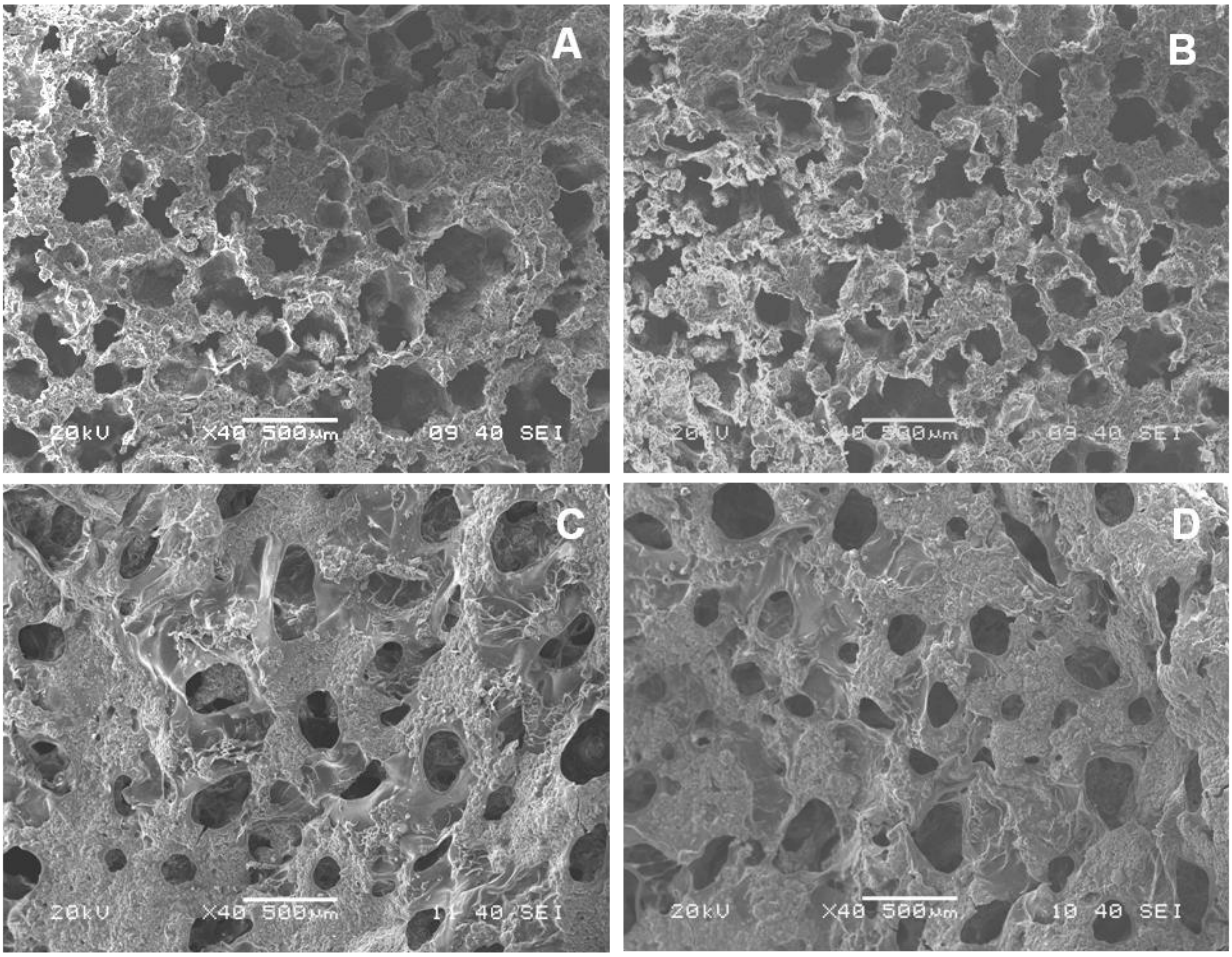

Figure 4.41 SEM microstructure of HA scaffolds, (A), (C) as freeze dried and (B), (D) 5h cryo-treated scaffolds HGS and HGF respectively.

4.5.5 Mercury pore size distribution of cryo-treated scaffold

Pore size distribution of 5h cryo-treated HA-gelatin scaffolds is represented in Figure 4.42. Pore size distribution of the HSG scaffold results monomodal distribution with average pore diameter ~ 90 µm and porosity of around ~ 82% (Figure 4.42(a)). Figure 4.42(b) shows the broad multimodal pore size distribution with average pore diameter ~85 µm and porosity ~ 78% resulted for HRG scaffold. HFG scaffold has narrow and intense multimodal pore size distribution with average pore diameter ~ 110 µm along with micron range pores of ~0.01-0.1 µm size and cumulative 85% porosity. Pores are well distributed in fibroid morphology, whereas for HSG and HRG scaffold shows a gradient of pores. In liquid nitrogen, the scaffold has higher porosity and pore size distribution is shifted to higher pore diameter compared to the as freeze dried HA gelatin scaffold.

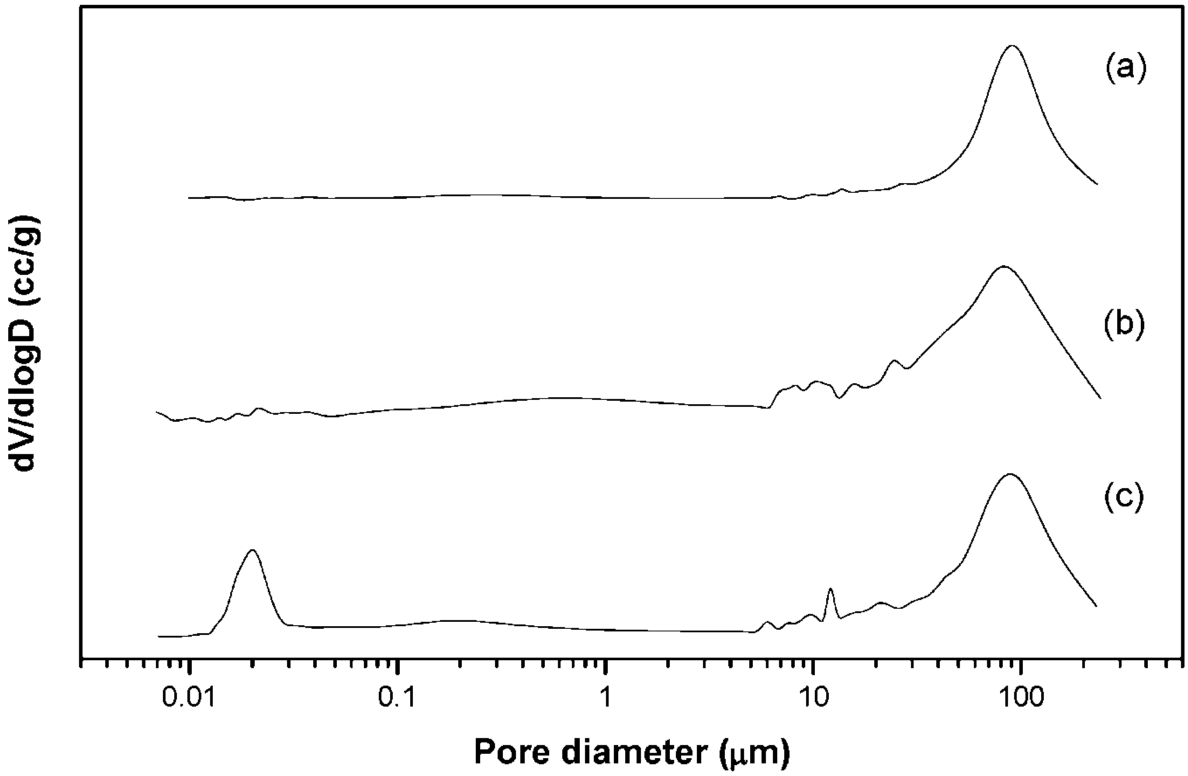

Figure 4.42 Pore size distribution of N_2 treated HA scaffold (a) HSG05, (b) HRG05 and (c) HRF05.

Table 4.10 Pore size before and after cryogenic treatment of as obtained from both SEM and mercury porosimetric observation

HA-Gelatin Scaffold	Freeze casted (-52°C)			Cryotreated scaffold (-192°C)		
HRG	Pore size (μm) SEM	Pore size (μm) Hg-Porosimetry	Pore Volume (%)	Pore size (μm) SEM	Pore size (μm) Hg-Porosimetry	Pore Volume (%)
	140	70	75	160	90	80

Pore size and pore volume of as-freeze casted and 5h cryotreated HA-gelatin scaffold is shown in Table 4.10. Different pore size, pore content and pore morphologies are influenced by the HA solid content, gelatin and PVA molecular interaction phenomena during freeze casting process and cryotreatment, which is revealed by SEM microstructure and mercury porosimeter data. Tiny closed pores are difficult to encounter through SEM microstructure, but mercury porosimeter evaluates all range of open and closed pores diameter (0.1 – 200 μm) and cumulative pore size shifted to lower region. In the same time, the liquid nitrogen temperature shrinks the polymer matrix which enhances the ~15% pore size and ~5% pore volume. However, the cryotreated scaffold exhibits a high degree of compressive strength because of strong polymer–ceramic interaction assisted by the negative coefficient of thermal expansion at 77 K [142].

4.5.6 Mechanical behaviour of different cryo-treated HA scaffolds

HA-gelatin scaffold under liquid nitrogen environment shows the higher mechanical properties compared with the untreated HA scaffold. The stress-strain behaviour of the liquid nitrogen treated scaffolds is shown in Figure 4.43. The stain rate 5% is observed for both HGS05 and HGR05, whereas 7% strain is observed in HGF05 scaffold. Low strain rate and high compressive strength reveals that the scaffold has brittle nature. The brittle nature results due to the polymer gelatin and PVA present in the fabricated scaffold. Yang et al. [141] prepared polymers (epoxy) nanocomposite and observed the significant improvement of mechanical properties of composite at the cryogenic temperature (77 K). In addition, Chen et al. [142] also reported that cryogenic tensile strength, young's modulus, ductility and impact strength are significantly increased at the cryogenic environment and stronger interfacial bonding in the material at 77 K as compared to RT.

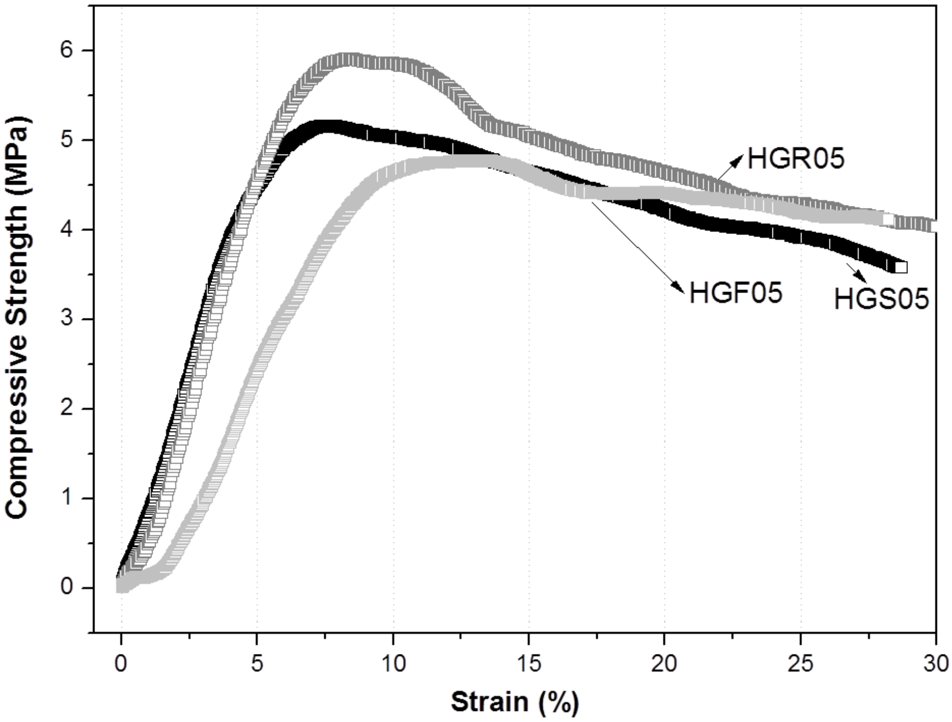

Figure 4.43 Stress-strain behavior of 5 h N_2 treated HA scaffold.

The study of compressive strength of the scaffold with variation of the soaking time inside liquid nitrogen is represented in Figure 4.44. Compression strength of the scaffolds shows highest at 5h for any HA-gelatin scaffolds then after strength is further reduced due to the microcracking under internal stress within the polymeric matrix.

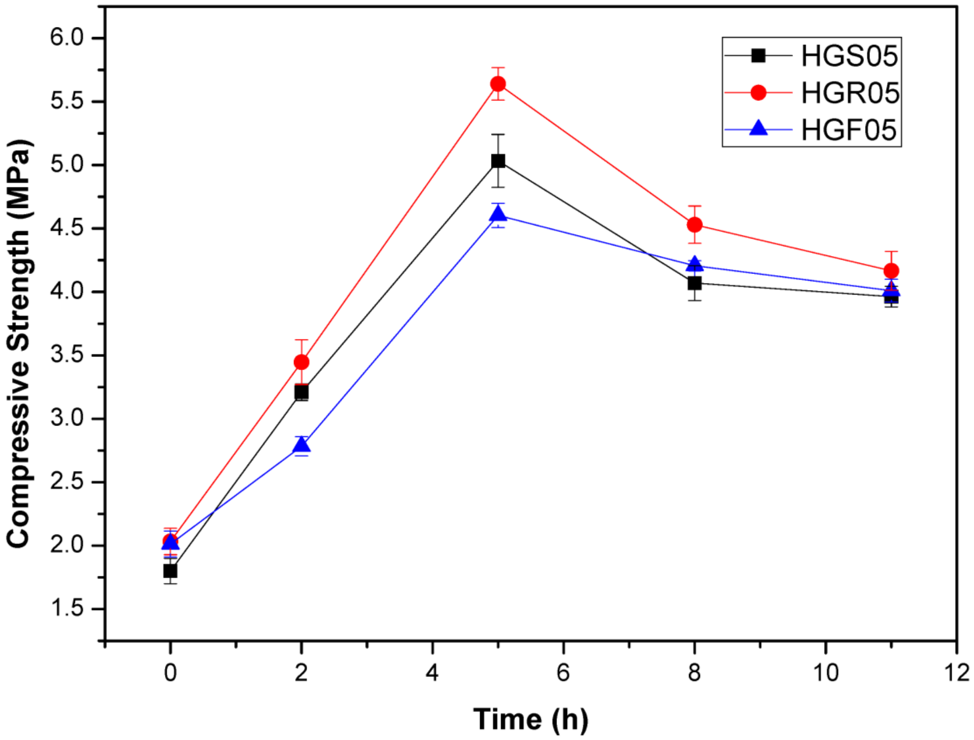

Figure 4.44 Compressive strength of the scaffold with varying the soaking time in liquid N_2.

4.5.7 Fracture behaviour of cryo-treated scaffold

The facture behaviour of the scaffolds under compression is shown in Figure 4.45. Longer curing in liquid nitrogen insists catastrophic fractured in the scaffolds. The result shows that the formation of zigzag microcracks around the outer edge of the HGS scaffolds (Figure 4.45(A)). The fracture behaviour of the HGR scaffold indicates that higher in the brittle nature scaffold. Longer uni-directional fracture is observed in the HGR scaffold (Figure 4.45(B)) because of the highest ductile–brittle transition and higher crystallinity of the scaffold. The temperature gradient in liquid nitrogen changes the internal stress and cluster of microcracks which finally changes the pore morphology of HGF scaffolds. Furthermore, this nature of change in the fracture behavior of different morphology of HA and hydrocarbon matrix strengthening are responsible for the transition of ductile to brittle transformation, which has a significant effect on ultimate room temperature mechanical properties of such porous scaffolds.

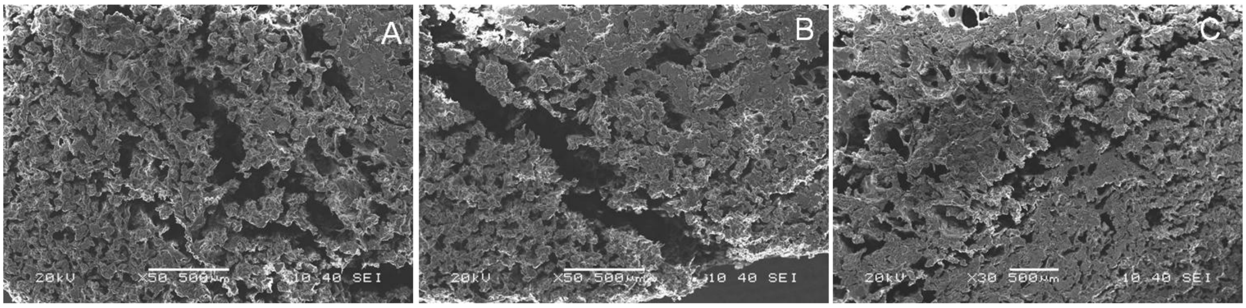

Figure 4.45 Fracture behavior of N_2 treated scaffold under compression (A) HSG05, (B) HGR05 and (C) HGF05.

4.5.8 Machining of the cryo-treated scaffold

A macroscopic view of cryotreated HA-gelatin scaffold is shown in Figure 4.46. Machining of the HA-gelatin scaffold samples is done through precision lathe machine. Figure 4.46(B) shows the drilled (cantered) as well as machined whereas machined HA-gelatin scaffold is represented in Figure 4.46 (C). Such a scaffold has an excellent machinability as exhibited by turning or drilling performance. These cylindrical shaped scaffolds of various sizes can be produced in a reproducible manner using the adopted fabrication route. In particular, the scaffolds with length of up to 100 mm and diameter of up to 20 mm can be conveniently prepared in this adopted method. Thus, the developed HA-gelatin scaffold support easy machinability which will assist for the selection any complicated shape as a placement of cancellous bone and tissue engineering.

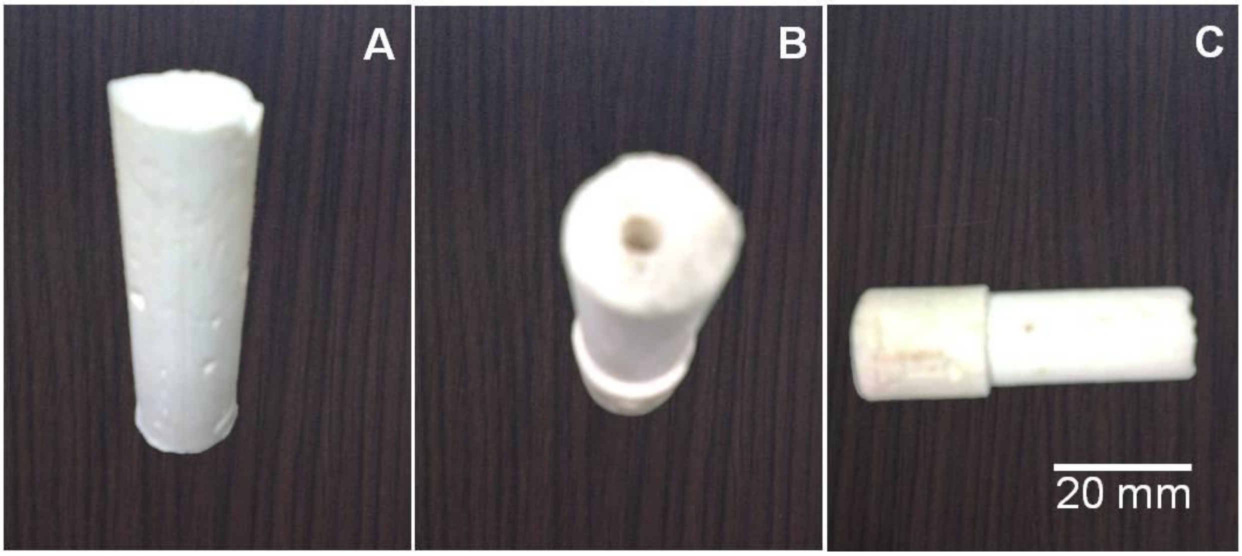

Figure 4.46 Images of freeze dried and subsequent cryotreated (A), centred drilled (B) and machined scaffold (C).

4.5.9 Conclusion

Cryogenic temperature has a significant impact to enhance the compressive strength. A prerequisite optimum 5h cryotreatment is needed to achieve a highest strength of such high porous scaffolds. The cryotreated scaffolds have a high degree of compressive strength 5.8 MPa, volume porosity ~80% and 160 µm average pore diameter in comparison of counterpart freeze casted scaffold. At cryogenic environment, polymeric matrix undergoes phase transformation from ductile to brittle nature, which results for the higher the compressive strength, higher the porosity and the pore diameter in the scaffold shifted to higher region. Bond characteristics and crystallinity of hydrocarbon matrix have influence on the compressive strength of a porous scaffold. Excessive time reduces the strength of scaffolds, because of mismatch thermal expansion, results internal stress and spontaneous failure. High porous and reasonable compressive strength of the scaffold could be considered as a suitable candidate for the bone tissue engineering, formation of neocartilage and growth of osteoblast cells.

4.6 Bioactivity, biodegradability and cytotoxicity of CHAMPS

The concept of bioactivity and biocompatibility, associated with a set of *in vitro* standardized tests, is introduced in order to assess the biological behaviour of synthetic scaffold materials. When synthetic materials are first used in biomedical applications, the only requirement is considered to achieve a suitable combination of physical properties to match those of the replaced tissue with minimal toxic response of the host. Bioactivity is the ability to interact in a biological environment to enhance the biological response, tissue/surface bonding and bioresorption through progressive degradation while new tissue regenerates and heals [178,256]. Evaluation of *in vitro* bioactivity of bioceramic scaffolds is to evaluate the apatite-formation ability of the scaffold in the SBF solution, and the other is to investigate *in vitro* bone cell response to scaffold [257,258]. Biomaterials combining biodegradability and bioactivity, once implanted, will help the body to heal itself. Details knowledge on bond and sustain capability within living bone and host material is mandatory to develop new bioactive ceramics for load bearing bone repair applications. Here in, *in vitro* bioactivity of scaffolds are evaluated through SBF solution whereas biodegradation has been studied in Tris-HCl solution. *In vitro* cytotoxicity and cell viability is analysed using L929 mouse fibroblast cells.

4.6.1 *In vitro* bioactivity

In vitro bioactivities of the fabricated cryo-treated HA-gelatin micro/macro porous scaffold (CHAMPS) is determined after incubation for a different period in simulated body fluid (SBF) solution at the temperature of 37 ^{o}C and pH ~ 7.4. The incubation period has a significant effect on the formation and deposition of apatite on porous scaffolds, which are represented in Figure 4.47. Interesting to note that the apatite particles concentration in presence of SBF is gradually increasing with time and preferably deposited around the porous region compare to continuous matrix of scaffolds. A comparative look within time dependent SBF treated scaffold reveals that most of the area is covered by apatite layer after 168h treatment and further confirmed by SEM/EDAX and FT-IR analysis. Spherical deposition is likely to be beginning around the pore wall and the pore struts. It has been observed that apatite deposition starts on the site, where the scaffold has higher porosity with well interconnected pores. The spherical deposition of apatite layer on the surface of the scaffold cross checked through EDAX of the SBF soaked HA scaffold. Combination of SEM and EDAX study confirms the bioaccessibility of the scaffold. In addition, nucleation of the apatite on HA scaffold as analysed through FT-IR is shown in Figure 4.48. The characteristic of carbonate bands is observed at wavenumbers 1640 cm^{-1} and 1493 cm^{-1}, respectively.

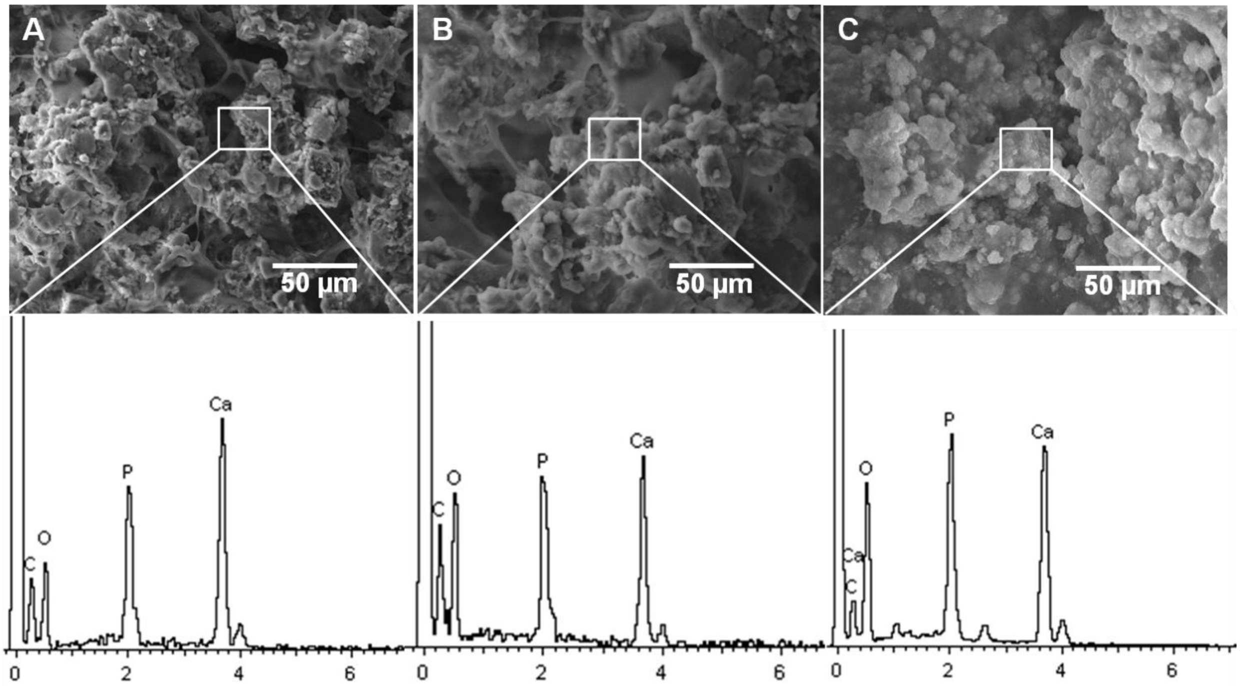

Figure 4.47 Apatite nucleation on the CHAMPS in SBF solution associated with EDX (A) 1 day, (B) 3 days and (C) 7 days.

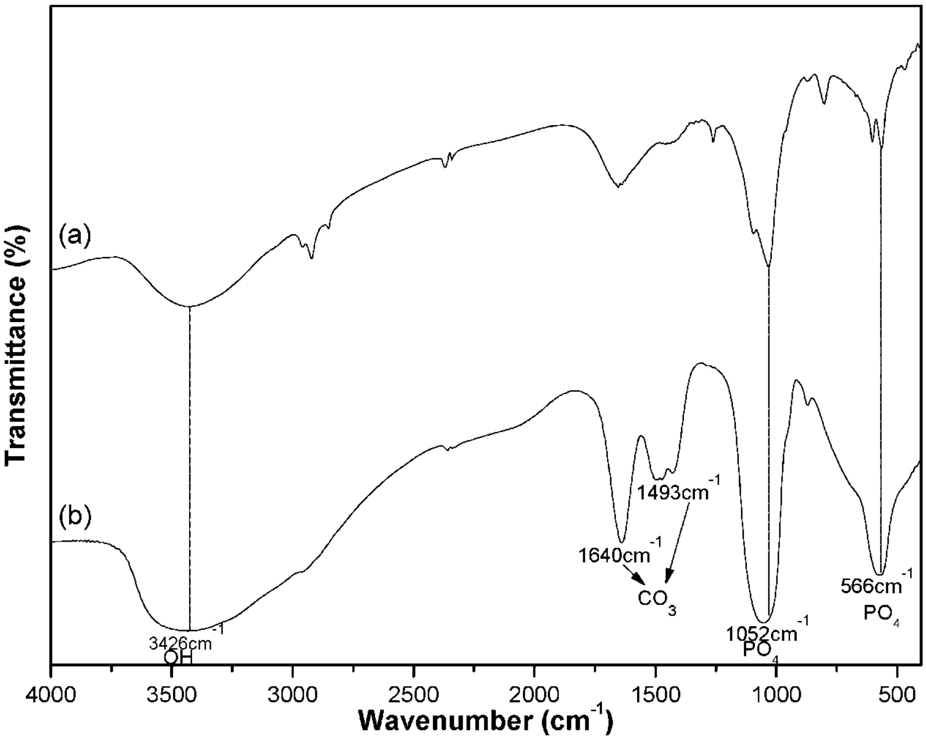

Figure 4.48 FT-IR analysis of SBF treated HA-gelatin scaffold (a) before SBF trearment and (b) after 7 days in SBF.

4.6.2 *In vitro* biodegradability

Figure 4.49 shows the biodegradation study of fabricated CHAMPS in Tris-HCl buffer solution at 37 °C and pH~7.4, where maximum 25 wt.% degradation is recorded for 7 days. The initial plateau exhibits very slow rate of degradation up to 3 days, but enhances up to 7 days and thereafter, follows steady state behaviour. A higher degradation of the scaffold is due to the release of polymeric small chains. Martinez-Valencia et al. [150] reveals a weight loss of 4% of the HA-polyurethane biocomposite scaffold for an incubation time of 56 days in tris-buffer solution pH~7.4. Similarly, Gou et al. [156] measured biodegradation up to 36 wt.% of calcium deficient HA scaffold after 12 week in tris-HCl solution. However, surface engineering or polymer modification can enhance the biocompatibity, cell proliferation and low biodegradation for futuristic tissue engineering application.

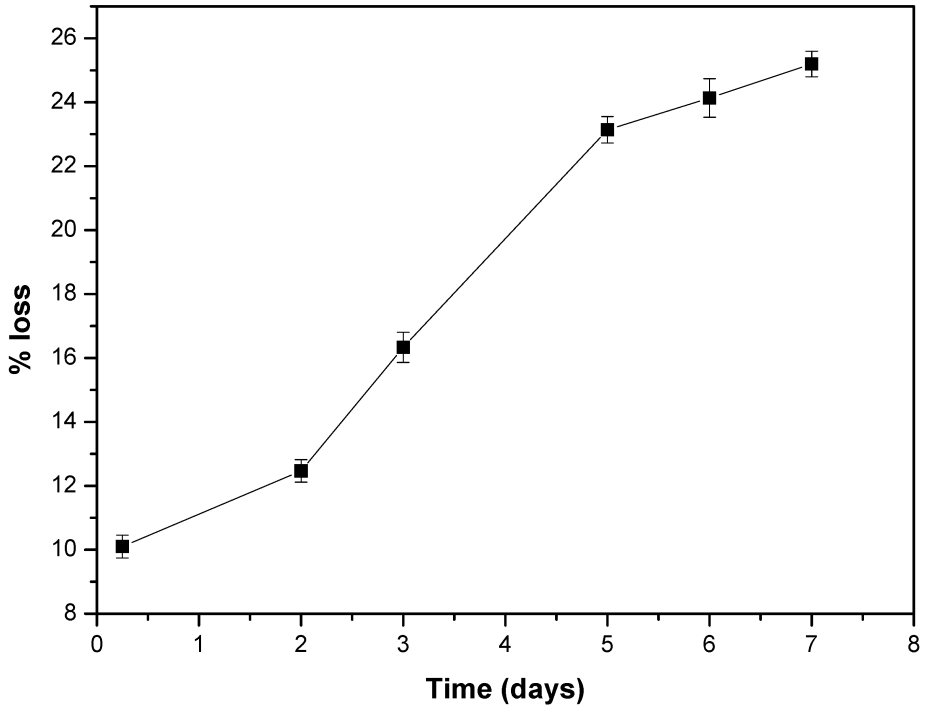

Figure 4.49 Biodegradation of CHAMPS studied as function of time.

4.6.3 Cytotoxicity of CHAMPS

In vitro cytotoxicity assessment of HA scaffolds carried out direct contact of L929 mouse fibroblast cells is represented in Figure 4.50. The cytotoxicity of the scaffold evaluated with following the ISO-10993-5 [180]. The test result performed on the extract of the HA scaffold exhibits spindle morphology characteristic of mouse fibroblast cell line and is analysed compared with the negative control (high density polyethylene) and positive control (stabilized PVC disc). The cell density on the negative control is very similar to the fibroblast-like morphology with cell-to-cell contact and filopodia extension as shown in Figure 4.50(A). In contrast, the L929 cells undergo apoptosis and necrosis on positive control revealing severs toxicity as represented in Figure 4.50(B). Similar to the positive control, the spindle shaped L929 cells are found to adhere and expands on HA-gelatin scaffold (Figure 4.50(C)). The fraction of globular shaped is similar on both positive control and CHAMPS. Apart from the reason, like the intrinsic characteristic of the used cells lines at specific passage, the observation of the globular shaped L929 cells can be the result of initial degradation rate of the HA-gelatin scaffold and the release of the polymeric small chains. The result of the cytotoxicity test reveals that the extract of the HA scaffold does not affect the cell viability and proliferation. Oliveira et al. [152] reveals fibroblast cells (L929) partially proliferated after prolong 72 h seeding on HA scaffold. After 24 h of contact, an almost confluent monolayer cell lines are observed, where improved proliferation with good morphology of the cells maintained. The results obtained by the extraction method indicate the viability and proliferation of L929 fibroblasts, clarified the well documented biocompatibility of the HA scaffold.

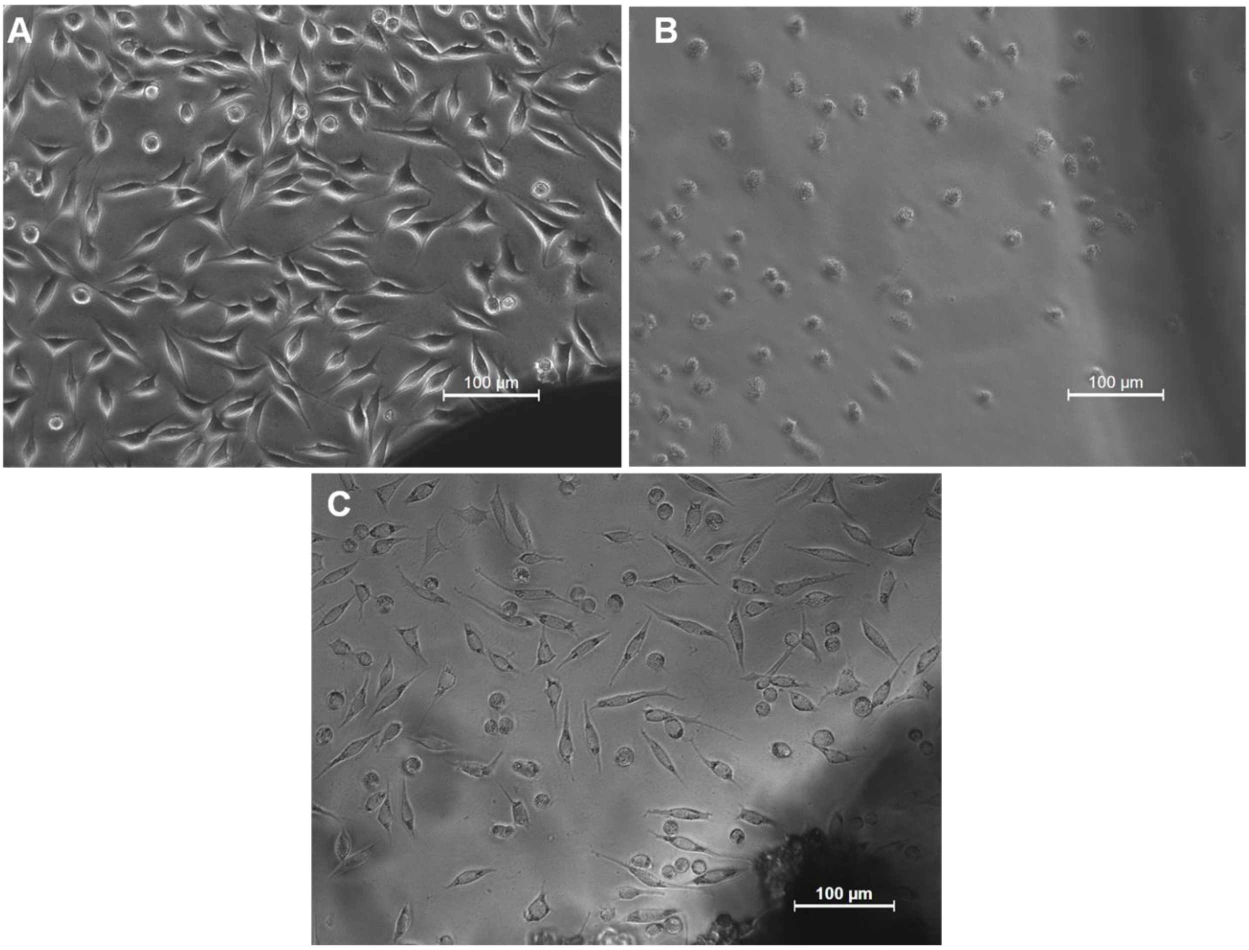

Figure 4.50 Fluorescence microscopic image revealing the adhesion of cultured L929 cells after one day of incubation: (A) negative control, (B) positive control and (C) CHAMPS.

4.6.4 MTT assay of CHAMPS

Metabolic activity of cells has been studied through MTT assay using mouse fibroblast cells and the difference in the cell viability index as shown in Figure 4.51. The cell viability and proliferation of the HA scaffold samples at different concentration is evaluated by compared to the controlled tissue culture plate. The MTT Assay of L929 cells after contacts with HA scaffold extract shows 40% metabolic activity. The amount of formazan produced is directly proportional to the number of mitochondrially active cells [259]. Clearly, the MTT assay results reveal that the metabolic activity of L929 cells decreases with the increase in the extract concentration of HA-gelatin scaffold *in vitro*, as shown in Figure 4.51. As far as the quantification of cells viability is concerned, 90% of the cells are viable on negative control and less than 10% cells on positive control. It is important to mention that at the HA-gelatin scaffold extract concentration at 12.5% and 25%, more than the 70 % of the cells are mitochondrially viable. Although significant decrease in cell viability at 100% extract is recorded, at least four times on larger cells population are mitochondrially active than compared to positive control. In contrast with 100% concentration compared that on positive control. Oliveira et al.[152] measured 90% L929 cells viability at 25% extract concentration on HA scaffold through MTT assay. The aforementioned study and relevant data confirms the cytocompatibility of HA-gelatin scaffold with L929 fibroblasts cell. The scaffold surfaces are able to support cell proliferation because of the metabolic activity, shows a good indication to the futuristic application.

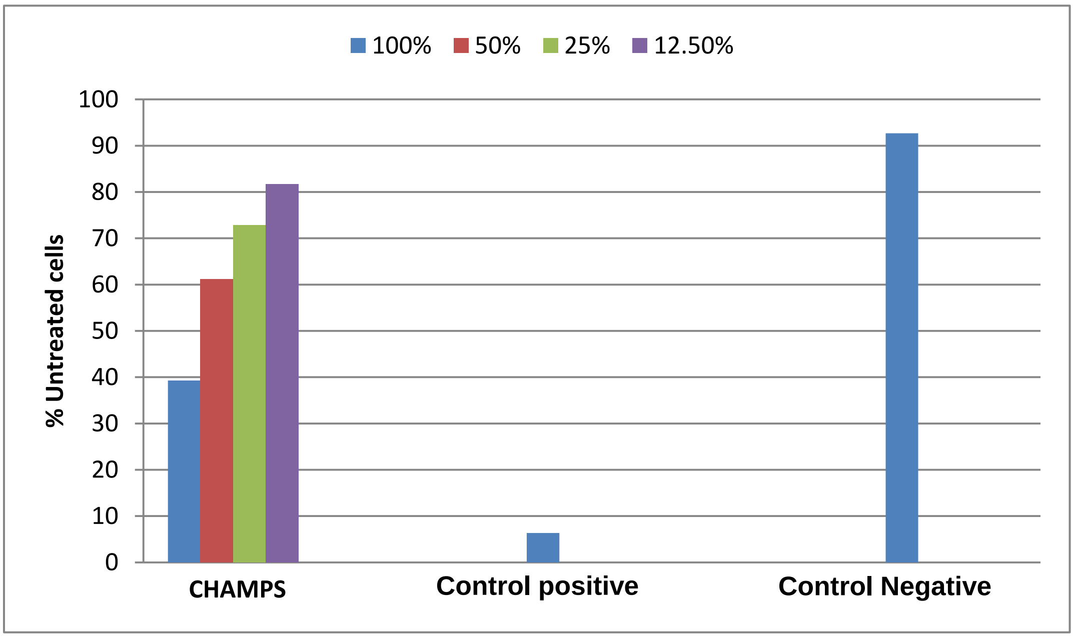

Figure 4.51 MTT Assay results of various extracts of CHAMPS scaffold along with control.

4.6.5 Conclusion

In vitro bio-assessment of the scaffold reveals about the deposition of apatite layers on the surface of the scaffold and apatite layer is completely covered in 7 days. The carbonated apatite layer has been nucleated within SBF solution and confirmed by FT-IR. Also, the biodegradation of scaffolds in tris-HCl solution exhibits a slow but systematic increase in weight loss over an incubation period up to 7 days. Spindle shaped L929 fibroblast cells are observed in the direct contact on the scaffold. Although higher extract concentration of CHAMPS induces toxicity to L929 cells in a statistically significant manner compared to positive /negative controls, lower extract concentration up to 25% does not cause a reduction in L929 cell viability. When compared to a negative control, the reduction in cell viability has been tentatively explained as a result of the release of small polymeric chains.

4.7 BSA adsorption and release on CHAMPS

Bovine serum albumin (BSA) has received significant attention to reduce the dissolution of synthetic HA, as well as enamel demineralization *in vitro* [260,261]. Thus, porous HA scaffold is considered as a potential delivery media for protein drugs, which could improve the transportation mechanism and protect the drug against inactivation, degradation and metabolization phenomena [262,263]. BSA protein is considered as model protein for the study of adsorption and release on HA-gelatin scaffold [264]. Hence, the assessment of protein interaction with a scaffold is of significance for tissue engineering. Keeping this in view, different *in vitro* analysis such as adsorption/release of BSA protein and an attempt has been made to correlate between structure and properties CHAMPS. In order to characterize both quantitative and qualitative pore architecture, micro computed tomography (micro-CT) technique is being used extensively for protein-loaded and as-fabricated HA-gelatin based porous nanobiocomposite scaffolds. Although some aspects of the gelatin/HA scaffold are studied from the perspective of the biomedical applications as also summarized above, the use of micro-CT to effectively characterization of the pore morphology/distribution has not been made in any of the previous studies. Therefore, the internal porous architecture of complex nature that one can achieve in such scaffolds after cryogenic treatment is also not being realized. The present study, therefore, provides the first set of micro-CT results on this aspect. It is expected that such results will open up various possibilities for further study to probe into the potentiality different biomedical applications.

4.7.1 Adsorption study of BSA on CHAMPS

The results of UV-Visible absorption study on CHAMPS are plotted in Figure 4.52, where maximum absorbance of standard BSA protein is measured at the wavelength A_{max} ~562 nm. The peak position of maximum absorbance is gradually shifted towards higher wavelength for absorption of beyond 48h. Figure 4.53 represents the time profile adsorption behaviour of BSA on CHAMPS as calculated using a predetermined standard concentration – intensity calibration curve [265]. Initial adsorption of BSA on the porous surface of HA rapidly increases and then follows a steady rate. In this study, the strong adsorption phenomena of BSA on HA can be attributed to the electrostatic interaction between Ca^{+2} cation and PO_4^{3-} anion of HA with COO^- anion and NH_3^+ cation of BSA protein, respectively [266]. BSA adsorption phenomenon is rapid due to the hydrophobicity of the scaffold surface, which attain a steady state after 48h incubation. Under this circumstance, the CHAMPS adsorbs highest amount of 51 mg protein per gram of scaffold.

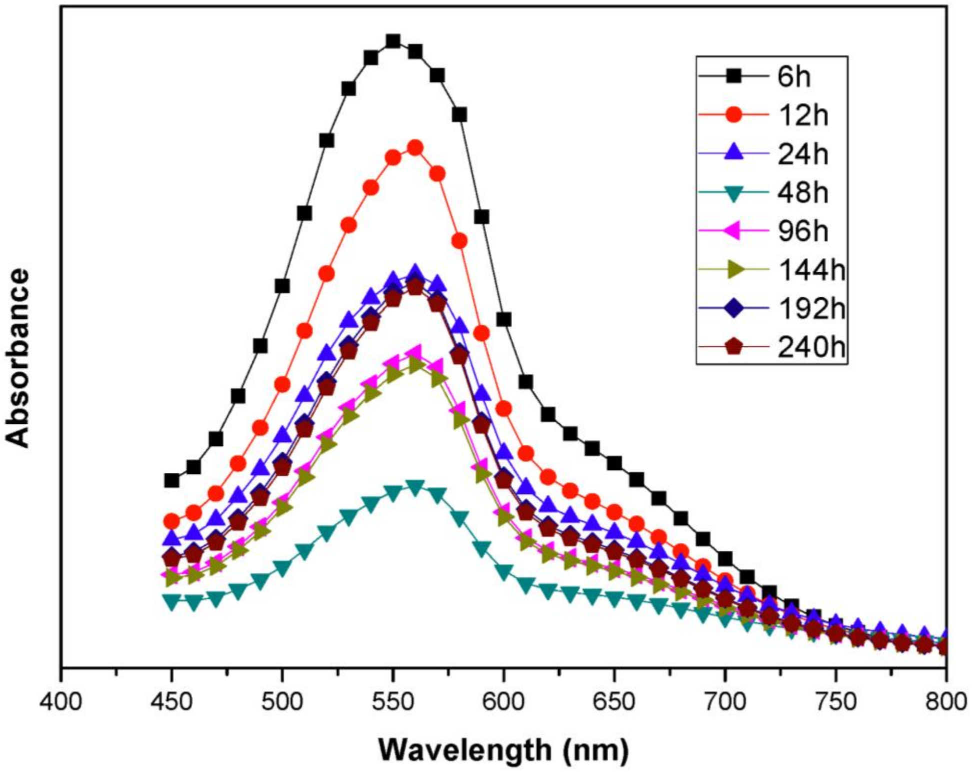

Figure 4.52 Analysis of maximum absorbance of adsorbed BSA on CHAMPS with time.

Adsorption isotherm of BSA on HA scaffold is shown in Figure 4.54. Interestingly, the BSA adsorption isotherm followed Langmuir isotherm and monolayer adsorption behaviour [267]. The maximum adsorption capacity is estimated from standard Langmuir equation: $q = [q_{max}C_e / [(1/a_L) + C_e]]$; where, q= amount of BSA adsorbed on HA scaffold (mg/g), q_{max} = maximum adsorption capacity (51.3 mg/g), C_e= BSA concentration in solution at equilibrium, a_L = Langmuir constant (0.213 ml/mg) and correlation factor (R^2) ~0.9902. Kim et al.[268] demonstrated the BSA adsorption on collagen derived HA-gelatin nanocomposite occurs at relatively much faster rate of within 24h. In case of chitosan-gelatin scaffold, the BSA adsorption occurs only after prolong time scale and typically reached a steady state over a period of 15 days [269]. The present study confirms that relatively faster adsorption behaviour of BSA proteins in CHAMPS scaffold occurs within 48h, although the time scale for the attainment for the steady state BSA adsorption is little longer than that reported in another related study [268].

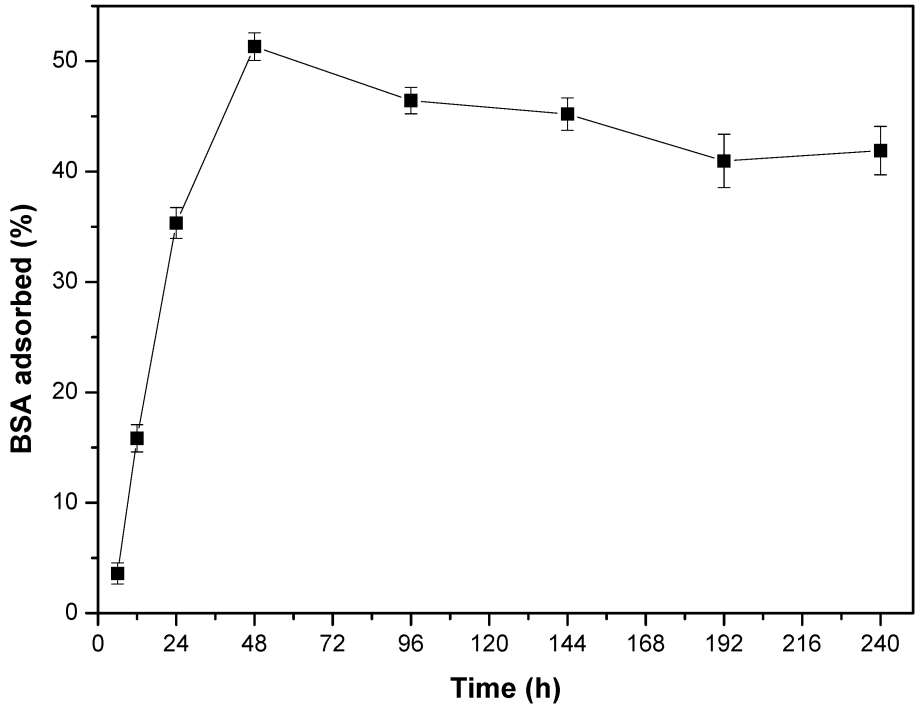

Figure 4.53 Amount of BSA adsorbed on CHAMPS with time.

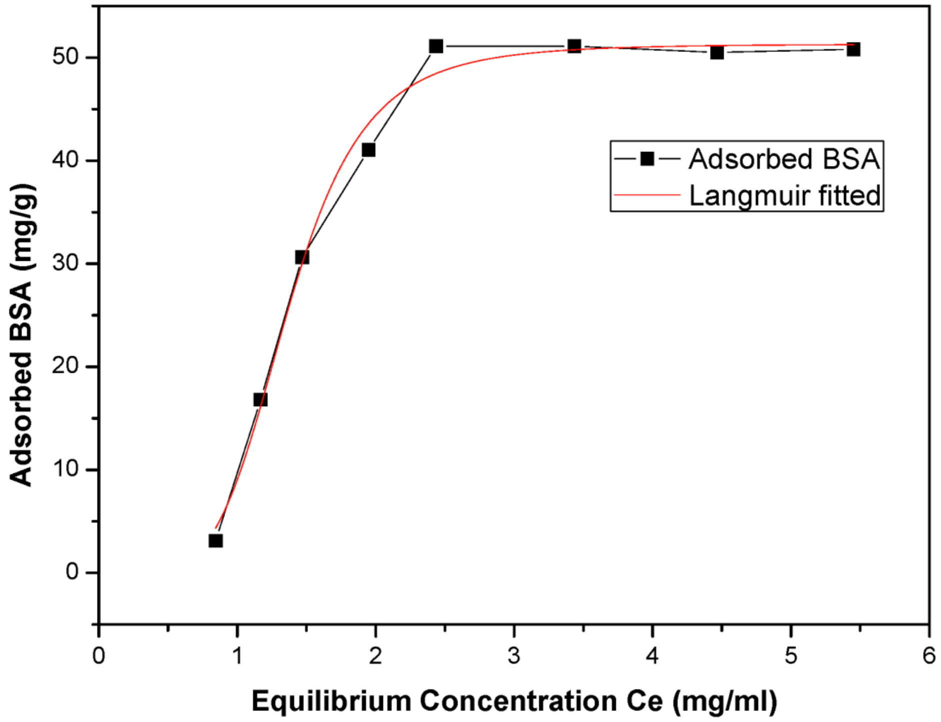

Figure 4.54 Adsorption isotherm of BSA on CHAMPS.

4.7.2 Microstructure after BSA protein adsorption

The CHAMPS adsorbs highest amount of BSA protein after 48h incubation, and they are further considered for microscopic analysis. Figure 4.55 represents the scanning electron microscopic image of CHAMPS scaffold after BSA protein adsorption. Overall, the spreading of proteins on

CHAMPS surface can be clearly seen. The adsorbed protein form a well spread sheet like structure and reflects good ability of CHAMPS scaffold to adsorb BSA protein. Hence, it is expected that the interconnected and highly porous scaffold surface adsorb more biomacromolecules as compared to relatively dense surface. The interconnected porous microstructure of the fabricated scaffold would support for the attachment of BSA through its pore walls. Interaction of BSA with porous HA is likely to be the electrostatic interaction, and it occurs on the pore surface [157]. Fabricated scaffold has hydrophobic surfaces, which interact with the hydrophobic surface of the water soluble BSA protein surfaces. The hydrophobic-hydrophobic surface has greater interaction between protein and porous HA as compared to the hydrophobic-hydrophilic surface interactions [270]. Thus the interaction between protein and porous HA is hydrophobic-hydrophobic, and their conjugate has moderate bonding interaction.

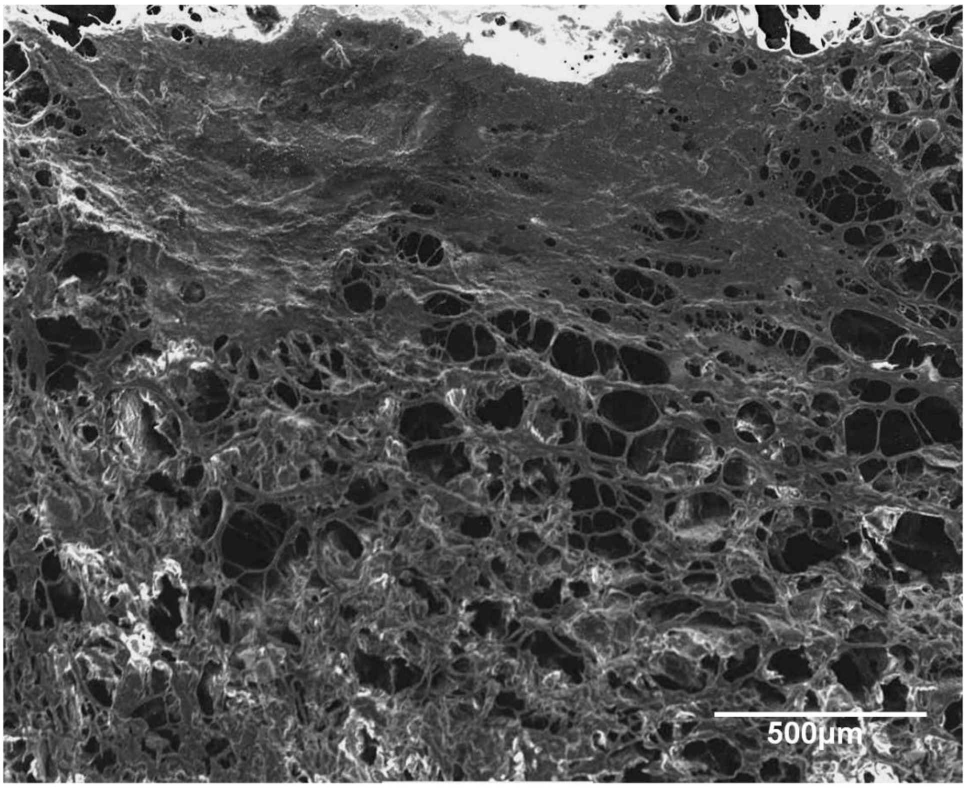

Figure 4.55 Typical SEM image after BSA protein absorption on CHAMPS.

4.7.3 Micro-CT scan analysis for CHAMPS and BSA protein loaded CHAMPS

In order to quantitatively and qualitatively characterize the pore architecture, micro computed tomography (micro-CT) technique is used extensively for protein-loaded and as-fabricated gelatin–HA based porous nanobiocomposite scaffolds. The critical analysis of micro CT results are carried out in terms of the strut thickness, pore size distribution and pore volume distribution across the entire three dimensional space of the nano HA/ gelatin scaffold, before and after protein adsorption experiments. As far as the total open porosity is concerned, the protein adsorption importantly increases the volume percent of open porosity from 63.5% to 71.8%. The amount of closed porosity in both the cases is less than 0.1%. It is clear that the protein adsorption makes the scaffold more porous, and this will definitely enhance the cell adhesion and proliferation. This is clear from the 2D slices presented in Figure 4.56. The homogeneous 2D spatial distribution of HA nanoparticles has been recorded in Figure 4.56(a). After protein loading, the available pore spaces become much finer and more interconnected in Figure 4.56(b).

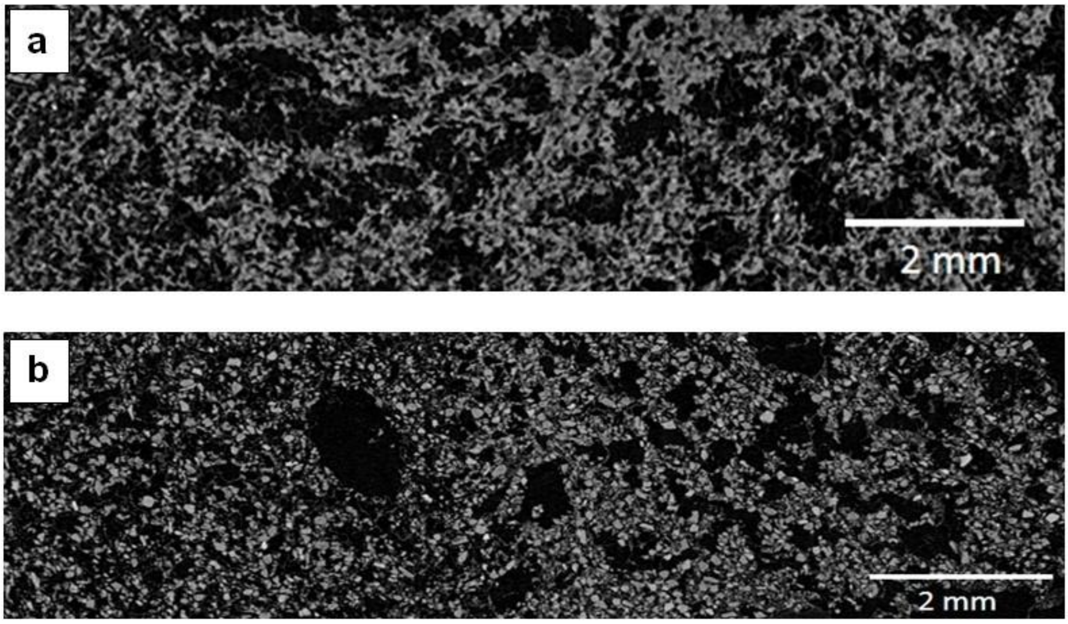

Figure 4.56 Representative 2D micro-CT slice showing the distribution of the solid volume (HA nanoparticles in 'a' and/or protein macromolecule in 'b') of CHAMPS (a) and BSA loaded CHAMPS (b). The brighter contrast indicates distribution of solid elements and darker region indicates low density gelatin matrix.

From several hundred such 2D slices, the pore size, pore wall thickness, pore interconnectivity, together with other parameters to describe the pore architecture are being measured. These results are plotted in Figure 4.57. The Gaussian fitting of the measured pore wall thickness data reveals a peak in distribution around 40 micron in the as processed scaffold, which is shifted to 20 micron in the BSA protein loaded scaffold (see Figure 4.57(b)). The overall shift of the pore wall thickness distribution towards left essentially reveals favorable protein absorption on the pore wall surfaces in a homogeneous manner. Also, the fact that the majority of the pores have pore wall thickness of around 40 to 50 micron reveals that such pores can support the ingrowth of biological tissues neobone. Hence, in terms of more quantification of pore size analysis, the distribution in pore sizes obtained from extensive analysis of the entire 3-D scaffold for as-synthesized and protein loaded HA/ gelatin scaffolds are presented in Figure 4.58. While the shape of the curve is qualitatively similar, the peak of the curve is shifted more towards left after the protein loading. From the peak of the curve, it can be said that the average porosity in the structure is around 40 µm and around 28 µm in the as synthesized and protein loaded HA/ gelatin scaffolds, respectively. The extended tail in the pore size distribution curve essentially indicates the presence of inhomogeneous pore size distribution with the presence of pores as large as 100 µm or larger (see Figure 4.57).

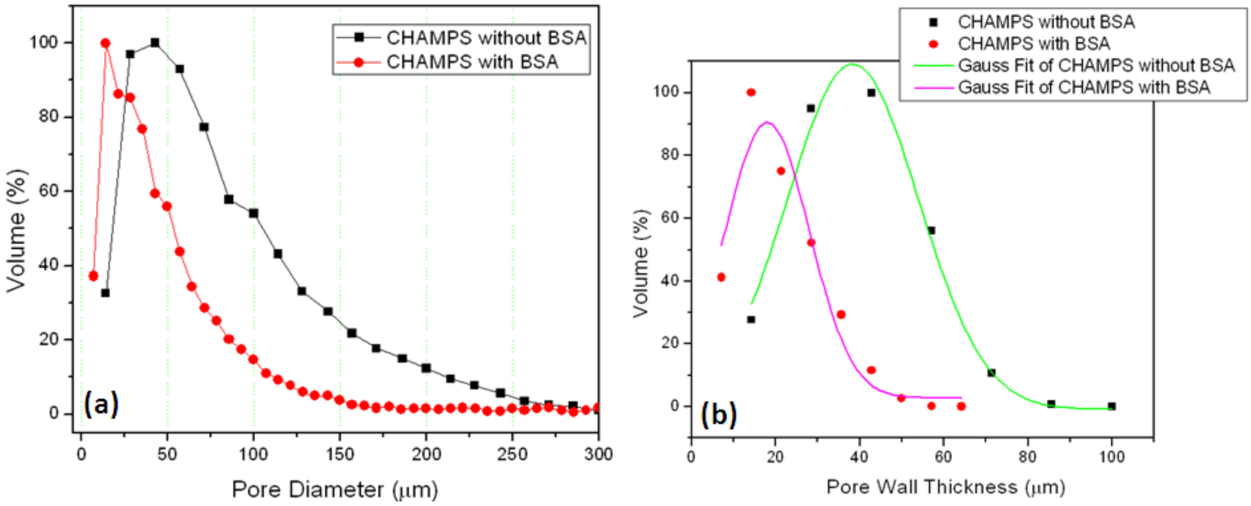

Figure 4.57 Plot of micro–CT scan analyzed data to quantify the pore size (a) and pore wall thickness (b) distribution for the as-synthesized CHAMPS and BSA protein-loaded CHAMPS.

More specifically, at least 6% of the total porosity has sizes of around 114 µm and at least 1% of the total pore volume has sizes of 228 µm, in case of as-synthesized scaffolds. Similarly, the volume fraction of the larger pores of 100 µm or above is around 1%. From the perspective of biomedical applications, the optimal pore size for bone tissue engineering scaffolds is around 40-200 µm [271,272]. Also, the pores of 40 µm or finer would help in the initial attachment of bone cells and the presence of larger pores of 100 µm would be useful for bone/ tissue ingrowth *in vivo*. The physical parameters observed from the micro-CT analysis of CHAMPS and BSA loaded CHAMPS are summarised in Table 4.11.

Table 4.11 Summary of the physical parameters describing the porous architecture of the CHAMPS scaffold loaded with and without BSA protein, as determined using extensive micro-CT analysis.

Physical parameters	CHAMPS without BSA Protein adsorption	CHAMPS with BSA Protein adsorption after 48h
Total Porosity	63.5 (%)	71.8 (%)
Total volume pore space	1.1 x 10^{11} (μm^3)	1.9 x 10^{10} (μm^3)
Fractal Dimension	2.61	2.54
Average Pore separation distance	86.8 μm	66.4μm
Degree of anisotropy	5.3	2.6
Connectivity Density	3.21 x 10^{-6} (μm^{-3})	3.30 x 10^{-5} (μm^{-3})

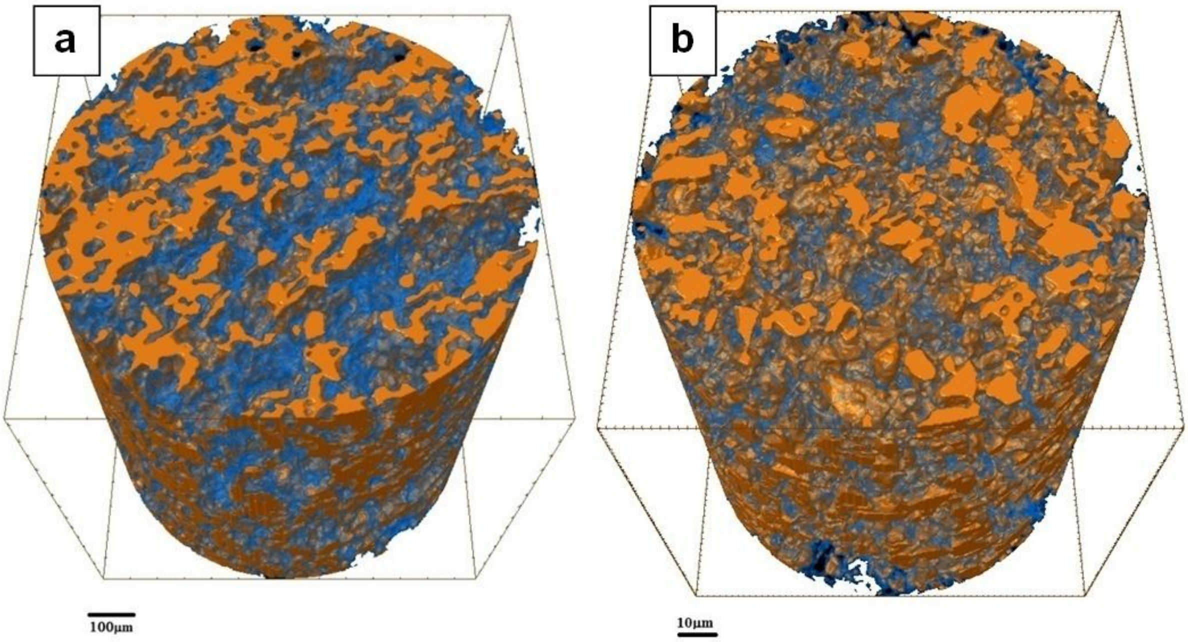

Figure 4.58 Representative 3D micro–CT scan image of the as-synthesized CHAMPS (a) and BSA protein loaded CHAMPS (b)

Since biological tissues are of different sizes, the extended tail in the pore size distribution of the currently investigated scaffold would be useful for better osseointegration property. As far as the total inter connectivity is concerned, the inter connectivity of pores increases from 528749 to 882899 with protein adsorption. Also, the connectivity density of the as synthesized scaffolds increases by one order of magnitude from 3.2 x 10^3 /mm^3 to 3.3 x 10^4 / mm^3 upon protein adsorption. Irregularity of the pore size can be assessed from the fractal dimensions. In the present case, the fractal dimension is 2.61 for as synthesized scaffolds and 2.53 for the protein loaded scaffolds. It is worthwhile to mention that the fractal dimension can be defined as a ratio indicating a statistical index of complexity as how the finer structural details in a designed object changes with the scale at which it the object is being characterized [273]. A more complex structure provides more the space filling and high value. Here, complexity of macroporous scaffold decreases from 2.61 to 2.53 when substantial amount of protein adsorbs on the surface of porous complex structure [274]. As per as the complexity of the pore size distribution concerned, the present investigated scaffold has a highly complex pore structure distribution as can be realized from the fractal dimension (FD) of 2.61. It is known that for a less complex porous scaffold FD=2 and for natural cancellous bone, FD=2.1 to 2.3 is expected [275]. Another important factor in the context of the pore architecture is degree of an isotropy (DA). Higher value of DA essentially indicates the anisotropic of pore orientation. In case of as processed scaffold, DA=5.3 and it is reduced to 2.6 after BSA protein absorption.

The large interconnectivity of 3.2X10^3 in case of as processed scaffold as well as 3.3X10^4 for protein loaded scaffold indicates that pores are highly connected and in fact, protein adsorption through complex pore favorably increases the interconnectivity density. It is important to mention here that high interconnectivity density would definitely facilitate the passage of nutrients, blood as well as waste products from the biological cells which would find easy passage to get into the available pore volume because of highly favorable pore architecture. From the above, it should be clear that highly interconnected porous microstructure with average pore diameter in the range of ~50-200 µm facilitated the attachment and delivery of BSA on hydrophobic gelatin-HA scaffold surfaces and enabled hydrophobic–hydrophobic surface conjugate interaction [270].

4.7.4 Secondary structure determination of BSA protein through FT-IR

FT-IR is a useful tool to determine the secondary structure, bond behaviour and phase purity. Details FT-IR spectrum of pure HA and major functional groups are provided in Figure 4.59(a) and Table 4.12 respectively. A characteristic vibrational band is detected at wavenumbers of 1024 and 559 cm^{-1} for PO_4^{3-} and 3344 and 610 cm^{-1} for OH^- in as-synthesized pure HA, respectively [276]. The weak stretching vibrational band at 1647 cm^{-1} for C=O bond and at 1463 cm^{-1} for N – H bond are attributed to the presence of gelatin in CHAMPS (Figure 4.59(b)) [277]. FT-IR spectrum of pure BSA is included in Figure 4.59(c). The weak vibrational band is observed at 2950 cm^{-1} for –CH stretching in pure BSA. A broad and strong stretching band at wavenumber of 3315 cm^{-1} is associated with –OH and –NH bond stretching of amino acid of BSA protein. The band at 1654 and 1542 cm^{-1} reflects the C=O stretching vibration for amide-I and N – H bending vibration for amide-II, because of α-helix structure of BSA [278]. FT-IR spectrum of adsorbed BSA on the surface of CHAMPS is shown in Figure 4.59(d). The adsorbed BSA on CHAMPS surface exhibits strong and more intense characteristic bands of N–H and C=O, which demonstrates the secondary structure of BSA protein without any denaturation. A strong and broad characteristic band at 3314 cm^{-1} is associated with –OH band for both HA and BSA. Also, the band at 603 cm^{-1} is related to the bending vibration of –OH group. The stretching and bending mode of vibration for PO_4^{3-} group of HA and CHAMPS are recorded at 1065 and 559 cm^{-1}, respectively [239]. Amide- I and Amide- II of polypeptide linkage of protein are also detected in case of BSA adsorbed CHAMPS and these results together confirmed the adhesion behaviour of protein molecule on the interconnected porous surface of CHAMPS scaffold.

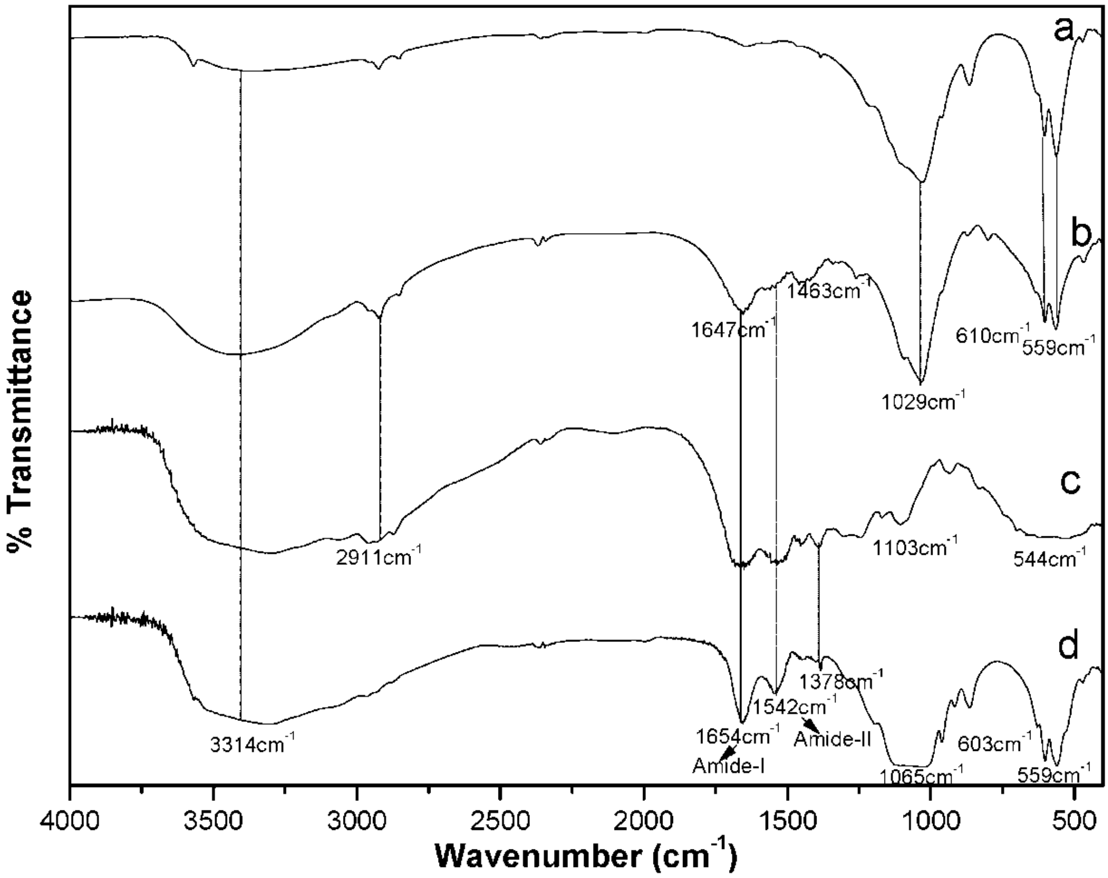

Figure 4.59 FT-IR spectrum of (a) NHR, (b) CHAMPS (c) BSA and (d) CHAMPS-BSA.

Table 4.12 Characteristic FT-IR bands for different groups present in of HA, CHAMPS, BSA and BSA adsorbed CHAMPS.

Functional Groups		HA	CHAMPS	BSA	BSA adsorbed
Groups	Mode of vibration	ν_o(cm^{-1})	ν_o(cm^{-1})	ν_o(cm^{-1})	CHAMPS ν_o(cm^{-1})
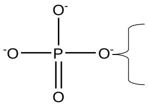	P–O stretching	1024 strong	1029 strong	-	1035 strong, broad
	P–O bending	559 weak	559 weak	-	603 weak
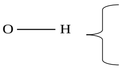	O–H stretching	3344 strong	3350 strong	3315 strong, broad	3314 strong, broad
	O–H bending	610 weak	605 weak	544 broad, strong	559 weak
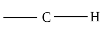	C–H stretching	–	2919 weak	2948 weak	2948 very weak
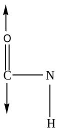	Amide-I stretching	–	1647 weak	1654 strong	1654 strong, intense
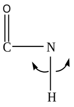	Amide-II stretching	–	1463 weak	1542 strong	1542 strong, intense

4.7.5 Release of loaded BSA from CHAMPS

The amount of BSA released from CHAMPS *in vitro* is estimated using UV-visible absorbance measurement. A maximum absorbance peak at 562 nm is shifted towards longer wavelength beyond 24h release time, as indicated in Figure 4.60. The initial rate of BSA release from CHAMPS is rapid from 6h up to 24h. However, same release remains at a steady state up to 240h, as shown in Figure 4.61. Overall, the BSA release kinetics analysis reveals around 60% release of BSA protein after 24h and this followed steady state Langmuir isotherm, as similar to protein adsorption phenomenon. However, the solution pH is constant for the entire release study. The release of BSA from CHAMPS is diffusion controlled in the first stage due to the smaller molecular weight of BSA [279]. The steady release rate, as recorded in the present case, might be beneficial for the proliferation of osteoblast cell in culture medium as well as in the drug delivery system. As far as the protein release is concerned, the CHAMPS scaffold clearly outperforms other biodegradable scaffolds as far as the BSA release over 10 days is concerned. For example, Jaklenec at al. [157] measured 40-50% of BSA release for PLGA microspheres loaded with 4.3% BSA *in vitro* over an incubation period of up to 10 days and BSA release does not attain the steady state even up to the period of 20 days. In contrast, the BSA release is around 70% after 24h incubation and reaches a steady state behaviour of 60% BSA release over an incubation period of 2-10 days. Such ability of the CHAMPS scaffold to release BSA proteins over a time span of 24h indicates that these scaffolds can be used for protein delivery applications.

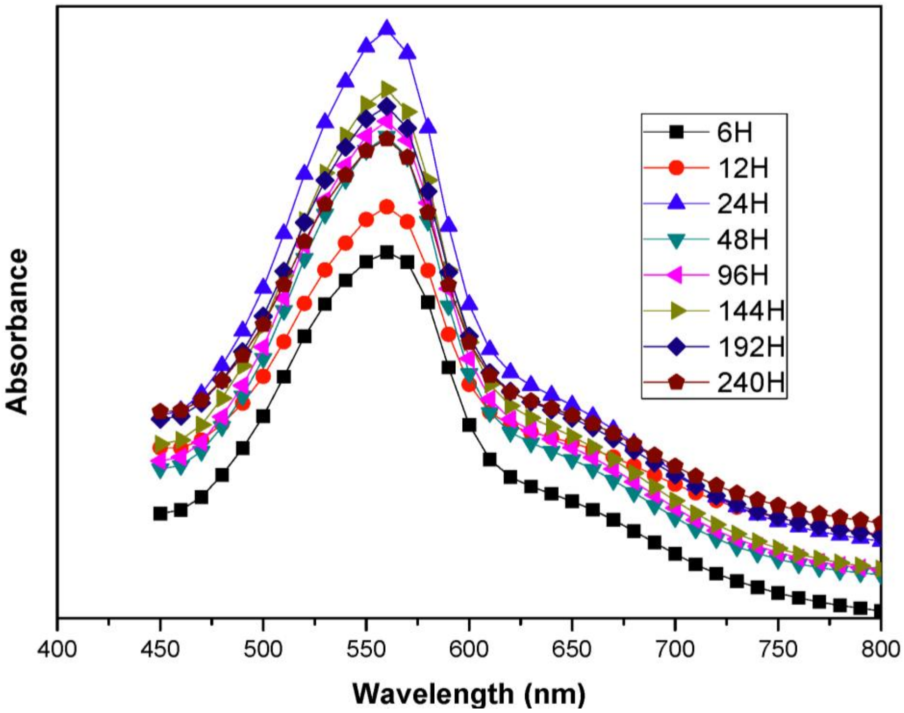

Figure 4.60 Release of BSA from CHAMPS UV study of absorbance with wavenumber.

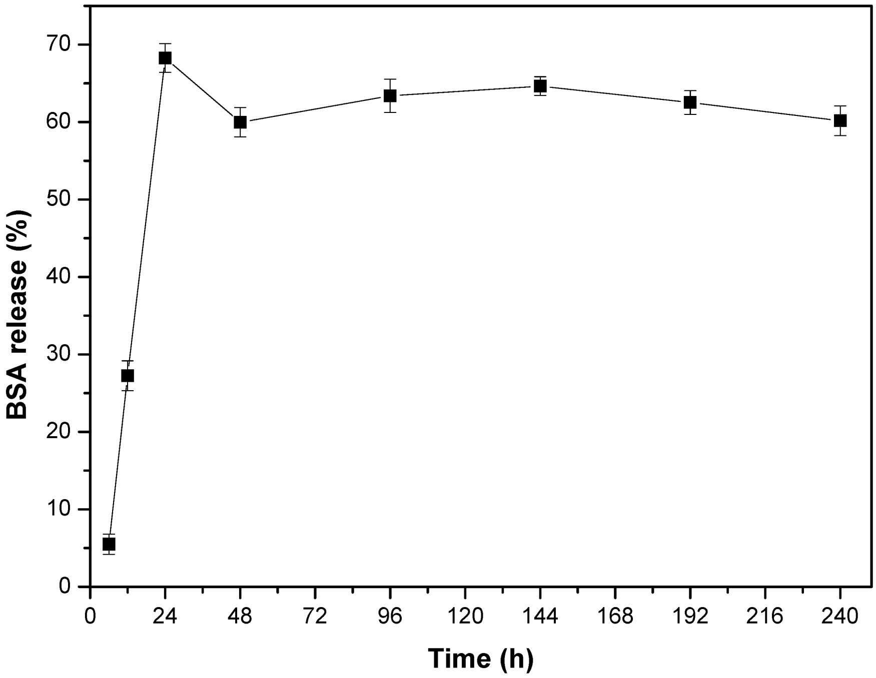

Figure 4.61 Amount of BSA released from the loaded BSA CHAMPS with time

4.7.6 Conclusion

HA-gelatine scaffold has higher affinity towards BSA molecules on its surface due to its porous structure. The result shows that 1gm of HA scaffold adsorbs about 51 mg of BSA protein. Peptide bond of protein remains unaltered after adherence with scaffold. Higher surface area and the interconnected porous structure of the scaffold facilitates the adherence of more amount of BSA compared to the as synthesized HA nanoparticles. BSA release is around 70% after 24h incubation, and reaches steady state behaviour after 60% BSA release over an incubation period of 2-10 days. Micro CT- analysis reveals that the inter connectivity increases with the adsorption of BSA on HA scaffold.

Chapter-5

Conclusions

Chapter 5 Conclusion

To fulfil the research objective, several steps have been considered and successfully executed to prepare HA nanoparticles and their dispersion; HA/protein conjugate and their adsorption/release; freeze casted macroporous scaffold and their compressive strength enhancement by cryogenic treatment; *in vitro* bioactivity, biodegradation, cytotoxicity, cell viability study and finally BSA protein adsorption/ release of CHAMPS scaffolds. Cumulative findings are summarized as follows:

i) Different morphologies of HA nanoparticles are synthesized through control of solution pH, temperature and Ca:P ratio from common precursors $Ca(CH_3COO)_2$ and KH_2PO_4.

ii) High hydroxyl ion concentration ($12.25 \geq pH \geq 10.5$) and low temperature (298K) favours isotropic non-confined spherical shape, intermediate concentration ($9.5 \geq pH \geq 7.75$) and low temperature (303K) initiates the anisotropic growth of rod particles and low concentration ($7 \geq pH \geq 5.25$), but high temperature (353K) accelerates the restricted expansion to fibroid morphology of HA.

iii) Spherical morphology is observed with an average diameter of around 10 nm, rod morphology with ~8 nm diameter and an aspect ratio of ~5 whereas fibroid morphology of HA shows micron size length with 30-40 nm diameter.

iv) Dispersion of HA nanoparticles prepared through the complexometric reaction with Na-citrate are stable for more than six months without appearance of sediments.

v) The as-synthesized nano metric HA particles are studied for the protein BSA adsorption and release. Rod morphology exhibits relatively higher BSA adsorption capacity compare to the counterpart spherical and fibroid HA nanoparticles. Higher surface area and Ca:P ratio of HA nanorod adsorbs 28 mg/(gm of HA) of BSA in 48h and around 75% release within 96h.

vi) The HA gelatin scaffold is successfully fabricated through the freeze casting method. Circular open pores are resulted with an average pore diameter ~150 µm. Compressive strength of the scaffold is observed within ~2 MPa.

vii) Compressive strength of the freeze casted scaffolds is improved by soaking in liquid nitrogen. The compressive strength of freeze casted high porous scaffold depends on curing time in liquid nitrogen environment. At cryogenic environment, polymeric matrix under goes phase transformation from ductile to brittle nature, which develops an optimum compressive strength with adequate pore diameter and pore volume.

viii) The combination of freeze casting and cryogenic curing for 5 h in liquid nitrogen develops HA-gelatin nanobiocomposite scaffolds with interconnected porosity and excellent protein adsorption / delivery property. Such scaffold exhibits 80 vol. % porosity with pores of 50-200 µm, moderate compressive strength 5 MPa and large strain failure up to 24%. Both the structure and compression response are similar to that of natural cancellous bone.

ix) Although higher extract concentration of HA scaffolds induces toxicity to L929 cells in an statistically significant manner compared to positive /negative controls, lower extract concentration up to 25% does not cause significant reduction in L929 cell viability. When compared to negative control, the reduction in cell viability has been tentatively explained as the result of release of small polymeric chains.

x) The biodegradation of scaffolds in tris-HCl solution exhibits a slow but systematic increase in weight loss over an incubation time period up to 7 days. Also, the nanosized apatite nodules are extensively formed within 7 days *in vitro*.

xi) HA gelatin scaffold has a higher affinity towards the adherence of BSA on surfaces due to its porous structure. Higher surface area and interconnected porous structure of the scaffold facilitates for adherence of more amount of BSA as compared to the synthesized HA nanopowders. One gram of the HA scaffold adsorbed 50 mg of BSA at 48h and 60 wt.% of release is observed in 24h of the loaded scaffold.

xii) The protein adsorption behaviour follows the classical Langmuir isotherm and the FT-IR analysis confirms that the secondary protein structure is retained upon adsorption for longer time period.

xiii) On the basis of the micro-computed tomography analysis, the investigated nano HA-gelatin scaffolds are characterized by the skewed pore size with a mean of 40 µm and an extended tail of up to 250 µm, as well as pore wall structure thickness varying in the range of 10-100 µm. A systematic shift towards finer pore size / pore wall distribution with BSA adsorption is also recorded. Further, the superior protein adsorption / delivery are attributed to the unique pore interconnectivity and anisotropy in addition to desired pore distribution.

xiv) The protein release study reveals a higher release rate of 60-70% from HA scaffolds and this is better than other biodegradable scaffolds.

In summary, the combination of protein adsorption and release study indicates that the scaffolds can be used as a suitable growth substrate for anchorage-dependent eukaryotic cells as well as for protein delivery. Also, the present study provided first comprehensive results to confirm the *in vitro* bioactivity, biodegradability and favourable protein interaction of CHAMPS scaffold.

5.1 Future Work

Apart from the brief conclusion on the current research program there are several scope for further improvement of performance of such nanobiocomposite macroporous scaffolds with consideration of following future work;

a) Detail study of HA nanoparticle growth kinetics and their crystal structures.
b) Protein molecule and direct cell adhesion phenomena study with respect to particle size and crystallinity.
c) Fabrication of freeze casting scaffold with varying gelatin content, gelatin molecular weight and freeze casting parameters.
d) Study on the effect of viscosity of slurry on pore morphologies and compressive strength.
e) Evaluation of CTE after cryotreatment and establish the polymeric phase transformation mechanism at that temperature.
f) Preparation of conjugate with other proteins (bone morphogenic protein, osteocalcine, human bovine serum albumin etc.) and study of their adsorption/release characteristics.
g) *In vivo* assessment of the scaffold in animal model.

References

References

[1] R.M. Deijkers, R.M. Bloem, P.C. Petit, R. Brand, S.W. Vehmeyer, M.R. Veen, Contamination of bone allografts:analysis of incidence and predisposing factors, J. Bone Joint Surg. 79 (1997) 161-166.

[2] G. Daculsi, O. Laboux, O. Malard, P. Weiss, Curent state of the art of biphasic calcium phosphate bioceramics, J. Mater. Sci. Mater. Med. 14 (2003) 195-200.

[3] A.I. Itala, H.O. Ylanen, C. Ekholm, K.H. Karlsson, H.T. Aro, Pore diameter of more than 100 micron is not requisite for bone ingrowth in rabbits, J. Biomed. Mater. Res. 58 (2001) 679-683.

[4] S.F. Hulbert, F.A.Young, R.S. Mathews, J.J. Klawitter, C.D. Talbert, F.H. Stelling, Potential of ceramic materials as permanently implantable skeletal prostheses, J. Biomed. Mater. Res. 4 (1970) 433-456.

[5] E.C. Moreno, M. Kresak, D.I. Hay, Adsorption of molecules of biological interest onto hydroxyapatite, Calcif. Tissue Int. 36 (1984) 48-59.

[6] S. Salmaso, S. Bersani, A. Semenzato, P.J. Caliceti, Nanotechnologies in protein delivery, J. Nanosci. Nanotechol. 6 (2006) 1-18.

[7] E. Engel, A. Michiardi, M. Navarro, Nanotechnology in regenerative medicine: the materials side, Trends Biotechnol. 26 (2007) 39-47.

[8] S.V. Dorozhkin, Bioceramics of calcium orthophosphates, Biomaterials 31 (2010) 1465-1485.

[9] L.L. Hench, Biomaterials: a forecast for the future, Biomaterials 19 (1998) 1419-1423.

[10] L.L. Hench, Bioceramics, J. Am. Ceram. Soc. 81 (1998) 1705-1728.

[11] A.S. Asran, S. Henning, G.H. Michler, Polyvinyl alcohol–collagen–hydroxyapatite biocomposite nanofibrous scaffold: Mimicking the key features of natural bone at the nanoscale level, Polymer 51 (2010) 868-876.

[12] S. Nimesh, A. Goyal, V. Pawar, S. Jayaraman, P. Kumar, R. Chandra, Y. Singh, K.C. Gupta, Polyethylenimine nanoparticles as efficient transfecting agents for mammalian cells, J. Control Release 110 (2006) 457-468.

[13] M. Peter, P.T. Sudheesh Kumar, N.S. Binulal, S.V. Nair, H. Tamura, R. Jayakumar, Development of novel a-chitin/nanobioactive glass ceramic composite scaffolds for tissue engineering applications, Carbohydrate Polym. 78 (2009) 926-931.

[14] C.Y. Xu, R. Inai, M. Kotaki, Electrospun nanofiber fabrication as synthetic extracellular matrix and its potential for vascular tissue engineering, Tissue Eng. 10 (2004) 1160–1168.

[15] L. Cerroni, R. Filocamo, M. Fabbri, C. Piconi, S. Caropreso, S.G. Condo, Growth of osteoblast-like cells on porous hydroxyapatite ceramics: an *in vitro* study, Biomol. Eng. 19 (2002) 119-124.

[16] C.A. Vacanti, The history of tissue engineering, J. Cell Mol. Med. 10 (2006) 569-576.

[17] D. Falconnet, G. Csucs, H.M. Grandin, Surface engineering approaches to micropattern surfaces for cell-based assays, Biomaterials 27 (2006) 3044-3063.

[18] B.L. Seal, T.C. Otero, A. Panitch, Polymeric biomaterials for tissue and organ regeneration, Mater. Sci. Eng. R Rep. 34 (2001) 147-230.

[19] B.D. Ratner, S.J. Bryant, Biomaterials: where we have been and where we are going, Annu. Rev. Biomed. Eng. 6 (2004) 41-75.

[20] R.Z. Wang, F.Z. Cui, H.B. Lu, H.B. Wen, C.L. Ma, H.D. Li, Synthesis of nanophase hydroxyapatite/collagen composite, J. Mater. Sci. Lett. 14 (1995) 490-492.

[21] S. Ber, G. Torun Köse, V. Hasirci, Bone tissue engineering on patterned collagen films: an *in vitro* study, Biomaterials 26 (2005) 1977-1986.

[22] E.H. Groeneveld, J.P. Van den Bergh, P. Holzmann, C.M. Ten Bruggenkate, D.B. Tuinzing, E.H. Burger, Mineralization processes in demineralized bone matrix grafts in human maxillary sinus floor elevations, J. Biomed. Mater. Res. 48 (1999) 393-402.

[23] F. Albert, T. Mahmet, Microengineering of cellular interactions, Annu. Rev. Biomed. Eng. 2 (2000) 227-256.

[24] H.W. Kang, Y. Tabata, Y. Ikada, Fabrication of porous gelatin scaffolds for tissue engineering, Biomaterials 20 (1999) 1339-1344.

[25] X.H. Liu, P.X. Ma, Polymeric scaffolds for bone tissue engineering, Annals. Biomed. Eng. 32 (2004) 477-486.

[26] A.G. Word, A. Courts, The science and technology of gelatin, London Academic Press(Ed.) (1977).

[27] A.W. Kenchington, Chemical modification of the side chains of gelatin, Biochem. J. 68 (1958) 458-468.

[28] Y.H. Koh, E.J. Lee, B.H. Yoon, J.H. Song, H.E. Kim, Effect of polystyrene addition on freeze casting of ceramic/camphene slurry for ultra-high porosity ceramics with aligned pore channels, J. Am. Ceram. Soc. 89 (2006) 3646-3653.

[29] J.P. Yang, G. Yang, G. Xu, S.Y. Fu, Cryogenic mechanical behaviors of MMT/epoxy nanocomposites, Comp. Sci.Technol 67 (2007) 2934-2940.

[30] L.F. Li, C.S. Hong, Y.Y. Li, Z. Zhang, Martensitic transformation in ZrO_2-based ceramics at cryogenic temperatures, Cryogenics 36 (1996) 7-l I.

[31] A.J. García, Get a grip: integrins in cell-biomaterial interactions, Biomaterials 26 (2005) 7525-7529.

[32] R. Barbucci, A. Magnani, Conformation of human plasma proteins at polymer surfaces: the effectiveness of surface heparinization, Biomaterials 15 (1994) 955-962.

[33] B.D.H. Ratner, A.S. Hoffman, F.J. Schoen, J.E. Lemons, Biomaterials science an introduction to materials in medicine, New York: Academic (2004).

[34] C.R. Jenney, J.M. Anderson, Adsorbed serum proteins responsible for surface dependent human macrophage behavior, J. Biomed. Mater. Res. 49 (2000) 435-447.

[35] J. Nakanishi, T. Takarada, K. Yamaguchi, M. Maida, Recent advances in cell micropatterning techniques for bioanalytical and biomedical sciences, Anal. Sci. 24 (2008) 67-72.

[36] B.D. Boyan, T.W. Hummert, D.D. Dean, Z. Schwartz, Role of material surfaces in regulating bone and cartilage cell response, Biomaterials 17 (1996) 137-146.

[37] K. Nakanishi, T. Sakiyama, K. Imamura, On the adsorption of proteins on solid surfaces, a common but very complicated phenomenon, J. Biosci. Bioeng. 91 (2001) 233-244.

[38] U.A. Stock, J.P. Vacanti, Tissue engineering: current state and prospects, Annu. Rev. Med. 52 (2001) 443-451.

[39] J. Panyam, V. Labhasetwar, Biodegradable nanoparticles for drug and gene delivery to cells and tissue, Adv. Drug Deliv. Rev. 55 (2003) 329-347.

[40] M.A. Wozniak, K. Modzelewska, L. Kwong, P.J. Keely, Focal adhesion regulation of cell behavior, Biochem. Biophys. Acta 1692 (2004) 103-119.

[41] J. Xie, S.M. Willerth, X. Li, M.R. Macewan, A. Rader, S.E. Sakiyama-Elbert, Y. Xia, The differentiation of embryonic stem cells seeded on electrospun nanofibers into neural lineages, Biomaterials 30 (2008) 354-362.

[42] R.G.T. Geesink, Osteoconductive coating for total joint arthroplasty, Clin. Orthop. Relat. Res. 395 (2002) 53-65.

[43] Z. Shi, X. Huang, Y. Cai, R. Tang, D. Yang, Size effect of hydroxyapatite nanoparticles on proliferation and apoptosis of osteoblast-like cells, Acta Biomater. 5 (2009) 338-345.

[44] W.L. Jaffe, D.F. Scott, Current concepts review: total hip arthroplasty with hydroxyapatite-coated prostheses, J. Bone Joint Surg. 78A (1996) 1918-1934.

[45] B. Palazzo, M.C. Sidoti, N. Roveri, A. Tampieri, M. Sandri, L. Bertolazzi, F. Galbusera, G. Dubini, P. Vena, R. Contro, Controlled drug delivery from porous hydroxyapatite grafts: An experimental and theoretical approach, Mater. Sci. Eng.- C 25 (2005) 207-213.

[46] F.W. Cooke, Ceramics in orthopedic surgery, Clin Orthop. Relat. Res. 276 (1992) 135-146.

[47] S. Koutsopoulos, Synthesis and characterization of hydroxyapatite crystals: a review study on the analytical methods, J. Biomed. Mater. Res. 62 (2002) 600-612.

[48] D.K. Dubey, V. Tomar, Role of hydroxyapatite crystal shape in nanoscale mechanical behavior of model tropocollagen–hydroxyapatite hard biomaterials, Mater. Sci. Eng.- C 29 (2009) 2133-2140.

[49] K. Anselme, M. Bigerelle, B. Noel, A. lost, P. Hardouin, Effect of grooved titanium substratum on human osteoblastic cell growth, J. Biomed. Mater. Res. 60 (2002) 529-540.

[50] L.L. Hench, J. Wilson, An introduction to bioceramics, World Scientific Singapore (1993).

[51] J. Malda, C.G. Frondoza, Microcarriers in the engineering of cartilage and bone, Trends Biotechnol. 26 (2006) 299-304.

[52] M.L. Alves da Silva, A. Crawford, J. Mundy, A. Martins, J.V. Araujo, P.V. Hatton, R.L. Reis, N.M. Neves, Evaluation of extracellular matrix formation in polycaprolactone and starch-compounded polycaprolactone nanofiber meshes when seeded with bovine articular chondrocytes, Tissue Eng. Part A 15 (2008) 377-385.

[53] B.P. Chan, K.W. Leong, Scaffolding in tissue engineering: general approaches and tissue-specific considerations, Eur. Spine J. 17 (2008) 467-479.

[54] G. Chen, T. Ushida, T. Tateishi, Scaffold design for tissue engineering, Macromol. Biosci. 2 (2002) 67-77.

[55] C. Liu, Z. Xia, J.T. Czernuszka, Design and developement of three dimentional scaffolds for tissue engineering, Chem. Eng. Res. des. 85 (2007) 1051-1064.

[56] E. Sachlos, J.T. Czernuszka, Making tissue engineering scaffold work. Review on the application of solid preform fabrication technology to the production of tissue engineering scaffold, Euro. Cell Mater. 5 (2003) 29-40.

[57] G. Wei, P.X. Ma, Structure and properties of nano-hydroxyapatite/polymer composite scaffolds for bone tissue engineering, Biomaterials 25 (2004) 4749-4757.

[58] T. Peters, F.W. Putman, The plasma proteins, Academic Press, San Diego (1975) 133-181.

[59] A.K. Wright, M.R. Thompson, Hydrodynamic structure of bovine serum albumin determined by transient electric birefringence, Biophys. J. 15 (1975) 137-141.

[60] S.S. Ozturk, B.O. Palsson, Examination of serum and bovine serum albumin as shear protective agents in agitated cultures of hybridoma cells, J. Biotechnol. 18 (1991) 13-28.

[61] M. Evecen, S. Pabucccuoglu, S. Alkan, I.K. Ileri, The effects of various BSA levels in different media on development in *in vitro* culture of mouse embryos, Turk. J. Vet. Anim. Sci. 28 (2004) 337-342.

[62] D. Gospodarowicz, C.R. Ill, Do plasma and serum have different abilities to promote cell growth, Proc. Nat. Acad. Sci. 77 (1980) 2726-2730.

[63] G.M. Lindner, J.F. Dickey, J.R. Hill, Effect of bovine serum albumin concentration on the development of ovine embryos *in vitro,* J. Anim. Sci. 57 (1983) 466-472.

[64] S. Curry, H. Mandelkow, P. Brick, N. Franks, Crystal structure of human serum albumin complexed with fatty acid reveals an asymmetric distribution of binding sites, Nat. Struct. Biol. 5 (1998) 827-835.

[65] G.D. Fullerton, K.M. Kanal, I.L. Cameron, Osmotically unresponsive water fraction on proteins: Non-ideal osmotic pressure of bovine serum albumin as a function of pH and salt concentration, Cell Biol. Int. 30 (2006) 86-92.

[66] M. De Castro, G. Orive, A.R. Gascon, R.M. Hernandez, J.L. Pedraz, Evaluation of human serum albumin as a substitute of foetal bovine serum for cell culture, Int. J. Pharm. 310 (2006) 8-14.

[67] R.G. Ham, Albumin replacement by fatty acids in clonal growth of mammalian cells, Science 140 (1963) 802-803.

[68] J. Hritz, S. Kascakova, J. Ulicny, P. Miskovsky, Influence of structure of human, rat, and bovine serum albumins on binding properties of photoactive drug hypercin, Biopolymers 67 (2002) 251-254.

[69] R. Solaro, F. Chiellini, A. Battisti, Targeted delivery of protein drugs by nanocarriers, Materials 3 (2010) 1928-1980.

[70] L. Brannon-Peppas, J.O. Blanchette, Nanoparticle and targeted systems for cancer therapy, Adv. Drug Deliv. Rev. 56 (2004) 1649-1659.

[71] G. Avila, K. Misch, P. Galindo-Moreno, H.L.Wang, Implant surface treatment using biomimetic agents, Implant Dent. 18 (2009) 17-26.

[72] D.K. Malik, S. Baboota, A. Ahuja, S. Hasan, J. Ali, Recent advances in protein and peptide drug delivery systems, Curr. Drug Deliv. 4 (2007) 141-151.

[73] T.J. Webster, C. Ergun, R.H. Doremus, R.W. Siegel, R. Bizios, Enhanced functions of osteoblasts on nanophase ceramics, Biomaterials 21 (2000) 1803-1810.

[74] M. Thanou, J.C. Verhoef, H. E. Junginger, Oral drug absorption enhancement by chitosan and its derivatives, Adv. Drug Deliv. Rev. 50 (2001) 91-101.

[75] K.A. Janes, P. Calvo, M.J. Alonso, Polysaccharide colloidal particles as delivery systems for macromolecules, Adv. Drug. Deliv. Rev. 47 (2001) 83-97.

[76] J.S. Temenoff, A.G. Mikos, Biomaterials the intersection of biology and material science, Wiley-Interscience, Publication Pearson: South Asia (2009) pp 279.

[77] R.D. Tilton, C.R. Robertson, A.P. Gast, Manipulation of hydrophobic interactions in protein adsorption, Langmuir 7 (1991) 2710-2718

[78] K. Kandori, S. Sawai, Y. Yamamotc, H. Saito, T. Ishikawa, Adsorption of albumin on calcium hydroxylapatite, Colloid Surf. 68 (1992) 283-289.

[79] R.A. Latour, Biomaterials: protein–surface interactions, Encyclopedia Biomater. Biomed. Eng. (2005) 1-15.

[80] M.J. Gorbunoff, The interaction of proteins with hydroxyapatite. I. Role of protein charge and structure, Anal. Biochem. 136 (1984) 425-432.

[81] C.O. Weill, S. Biri, A. Adib, P. Erbacher, A practical approach for intracellular protein delivery, Cytotechnology 56 (2008) 41-48.

[82] M.C. Morris, J. Depollier, J. Mery, F. Heitz, G. Divita, A peptide carrier for the delivery of biologically active proteins into mammalian cells, Nat. Biotechnol. 19 (2001) 1173-1176.

[83] O. Zelphati, Y. Wang, S. Kitada, J.C. Reed, P.L. Felgner, J. Corbeil, Intracellular delivery of proteins with a new lipidmediated delivery system, J. Biol. Chem. 276 (2001) 35103-35110.

[84] P. Saalik, A. Elmquist, M. Hansen, K. Padari, K. Saar, K. Viht, U. Langel, M. Pooga, Protein cargo delivery properties of cell-penetrating peptides. A comparative study, Bioconjug. Chem. 15 (2004) 1246-1253.

[85] J.C. Elliott, R.M. Wilson, S.E.P. Dowker, Apatite structures, Adv. X-ray Anal. 45 (2002) 171-181.

[86] M.V. Regi, J.M. González-Calbet, Calcium phosphates as substitution of bone tissues, Prog. Solid State Chem. 32 (2004) 1-31.

[87] J.C. Elliott, Calcium phosphate biominerals, Rev. Mineral. Geochem. 48 (2002) 427-453.

[88] S. Náray-Szabó, Structure of apatite, Zeit. Krist. 75 (1930) 387-398.

[89] M. Mehmel, structure of apatite Zeit. Krist. 75 (1930) 323-331.

[90] J.C. Elliott, Structure and chemistry of the apatites and other calcium orthophosphates, Amsterdam Elsevier (1994).

[91] S.B. Hendricks, W.L. Hill, The inorganic constitution of bone, Science 96 (1942) 255-257.

[92] T. Nakano, K. Kaibara, Y. Tabata, N. Nagata, S. Enomoto, E. Marukawa, Y. Umakoshi, Unique alignment and texture of biological apatite crystallites in typical calcified tissues analyzed by microbeam X-Ray diffractometer system, Bone 31 (2002) 479–487.

[93] A. Siddharthan, S.K. Seshadri, T.S. Sampath Kumar, Influence of microwave power on nanosized hydroxyapatite particles, Scripta Mater. 55 (2006) 175-178.

[94] R. Murugan, T.S. Sampath Kumar, K.P. Rao, Fluorinated bovine hydroxyapatite: preparation and characterization, Mater. Lett. 57 (2002) 429- 433.

[95] W. Feng, L. Mu-sen, L. Yu-peng, Q. Yong-xin, A simple sol–gel technique for preparing hydroxyapatite nanopowders, Mater. Lett. 59 (2005) 916- 919.

[96] C. Qiu, X. Xiao, R. Liu, Biomimetic synthesis of spherical nano-hydroxyapatite in the presence of polyethylene glycol, Ceram. Int. 34 (2008) 1747-1751.

[97] Y. Zhang, J. Lu, A simple method to tailor spherical nanocrystal hydroxyapatite at low temperature, J. Nanopart. Res. 9 (2007) 589-594.

[98] S. Meejoo, W. Maneeprakorn, P. Winotai, Phase and thermal stability of nanocrystalline hydroxyapatite prepared via microwave heating, Thermochem. Acta 447 (2006) 115-120.

[99] A. Wang, D. Liu, H.B. Yin, Size-controlled synthesis of hydroxyapatite nanorods by chemical precipitation in the presence of organic modifiers, Mater. Sci. Eng. C 27 (2007) 865-869.

[100] Y. Liu, D. Hou, G. Wang, A simple wet chemical synthesis and characterization of hydroxyapatite nanorods, Mater. Chem. Phy. 86 (2004) 69-73.

[101] S. Suzuki, M. Ohgaki, M. Ichiyanagi, M. Ozawa, Preparation of needle-like hydroxyapatite, J. Mater. Sci. Lett. 17 (1998) 381-383.

[102] K. Furuichi, Y. Oaki, H. Imai, Preparation of nanotextured and nanofibrous hydroxyapatite through dicalcium phosphate with gelatin, Chem. Mater. 18 (2006) 229-234.

[103] C. Zhang, J. Yang, Z. Quan, P. Yang, C. Li, Z. Hou, J. Lin, Hydroxyapatite nano and microcrystals with multiform morphologies: Controllable synthesis and luminescence properties, Crystal Growth & Design 9 (2009) 2725-2733.

[104] B. Li, B. Guo, H. Fan, X. Zhang, Preparation of nano-hydroxyapatite particles with different morphology and their response to highly malignant melanoma cells *in vitro*, Appl. Surf. Sci. 255 (2008) 357-360.

[105] H.G. Zhang, Q. Zhu, Y. Wan, Morphologically controlled synthesis of hydroxyapatite with partial substitution of fluorine, Chem. Mater. 17 (2005) 5824-5830.

[106] I.S. Neira, Y.V. Kolenko, O.I. Lebedev, G.V. Tendeloo, H.S. Gupta, F. Guitian, M. Yoshimura, An effective morphology control of hydroxyapatite crystals via hydrothermal synthesis, Crystal Growth & Design 9 (2009) 466-474.

[107] P.W. Brown, M. Fulmer, Kinetics of hydroxyapatite formation at low temperature, J. Am. Ceram. Soc. 74 (1991) 934-940.

[108] J. Tan, M. Chen, J. Xi, Water-dispersible hydroxyapatite nanorods synthesized by a facile method, Appl. Surf. Sci. 255 (2009) 8774-8779.

[109] Y. Han, X. Wang, S. Li, A simple route to prepare stable hydroxyapatite nanoparticles suspension, J. Nanopart. Res. 11 (2009) 1235-1240.

[110] L. Borum-Nicholas, O.C. Wilson Jr, Surface modification of hydroxyapatite. Part I. Dodecyl alcohol, Biomaterials 24 (2003) 3671-3679.

[111] C. Li, L. Zhao, J. Han, R. Wang, C. Xiong, X. Xie, Synthesis of citrate-stabilized hydrocolloids of hydroxyapatite through a novel two-stage method: A possible aggregates–breakdown mechanism of colloid formation, J. Colloid Interf. Sci. 360 (2011) 341-349.

[112] M. Sadat-Shojai, M. Atai, A. Nodehi, L.N. Khanlar, Hydroxyapatite nanorods as novel fillers for improving the properties of dental adhesives: Synthesis and application, Dental Mater. 26 (2010) 471-482.

[113] F. Macritchie, The Adsorption of proteins at the solid/liquid interface, J. Colloid Interf. Sci. 38 (1972) 484-488.

[114] Y. Boonsongrit, H. Abe, K. Sato, M. Naito, M. Yoshimur, H. Ichikawa, Y. Fukumori, Controlled release of bovine serum albumin from hydroxyapatite microspheres for protein delivery system, Mater. Sci. Eng.- B 148 (2008) 162-165.

[115] M. Shirkhanzadeh, G.Q. Liu, Biocompatible delivery systems for osteoinductive proteins: immobilization of L-lysine in micro-porous hydroxyapatite coatings, Mater. Lett. 21 (1994) 115- 118.

[116] X. Wu, X. Song, D. Li, J. Liu, P. Zhang, X. Chen, Preparation of mesoporous nano-hydroxyapatite using a surfactant template method for protein delivery, J. Bionic Eng. 9 (2012) 224-233.

[117] M. Iafisco, P. Sabatino, I.G. Lesci, M. Prat, L. Rimondini, N. Roveri, Conformational modifications of serum albumins adsorbed on different kinds of biomimetic hydroxyapatite nanocrystals, Colloid Surf. B: Biointerf. 81 (2010) 274-284.

[118] Q. Hou, D.W. Grijpma, J. Feijen, Porous polymeric structures for tissue engineering prepared by a coagulation, compression moulding and salt leaching technique, Biomaterials 24 (2003) 1937-1947.

[119] S.H. Li, J.R. de Wijn, P. Layrolle, K. de Groot, Novel method to manufacture porous hydroxyapatite by dual- phase mixing, J. Am. Ceram. Soc. 86 (2003) 65-72.

[120] M. Potoczek, Hydroxyapatite foams produced by gelcasting using agarose, Mater. Lett. 62 (2008) 1055-1057.

[121] D. Tadic, F. Beckmann, K. Schwarz, M. Epple, A novel method to produce hydroxyapatite objects with interconnectingporosity that avoids sintering, Biomaterials 25 (2004) 3335-3340.

[122] H.R. Ramay, M. Zhang, Biphasic calcium phosphate nanocomposite porous scaffolds for load-bearing bone tissue engineering, Biomaterials 25 (2004) 5171-5180.

[123] S.H. Kwon, Y.K. Jun, S.H. Hong, I.S. Lee, H.E. Kim, Calcium phosphate bioceramics with various porosities and dissolution rate, J. Am. Ceram. Soc. 85 (2002) 3129-3131.

[124] S.K. Swain, S. Bhattachryya, D. Sarkar, Preparation of porous scaffold from hydroxyapatite powders, Mater. Sci. Eng. - C 31 (2011) 1240-1244.

[125] N. Koc, M. Timucin, F. Korkusuz, Fabrication and characterization of porous tricalcium phosphate ceramics, Ceram. Int. 30 (2004) 205-211.

[126] K. Lin, J. Chang, Y. Zeng, W. Qian, Preparation of macroporous calcium silicate ceramics, Mater. Lett. 58 (2004) 2109-2113.

[127] E. Ebaretonbofa, J.R.G. Evans, High porosity hydroxyapatite foam scaffolds for bone substitute, J. Por. Mater. 9 (2002) 257-263.

[128] X. Huang, X. Miao, Novel porous hydroxyapatite prepared by combining H_2O_2 foaming with PU sponge and modified with PLGA and bioactive glass, J. Biometer. Appl. 21 (2007) 351-374.

[129] S. Deville, E. Saiz, A.P. Tomsia, Freeze casting of hydroxyapatite scaffolds for bone tissue engineering, Biomaterials 27 (2006) 5480-5489.

[130] Q. Fu, M.N. Rahaman, F. Dogan, B.S. Bal, Freeze casting of porous hydroxyapatite scaffolds. II. Sintering, microstructure and mechanical behavior, J. Biomed. Mater. Res. Part B: Appl. Biomater. 86 (2008) 514-522.

[131] E. Landi, F. Valentini, A. Tampieri, Porous hydroxyapatite/gelatine scaffolds with ice-designed channel-like porosity for biomedical applications, Acta Biomater. 4 (2008) 1620-1626.

[132] S. Panzavolta, M. Fini, A. Nicoletti, B. Bracci, K. Rubini, R. Giardino, A. Bigi, Porous composite scaffolds based on gelatin and partially hydrolyzed a-tricalcium phosphate, Acta Biomater. 5 (2009) 636-643.

[133] Y. Zhang, K. Zuo, Y.P. Zeng, Effects of gelatin addition on the microstructure of freeze-cast porous hydroxyapatite ceramics, Ceram. Int. 35 (2009) 2151-2154.

[134] K.H. Zuo, Y.P. Zeng, D. Jiang, Effect of polyvinyl alcohol additive on the pore structure and morphology of the freeze-cast hydroxyapatite ceramics, Mater. Sci. Eng.-C 30 (2010) 283-287.

[135] M. Azami, M. Rabiee, F. Moztarzadeh, Glutaraldehyde crosslinked gelatin/hydroxyapatite nanocomposite scaffold, engineered via compound techniques, Polym. Composites 31 (2010) 2112-2120.

[136] H.W. Kim, J.C. Knowles, H.E. Kim, Hydroxyapatite and gelatin composite foams processed via novel freeze-drying and crosslinking for use as temporary hard tissue scaffolds, J. Biomed. Mater. Res. 72 (2005) 136-145.

[137] S.W. Yook, H.E. Kim, B.H. Yoon, Y.M. Soon, Y.H. Koh, Improvement of compressive strength of porous hydroxyapatite scaffolds by adding polystyrene to camphene-based slurries, Mater. Lett. 63 (2009) 955-958.

[138] S. Heinemann, C. Heinemann, M. Jager, J. Neunzehn, H.P. Wiesmann, T. Hanke, Effect of silica and hydroxyapatite mineralization on the mechanical properties and the biocompatibility of nanocomposite collagen scaffolds, ACS Appl. Mater. Interfaces 3 (2011) 4323-4331.

[139] A. Asefnejad, A. Behnamghader, M.T. Khorasani, B. Farsadzadeh, Polyurethane/fluor-hydroxyapatite nanocomposite scaffolds for bone tissue engineering. Part I: morphological, physical and mechanical characterization, Inter. J. Nanomed. 6 (2011) 93-100.

[140] R.J. Kane, R.K. Roeder, Effects of hydroxyapatite reinforcement on the architecture and mechanical properties of freeze-dried collagen scaffolds, J. Mech. Behav. Biomed. Mater. 7 (2012) 41-49.

[141] J.P. Yang, Z.K. Chen, G. Yang, S.Y. Fu, L. Ye, Simultaneous improvements in the cryogenic tensile strength, ductility and impact strength of epoxy resins by a hyperbranched polymer, Polymer 49 (2008) 3168-3175.

[142] Z.K. Chen, J.P. Yang, Q.Q. Ni, S.Y. Fu, Y.G. Huang, Reinforcement of epoxy resins with multi-walled carbon nanotubes for enhancing cryogenic mechanical properties, Polymer 50 (2009) 4753-4759.

[143] H. Yamaoka, K. Miyata, O. Yano, Cryogenic properties of engineering plastic films, Cryogenics 35 (1995) 787-789.

[144] H.M. Kim, T. Himeno, T. Kokubo, T. Nakamura, Process and kinetics of bonelike apatite formation on sintered hydroxyapatite in a simulated body fluid, Biomaterials 26 (2005) 4366-4373.

[145] H. Takadama, H.M. Kim, T. Kokubo, T. Nakamura, Mechanism of biomineralization of apatite on a sodium silicate glass: TEM-EDX study *in vitro*, Chem. Mater. 13 (2001) 1108-1113.

[146] T. kokubo, Apatite formation on surfaces of ceramics, metals and polymers in body environment, Acta. Mater. 46 (1998) 2519-2527.

[147] A.C. Tas, Synthesis of biomimetic Ca-hydroxyapatite powders at 37 ^{o}C in synthetic body fluids, Biomaterials 21 (2000) 1429-1438.

[148] M. Okazaki, Y. Moriwaki, T. Aoba, Y. Doi, J. Takahashi, Dissolution rate behavior of fluoridated apatite pellets, J. Dent. Res. 60 (1981) 1907-1911.

[149] L. Xu, Z.C. Xiong, D. Yang, L.F. Zhang, J. Chang, C.D. Xiong, Preparation and *in vitro* degradation of novel bioactive polylactide/wollastonite scaffolds, J. Appl. Polym. Sci. 114 (2009) 3396-3406.

[150] A.B. Martínez-Valencia, G.C. Torre, A.D. Moller, H.E. Ponce, M.A. Medina, Study of bioactivity, biodegradability and mechanical properties of polyurethane/nano-hydroxyapatite hybrid composites, Inter. J. Phy. Sci. 6 (2011) 6681-6691.

[151] F.C. Filho, G.C. Menezes, Osteoblasts attachment and adhesion: how bone cells fit fibronectin-coated surfaces, Mater. Sci. Eng.- C 24 (2004) 637-641.

[152] J.M. Oliveira, M.T. Rodrigues, S.S. Silva, P.B. Malafaya, M.E. Gomes, C.A. Viegas, I.R. Dias, J.T. Azevedo, J.F. Mano, R.L. Reis, Novel hydroxyapatite/chitosan bilayered scaffold for osteochondral tissue-engineering applications: Scaffold design and its performance when seeded with goat bone marrow stromal cells, Biomaterials 27 (2006) 6123-6137.

[153] H.W. Kim, J.C. Knowles, H.E. Kim, Hydroxyapatite and gelatin composite foams processed via novel freeze-drying and crosslinking for use as temporary hard tissue scaffolds, J. Biomed. Mater. Res. 72A (2005) 136-145.

[154] L.D. Silvio, M.J. Dalby, W. Bonfield, Osteoblast behaviour on HA/PE composite surfaces with different HA volumes, Biomaterials 23 (2002) 101-107.

[155] M.J. Dalby, M.V. Kayser, W. Bonfield, L. Di Silvio, Initial attachment of osteoblasts to an optimised HAPEX topography, Biomaterials 23 (2002) 681-690.

[156] H. Guo, J. Su, J. Wei, H. Kong, C. Liu, Biocompatibility and osteogenicity of degradable Ca-deficient hydroxyapatite scaffolds from calcium phosphate cement for bone tissue engineering, Acta Biomater. 5 (2009) 268-278.

[157] A. Jaklenec, E. Wan, M.E. Murray, E. Mathiowitz, Novel scaffolds fabricated from protein-loaded microspheres for tissue engineering, Biomaterials 29 (2008) 185-192.

[158] N. Mohan, P.D. Nair, Y. Tabata, A 3D biodegradable protein based matrix for cartilage tissue engineering and stem cell differentiation to cartilage, J. Mater. Sci. Mater. Med. 20 (2009) 49-60.

[159] S.R. Lyu, Y.C. Kuo, M.H. Lin, W.H. Hsieh, C.W. Chuang, Application of albumin-grafted scaffolds to promote neocartilage formation, Colloid Surf. B: Biointer. 91 (2012) 296- 301.

[160] A.A. Sawyer, K.M. Hennessy, S.L. Bellis, The effect of adsorbed serum proteins, RGD and proteoglycan-binding peptides on the adhesion of mesenchymal stem cells to hydroxyapatite, Biomaterials 28 (2007) 383-392.

[161] Y.C. Kuo, C.Y. Chung, Chondrogenesis in scaffolds with surface modification of elastin and poly-l-lysine, Colloid Surf. B: Biointer. 93 (2012) 85- 91.

[162] K.L. Kilpadi, P.L. Chang, S.L. Bellis, Hydroxylapatite binds more serum proteins, purified integrins and osteoblast precursor cells than titanium or steel, J. Biomed. Mater. Res. 57 (2001) 258-267.

[163] S. Segvich, H.C. Smith, L.N. Luong, D.H. Kohn, Uniform deposition of protein incorporated mineral layer on three-dimensional porous polymer scaffolds, J. Biomed. Mater. Res. B Appl. Biomater. 84 (2008) 340–349.

[164] J.L. Simon, E.D. Rekow, V.P. Thompson, H. Beam, J.L. Ricci, J.R. Parsons, MicroCT analysis of hydroxyapatite bone repair scaffolds created via three-dimensional printing for evaluating the effects of scaffold architecture on bone ingrowth, J. Biomed. Mater. Res. 85A (2008) 371-377.

[165] A.M. Henslee, P.P. Spicer, D.M. Yoon, M.B. Nair, V.V. Meretoj, K.E. Witherel, J.A. Jansen, A.G. Mikos, F.K. Kasper, Biodegradable composite scaffolds incorporating an intramedullary rod and delivering bone morphogenetic protein-2 for stabilization and bone regeneration in segmental long bone defects, Acta Biomater. 7 (2011) 3627-3637.

[166] G.H. Jeffery, J. Bassett, J. Mendham, R.C. Denney, (Ed.), Vogel’s test book of quantitative chemical analysis, Longman, UK, 1984.

[167] P. Scherrer, Gottinger Nachrichten Vol. 2 (1918) p 98.

[168] A.L. Petterson, The Scherrer formula for X-Ray particle size determination, Phys. Review 56 (1969) 978-982.

[169] L.B. McCusker, R.B. Von Dreele, D.E. Cox, D. Louer, P. Scardi, Rietveld refinement guidelines, J. Appl. Cryst. 32 (1999) 36-50.

[170] S. Brunauer, P.H. Emmett, E. Telle, Adsorption of gases in multimolecular layers, Bur. Chem. Soil 60 (1938) 309-319.

[171] L. Jelinek, E. sz Kovats, True surface areas from nitrogen adsorption experiments, Langmuir 10 (1994) 4225-4231

[172] D. Holzmann, D. Holzinger, G. Hesser, T. Schmidt, G. Knor, Hydroxyapatite nanoparticles as novel low-refractive index additives for the long-term UV-photoprotection of transparent composite materials, J. Mater.Chem. 19 (2009) 8102-8106.

[173] D.A. Skoog et al., Principles of instrumental analysis, Thomson Brooks/Cole 6th ed (2007) 169-173.

[174] S.M. Kelly, N.C. Price, The use of circular dichroism in the investigation of protein structure and function, Cur. Protein Peptide Sci. 1 (2000) 349-384.

[175] M. Yang, Y. Shuai, W. He, S. Min, L. Zhu, Preparation of porous scaffolds from silk fibroin extracted from the silk gland of bombyx mori, Int. J. Mol. Sci. 13 (2012) 7762-7775.

[176] E.W. Washburn, The dynamics of capillary flow, Phy. Review 17 (1921) 273-283.

[177] F.P. Beer, E.R. Johnston, J. Dewolf, D. Mazurek, Mechanics of materials, McGraw Hill (2009) p.56.

[178] T. Kokubo, H. Takadama, How useful is SBF in predicting *in vivo* bone bioactivity?, Biomaterials 27 (2006) 2907-2915.

[179] P. Li, K. Nakanishi, T. Kokubo, K. de Groot, Induction and morphology of HA precipitated from metastable simulated body fluids on sol-gel prepared silica, Biomaterials 14 (1993) 963-968.

[180] I.S.O. 10993-5, Biological evaluation of medical products, test for *in vitro* cytotoxicity Part 5 (1999).

[181] H. Liu, T.J. Webster, Mechanical properties of dispersed ceramic nanoparticles in polymer composites for orthopedic applications, Int. J. Nanomed. 5 (2010) 299-313.

[182] D. Khang, M. Sato, R.L. Price, A.E. Ribbe, T.J. Webster, Selective adhesion and mineral deposition by osteoblasts on carbon nanofiber patterns, Int. J. Nanomed. 1 (2006) 65-72.

[183] T. Welzel, W. Meyer-Zaika, M. Epple, Continuous preparation of functionalised calcium phosphate nanoparticles with adjustable crystallinity, Chem. Commun. 10 (2004) 1204-1205.

[184] F.C.M. Driessens, R.M.H. Verbeeck, FL: CRC Press, Boca Raton, Biominerals (1990) p 179-209.

[185] S. Weiner, H.D. Wagner, The material bone: Structure-mechanical function relations, Annu. Rev. Mater. Sci. 28 (1998) 271-298.

[186] K. Kandori, T. Kuroda, S. Togashi, E. Katayama, Preparation of calcium hydroxyapatite nanoparticles using microreactor and their characteristics of protein adsorption, J. Phys. Chem. B 115 (2011) 653-659.

[187] T. Matsumoto, K.I. Tamine, R. Kagawa, Y. Hamada, M. Okazaki, J. Takahashi, Different behaviour of implanted hydroxyapatite depending on morphology, size and crystalinity J. Ceram. Soc. Jpn. 114 (2006) 760-762.

[188] W. Zhang, S.S Liao, F.Z Cui, Hierarchical self-assembly of nano-fibrils in mineralized collagen, Chem. Mater. 15 (2003) 3221-3226.

[189] W. Bu, Y. Xu, N. Zhang, H. Chen, J. Shi, Controlled construction of uniform pompon-shaped microarchitectures self-assembled from single-crystalline lanthanum molybdate nanoflakes, Langmuir 23 (2007) 9002-9007.

[190] S.K. Swain, D. Sarkar, A comparative study: Hydroxyapatite spherical nanopowders and elongated nanorods, Ceram. Int. 37 (2011) 2927-2930.

[191] R.M. Wilson, J.C. Elliott, S.E.P. Dowker, L.M. Rodriguez-Lorenzo, Rietveld refinements and spectroscopic studies of the structure of Ca-deficient apatite, Biomaterials 26 (2005) 1317-1327.

[192] M. Okazaki, M. Taira, J. Takahashi, Rietveld analysis and Fourier maps of hydroxyapatite, Biomaterials 18 (1997) 795-799.

[193] H. Morgan, R.M. Wilson, J.C. Elliott, S.E.P. Dowker, P. Anderson, Preparation and characterisation of monoclinic hydroxyapatite and its precipitated carbonate apatite intermediate, Biomaterials 21 (2000) 617-627.

[194] R.M. Wilson, J.C. Elliott, S.E.P. Dowker, Rietveld refinement of the crystallographic structure of human dental enamel apatites, Am. Mineralogist 84 (1999) 1406-1414.

[195] S.J. Gadaleta, E.P. Paschalis, F. Betts, R. Mendelsohn, A.L. Boskey, Fourier transform Infrared Spectroscopy of the solution-mediated conversion of amorphous calcium phosphate to hydroxyapatite: New correlations between X-ray diffraction and Infrared Data, Calif. Tissue Int. 58 (1996) 9-16.

[196] E. Boanini, G. Gazzano, K. Rubini, A. Bigi, Composite nanocrystals provide new insight on alendronate interaction with hydroxyapatite structure, Adv. Mater. 19 (2007) 2499-2502.

[197] D. Sarkar, D. Mohapatra, S. Roy, S. Bhattacharya, S. Adak, N.K. Mitra, Synthesis and characterization of sol-gel derived ZrO_2 doped Al_2O_3 nanopowder, Ceram. Int. 33 (2007) 1275-1282.

[198] K.S.W. Sing, D.H. Everett, R.A.W. Hawl, L. Mosco, R.A. Parroti, J. Rouquerol, T. SieMiewska, Reporting physisorption data for gas/solid systems with special reference to the determination of surface area and porosity, Pure Apply. Chem. 57 (1985) 603-619.

[199] S.K. Swain, S.V. Dorkhkin, D. Sarkar, Synthesis and dispersion of hydroxyapatite nanopowders, Mater. Sci. Eng. - C 32 (2012) 1237-1240.

[200] R. Tang, L. Wang, C.A. Orme, T. Bonstein, P.J. Bush, G.H. Nancollas, Dissolution at the nanoscale: Self-preservation of biominerals, Angew. Chem. Int. Ed. 43 (2004) 2697-2701.

[201] E. Sada, H. Kumazawa, Y. Murakami, Hydrothermal synthesis of crystalline hydroxyapatite ultrafine particles, Chem. Eng. Commun. 103 (1991) 57-64.

[202] Y. Fang, D.K. Agrawal, D.M. Roy, R. Roy, P.W. Brown, Ultrasonically accelerated synthesis of hydroxyapatite, J. Mater. Res. 7 (1992) 2294-2298.

[203] A. Yoshida, silica nucleation, polymerization and growth preparation of monodispersed sol, Adv. Chem. 234 (1994) 51-66.

[204] M. Supova, Problem of hydroxyapatite dispersion in polymer matrices: a review, J. Mater. Sci: Mater. Med. 20 (2009) 1201-1213.

[205] S. Chander, D.W. Fuerstenau, On the dissolution and interfacial properties of hydroxyapatite, Colloids Surf. 4 (1982) 101-120.

[206] C. García, C. García, C. Paucar, Controlling morphology of hydroxyapatite nanoparticles through hydrothermal microemulsion chemical synthesis, Inorg. Chem. Comm. 20 (2012) 90-92.

[207] S.K. Swain, D. Sarkar, Study of bovine serum albumin adsorption and release on hydroxyapatite nanoparticles, Appl. Surf. Sci. 286 (2013) 99-103.

[208] K. Tomoda, H. Ariizumi, T. Nakaji, K. Makino, Hydroxyapatite particles as drug carriers for proteins, Colloids Surf. B: Biointerf. 76 (2010) 226-235.

[209] H. Liu, T.J. Webster, Ceramic/polymer nanocomposites with tunable drug delivery capability at specific disease sites, J. Biomed. Mater. Res. A 93 (2010) 1180-1192.

[210] L. Cerroni, R. Filocamo, M. Fabbri, C. Piconi, S. Caropreso, S.G. Condo, Growth of osteoblast-like cells on porous hydroxyapatite ceramics: an *in vitro* study, Biomol. Eng. 19 (2002) 119-124.

[211] M.W. Saltzman, S.P. Baldwin, Materials for protein delivery in tissue engineering, Adv. Drug. Deliv. Rev. 33 (1998) 71-86.

[212] J. Ellingsen, A study on the mechanism of protein adsorption to TiO_2, Biomaterials 12 (1991) 593-596.

[213] C.A. van Blitterswijk, J.J. Grote, W. Kuijpers, C.J.G. Blok-van Hoek, W.T. Deams, Bioreactions at the tissue/hydroxyapatite interface, Biomaterials 6 (1985) 243-251.

[214] L.M. Pandey, S.K. Pattanayek, D. Delabouglise, Properties of adsorbed bovine serum albumin and fibrinogen on self-assembled monolayers, J. Phys. Chem. C 117 (2013) 6151−6160.

[215] A.J. Brenner, E.D. Harris, A quantitative test for copper using bicinchoninic acid, Anal. Biochem. 226 (1995) 80-84.

[216] T. Peters, F.A. Blumenstock, Copper-binding properties of bovine serum albumin and its amino-terminal peptide fragment, J. Biol. Chem. 242 (1967) 1574-1578.

[217] R. Kessler, D. Fanestil, Interference by lipids in the determination of protein using bicinchoninic acid, Anal. Biochem. 159 (1986) 138-142.

[218] D.H. Wassell, R.C. Hall, G. Embery, Adsorption of bovine serum albumin onto hydroxyapatite, Biomoterials 16 (1995) 697-702.

[219] E.C. Reynolds, A. Wong, Effect of adsorbed protein on hydroxyapatite zeta potential and streptococcus mutans adherence, Infect. Immun. 39 (1983) 1285-1290.

[220] E. Mavropoulos, A.M. Costa, L.T. Costa, C.A. Achete, A. Mello, J.M. Granjeiro, A.M. Rossi, Adsorption and bioactivity studies of albumin onto hydroxyapatite surface, Colloid Surf. B: Biointerf. 83 (2011) 1-9.

[221] S. Shimabayashi, Y. Tanizawa, K. Ishida, Effect of phosphorylated organic compounds on the adsorption of bovine serum albumin by hydroxyapatite, Chem. Pharm. Bull. 39 (1991) 2183-2188.

[222] M.A. Rauschmann, T.A. Wichelhaus, V. Stirnal, E. Dingeldein, L. Zichner, R. Schnettler, V. Alt, Nanocrystalline hydroxyapatite and calcium sulphate as biodegradable composite carrier material for local delivery of antibiotics in bone infections, Biomaterials 26 (2005) 2677-2684.

[223] J. Xie, C. Riley, M. Kumar, K. Chittur, FT-IR/ATR study of protein adsorption and brushite transformation to hydroxyapatite, Biomaterials 23 (2002) 3609-3616.

[224] W. Kabsch, C. Sander, Dictionary of protein secondary structure: Pattern recognition of hydrogen-bonded and geometrical features, Biopolymers 22 (1983) 2577-2637.

[225] N. Brandes, P.B. Welzel, C. Werner, L.W. Kroh, Adsorption-induced conformational changes of proteins onto ceramic particles:Differential scanning calorimetry and FT-IR analysis, J. Colloid Interf. Sci. 299 (2006) 56-69.

[226] S. Dasgupta, S.S. Banerjee, A. Bandyopadhyay, S. Bose, Zn- and Mg-doped hydroxyapatite nanoparticles for controlled release of protein, Langmuir 26 (2010) 4958-4964.

[227] B. Yuan, K. Murayama, H. Yan, Study of thermal dynamics of defatted bovine serum albumin in D_2O solution by fourier transform infrared spectra and evolving factor analysis, Appl. Spectroscopy 61 (2007) 921-927.

[228] A. Gebregeorgis, C. Bhan, O. Wilson, D. Raghavan, Characterization of silver/bovine serum albumin (Ag/BSA) nanoparticles structure: Morphological, compositional, and interaction studies, J. Colloid Interf. Sci. 389 (2013) 31-41.

[229] A. Michnik, Thermal stability of bovine serum albumin DSC study, J.Ther. Anal. Calor. 71 (2003) 509-519.

[230] Z. Yang, C. Zhang, Adsorption/desorption behavior of protein on nanosized hydroxyapatite coatings: A quartz crystal microbalance study, Appl. Surf. Sci. 255 (2009) 4569-4574.

[231] T. Goto, T. Narushima, K. Ueda, Biological and biomedical coatings handbook - processing and characterization, CRC Press, ISBN1439849951 (2011).

[232] G. Daculsi, Biphasic calcium phosphate concept applied to artificial bone implant coating and injectable bone substitute, Biomaterials 19 (1998) 1473-1478.

[233] P. Sepulveda, J.G.P. Binner, S.O. Rogero, Production of porous hydroxyapatite by a gel casting of foams and cytotoxic evaluation, J. Biomed. Mater. Res. 50 (2000) 27-34.

[234] R.A. White, J.N. Weber, E.W. White, Replamineform:A new process for preparing porous ceramics, metal and polymer prosthetic materials, Science 176 (1972) 922-924.

[235] R. Mishra, B. Basu, A. Kumar, Physical and cytocompatibility properties of bioactive glass–polyvinyl alcohol–sodium alginate biocomposite foams prepared via sol–gel processing for trabecular bone regeneration, J. Mater. Sci: Mater. Med. 20 (2009) 2493-2500.

[236] H.W. Kang, Y. Tabata, Y. Ikada, Fabrication of porous gelatin scaffolds for tissue engineering, Biomaterials 20 (1999) 1339-1344.

[237] M.C. Dalconi, C. Meneghini, S. Nuzzo, R. Wenk, S. Mobilio, Structure of bioapatite in human foetal bones: An X-ray diffraction study, Nucl. Instr. Meth. Phys. Res. B 200 (2003) 406-410.

[238] K. Pal, A.K. Banthia, D.K. Majumdar, Biomedical evaluation of polyvinyl alcohol-gelatin esterified hydrogel for wound dressing, J. Mater. Sci: Mater. Med. 18 (2007) 1889-1894.

[239] A. Slosarczyk, Z. Paszkiewicz, C. Paluszkiewicz, FT-IR and XRD evaluation of carbonated hydroxyapatite powders synthesized by wet methods, J. Mol. Stru. 744-747 (2005) 657-661.

[240] S. Mobini, J. Javadpour, M. Hosseinalipour, M. Ghazi-Khansari, A. Khavandi, H.R. Rezaie, Synthesis and characterisation of gelatin–nano hydroxyapatite composite scaffolds for bone tissue engineering, Adv. Appl. Ceram. 107 (2008) 4-8.

[241] S. Sanchez-Salcedo, F. Balas, I. Izquierdo-Barba, M. Vallet-Regi, *In vitro* structural changes in porous HA/β-TCP scaffolds in simulated body fluid, Acta Biomater. 5 (2009) 2738-2751.

[242] A. Fritsch, L. Dormieux, C. Hellmich, J. Sanahuja, Mechanical behavior of hydroxyapatite biomaterials: An experimentally validated micromechanical model for elasticity and strength, J. Biomed. Mater. Res. A 88 (2009) 149-161.

[243] N. Degirmenbasi, D.M. Kalyon, E. Birinci, Biocomposites of nanohydroxyapatite with collagen and poly(vinyl alcohol), Colloid Surf. B: Biointer. 48 (2006) 42-49.

[244] G.S. Sailaja, P. Ramesh, H.K. Varma, Ultrastructural evaluation of *in vitro* mineralized calcium phosphate phase on surface phosphorylated poly(hydroxy ethyl methacrylate-co-methyl methacrylate), J. Mater. Sci. Mater. Med. 21 (2010) 1183-1193.

[245] M.C. Van der Meulen, K.J. Jepsen, B. Mikic, Understanding bone strength: Size is n't everything, Bone 29 (2001) 101-104.

[246] R.W. McCalden, J.A. McGeough, C.M. Court-Brown, Age-related changes in the compressive strength of cancellous bone: The relative importance of changes in density and trabecular architecture, J. Bone. Joint. Surg. Am. 79 (1997) 421-427.

[247] S. Kalmodia, S. Goenka, T. Laha, D. Lahiri, B. Basu, K. Balani, Microstructure, mechanical properties, and in vitro biocompatibility of spark plasma sintered hydroxyapatite–aluminum oxide–carbon nanotube composite, Mater. Sci. Eng- C 30 (2010) 1162-1169.

[248] S.M. Pawde, K. Deshmukh, Characterization of polyvinyl alcohol/gelatin blends hydrogel films for biomedical applications, J. Appl. Polym. Sci. 109 (2008) 3431-3437.

[249] J.B. Schutz, Properties of composite materials for cryogenic applications, Cryogenics 38 (1998) 3-12.

[250] D. Ceccaldi, M. Ghelfenstein, H. Szwarc, Thermal expansion of crystals and phonon momentum, J. Phys.C: Solid State Phys. 8 (1975) 417.

[251] M. Wang, W. Bonfield, Chemically coupled hydroxyapatite- polyethylene composites structure and properties, Biomaterials 22 (2001) 1311-1320.

[252] J. Zollfrank, J. Friedrich, Structural relaxation patterns of an optically labelled polymer at cryogenic temperatures, Polymer 30 (1989) 231-236.

[253] M.G. Worster, J.S. Wettlaufer, Natural convection, solute trapping and channel formation during solidification of saltwater, J. Phys. Chem. B 101 (1997) 6132-6136.

[254] S. Chatterjee, H.B. Bohidar, Effect of cationic size on gelation temperature and properties of gelatin hydrogels, Inter. J. Biol. Macromol. 35 (2005) 81-88.

[255] P.E. Fabian, T.S. Bauer-McDaniel, R.P. Reed, Low temperature thermal properties of composite insulation systems, Cryogenics 35 (1995) 719-722.

[256] L.L. Hench, Biomaterials, Science 208 (1980) 826-831.

[257] D. Sarkar, S.K. Swain, S. Adhikari, B.S. Reddy, H.S. Maiti, Synthesis, mechanical properties and bioactivity of nanostructured zirconia, Mater. Sci. Eng.-C 33 (2013) 3413-3417.

[258] S. Nath, R.Tu, T. Goto, Apatite formation in Hanks' solution on β-Ca_2SiO_4 films prepared by MOCVD, Surf. Coatings Technol. 206 (2011) 172-177.

[259] F. Unger, M. Wittmar, T. Kissel, Branched polyesters based on poly[vinyl-3-(dialkylamino)alkylcarbamate-co-vinyl acetate-co-vinyl alcohol]-graftpoly (D,L-lactide-co-glycolide): Effects of polymer structure on cytotoxicity, Biomaterials 28 (2007) 1610-1619.

[260] J. Arends, J. Schuthof, J. Christoffersen, Inhibition of enamel demineralization by albumin *in vitro*, Caries Res. 20 (1986) 337-340.

[261] O. Mahony, J.R. Jones, Porous bioactive nanostructured scaffolds for bone regeneration: a sol-gel solution, Nanomed. 3 (2008) 233-245.

[262] L. Brannon-Peppas, J.O. Blanchette, Nanoparticle and targeted systems for cancer therapy, Adv. Drug Deliv. Rev. 56 (2004) 1649-1659.

[263] K. Kandori, S. Mizumoto, S. Toshima, M. Fukusumi, Y. Morisada, Effects of heat treatment of calcium hydroxyapatite particles on the protein adsorption behavior, J. Phys. Chem. B 113 (2009) 11016-11022.

[264] B. Basu, S.K. Swain, D. Sarkar, Cryogenically cured hydroxyapatite–gelatin nanobiocomposite for bovine serum albumin protein adsorption and release, RSC Adv. 3 (2013) 14622-14633.

[265] P.K. Smith, R.I. Krohn, G.T. Hermanson, A.K. Mallia, F.H. Gartner, M.D. Provenzano, E.K. Fujimoto, N.M. Goeke, B.J. Olson, D.C. Klenk, Measurement of protein using bicinchoninic acid, Anal. Biochem. 150 (1985) 76-85.

[266] D. Zhang, N. Udagawa, I. Nakamura, H. Murakami, S. Saito, K. Yamasaki, Y. Shibasaki, N. Morii, S. Narumiya, N. Takahashi, T. Suda, The small GTP-binding protein, rho p21, is involved in bone resorption by regulating cytoskeletal organization in osteoclasts, J. Cell Sci. 108 (1995) 2285-2292.

[267] D.T.H. Wassell, R.C. Hall, G. Embery, Adsorption of bovine serum albumin onto hydroxyapatite, Biomoterials 16 (1995) 697-702.

[268] H. Kim, H.E. Kim, V. Salih, Stimulation of osteoblast responses to biomimetic nanocomposites of gelatin-hydroxyapatite for tissue engineering scaffolds, Biomaterials 26 (2005) 5221-5230.

[269] F. Zhao, W.L. Grayson, T. Ma, B. Bunnell, W.W. Luc, Effects of hydroxyapatite in 3-D chitosan-gelatin polymer network on human mesenchymal stem cell construct development, Biomaterials 27 (2006) 1859-1867.

[270] K. Takaoka, M. Koezuka, H. Nakahara, Telopeptide-depleted bovine skin collagen as a carrier for bone morphogenetic protein, J. Orthop. Res. 9 (1991) 902-907.

[271] S.N. Park, J.C. Park, H.O. Kim, M.J. Song, H. Suh, Charachterization of porous collagen/hyaluronic acid scaffold modified by 1-ethyl-3-(3-dimehylaminopropyl) cabodiimide cross-linking, Biomaterials 23 (2002) 1205-1212.

[272] S.B. Lee, Y.H. Kim, M.S. Chong, Y.M. Lee, Preparation and characteristics of hybrid scaffolds composed of beta-chitin and collagen, Biomaterials 25 (2004) 2309-2317.

[273] F. Kenneth, Fractal geometry, New York: Wiley. ISBN 978-0-470-84862-3 (2003) p.308.

[274] J.W. Baish, R.K. Jain, Fractals and cancer, Cancer Res. 60 (2000) 3683-3688.

[275] T. Uchiyama, T. Tanizawa, H. Muramatsu, N. Endo, H.E. Takahashi, Three-dimensional microstructural analysis of human trabecular bone in relation to its mechanical properties, Bone 25 (1999) 487-491.

[276] Z.H. Cheng, A. Yasukawa, K. Kandori, T. Ishikawa, FT-IR study on incorporation of CO_2 into calcium hydroxyapatite, J. Chem. Soc. - Faraday Trans. 94 (1998) 1501-1505.

[277] S. Dasgupta, A. Bandyopadhyay, S. Bose, Reverse micelle-mediated synthesis of calcium phosphate nanocarriers for controlled release of bovine serum albumin, Acta Biomater. 5 (2009) 3112-3121.

[278] S. Krimm, J. Bandekar, Vibrational spectroscopy and conformation of peptides, polypeptides and proteins, Adv. Protein. Chem. 38 (1986) 181−364.

[279] A. Cosijns, C. Vervaet, J. Luyten, S. Mullens, F. Siepmann, L.V. Hoorebeke, B. Masschaele, V. Cnudde, J.P. Remon Porous hydroxyapatite tablets as carriers for low-dosed drugs, Eur. J. Pharm. Biophar. 67 (2007) 498-506.

List of publications based on the research work

Peer Reviewed International Journal

1. **S.K. Swain**, S.V. Dorozhkin and D. Sarkar, Synthesis and dispersion of hydroxyapatite nanopowders, ***Mater. Sci. Eng.-C*** 32 (2012) 1237-1240. **(IF-2.404)**
2. **S.K. Swain** and D. Sarkar, Preparation of nanohydroxyapatite-gelatin porous scaffold and mechanical properties at cryogenic environment, ***Mater. Lett.*** 92 (2013) 252-254. **(IF-2.224)**
3. B. Basu, **S.K. Swain** and D. Sarkar, Cryogenically cured hydroxyapatite-gelatin nanobiocomposite for bovine serum albumin protein adsorption/release, ***RSC Advances*** 3(2013) 14622-14633. **(IF-2.562)**
4. **S.K. Swain** and D. Sarkar, Study of bovine serum albumin adsorption and release on hydroxyapatite nanoparticles, ***Appl. Sur. Sci.*** 286 (2013) 99-103. **(IF-2.112)**
5. **S.K. Swain** and D. Sarkar, Fabrication, cryotreatment, *in vitro* cytotoxicity and cell viability study of hydroxyapatite-gelatin macroporous scaffold, **Mater. Sci. Eng. C** (2013) under review.

Conference proceeding

1. S.K. Swain and D. Sarkar, Freeze dried porous hydroxyapatite scaffold for tissue engineering, National symposium on materials and processing-2012, BARC, Mumbai, India.

Curriculum Vitae

Sanjaya Kumar Swain
S/O: Bipra Swain
At-Ustali, P.O- Chingudikhol, Via-Kodala,
Dist. - Ganjam (Odisha), Pin – 761032, India.
Email: skswaincr@gmail.com, Mobile:+91-9861581183
Date of Birth: 03.02.1984

Education: Ph.D. (Ceramic Engg.), (2013) NIT Rourkela, Odisha, India

M.Tech. (Ceramic Engg.), (2009) NIT Rourkela, Odisha, India

M.Sc. (Analytical Chemistry), (2006) Berhampur University, Odisha, India

B.Sc. (Chemistry) (2004) Berhampur University, Odisha, India

Research Interest: Biomaterials, Porous materials, Nanomaterials

Technical Exposure: Publication-10, Conference-2

Work experience: A dissertation submitted in partial fulfilment of the requirements for the degree of Master of Technology "Processing of porous hydroxyapatite scaffold".

Publication:

Peer Reviewed International Journal

1. **S.K. Swain**, S. Bhattacharyya and D. Sarkar, Preparation of porous scaffold from hydroxyapatite powders, ***Mater. Sci. Eng.-C*** 31(2011)1240-1244. **(IF-2.404)**
2. **S.K. Swain** and D. Sarkar, A comparative study: Hydroxyapatite spherical nanopowder and elongated nanorods, ***Ceram. Int.***37 (2011) 2927-2930. **(IF-1.789)**
3. **S.K. Swain**, S.V. Dorozhkin and D. Sarkar, Synthesis and dispersion of hydroxyapatite nanopowders, ***Mater. Sci. Eng.-C*** 32(2012)1237-1240. **(IF-2.404)**
4. **S.K. Swain** and S. Bhattacharyya, Preparation of high strength macro porous hydroxyapatite scaffold, ***Mater. Sci. Eng. -C*** 33 (2013) 67-71. **(IF-2.404)**
5. **S.K. Swain** and D. Sarkar, Preparation of nanohydroxyapatite – gelatin porous scaffold and mechanical properties at cryogenic environment, ***Mater. Lett.*** 92 (2013) 252-254. **(IF-2.224)**
6. D. Sarkar, **S.K. Swain**, S. Adhikari, B.S. Reddy and H.S. Maiti, Synthesis, mechanical properties and bioactivity of nanostructured zirconia, ***Mater. Sci. Eng.-C*** 33 (2013) 3413-3417. **(IF-2.404)**
7. B. Basu, **S.K. Swain** and D. Sarkar, Cryogenically cured hydroxyapatite-gelatin nanobiocomposite for bovine serum albumin protein adsorption/release, ***RSC Advances*** 3(2013) 14622-14633. **(IF-2.562)**
8. **S.K. Swain** and D. Sarkar, Study of bovine serum albumin adsorption and release on hydroxyapatite nanoparticles, ***Appl. Sur. Sci.*** 286 (2013) 99-103. **(IF-2.221)**
9. **S.K. Swain**, S. Bhattacharyya, D. Sarkar, Fabrication of porous hydroxyapatite scaffold via polyethylene glycol and polyvinyl hydrogel state, ***Mater. Res. Bull.*** (2013) Under Review.
10. **S.K. Swain** and D. Sarkar, Fabrication, cryotreatment, *in vitro* cytotoxicity and cell viability study of hydroxyapatite-gelatin macroporous scaffold, ***Mater. Sci. Eng. C*** (2013) Under Review.

Conference proceeding

1. S.K. Swain, S. Bhattacharyya and D. Sarkar, Processing of porous hydroxyapatite scaffold, International conference on recent trends in material characterization (2010) NIT Surathakal, India.
2. S.K. Swain and D. Sarkar, Freeze dried porous hydroxyapatite scaffold for tissue engineering, National symposium on materials and processing-2012, BARC, Mumbai, India